



ALMA MATER STUDIORUM
UNIVERSITÀ DI BOLOGNA

*Dottorato di Ricerca in Geofisica
XXIV ciclo*

InSAR deformation measurements of the earthquake cycle in transcurrent tectonic domains, analytical and analog modeling

Settore concorsuale di afferenza: 04/A4/Geo10: Geofisica della terra solida

Candidato

Giuseppe Pezzo

Coordinatore scuola Dottorato

Michele Dragoni

Relatore

Stefano Salvi

Esame finale Anno 2012

Abstract

I used classical and multitemporal InSAR (Interferometric Synthetic Aperture Radar) methods to measure the crustal deformation associated to the interseismic and coseismic phases of the earthquake-cycle. In this work I did not consider crustal deformation caused by the viscoelastic rebound, and I focused my attention to the interseismic and, in part, to the coseismic phases.

I applied the SBAS DInSAR method to the Mattinata Fault (MF) (Southern Italy) and to the Doruneh Fault System (DFS) (Central Iran). In the first case, I processed an ascending and descending dataset observing limited internal deformation. SAR data allow to determine the right lateral kinematic pattern of the MF and to highlight a compressional deformation pattern in the northern sector of the fault and an extensional one in the southern. Using the Okada model I inverted the observed velocity field: although my model fits the velocity maps only roughly, it defines a right lateral strike slip solution for the MF. Even if it fits the DInSAR data within the uncertainties, the modeled slip rate of 13-15 mm yr⁻¹ seems too high with respect to the 0.8-0.9 mm yr⁻¹ velocities from the geological record. Concerning the Western termination of Doruneh Faults (WFZ), the three processed datasets confirm the main left lateral transcurrent kinematics of this fault segment, but reveal a compressional component as well, in agreement with recent field works. My analytical model fits successfully the observed data and quantifies the slip in ~4 mm yr⁻¹ of pure horizontal movement and ~2.5 mm yr⁻¹ of pure vertical displacement (first quantitative estimation). The horizontal velocity is compatible with geological record.

The use of the elastic dislocation model of Okada has demonstrated to be a useful tool to investigate the interseismic source parameters where the majority

of the ground deformation can be attributed to a geologically well defined fault; it allows to discern the deformation character at regional scale when it can be referred to a well defined tectonic structure, but it is inadequate to fit more local deformation, especially for poorly known sources.

I applied classic SAR interferometry to the October–December 2008 Balochistan (Central Pakistan) seismic swarm; I discerned the different contributions of the three $M_w > 5.7$ earthquakes using classical DInSAR technique and ENVISAT SAR images. I determined fault positions, lengths, widths, depths and slip distributions, constraining the other source parameters using different Global CMT solutions. A well constrained solution has been obtained for the 09 December 2008 aftershock, whereas concerning the October 2008 mainshocks, I tested two possible fault solutions derived from those proposed by the Global CMT catalogue. Since the RMS values and the displacement distributions are very similar for two solutions, it is not possible to favor one of the solutions without independent constraints derived from geological data. The difficulty in the identification of the 2008 sources discouraged the analysis of the pre-event SAR data, since any interseismic signal detected in the area would have been even more difficult to model than the coseismic one.

Finally I approached the study of the earthquake-cycle in transcurrent tectonic domains using analog modeling; I successfully joined in the same model, the study of finite deformation in transcurrent tectonic domains with the study of the earthquake cycle and sudden dislocation (earthquakes), using alimentary gelatins like crust analog material. A large number of seismic cycles was reproduced and even if I present here only preliminary results, a characteristic earthquake is recognizable in terms of displacement, coseismic velocity and recurrence time.

Table of contents

Abstract	1
Table of contents	3
Acknowledgements	7
Introduction	9
1. Observing and modeling the seismic cycle	15
1.1. The concept of seismic cycle	15
1.2. Observations and models of the seismic cycle in transcurrent domains	20
1.2.1. Time-independent elastic half-space models	20
1.2.2. Viscoelastic slip models	23
1.2.3. 3-D evolution of the local stress field.	28
1.2.4. Others approach	30
1.3. The Parkfield experiment	32
2. SAR interferometry for the measurement of the seismic cycle	37
2.1. Differential SAR Interferometry	37
2.1.1. Side-looking real-aperture radar	38
2.1.2. Synthetic Aperture Radar (SAR) images	41
2.1.3. Amplitude of SLM image	46
2.1.4. The phase of SLM image	47
2.1.5. SAR Image Geometry	47

2.1.6.	SAR Interferometry: fundamental principle	48
2.1.7.	SAR Interferometry: limits	49
2.1.8.	SAR Interferometry: contribution from viewing geometry	49
2.1.9.	SAR Interferometry: contribution from topography	51
2.1.10.	SAR Interferometry: surface deformation	52
2.1.11.	SAR Interferometry: the atmospheric path delay	54
2.2.	Multitemporal DInSAR techniques	56
2.2.1.	Methods	56
2.2.2.	Difference and similarity among methods	59
2.3.	The SBAS technique	60
2.4.	Post-processing techniques	63
2.4.1.	Data validation	64
2.4.2.	Residual ramp removal	64
2.4.3.	North and up component analysis	65
3.	Modeling of crustal deformation	69
3.1.	Modeling approaches	69
3.1.1.	Analytical models	69
3.1.2.	Numerical models	70
3.1.3.	Analog modeling	74
3.2.	Seismic source inversion	75
3.3.	Interseismic deformation modeling	77
4.	Interseismic deformation analysis of the Gargano area (Southern Italy)	81
4.1.	Introduction	81
4.2.	Geological and seismotectonic framework	82
4.3.	Seismicity	85
4.4.	DInSAR Data Processing	87
4.5.	Modeling	94
4.6.	Discussion	101

4.7. Conclusion	105
5. Interseismic deformation analysis of the Doruneh fault (Central Iran)	107
5.1. Introduction	107
5.2. Tectonic framework	108
5.3. Seismicity	113
5.4. Multitemporal DInSAR – SBAS data processing	115
5.4.1. Mean ground velocity maps	115
5.4.2. Displacement time series	125
5.4.3. North and up component analysis	126
5.5. 3D analytical modeling	130
5.6. 2D analytical model approach	136
5.7. Discussion and conclusion	140
6. Coseismic deformation analysis of 2008 Balochistan seismic sequence	143
6.1. Introduction	143
6.2. Geodynamical and seismotectonic frameworks	144
6.2.1. Geodynamical context	144
6.2.2. Seismicity	146
6.2.3. The October 2008 Balochistan seismic sequence	150
6.3. The DInSAR data	152
6.3.1. The ALOS interferograms	155
6.3.2. The ENVISAT wide-swath interferogram	156
6.3.3. The ENVISAT image mode interferograms	157
6.4. Non Linear Inversions	163
6.4.1. DInSAR data inversion for the 09/12/2008 earthquake	163
6.4.2. DInSAR data inversion: 28 and 29/10/2008 earthquakes	166
6.5. Linear Inversions	170
6.6. Coulomb Failure Function	171
6.7. Discussion	176

7. Analogue model of earthquake-cycle in transcurrent tectonic domains	179
7.1. Analogue modeling of tectonic process: an overview	179
7.1.1. What is an analog model and why should we use it?	179
7.1.2. Designing an analog model	180
7.2. Laboratory model of transcurrent tectonic domain	184
7.2.1. Properties of materials and scaling	185
7.2.2. Strike-Slip-Fault-Box	190
7.3. Preliminary results	193
Conclusions	199
Reference list	209

Acknowledgements

I am greatly indebted to the Italian Space Agency (ASI) for supporting this doctoral project and the European Space Agency for providing SAR ERS-ENVISAT data for the Category-1 Project no. 5605 within the ASI-SIGRIS Project. The DEM was obtained from NASA SRTM archives. Precise ERS 1/2 satellite orbit state vectors are courtesy of Technical University of Delft, The Netherlands. I also thank Riccardo Lanari and the IREA working group for providing SBAS software.

My greatest debt of gratitude goes to Stefano Salvi, who once told me :“Non c’è niente che tu non possa fare con l’impegno e lo studio!”.

I am also grateful to Simone Atzori and Cristiano Tolomei for guiding me through this work and for transferring me their experiences, their enthusiasm and a lot of their time!

I thank Francesca Funiciello and Fabio Corbi for introducing me to the wonderful world of Analog modeling and for their great passion for Geology.

I am much obliged to Claudio Faccenna who strongly encouraged me in pursuing my academic career, thereby giving start to a chain of events that lead to the point where I am now.

I would also like to thank Olivier Bellier, Esmaeil Shabanian and Yassaman Farbod for warmly welcoming me in Aix-en-Provence, and for bearing with my absolute-beginner French.

A special thank goes to Sandra Orebi, Sylvia Orebi, Betta Del Bello and Stella Lucifora for taking the burden of fighting against my English!

I am also grateful to other PhD students who shared study and laughter in Rome and Bologna: special thanks to Betta Del Bello, Valentina Magni, Stella Lucifora, Irene Mannino, Fabio Manca, Danilo Seccia and Fabio Canova for their friendship, happiness, support and help.

Finally, I am forever grateful to my parents for coping with my never-ending education, to Emanuele for his support, encouragements and brotherhood, and to Giulia, for her patience, laughter and love.

Introduction

The principal topic of this doctoral thesis is the measurement and modeling of the earthquake cycle in transcurrent tectonic domains. To measure the crustal deformation associated to the interseismic and coseismic phases of the earthquake-cycle I used classical and multitemporal InSAR (Interferometric Synthetic Aperture Radar) methods. Nowadays, these techniques, applied to satellite SAR data, allow to measure short term ground displacement with a sub-centimetric accuracy, and ground velocities with an accuracy better than one millimeter per year over long time periods (several years) (Casu *et al.*, 2006). This level of accuracy makes the interferometric methods suitable for the study of tectonic processes, typically affected by deformation rates from millimeters to centimeters per year. The InSAR methods enable to measure ground movements occurring on different time scales, from the nearly instantaneous deformation caused by seismic dislocations (Massonnet *et al.*, 1993), to the slow strains of the interseismic phase (Wright *et al.*, 2001). Where the surface properties are favorable, the InSAR measurements are continuous, meaning that hundreds of thousands of measurements can be provided by a single SAR Interferogram.

Thus, the InSAR technique allows to measure ground displacement fields related to different phases of the earthquake cycle. The study of the surface deformation is one of the most important topics to improve the knowledge of the deep mechanisms governing the seismic cycle itself and, eventually, improve the seismic hazard assessment.

As shown in Chapter 1, many conceptual, numerical, analytical and analog models of the earthquake cycle have been proposed to explain seismological, geological, geomorphological and geodetic data. It is today accepted that the seismic cycle can

be subdivided in three main different phases: interseismic, coseismic and postseismic (e.g. Scholz & Kato, 1978). In reality, the interseismic phase can be again subdivided into a purely interseismic step and a preseismic one, but the state of knowledge relative to the last one is still vague and it will not be treated in this work (e.g. Deng *et al.*,1992).

The postseismic deformation occurs soon after the seismic event and it can be subdivided in two phases, characterized by short and long term deformation. The short term deformation can usually be attributed to afterslip and/or pore pressure readjustments, going on for periods ranging from few hours to few months after the earthquake. This deformation cannot be accurately measured by interferometric methodologies if the image sampling interval over the area is too long (several days or months). In this work I used ERS and ENVISAT data which have a minimum repeat pass of 35 days, so I did not attempt to measure short term postseismic deformation.

The long term postseismic deformation is instead related to the viscoelastic relaxation that occurs in the lower crust and upper mantle, following several months or years (depending on the magnitude) after the earthquake (e.g. Segall, 2002). This kind of deformation, also called viscoelastic rebound, is difficult to be isolated using InSAR data, because: a) it is often characterized by ground velocities at the lower boundary of the InSAR measurement capacity (<1 mm/yr); b) is spread over long distances and can be confused with interseismic deformation. In this work I did not consider crustal deformation caused by the viscoelastic rebound, and I focused my attention to the interseismic and, in part, to the coseismic phases.

From the geological point of view, the earthquake cycle manifests itself through field evidence as abrupt offsets or diffuse deformation of lithological reference layers, fluvial or marine terraces, depositional or erosional landforms, faults escarpments, etc (e.g Fattahi *et al.*, 2007). The seismic cycle and the fault activity is also studied using paleo-seismological trenches, where geologists can measure and date stratigraphic layers to evaluate long term averages of strain rates and

displacements. Starting from geological or paleoseismological field data, it is possible to evaluate the mean slip rate along a fault, and recognize the main seismic events (those which rupture the surface); these slip rates are usually averaged over a time span of thousands or tens of thousands of years (Pantosti *et al.* 1993).

The earthquake cycle is also identifiable by using geodetic data as InSAR and GPS, which provide diffuse and spot displacement measurements respectively; geodetic data can provide present day ground velocity and deformation maps, since they cover a period of few tens of years (e.g. Fialko, 2006).

InSAR and GPS data are complementary and should be used together to enhance their intrinsic capabilities: the GPS measurements provide highly precise 3D (vectorial) site displacements which are used to refine and/or verify the less precise and scalar, but continuous, InSAR measurements.

To study the seismic cycle in the long term, we need to integrate geological and geodetic data, that means to integrate slip rates averaged over many seismic cycles, and present day ground velocity maps. To reconcile these different data we need to identify the sources responsible for the present day strain accumulation (and geodetic velocity), and possibly know the long term slip rate along them. In this way we can compare the geologic and the geodetic slip rates. The "geodetic" slip rate can only be obtained by appropriate modeling of the geodetic data; in this work I use a simplified, but well established procedure, based on the inversion of analytical dislocation models. In this context it is very important to understand what the geodetic signal says and which are the assumptions and approximations of the inversion data methods (Chapter 1 and 3). In fact normal methods the inversion of interseismic geodetic data neglect transient deformation processes and estimate slip rates by assuming that slip on a fault occurs by steady creep only below a locking depth, in an elastic half-space, over the course of the earthquake cycle.

In this study I perform interferometric data inversions using the elastic model of Okada (1985), with the aim to investigate its applicability in the general context of the study of the earthquake-cycle in transcurrent tectonic domains.

As shown in Chapter 1, there are many different models of seismic cycle, each of which involves different a priori assumptions. So we can roughly distinguish two family of models. In the first ones the continental lithosphere can be viewed as a weak lower crust sandwiched between a strong upper crust and the uppermost mantle; in this case the ductile lower lithosphere controls the surface motions (e.g. Savage and Prescott, 1978). In the second family of models the continental lithosphere is dominated by the strength of its brittle upper crust; in this case the interseismic deformation of the crust is driven by creep at depth on well defined discontinuities, occurring below the locking depth (e.g. Savage and Burford, 1973). The creeping (dislocating) plane can be modeled with the analytic solution obtained by Okada.

In this work I apply different InSAR methods (classic and multitemporal, Chapter 2) to different test areas characterized by active transcurrent tectonics and different seismic contexts. One of the objectives of my work was also to test the use of the multitemporal InSAR-SBAS technique (Berardino *et al.*, 2002) for the measurement of low interseismic ground velocities in very different environmental contexts.

In Chapters 4 and 5 I describe my study of the interseismic deformation applied to the Gargano promontory (Southern Italy) and to the Doruneh region (Northern Iran). In both cases I focused the attention (i.e. the modeling) on the most prominent tectonic structures of the areas, the Mattinata Fault, for the Gargano, and the Doruneh Fault System for Northern Iran. Both test sites are characterized by prevalent transcurrent tectonic regimes with low deformation rates (few mm/yr).

I apply classic SAR interferometry to the October–December 2008 Balochistan (Central Pakistan) seismic swarm, as shown in Chapter 6. In this study I discern the different contributions of the three $M_w > 5.7$ earthquakes and I define three

main sources, in terms of fault parameters and slip distribution, using InSAR data inversion. Starting from the identification of the sources I define the relationship between the three seismic events using the Coulomb Failure Function (CFF). In fact the two main shocks have only 12 hours of temporal baseline and the aftershock sequence is characterized by another large event after 2 month. This is a perfect test case to apply the CFF method and quantify the stress accrual on fault planes due to the previous shocks.

In Chapter 7 I approach the study of the earthquake-cycle in transcurrent tectonic domains using analog modeling. The use of laboratory experiments allows to follow each step of the cycle and his evolution through time. Furthermore, I was able to simulate sudden dislocation (earthquakes) in the analog material; thus, it was possible to close the entire deformation cycle. Here I present the preliminary experiments performed using viscoelastic materials and a new strike-slip fault box, with the aim to investigate the capabilities of the methodology, and to compare the deformation field with the real InSAR deformation data.

In summary, in this work I: a) investigated the use of the Okada model to fit interseismic velocity signal from SAR interferometry in low velocity areas, low slip rate faults, and in an intra-plate geodynamical context; b) indirectly investigated if the deformation of the continental lithosphere is dominated by the strength of its brittle upper crust, at the first order; c) built an analog model able to reproduce an entire seismic cycle on a strike slip fault. In other words I reproduced in the same model the elastic deformation acting during the coseismic phase and the viscoelastic deformation acting during the interseismic phase.

Chapter 1

Observing and modeling the seismic cycle

1.1 The concept of seismic cycle

At the beginning of the XIX century, Reid (1910) introduced the concept of seismic loading cycle to study the mechanism of the California earthquake (1906). He proposed a concept model in which the release of elastic strains through slip on the San Andreas Fault was the cause of the earthquake. The idea at the base of the model is that the continuous movement, in opposing directions of the blocks on either side of the fault caused the accumulation of strains during a long period of time (Figure 1.1a). After an extended period of strain accumulation, an earthquake occurs along the fault; the strain released (Figure 1.1b) during the quake, called coseismic strain, is equal and opposite to the strain accumulated since the last earthquake, called interseismic strain: this is the elastic rebound model. This model implies that long-term displacement is entirely recorded on the fault plane and no long-term finite strain is accumulated within the regions either side of the fault (Figure 1.1c).

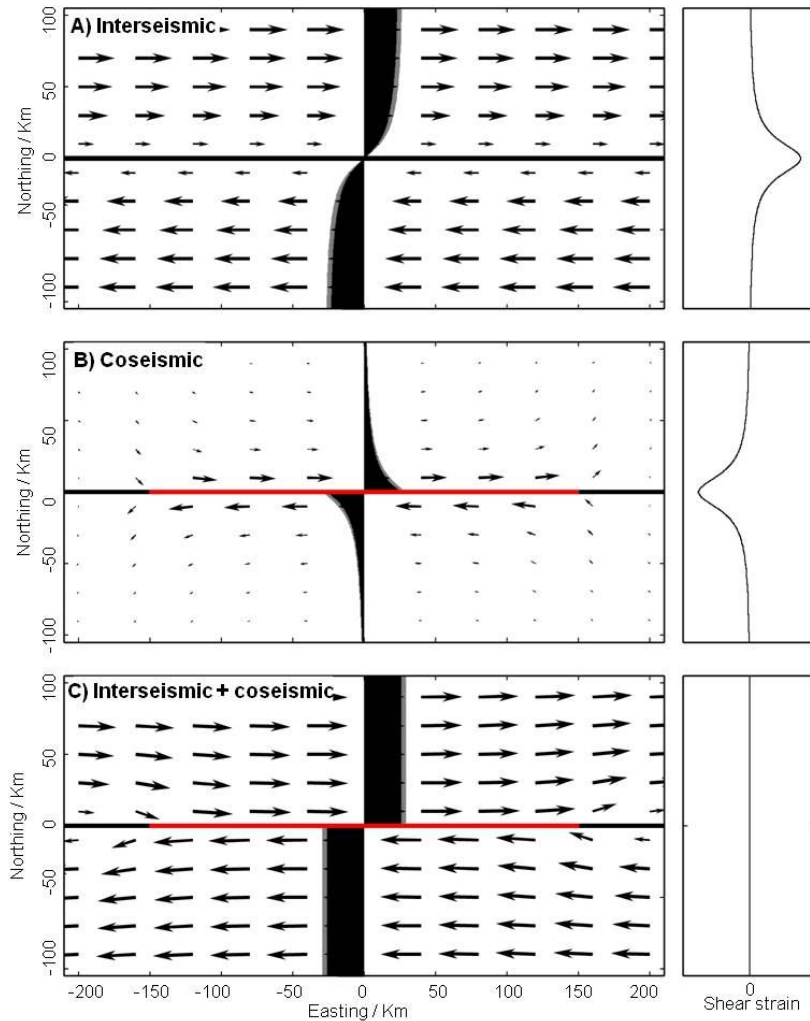


Figure 1.1: The elastic rebound model of Reid (1910). A) Displacement field (Black arrows) during the interseismic phase across an infinitely strike-slip fault (Black line); on the right we show an hypothetical shear strain profile. B) Coseismic displacement field and related shear strain profile due to an earthquake occurred along the red segment of the fault. C) Displacement field and shear strain after the earthquake. (Wright, 2000)

This model was the first step to understand the natural process at a conceptual level; however it did not consider the existence of the postseismic phase, later evidenced by many authors (e.g. Scholz & Kato, 1978; Thatcher & Rundle, 1984; Thatcher, 1984; Scholz, 1990; Yu *et al.*, 1999; Reilinger *et al.*, 2000). Generally, the postseismic phase shows deformation rates one order of magnitude smaller than the coseismic one, it is due to various phenomena (see later), and may be characterized by longer spatial wavelengths. Evidences of the preseismic phase in crustal deformation signals are instead sparse and not clear (e.g. Scholz, 1990). Another important over simplification of the Reid's model is that it considers

strain accumulating across a single fault. In reality, the deformation is usually distributed over many faults; for example the San Andreas Fault Zone (Southern California) shows a deformation zone of 250 km wide where at least 4 parallel active faults are recognizable (Figure 1.2).

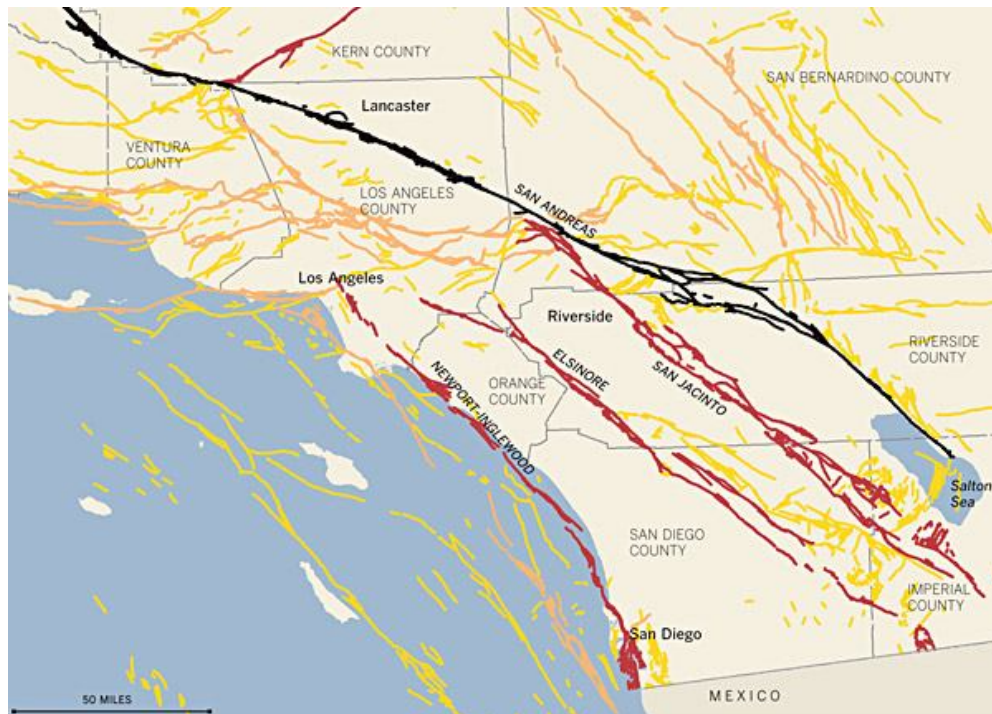


Figure 1.2: Faults distribution in the Southern California area. In black is reported the San Andreas Fault; in red the other main tectonic structures of the area (United States Geological Survey).

Although Reid (1910) did not explicitly consider events of different sizes, he did propose that following a large earthquake the next major event would not recur until the strain released by the previous shock had completely re-accumulated and he implied that this build up would occur at a nearly uniform rate. These idealized features are illustrated in Figure 1.3.

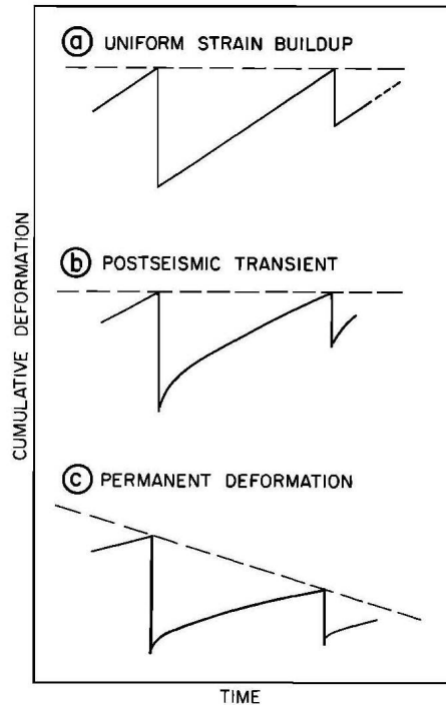


Figure 1.3: Simplified forms of seismic cycle from Thatcher (1984). The figure shows the cumulative deformation with respect to time. Step offsets correspond to the occurrence of major earthquakes. A) Simple seismic cycle in which only interseismic and coseismic phases are considered. B) post seismic contribution is introduced. C) earthquake cycle with permanent deformation.

In figure 1.3a the inter event time would be given by the ratio of the coseismic strain drop to the strain rate at any time during the cycle. Considering the presence of a postseismic transient (Figure 1.3b) and permanent inelastic deformation (Figure 1.3c), the Reid's cycle is modified: the rate of nearly steady interseismic strain relative to the uniform strain build up model, decreases. If these features are neglected, the recurrence time is overestimated.

In the 1980, Shimazaki and Nakata presented three examples of seismic sequences of large thrust-faults in Japan, using historical documents and geomorphological data. They highlighted regularity in the largest coseismic events: “the time-interval between two successive large earthquakes is approximately proportional to the amount of seismic displacement of the preceding earthquake, and not of the following earthquake”. Similar results were already found by Bufe *et al.* (1977) for small earthquakes ($M=3$) on the Calaveras fault in California

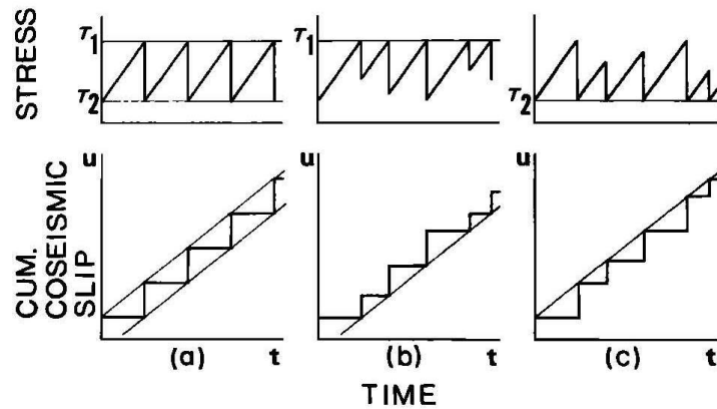


Figure 1.4: Three different recurrence models where the stress and cumulative coseismic slip are shown with respect to time (from Shimazaki and Nakata, 1980). A) Both initial and final stresses are time-independent; B) “time-predictable” model where the final stress is supposed variable with respect to time; C) “slip-predictable” model where the initial stress is variable and the final one is time-independent.

Considering a constant tectonic-stress rate in time, it is possible to study the characteristics of the earthquake cycle with respect to the initial (T_1) and final (T_2) stress levels during the coseismic rupture, as shown in figure 1.4: the stress drop, under the assumption that the same seismic cycle occurs on the same fault, is always proportional to the coseismic slip. In Figure 1.4a, Shimazaki and Nakata show the idealized case which both the initial and final stresses are time-independent and, consequently, the process is strictly periodic, but the data do not support this hypothesis. In the second case (Figure 1.4b), the final stress is supposed variable and, consequently, the model is “time-predictable” because, by knowing the amount of the stress drop, we are able to predict the occurrence time of the next earthquake. Bufe *et al.* (1977) already arrived to predict an $M=3$ quake for the Calaveras fault using a similar method. The last case (Figure 1.4c) refers to a model in which the initial stress is variable and the final one is time-independent. In this case we could predict the slip of the following earthquake, and the model is called “slip-predictable”. No regularity can be found if both the initial and final stresses vary in time. Shimazaki and Nakata favour the time-predictable model to the slip-predictable one.

1.2 Observation and models of the seismic cycle in transcurrent domain

Since Reid's first idea, many authors have proposed different models of the seismic cycle starting from different assumptions and observations; often they used data coming from a natural laboratory for the seismic cycle study that is the San Andreas Fault in California. It is roughly possible to subdivide the models into two different typologies: time-independent elastic half-space models; viscoelastic slip models and numerical models of 3-D evolution of the local stress field due to coseismic and postseismic stress transfer.

1.2.1 Time-independent elastic half-space models

Time-independent elastic half-space models have been used to match geodetic observations of surface displacement of portions of large strike slip fault, mainly the San Andreas Fault System.

One of the most important models (called the screw dislocation model) was proposed by Savage and Burford in 1973 for interseismic surface deformation. They proposed the modeling of the interseismic surface strain rate profiles near strike-slip faults by means of a buried screw dislocation in an elastic half-space; both the upper and lower crust are assumed to be elastic. This model was successively employed by many authors (e.g. Prescott *et al.*, 1979; McGarr *et al.*, 1982; Savage, 1983; King and Savage, 1984). In their model no slip is assumed along the shallower fault plane within a presently locked seismogenic depth range. For the deeper part of the fault, a uniform relative slip rate is assumed (Figure 1.5 and 1.6a). This is conceptually the relative velocity of the plate that is imposed to be localized along the downward continuation of the locked shallower fault. This is a convenient simplification, as the authors say, because the motion at the transform margin below the locked zone would need a more complete model accounting for of driving by deep-seated mantle motion and its coupling to the surface plates.

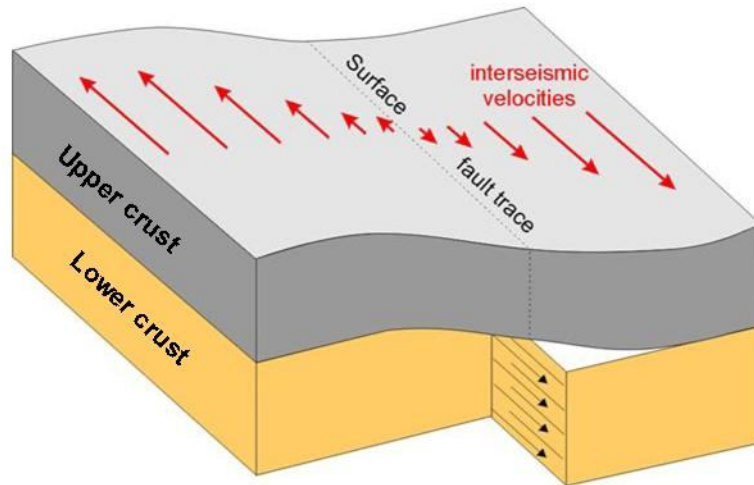


Figure 1.5: The screw dislocation model proposed by Savage and Burford (1973).

In 1985, Okada developed an elastic dislocation model in which he proposed the explicit solution to the integral that describes the dislocation in an isotropic medium, across a plane rectangular surface. Under the hypothesis of an elastic half-space, he enabled the efficient analytical calculation of displacements, strains and tilts due to shear and tensile displacements on faults. In this model the displacement is imposed to be localized to the fault plane, consequently it decreases moving away from the fault, contrary to the Savage and Burford (1973) model where the displacement increases moving away from the fault.

In 1990, Savage proposed a model of deformation at the free surface produced throughout the earthquake cycle by slippage on a long strike-slip fault in an Earth model consisting of an elastic plate (lithosphere) overlying a viscoelastic half-space (asthenosphere) can be duplicated by prescribed slip on a vertical fault embedded in an elastic half-space. The author compared an elastic half-space model with an elastic lithosphere – viscoelastic asthenosphere model concluding that in half-space model the relaxation is accomplished by aseismic slip on the discrete fault plane whereas in the lithosphere-asthenosphere model it is accomplished by continuous shear in the asthenosphere, shear that is concentrated near the down-dip end of the coseismic rupture. For this reason he sustained that it is very unlikely that observations of surface deformation will be able to prove that

viscoelastic relaxation in the asthenosphere is responsible for time-dependent deformation observed at the surface

Using the velocity field from surveys of trilateration networks during 1973-1989, within a 100 km broad zone centred on the San Andreas Fault between the Mexican border and San Francisco Bay, Lisowski *et al.* (1991) shows how simple dislocation models (Savage and Burford, 1973; Savage, 1990) can explain most of the features of the observed velocity field, but those explanations are not unique. They measure about 35 mm yr^{-1} of relative plate motion; geologic studies indicate that the secular slip rate on the San Andreas Fault is about 35 mm yr^{-1} . This agreement implies that most of the strain accumulation is elastic and will be recovered in subsequent earthquakes

In 1993 Feigl *et al.* utilized Okada's elastic dislocation model (1985) to remove the tectonic signal, imputable to the San Andreas Fault, to the GPS geodetic signal across the fault; remaining signal cannot be attributable to the San Andreas Fault; this means that the Okada model successfully fits the interseismic velocity field.

Murray and Segall (2001) proposed, for the San Francisco Bay area, a first-order method for modelling broadscale deformation consistent with both plate tectonic motions and elastic strain accumulation on plate boundary faults using continuous GPS data. The interseismic deformation was assumed to be a superimposition of long-term rigid-body motions between faults, defined by angular velocities of spherical plate and backslip on shallow locked portions of faults in an elastic half-space.

A block model including the effects of block rotation and elastic strain accumulation consistent with a simple model of the earthquake cycle was proposed by Meade and Hager in 2005. Discrepancies between geodetic and geologic slip rate estimates along the San Andreas and San Jacinto faults, as well as in the Eastern California Shear Zone, may be explained by a temporal change in fault system behaviour (Meade and Hager, 2005).

These kinds of models are generally more simple and their analytical solutions, when available, provide very useful tools to first-order model a broadscale deformation field.

1.2.2 Viscoelastic slip models

Viscoelastic slip models consist of an elastic plate overlying a viscoelastic half-space. They have been developed to match geodetically measured inter and postseismic surface velocities.

By means of a two-dimensional, elastic edge crack model, Turcotte and Spence (1974) analyzed the near-fault surface deformation. The crack faces sliding under resistive shear stresses below the locked zone which remain uniform in time; it is the equivalent of the aseismic stable sliding portion of the Savage and Burford (1973) model, that is the sliding portion of the plate margin. Loading is imposed like a far field, at the remote edge of the plates; this constant stress condition is equivalent to treating the crack surfaces as freely slipping. Assuming a viscous deformation and strongly nonlinear stress dependence for the deeper fault zone, the local shear stresses will vary only modestly over appreciable changes in slip rate and will be uniform in time for the interseismic and long term postseismic period. The slip distribution from the nearby mantle to the base of the locked zone tapers to zero.

Even if this model appears more realistic than the Savage and Burford (1973) model, eliminating the unrealistic slip discontinuity of the uniform dislocation model, it remains of limited application because they neglect for simplicity the coupling with the mantle below. In this way they could only load the system by remotely applied forces and could not directly relate the loading to ongoing plate motion.

Using a viscoelastic half-space coupled to an elastic layer, Nur and Mavko (1974) had modeled the aseismic deep slip, introducing the important idea that the strain accumulation over a seismic cycle is not linear with time.

Thatcher (1975), starting from previously elastic models, proposed a qualitative model for strain accumulation and release of the 1906 San Francisco earthquake. In this model the tectonic plates are considered rigid and the deformation is localized along the plate boundaries; the fault is locked in the upper 10 km, which is the focal depth. This portion of the fault was broken during the 1906 earthquake, when the accumulated strain was released. During the postseismic phase, the

deepest part of the fault slides more rapidly, being driven by the stress shed onto it, and the asthenosphere below, by the earthquake. In this model the surface strain rate during the postseismic phase gradually decreases in time because of the inelastic relaxation of the fault zone material below the seismogenic layer and the coupling between the elastic lithosphere and the viscoelastic asthenosphere.

Savage and Prescott (1978) further developed the Nur and Mavko (1974) model to include interseismic strain accumulation due to a constant far-field plate velocity resulting in an infinite sequence of periodically repeating earthquakes (Figure 1.6b). This model incorporates steady interseismic creep on the down-dip extension of the coseismic rupture. The earthquake ruptures the lithosphere from the free surface down to depth D ; the latter creeps at a constant slip rate from depth D to the bottom of the elastic plate.

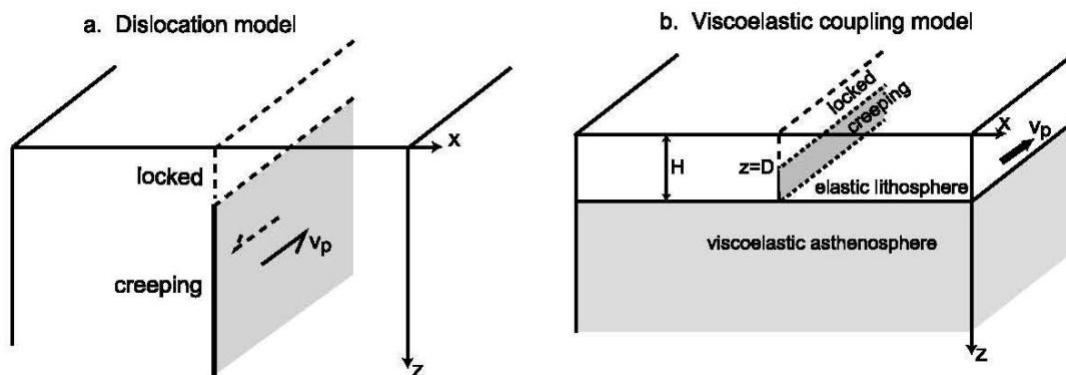


Figure 6: A) The screw dislocation model proposed by Savage and Burford (1973). The interseismic deformation is modeled as slip on a buried dislocation that slides at the plate rate, v_p . B) The coupling model proposed by Savage and Prescott (1978). Cyclic motion down to depth D and steady sliding below D on a fault in an elastic layer overlying a viscoelastic half-space. Slip rate on the fault is equal to the plate velocity, v_p . (Figure from Johnson and Segall, 2004)

The aseismic deep slip was also modeled by Thatcher (1983) using an elastic half-space where postseismic transient slip with exponential time decay is imposed kinematically as a spatially uniform dislocation. Like in the Nur and Mavko (1974) model also in this model the strain accumulation over a seismic cycle is not linear with time. Thatcher used a thin lithosphere model in which transient deformation results from flow in the asthenosphere due to stress relaxation following faulting through most or all of the lithosphere. For an earth model with a thick elastic

lithosphere, in which the plate thickness corresponds to the depth of seismic slip, transient motions are due to post-earthquake aseismic slip below the coseismic fault plane.

Sibson (1982) and Meissner and Strehlau (1982) introduced in their model changes of temperature and pressure with depth, proposing an aseismic creep for the deeper part of the fault. They explained the elevated strain rates near the fault across the strike slip plate boundaries, like in the San Andreas Fault case, with the aseismic creep along the deeper portion of the fault plane below a shallower portion of fault located into a brittle and elastic crust. Because of the temperature and pressure increase at depth, the crustal materials change their rheology from brittle to viscous; in this model they expected an aseismic deformation accumulating continuously at depth, while the upper crust accommodates relative plate movements by seismic faulting.

A more complex model was proposed by Tse and Rice (1986), where the temperature and hence the slip variation with depth is considered for two plates in a transform margin. Their results show how a depth-variable slip is consistent with a shallower locked zone over a deeper aseismic, stable sliding zone; the locked zone recovers the slip gap regarding the deep zone during the coseismic phase.

Li and Rice (1987) proposed a model without the kinematic imposition of motion directly beneath the seismogenic zone: the deepest fault zone moves driven by mantle motion (through a viscoelastic asthenosphere), maintaining the constant resistive stress boundary condition; this causes the variation of the deep slip rate during the whole cycle.

Viscoelastic coupling models (e.g., Thatcher, 1983; Li and Rice, 1987), with an elastic layer overlying one or more viscoelastic layers, demonstrate transient crustal deformation after an earthquake.

In 1998 Savage and Lisowski presented a model for a single vertical strike-slip fault in an elastic layer (brittle upper crust) over a viscoelastic half space (ductile lower crust and upper mantle). In this model, the broad distribution of deformation of trilateration network along this segment implies a locking depth of at least 25 km as interpreted by the conventional model of strain accumulation (continuous

slip on the fault below the locking depth at the rate of relative plate motion), where as the observed seismicity and laboratory data on fault strength suggest that the locking depth should be no greater than 10 to 15 km. The discrepancy is explained by the viscoelastic of coupling model which account for the viscoelastic response of the lower crust.

In the same year, by using GPS measurements and InSAR images, Deng *et al.*(1992) studied the 1992 Landers earthquake. They used a three dimensional model to show that afterslip can only explain one horizontal component of the postseismic deformation, whereas viscoelastic flow can explain the horizontal and near-vertical displacements. In their model the viscoelastic behaviour of the lower crust may help to explain the extensional structures observed in the Basin and Range province and it may be used for the analysis of earthquake hazard.

Nonlinear upper mantle viscosity was invoked by Pollitz *et al.* (2001) to model the Hector Mine, California, earthquake from interferometric synthetic aperture radar data; the model initially needs low viscosity after the earthquake, increasing with time.

Johnson and Segall (2004) showed that is not necessary to invoke different relaxation times (viscosities) for northern and southern California to fit GPS and triangulation data, if the fault below the coseismic rupture is considered as a zone characterized by linear viscous shear. They studied the interseismic deformation using boundary element models in which the lower lithosphere is characterized by stress driven creep and the asthenosphere is characterized by viscoelastic flow. Four different viscoelastic coupling models of interseismic deformation along strike-slip faults are compared in figure 1.7 (Johnson and Segall, 2004). Figure 1.7a shows the “no-creep” model of Savage and Prescott (1978), where no interseismic creep on the fault is considered and the fault breaks the entire elastic plate. Figure 1.7b represents the Savage and Prescott (1978) “constant-creep model”, characterized by stable sliding (creep equal to the plate velocity) from depth D to the bottom of the elastic layer and by a locked shallower elastic plate (from depth D to surface) during the interseismic phase. Figure 1.7c and 1.7d represent models (Johnson and Segall, 2004) where the creep is incorporated using

boundary element techniques: figure 1.7c represents a “constant-stress” model where a constant resistive shear stress below depth D drives the fault creep during the seismic cycle, whereas the “viscous-creep” model (Figure 1.7d) shows a linear viscous shear in the fault zone below depth D.

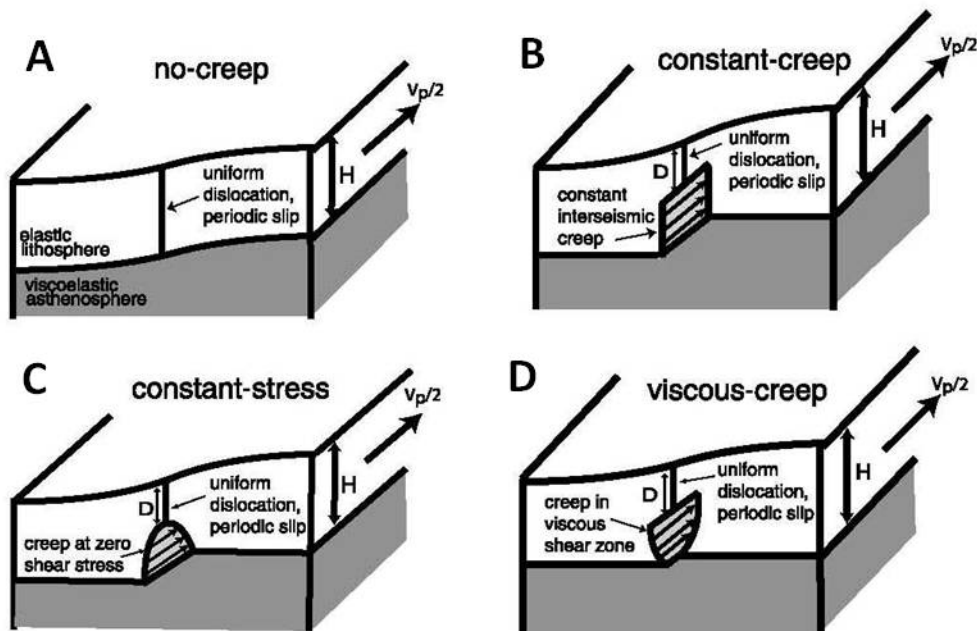


Figure 1.7: Four different viscoelastic coupling models of interseismic deformation. A) The “no-creep” model of Savage and Prescott (1978), where the coseismic rupture breaks the entire elastic plate. B) The Savage and Prescott (1978) model, called “constant-creep model”, in which the creeping part of fault slides at constant slip rate. C) “Constant-stress” model, where the creeping part slides at constant resistive shear stress. D) “Viscous creep” model, in which the creeping part deforms as a linear viscous shear zone. (Figure from Johnson and Segall, 2004).

Hilley *et al.* (2010) re-analyzed and modeled all global positioning system (GPS) data from northern Tibet to determine if the difference between short-term geodetic and long-term geologic fault slip rate, might be explained by previously unmodeled transient processes associated with the earthquake cycle, which can bias slip-rate estimates from geodetic data. They concluded that these effects cannot reconcile the geodetic data with the lowest bounds on the geologic slip rates even in the presence of low ($<10^{18}$ Pa s) viscosities within the mid-crust or crust and mantle lithosphere. Models with high-viscosity ($\geq 10^{18}$ Pa s) middle to lower crust and mantle lithosphere can best fit GPS surface velocities.

These kind of models are very useful to simulate and to understand some deeper process that are here considered time-dependent like interseismic and postseismic deformation, but they are generally more complicated with respect to the time-independent elastic half-space models and are not immediately usable to make geodetic velocity inversions.

1.2.3 3-D evolution of the local stress field.

Many studies have focused on the 3-D evolution of the local stress field due to coseismic and postseismic stress transfer. For example, Pollitz and Sacks' (1992) modeled the 1857 earthquake and plate tectonic load using triangulation data; the postseismic displacements have been calculated using an elastic-viscoelastic coupling model that, for any fault geometry, yields the exact displacements on a spherically stratified earth. The southern California crust and upper mantle are modeled as an upper elastic plate underlain by a viscoelastic asthenosphere. They performed some inversion for the coseismic slip distribution using different structural parameters resolving a triangular slip distribution, an elastic plate thickness of 16 km, a crustal thickness of 16 to 33 km and a mantle viscosity of 0.4 to $0.8 \cdot 10^{19}$ Pa-s. They also concluded that Inferred fault slip exceeding known surface slip implies either unrecognized secondary faulting or a slip deficit at the surface relative to the slip at depth.

Reches *et al.* (1994) developed a finite element model with nonlinear crustal rheology using GPS and triangulation data along the San Andreas Fault. Numerical models must be conditioned by running the calculations through many earthquake cycles until the flow in the asthenosphere is in a steady state; that is, the flow pattern repeats in time with the cyclic pattern of slip on the fault.

Linker and Rice (1997) developed numerical models in an elastic layer coupled to a viscoelastic substrate to model dynamic process of post seismic creep. On the contrary, Hearn *et al.* (2002) developed numerical models for strike-slip fault in an elastic half-space, in which postseismic creep, related to viscoelastic flow in the asthenosphere, is driven by stress on the San Andreas Fault released after the 1906 San Francisco earthquake.

Interseismic loading (stress recovering) between earthquakes for the faults located in the San Francisco Bay area, has been proposed by Parson (2002); the model reproduces observed geologic slip rates on major strike-slip faults and produces surface velocity vectors comparable to geodetic measurements. Fault stressing rates calculated with the finite element model are evaluated against numbers calculated using deep dislocation slip. In addition, tectonic stressing was distributed throughout the crust and upper mantle, whereas tectonic stressing calculated with dislocations is focused mostly on faults. Moreover, the model incorporates postseismic effects such as deep afterslip and viscoelastic relaxation in the upper mantle. The author calculates about 75 years of shadow stress that may explain the 75 years period of seismic quiet that followed the 1906 earthquake.

Segall (2002), using the Savage-Prescott coupling model with a coseismic slip distributed along the entire elastic plate without interseismic creep on the fault, demonstrated how the GPS measurements of interseismic velocities across the Carrizo Plain segment of the San Andreas fault imply a longer relaxation time (higher viscosity) than the northern area of San Francisco Bay (from strain rate data referred to the post deformation of the 1906 San Francisco earthquake obtained from triangulation surveys).

Kenner and Segall (2003) jointed the work of Linker and Rice (1997) and of Hearn *et al.* (2002) using elastic layer coupled to a viscoelastic substrate where there is a relation between the asthenospheric flow and the stress release on the San Andreas Fault after the 1906 earthquake. In particular aseismic creep on a discrete fault zone below the coseismic rupture fault plane was used by the authors for the postseismic deformation, using a creeping fault in an elastic lithosphere placed above a viscoelastic half-space with a 200 year relaxation time. In fact many authors (Henstock *et al.*, 1997; Parsons, 1998; Parsons and Hart, 1992; Zhu, 2000) hypothesized from seismic tomography that the major faults in the San Francisco Bay extend well below the cutoff depth of seismicity as a discrete zone.

1.2.4 Others approach

Smith and Sandwell (2004) developed a 3-D semi-analytic solution for the vector displacement and stress tensor of an elastic plate overlying a viscoelastic half-space in response to a vertical strike-slip dislocation. The problem is solved analytically in both the vertical and time dimensions (z, t), while the solution in the two horizontal dimensions (x, y) is developed in the Fourier transform domain to exploit the efficiency offered by the convolution theorem. The restoring force of gravity is included to accurately model vertical deformation. Arbitrarily complex fault traces and slip distributions can be specified without increasing the computational burden.

In the approach of Scholz (1998), the model only obeys to the friction law. In figure 1.8 the friction model of the seismic cycle of the San Andreas Fault fault (from Scholz, 1998), is shown, as the slip on the fault as a function of depth at different times during the seismic cycle. The unstable-stable transition interface is located at depth of 11 km, according with the geothermal gradient for the San Andreas Fault.

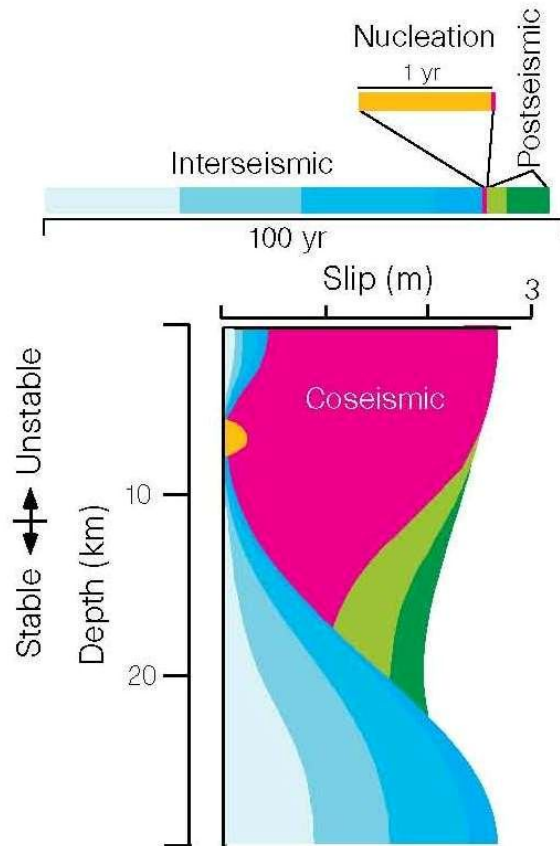


Figure 1.8: Deep slip distribution in the time over an earthquake cycle related to a strike slip fault (San Andreas Fault). The figure represents a frictional model in which the transition interface from unstable to stable sliding is located at 11 km. (from Scholz, 1998)

Steady slip on the deep and stable portion of the fault load shallower parts of the fault during the interseismic period (blue area in figure 1.8). The preseismic phase, in orange, occurs just before the earthquake; from the nucleation the coseismic motion, in red, occurs and the slip accelerates. The coseismic slip enters the stability boundary and reloads that region; this causes the postseismic relaxation, in green, that occurs in a variable period of time. In fact, it decays exponentially with time, within few years after the mainshock. Works of Thatcher (1978) and Gilbert *et al.* (1994) on geodetic data are in agreement with this model and support the idea of an interseismic strain accumulation resulting from deeper stable sliding under a locked plate where the slip occurs during the coseismic phase.

1.3 The Parkfield Experiment

The Parkfield Experiment is a comprehensive, long-term earthquake research project on the San Andreas Fault. Led by the USGS and the State of California, the experiment's purpose is to better understand the physics of earthquakes; what actually happens on the fault and in the surrounding region before, during and after an earthquake. Moderate-size earthquakes ($M \sim 6$) have occurred regularly (1857, 1881, 1901, 1922, 1934, and 1966) on the Parkfield section of the San Andreas Fault (Figure 1.9). The first one is considered a foreshock to the great Fort Tejon earthquake which ruptured the fault from Parkfield to the southeast for over 180 miles. In general, all earthquakes have shown about the same magnitude and ruptured at about the same area on the fault; for these reasons they could be considered like “characteristic earthquakes” (USGS web site).

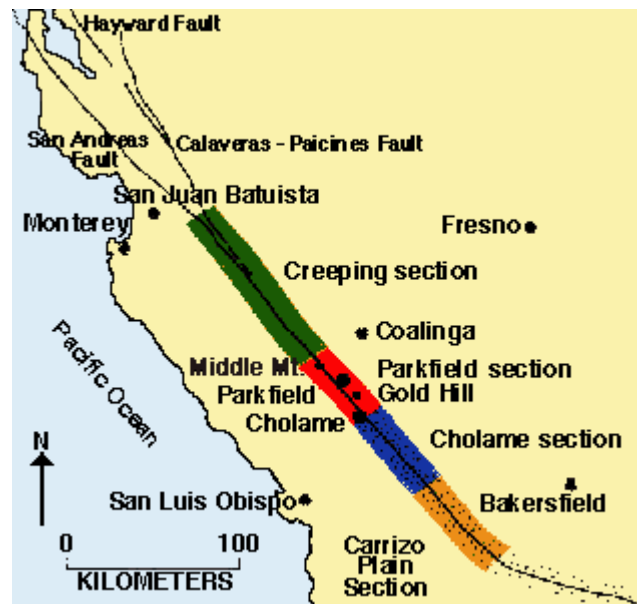


Figure 9: (from USGS web site). The San Andreas fault in central California. A "creeping" section (green) separates locked stretches north of San Juan Bautista and south of Cholame. The Parkfield section (red) is a transition zone between the creeping and southern locked section. Stippled area marks the surface rupture in the 1857 Fort Tejon earthquake.

A multi-year, integrated observation program at Parkfield, combining seismic, geodetic, creep, strain, tilt and magnetic measurements with theoretical models of fault mechanics was proposed in 1978 by Allan Lindh of the USGS.

Bakun and McEvilly (1979) with the "characteristic Parkfield earthquake" model, supposed a nearly regular occurrence of earthquakes of similar size that ruptured the same part of the fault. The seismograms that recorded the earthquakes in 1901 and 1922 supported this hypothesis. They argued that the largest earthquakes at Parkfield since 1857 are consistent with a regular occurrence of one every 22 years.

Bakun and Lindh (1985) summarized the state of the art in the Parkfield Prediction Experiment, and predicted that a moderate-size earthquake would occur at Parkfield between 1985 and 1993 with high precision in location, time and magnitude and high degree of confidence (95% within the 9-year window). They also predicted an extended rupture of the San Andreas Fault to the southeast, possibly growing to magnitude 6.5 to 7.0.

Using statistics of past events and with the assumption that Parkfield earthquakes are a response to a slip deficit near Middle Mountain, Ben-Zion *et al.* (1993) predicted the next event in 1992 ± 9 years for a 7.5 km thick lower crust having a relaxation time of 15 years, and in 1995 ± 11 years if the 7.5 km thick lower crust is characterized by a relaxation time of 7.5 years. These predictions were presented under the assumption of a 17.5 km thick elastic crustal layer.

“When the earthquake did not occur by 1993, an independent review of the Parkfield experiment was conducted; the review concluded that Parkfield was still the best place to capture a moderate earthquake and that the monitoring effort should continue. With time, some instruments were upgraded or replaced, a few died, and a few were forgotten, but the majority of the monitoring effort continued and most of the instruments at Parkfield were operational at the time of the 2004 Parkfield earthquake. Inter-seismic, co-seismic, and post-seismic deformation and seismicity accompanying the earthquake were recorded on networks of creepmeters, GPS (which has replaced the two-color EDM), strainmeters, magnetometers, pore pressure sensors, and a diverse set of seismic networks. The strong motion arrays, in conjunction with other digital seismic instruments in the area, recorded on-scale 3-component seismograms at over 100 near-field sites,

making this one of the best recorded earthquakes for seismic engineering purposes” (Bakun *et al.*, 2004).

Understanding the behaviour of seismic activity along an active fault like the San Andreas Fault system is a first step towards prediction. The Parkfield experiment shows that even in a situation where a characteristic earthquake occurs around a limited section of a well studied fault, the prediction in time is cumbersome. Speculations on the reasons for this seemingly unsuccessful prediction include the effect of several large earthquakes in the neighbourhood, influencing the stress pattern around Parkfield, and the assumptions on the models behind the repeat times (Langbein *et al.* 2005).

In the Parkfield experiment many kinds of data are used to measure the earthquake cycle, especially for the coseismic phase, like creepmeters, GPS, SAR Interferometry, strainmeters, magnetometers, pore-pressure sensors, and a diverse set of seismic networks, in addition to strong motion arrays data. All these techniques provide different kind of information to the same natural phenomena: the strain accumulation in a well defined area (a single fault, a fault system or a deforming area) and the subsequent released strain.

In this chapter a large number of seismic cycle models have been shown, covering different cycle phases or different topics like the crust-mantle rheology, the mantle viscosity, the stick-slip or stable sliding fault behaviours, the discrepancy between geodetic and geologic slip rate estimation, etc. Moreover different kind of models have been show like possible tools to understand and simulate the earthquake cycle, like the Parkfield experience collects a lot of themes around the seismic cycle.

As previously seen, one of the most important topics of study on the earthquake cycle is the study of the ground deformation patterns during the different phases of the earthquake cycle. In fact, for many years, all topics around the earthquakes cycle study have been considered only the domain of seismologists, this was mainly due to the remote nature of the observations and to the low availability of geodetic data up to the 1992. Since the advent of Interferometric Syntetic Aperture

Radar (InSAR) technology, detailed geodetic measurements have become available for an increasing number of earthquakes allowing a comparison with the seismological observations. In the postseismic and interseismic phases of earthquake cycle, a minimal role is played by seismology since they are characterised mainly by limited seismicity or microseismicity. Continuous GPS and multitemporal SAR interferometry have become the most important tools to measure the ground deformation and thus the seismic cycle. This work explores the use of the SBAS multitemporal InSAR technique for the measurement of the interseismic deformation, and simple elastic modeling to extract first order information on the seismic cycle.

Chapter 2

SAR interferometry for the measurement of the seismic cycle

2.1 Differential SAR Interferometry

Interferometry from Synthetic Aperture Radar (InSAR) is a technique based on the comparison of the phase content of radar images acquired at different times in the same area. Its suitability in the imaging of subtle and large scale displacement made InSAR play a key role in geodesy, next and complementary to GPS data.

Shapiro *et al.* (1972) first used InSAR to measure topographic relief on the moon with a ground based radar. However, only after the launch of ERS-1 (from the European Space Agency) the systematic acquisition and the huge availability of radar images with a short revisiting time, about one month, allowed the spread of InSAR. The technique gained the cover of Nature with the work of Massonnet *et al.* in 1993, demonstrating its suitability in mapping the permanent surface deformation caused by an earthquake. They applied the InSAR technique to the 1992 Landers earthquake, and showed the first interferogram of a coseismic deformation field (Figure 2.1). Their work demonstrated the enormous potential of InSAR and it was a milestone for the earth science community.

The basic physical principles behind creating SAR images and interferograms are described hereinafter, although a full description of this technique is beyond the

scope of this thesis. For a more complete discussion of the principles of SAR, see Curlander & McDonough (1991), and for InSAR applications, refer to Bürgmann *et al.* (2000) and Franceschetti and Lanari (1999).

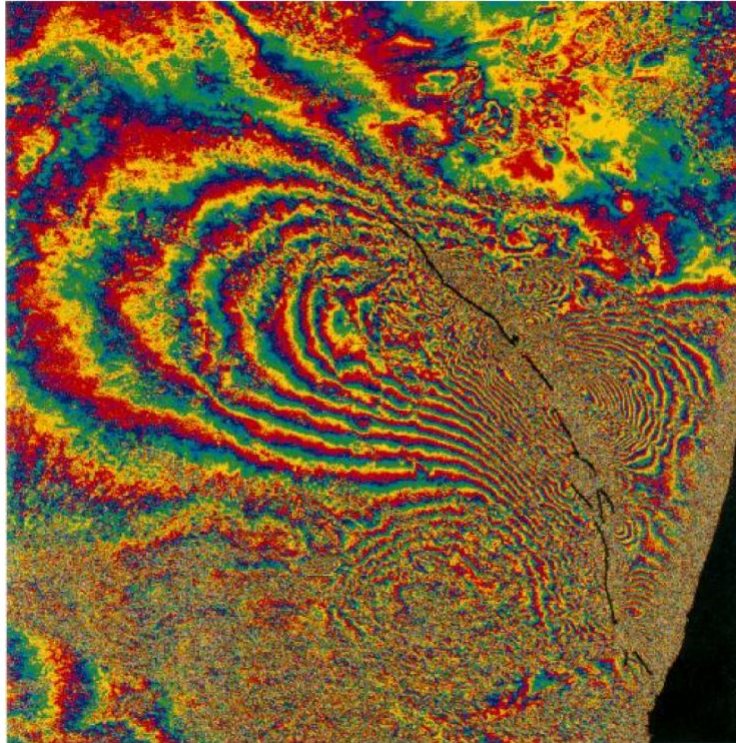


Figure 2.1: First interferogram of a coseismic deformation field (1992 Landers earthquake) captured by the InSAR technique (after Massonnet *et al.*, 1993). Each color cycle (fringe) is the result of a relative change in the satellite to ground path (range) of 28 mm. The black line represents the mapped fault trace.

2.1.1 Side-looking real-aperture radar

The antenna equipped on the satellite emits electromagnetic pulses in the microwave frequencies, and the distance to, and nature of, illuminated targets is determined by the timing and character of the reflection.

Figure 2.2 shows a simplified acquisition geometry of a side-looking real-aperture radar, where the dimensions of the antenna determine the size of the radar beam and its ground footprint. The width of the antenna, W_a sets the beam width, $\theta_v = \lambda/W_a$, whose intersection with the ground surface determines the swath width:

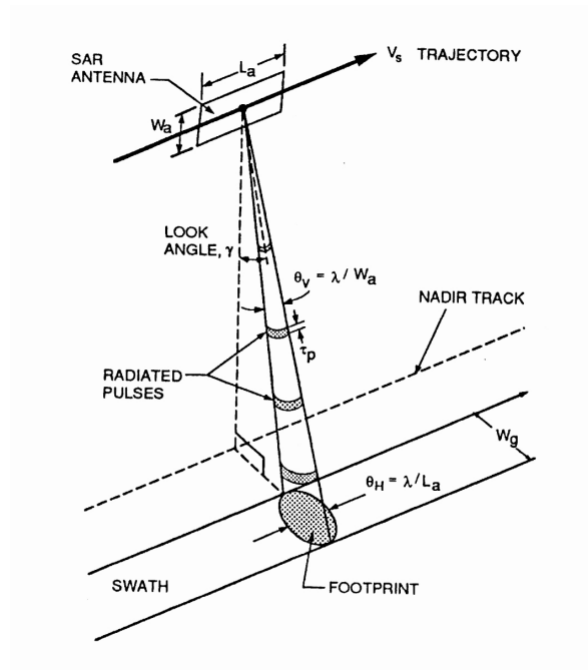


Figure 2.2: A side-looking real-aperture radar: simplified acquisition geometry. All terms are defined in the text (after Curlander & McDonough, 1991).

$$W_g \approx (\lambda R_m) / (W_a \cos \eta) \quad (2.1)$$

With R_m = slant range (shortest distance from the radar antenna to the centre of the ground footprint); η = incidence angle of the radar beam (in this case equal to the look angle of the radar γ). The minimum separation of two points on the ground surface in the direction perpendicular to the antenna trajectory that can be separately identified is called *ground range* resolution of the radar (ΔR_g) as shown in figure 2.3.

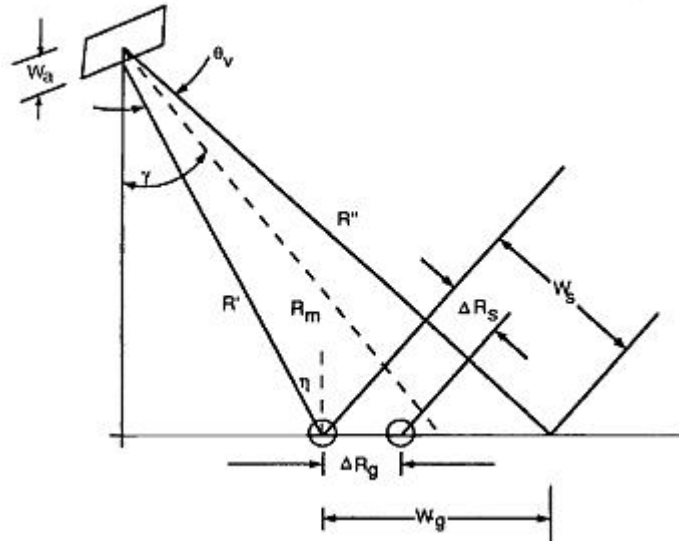


Figure 2.3: Illustration of swath width, W_g , and ground range resolution, ΔR_g , for a real-aperture radar (after Curlander & McDonough, 1991). Other terms are defined in the text.

Two points on the ground are resolved if the difference in two-way travel times is greater than τ_p (radar pulse). The ground range resolution is independent on the time duration of each individual radar pulse or the sampling frequency, v_s . Thus,

$$\Delta R_g = (c \tau_p) / (2 \sin \eta) = c / (2 v_s \sin \eta) \quad (2.2)$$

For example, the European Remote Sensing satellite (ERS) has 18.96 MHz of frequency and the incidence angle ranges from 18° (at the near range) to 26° (at the far range); consequently the ground resolution ranges from 26m to 18m at the near and far range, respectively. Curlander and McDonough (1991) show like at this frequency, individual distinct pulses cannot provide sufficient energy to produce the required signal to noise ratio. Instead a frequency modulated, or chirped, pulse is used with frequency bandwidth B , giving a resolution in time of $1/B$. Thus, the ground range resolution is:

$$\Delta R_g = c / (2 B \sin \eta) \quad (2.3)$$

In the ERS satellites cases, $B = 15.5$ MHz, thus we have 31m and 22m at near and far range, respectively. By use of time delay, it is possible to focus the radar

echoes in the range direction, but not in the azimuth direction, because of the lines of equal exist. The azimuth resolution A_g depends on the azimuth beam width $\theta_H = \lambda / L_a$ with $L_a =$ length of the antenna (Figure 2.2). Two ground points can only be resolved if they are not within the same beam width, consequently the azimuth resolution is:

$$\Delta A_g = R_m (\lambda / L_a) \quad (2.4)$$

If R_m is small, for example for airborne radar, we can have high resolution imagery using reasonable antenna sizes, but if R_m is big, for example for space-borne radars, we would have low resolution imagery using realistic antenna sizes. For examples, in the case of ERS satellites R_m is about 850 Km, this means that points at distance of 5 Km cannot be resolved using 10 m antenna. To obtain a 20 m ground resolution we would need an antenna over 2 Km long; obviously this is impossible, thus the unique solution of the problem is the use of a Synthetic Aperture Radar (SAR), like first suggested by Wiley (1965).

2.1.2 Synthetic Aperture Radar (SAR) images

The Synthetic Aperture Radar was born with the idea to simulate a very large antenna using the radar signals from successive pulses that illuminate the same portion of earth surface (Figure 2.4).

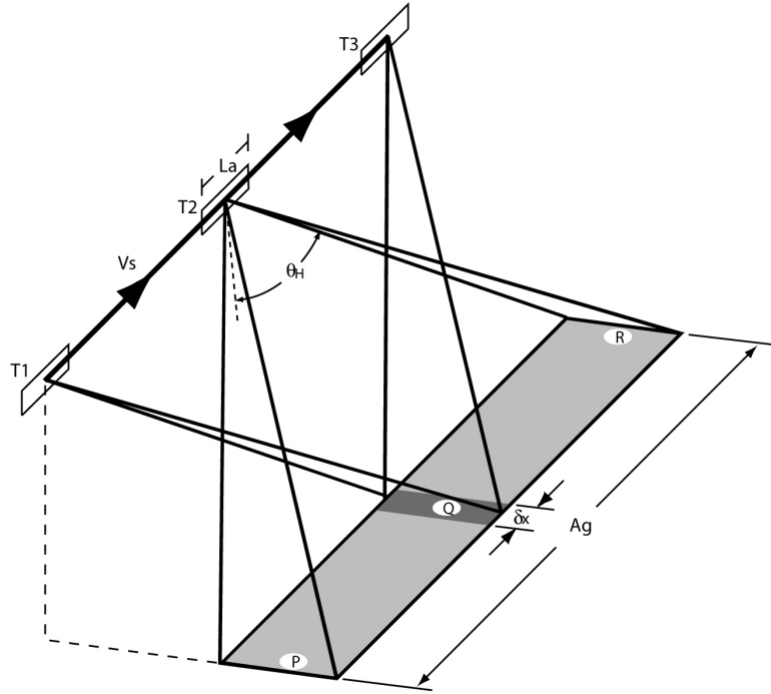


Figure 2.4: The synthetic aperture radar use a radar antenna of length L_a ; illuminating the same point on the ground (Q) from time $T = T_1$ to $T = T_3$, it is possible to simulate an antenna that is much longer, with a resolution improved from A_g to θx .

The SAR system operates illuminating the same point (Q in figure 2.4) not only when the satellite is at its closest point (at time T_2 in figure 2.4), but also during the whole time span from T_1 to T_3 , as shown in Figure 2.4. The azimuth beam width of the real aperture is equal to the distance travelled during this interval $A_g = R m_s = L_a$ (Equation 2.4) (5 km for ERS). This is equivalent to the length of the simulated antenna, known as the synthetic aperture.

Now the problem is to separate the radar echoes relative to the point Q respect to the others echoes that arrive to the radar during the time step from T_1 to T_2 . The key solution was found by Wiley (1965) that proposed the use of the Doppler frequency shifts of the return echoes due to the movement along the track of the satellite itself. A Doppler shift in frequency ν_d is induced by the difference in relative velocity between the satellite and a ground point during the time step of the acquisition.

$$\nu_d = 2(V_s \sin\theta) / \lambda \approx 2V_s x / \lambda R \quad (2.5)$$

with θ = angle between the line joining the satellite and the ground point (Q) and the line perpendicular to ground track; x = along track distance from the point of closest approach; a factor of 2 is used because it refers to the two-way travel time (Figure 2.5).

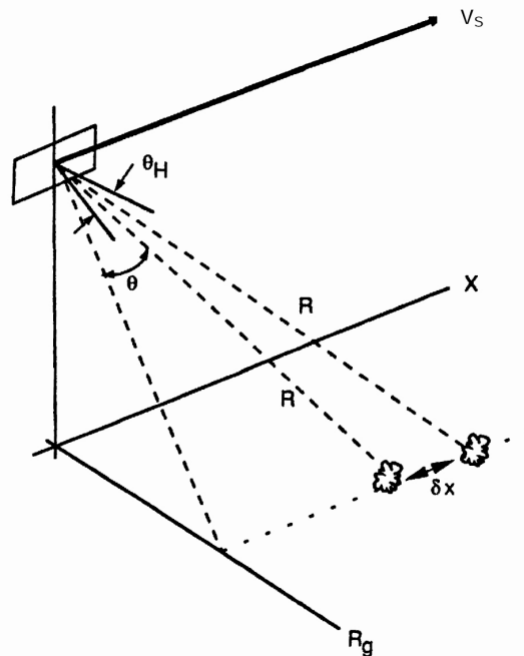


Figure 2.5: Geometry of the synthetic aperture radar and the azimuth resolution of SAR (after Curlander and McDonough, 1991)

Thus, this approach allows determining the along-track coordinate x using the Doppler frequency:

$$x = (\lambda R v_d) / (2 V_s) \quad (2.6)$$

Thus, by means of their Doppler shift, we can discriminate targets within the same beam, but at constant range, using a coherent source of illumination. The focused azimuth resolution, δx , is simply dependent on the measurement resolution of v_d :

$$\delta x = (\lambda R / 2 V_s) \delta v_d \quad (2.7)$$

where δv_d is the inverse of the time span Δt , that is the time for which any target remains illuminated (Figure 2.4)

$$\Delta t = T_3 - T_1 = A_g / V_s = \lambda R / L_a V_s \quad (2.8)$$

Therefore

$$\delta x = (\lambda R / 2 V_s) (L_a V_s / \lambda R) = L_a / 2 \quad (2.9)$$

From the 2.9 we conclude that for Synthetic Aperture Radar, to improve the azimuth resolution, we have to decrease the radar antenna dimension; exactly the opposite of the real aperture radar where to improve the azimuth resolution it is necessary to increase the antenna size. Following the example of the ERS satellites, the use of SAR improves the ground resolution by tree orders of magnitude (from 5Km to 5m). If we followed this reasoning to the extreme, a pin point precision could be obtained by use of pin point antenna; obviously this is impossible. The problem is that the radar antenna works not only in transmission, but also as a receiver; first a pulse is transmitted by the antenna and then the same antenna has to go in listening mode before the transmission of another pulse. To avoid confusing far-range echoes from one pulse with near-range echoes from the next pulse, the difference in time between echoes from the near range ($2R'/c$) and far range must be less than the time between pulses $1 / v_p$, thus

$$W_s = (R'' - R') \leq c / 2 v_p \quad (2.10)$$

And the maximum swath width is:

$$W_g \approx c / (2v_p \text{ sen } \eta) \quad (2.11)$$

Therefore, large swath widths require small pulse repetition frequencies. Following the example of ERS we have that v_p is 1680 Hz and the maximum

theoretical swath width is about 230Km. Moreover, the Doppler frequency shift must be calculated to place echoes in the azimuth direction. Curlander and McDonough (1991) showed that to relate an observed incremental phase change to a Doppler frequency, the bandwidth Bd of the Doppler signal must be less than the pulse repetition frequency v_p , thus

$$\begin{aligned}
 Bd &= v_{p - high} - v_{p - low} = \\
 &= (2V_s / \lambda) [\text{sen}(\theta_h/2) - \text{sen}(-\theta_h/2)] \approx 2V_s \theta_h / \lambda = \\
 &= 2V_s / L_a = V_s / \delta x < v_p
 \end{aligned} \tag{2.12}$$

Hence, in the time between consecutive pulses ($1/v_p$), the radar antenna travels a distance less than or equal to half its length ($L_a/2$). Even if the azimuth resolution (δx) increases using smaller antennae, these require larger pulse repetition frequencies, which reduce the swath width; this represents the lower bound on the sizes of the SAR antennae. In the case of the ERS satellite, it is equipped with a 10m long and 1m wide antenna emitting one pulse every four meters travelled along track. ERS single-look images have range and azimuth resolutions of 20 m and 4 m respectively, without averaging.

The SAR images contain two kind of information, the amplitude and the phase of the signal (complex numbers images) because for the Doppler-focusing of the synthetic aperture, is fundamental to know the radar phase. The focusing is the image formation from row data. It is also crucial for radar interferometry; after the processing a radar image is also called Single-Look Complex image (SLC). A simple schema of SAR focusing technique is shown in Figure 2.5.

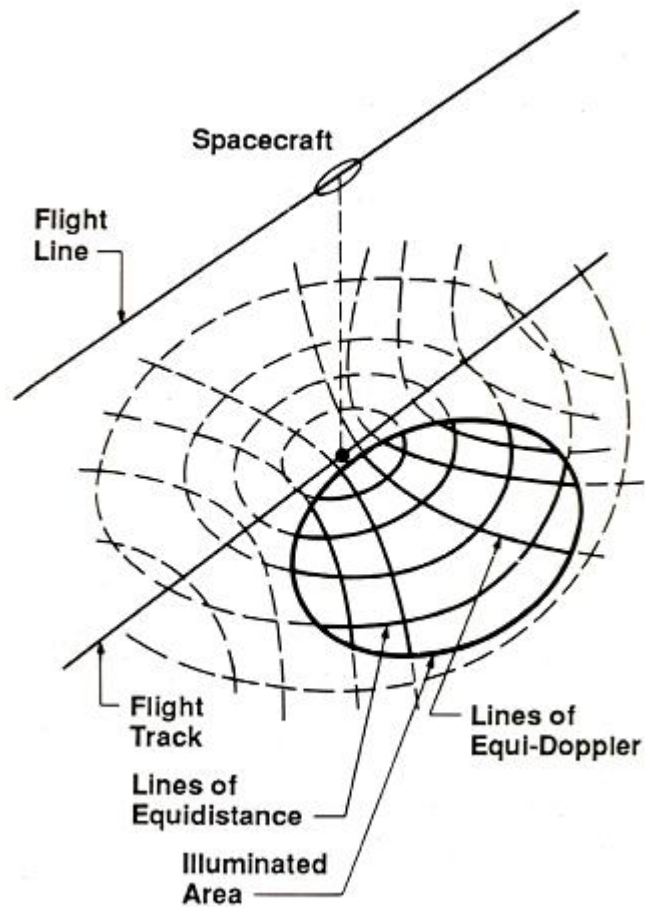


Figure 2.6: Summary cartoon to illustrate SAR focusing technique (after Ford *et al.*, 1989)

2.1.3 Amplitude of SLC image

The radar reflectivity (backscatter) of the illuminated surface is recorded in the SLC image like the “amplitude” of the signal. We define the roughness R of a surface the variation in height of the surface itself; the backscatter does not depend only on R . Under the hypothesis that the roughness R is much smaller than the wavelength λ of the radar signal, then the surface illuminated is smooth and all radar energy is reflect away from the sensor, like a mirror. In this case just a little part of the total energy arrives at the satellite and the amplitude is about zero: the area appears dark; this is typical of very flat surfaces like sea or lake when there is no wind. On the other hand, when R is bigger than λ , the surface reflects in a diffuse fashion, and a lot of energy arrives at the sensor, that records higher amplitude (bright areas). Nevertheless, the SAR images are different from the optical ones and single pixel amplitude depends not only on the reflective

characteristics of the surface. All the individual targets within the pixel sum to form the returning waveform; different contribution could be in phase or out of phase and create bright or dark return signal, respectively; this variation is called speckle. To obtain better estimates of backscatter, it is possible to average the contribution of many pixel (a process called multilooking or taking looks).

2.1.4 The phase in a SLC image

Each pixel of a SLC image contains a phase value that depends on the ground-satellite distance. Even when this distance is constant the phase signal is subject to delays caused by the atmosphere, and shifts due to the interaction with the surface. The wavelength of the signal is smaller than the ground surface element forming the pixel, thus normally hundreds of individual elementary targets are contained into a pixel, whose returning phase is averaging the single contributions of all targets, each with a different complex reflection coefficient. Thus, the phase shift for any one pixel is in fact random (from 0 to 2π) because the resultant phase depends on the combination of hundreds of unknown complex numbers. Being the pixel phase random, useful information can be extracted only differencing the phase of the same pixel between two different SAR images: this is the principle of radar interferometry.

2.1.5 SAR Image Geometry

SAR image acquisition geometry differs from optical imagery because radar discerns targets using the distance to the antenna (range), while optical sensors use the angular separation of targets (Figure 2.7). The geometric distortions of foreshortening, layover and shadowing are due to this characteristic. The foreshortening effect is the distance shortening in LoS direction that occurred when the topography surface is dipped toward the radar, like the segments BT in figure 2.7, the time difference between the top (T) and the bottom (B) is reduced and they appear closer together in the image; furthermore the echo from T arrives before the echo from B; this causes the toppling of the slope: the top is plotted on the wrong side of the slope and vice versa (layover effect).

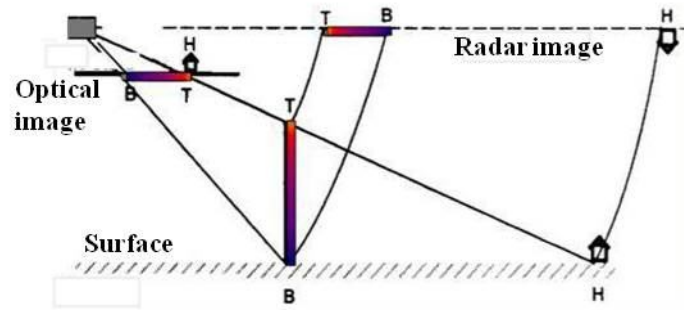


Figure 2.7: The effect of surface slope on LoS of optical and SAR images. In SAR image the top (T) of the object is closer to the satellite with respect to the base (B); the contrary in optical one. The house appears turned and it is located at the real distance from the BT object base..

The layover causes the mixing of the slope phase with the phase of neighboring area. When the topographic relief blocks the incoming signal, we have the shadowing, this is a classic problem of shallow incidence angle radars, whereas the layover is a particular problem of steep angle SAR. Even though it is possible to correct some of these geometrical distortions using, for example, a Digital Elevation Model (DEM) of the surface, it is not possible to recover information from layover and shadowing areas.

2.1.6 SAR Interferometry: fundamental principle

Radar interferometry is based on the evaluation of the variations of the phase values between two different radar images acquired from (nearly) the same point of view. As previously said, the single pixel phase in a SLC is random; but, if the phase values of two radar images corresponding to the same area are differenced and the backscatter characteristics of the ground surface are unchanged, we can remove the random contribution. The residual phase depends only on two factors: variation in path length and atmospheric path delay between the two radar passes. Thus the factors that contribute to the phase changes are the line of sight geometry, the topography and the surface deformation (which influence the path length) and the atmospheric physic-chemical properties. By removing the first two components using the accurate knowledge of satellite ephemerides and a DEM and

hypothesizing that the atmospheric path delay is small, it is possible to isolate the surface deformation contribution.

2.1.7 SAR Interferometry: limits

For SAR interferometry there is an indispensable condition: in each radar image the phase characteristics of a single pixel must be identical; if a field is ploughed or there is a wet snow cover in one of the two images, the fundamental condition is not verified.

Moreover, if we consider a pixel length L_p (perpendicular to the satellite orbit), we have a change in path-length between echoes from the near and far side of the pixel $2L_p \sin\gamma$, with γ = radar incidence angle. It is a fundamental condition that this difference should not exceed the radar wavelength. If this occurs, the phase will be incoherent and the interferometry is not practicable.

This implies that the two images need to be taken from very close points of view. Considering γ_1 and γ_2 the incidence angles of the two images referred to the same ground pixel, the condition is:

$$2L_p(\sin\gamma_2 - \sin\gamma_1) < \lambda \quad (2.13)$$

This means, taking the example of the ERS satellite, that it is possible to do interferometry only with radar images with orbit separation of less than one kilometer.

2.1.8 SAR Interferometry: contribution from viewing geometry

If two radar images are taken from satellites in different positions, on the same ground point there a difference in path length (δ). This depends on the baseline separation of the two antennae (Figure 2.8).

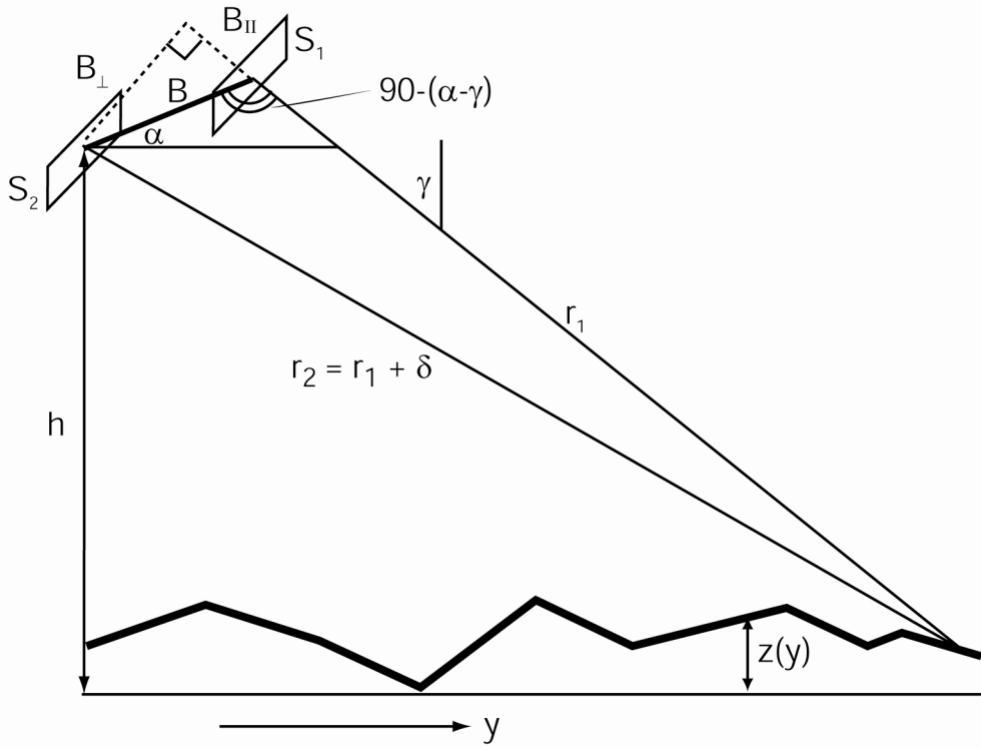


Figure 2.8: simplified imaging geometry for radar interferometry: two radar images are taken from satellites in different positions. The satellite antennae ($S_{1,2}$) are separated by a baseline distance (B) which can be resolved into components parallel and perpendicular to the look direction, B_{\parallel} and B_{\perp} . (from Wright, 2000)

The corresponding phase shift is $\phi = 4\pi\delta/\lambda$, and if we consider the r_1, r_2, B triangle, we can write:

$$(r_1 + \delta)^2 = r_1^2 + B^2 + 2r_1B\text{sen}(\gamma - \alpha) \quad (2.14)$$

And, considered that B and δ are $\ll r_1$ we have:

$$\delta \approx B\text{sen}(\gamma - \alpha) \quad (2.15)$$

We can write the 2.15 in term of phase difference

$$\phi = 4\pi B\text{sen}(\gamma - \alpha) / \lambda \quad (2.16)$$

Considering a constant topography, $z(y)$, we can express the change in the phase in the range direction by a change in incidence angle

$$\partial\phi / \partial\gamma = 4\pi B_{\perp} \sin(\gamma - \alpha) / \lambda = 4\pi B_{\perp} / \lambda \quad (2.17)$$

Consequently, there is a phase change that only depends on the perpendicular baseline separation of the position of two antennae because γ changes across the radar swath. Now, considering $y = h \tan\gamma$ and assuming a flat earth geometry and $B_{\perp} = \text{constant}$, we can express the change in phase in ground range direction:

$$\partial\phi_g / \partial y = 4\pi B_{\perp} \cos^2\gamma / h\lambda \quad (2.18)$$

Such range phase ramp depending on the perpendicular baseline can be simply calculated and removed from the final interferogram using orbital knowledge. Changes in B_{\parallel} along the satellite track introduce along-track direction phase ramps, because the parallel baseline simply adds a phase shift to the interferogram, variable slightly across the swath due to the change with the incidence angle. Whereas ramps in along-track direction have gradients equal to the rate of change of B_{\parallel} with azimuth, changes in B_{\perp} in the along-track direction cause a twist to the phase ramp, where its gradient in the range direction changes with azimuth.

2.1.9 SAR Interferometry: contribution from topography

Considering a more realistic topography (not constant) contributing to the phase variation, considering the figure 2.8, we have

$$z(r, \gamma) = h - r \cos\gamma \quad \text{and} \quad \partial z / \partial\gamma = r \sin\gamma \quad (2.19) \text{ and } (2.20)$$

And from equation 2.17

$$\partial\phi / \partial z = 4\pi B_{\perp} / r\lambda \sin\gamma \quad (2.21)$$

Now we define h_a , the altitude of ambiguity, like the magnitude of topography that results in a single interference fringe. From the 2.21 it follows that:

$$h_a = (\partial z / \partial \phi) 2\pi = r\lambda \sin\gamma / 2B_{\perp} \quad (2.22)$$

Without any topographic correction an interferogram shows a set of fringes surrounding the topography. These are h_a spaced and are inversely proportional to the perpendicular baseline. Bürgmann *et al.* (2000) show as it is possible to use this effect to derive a topographic model of the terrain from InSAR. On the other hand, by using a digital elevation model (DEM), we can remove the topographic phase contribution from the final interferogram to measure the ground deformation. In this case h_a becomes the magnitude of the height error that results in a single interference fringe. Thus, topographic errors in surface change measurements are low for image pairs with small values of B_{\perp} , i.e. large values of h_a .

2.1.10 SAR Interferometry: surface deformation

After the correction of the viewing geometry and of the topographic contribution, we can attribute the remaining phase difference to two causes: the atmospheric path delay and the surface deformation. If we neglect the former, the phase changes ($\Delta\phi$) in an interferogram are due to the changes in range (Δr), that is to surface displacement, u whose direction is \check{n} , unit vector pointing from the observation point to the satellite.

$$\Delta\phi = 4\pi\Delta r / \lambda = -(4\pi / \lambda) \check{n} \cdot u \quad (2.23)$$

If we have a displacement of $\lambda/2$ (2.8 cm for the satellite ERS and ENVISAT), the interferogram will show an interference fringe ($\Delta\phi = 2\pi$), this is much smaller than the magnitude of a topographic error necessary to produce an interference fringe. This characteristic of sensitivity makes the Differential InSAR (DInSAR) a fundamental geodetic tool to monitoring the ground deformation.

DInSAR measurements of deformation are relative: we only can observe the deformation gradient and not the absolute value of deformation. This means that if all pixel of the image are moving towards or away from the satellite by the same amount, the phase change is the same for all pixels. Moreover only clear pattern of deformation can be detected; in fact if we are observing very slow or linear phase variation, we will probably remove it during the orbital correction. Thus DInSAR technique can detect only limited kinds of deformation with well defined magnitude and spatial scale. Massonnet and Feigl (1998) identify five physical limits (Figure 2.9). First of all the Pixel size is a limit because any deformation phenomena smaller than the pixel cannot be detected. The second one is the swath width: measure of phenomena larger than the swath are problematic because it is difficult to join adjacent swaths for the reason that the interferograms will have different acquisition times, and there would be an abrupt change in the line-of-sight vector at the join. The third limit is for steep gradients; in fact, since the phase measurements are relative and enclosed between $\pm \pi$, only variation in phase smaller than π ($\Delta r = \lambda/4$) between two adjacent pixel are not ambiguous. In the case of the ERS satellite we have an upper bound of strain $\sim 10^{-3}$ in range direction. The lower boundary (fourth limit) of deformation gradient is $\sim 10^{-7}$, about one fringe for the entire image. The last limit is represented by the cycle slice; it is very difficult discern values smaller than a tenth of fringe (for C band, like ERS, the limit is at few millimeters).

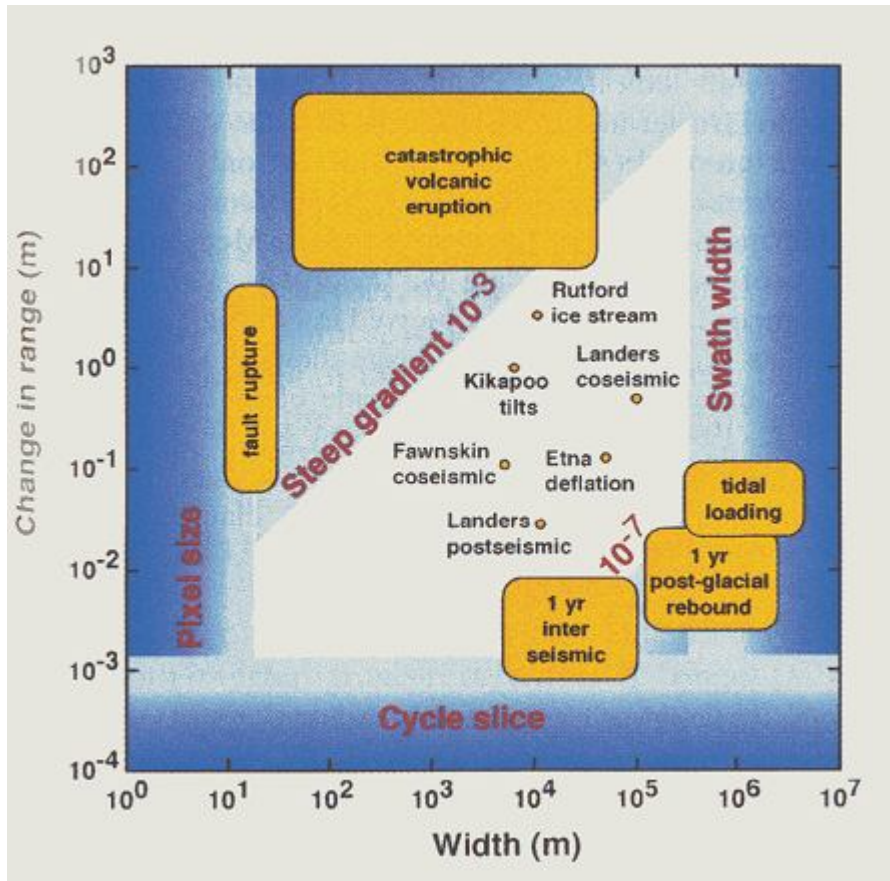


Figure 2.9: Reassuring panel of crustal deformation signals that can be detected with InSAR (after Massonnet and Feigl, 1998). Detectable deformation signals fall into the white polygon, bounded by physical limits discussed in the text.

Concerning the deformation due to the earthquake cycle, we can argue that both coseismic and interseismic deformation are detectable, even though the last one falls near the lower bound of the detectable interval of deformation and, for longer period interferograms, decorrelation problems become important.

2.1.11 SAR Interferometry: the atmospheric path delay

As previously mentioned, the waves pass through the atmosphere and here, they are subjected to change in phase:

$$\tau = \int (n-1) dz \quad (2.24)$$

With the integral from 0 to z_a ; n = refractive index; z = height and z_a = effective thickness of the atmosphere. The refractive index is independent of the wavelength

for electromagnetic waves of radio wavelengths, but dependent on the pressure, temperature and water vapour pressure. Normally the atmosphere is not temporally stable nor homogeneous, and the variable path delay can limit the InSAR accuracy for deformation measurements (e.g. Goldstein, 1995; Massonnet and Feigl, 1995a; Delacourt *et al.*, 1998). For example given different temperatures, pressures and humidity, a phase signal correlated with topography would be probable, like Delacourt *et al.* (1998) showed for the Monte Etna, where up to 6 ± 3 centimeters of delay for some interferograms are predicted. On the other hand, there is the possibility that the atmospheric signal is more localized and uncorrelated with elevation: interferograms with evidence for a variety of meteorological phenomena, including precipitating rain clouds, weather fronts and convective rolls, are presented by Hanssen *et al.* (1999) and the phase delay observed is up to three fringes. The same order of magnitude was found by Massonnet & Feigl (1995a) with five to ten kilometers irregular deformation patterns. The authors attribute these phenomena to localized thunderstorms. Because the atmospheric path delay depends on the atmospheric condition over a determinate area and at one precise acquisition time, then it is characteristic of each SLC image and it can be identified, but not removed, by processing several interferometric pairs. We can attribute to atmospheric effects a particular phase signal present in an interferogram by considering the SLC images used in the interferometric pair, and verifying the presence of the same signals in other interferograms, covering the same time interval, made with different pairs. The problem of atmospheric signal removal can be dealt with using multitemporal techniques, using large interferogram stacks. Since the atmospheric path delay (at least that due to turbulent phenomena) is not temporally correlated, while the deformation signal is slowly variable with time, we can isolate the deformation pattern with respect to the atmospheric one.

2.2 Multitemporal DInSAR techniques

2.2.1 Methods

In the previous section we have seen as classic differential SAR interferometry is a powerful tool to investigate natural phenomena of ground deformation. InSAR is mainly used to measure ground deformation related to fast ground movements and the coseismic phase of the earthquake cycle (e.g. Massonnet and Feigl, 1998; Burgmann *et al.*, 2000; Massonnet *et al.*, 1993). Fault creep has also been measured using interferometry (e.g. Rosen *et al.*, 1998); the ground displacements caused by creep are discontinuous, producing steps in interferograms that are relatively easy to detect.

We have seen also as it is possible to detect interseismic deformation, if the rate of deformation is high, but in practice interseismic crustal deformation seldom exceeds rates of a few millimeters per year distributed over 30-150 km, and it has proved difficult to measure using classic InSAR.

The multitemporal approach to the InSAR technique was developed with the aim of monitoring deformation phenomena characterized by continuous deformation in time and small deformation rates, like interseismic and postseismic deformation, landslides, subsidence, tectonic or volcanic uplift or the tectonic plate movement at the plate boundaries. In the last ten years, several techniques that allow the generation of time series have been proposed, first using conventional DInSAR (Amelung *et al.*, 1999; Hoffmann *et al.*, 2003).

During several years of study Usai *et al.* (1997; 1998; 1999) argued that some objects, mainly of anthropogenic nature, such as buildings, bridges, railways and roads, highly and reliably coherent in spite of the long-time intervals, manifest themselves as strong, nearly point-like bright dots in almost completely decorrelated interferograms. The Advanced D-InSAR techniques then hunt for and utilize these point-wise targets to track the temporal evolution of the deformation. On the basis of the strategy and processing methods the advanced techniques developed are classified as: Least Square approach (LS) and Stacking; Permanent Scatterer SAR Interferometry (PSInSAR); Small BAseline Subset (SBAS),

Interferometric Point Target Analysis (IPTA); Coherent Pixel Technique (CPT) and StaMPS method, which will be introduced in some detail.

Usai *et al.* (1997,1999), after analyzing the phase stability of some man-made features, presented a new approach, known as Least Square approach (LS), for the long-term monitoring of terrain deformations with DInSAR. The base concept of this approach is to solve all the deformation velocities, of a database of interferograms, as a unique least squares problem providing a chronologically ordered sequence to describe the evolution of the deformation in time (Usai, 2002). Wright *et al.* (2001) successfully used a simple technique to link interferograms to obtain mean ground velocity maps. The authors show like the errors due to atmospheric, topographic and orbital signals, that normally delete the smaller interseismic signal, can be reduced by stacking multiple interferograms, after screening for atmospheric anomalies, effectively creating a new interferogram that covers a longer time interval.

Ferretti *et al.* (2001) proposed a new approach to the multitemporal DInSAR with a method called Permanent Scatterers (hereinafter PS) based on the observation that a subset of targets, called permanent scatterers, is not affected by temporal decorrelation problems. They maintain the same “electromagnetic signature” across the entire SAR image stack; in other word they maintain the phase information during the time: We have seen that the phase value for each pixel is the coherent sum of contributions from all scatterers; relative movement of these scatterers, or a change in the look or squint angle, causes the contributions to sum differently, an effect known as decorrelation (Zebker and Villasenor, 1992); for ground resolution elements containing a persistently dominant scatterer, if the dimmer scatterers move with respect to the dominant scatterer, the phase due to decorrelation varies little with time. Moreover, when viewed from different look and squint angles, this variation is small; this is the principle behind a PS pixel. PS are typically buildings, metallic structures, outcrops of rock without vegetation and all ground elements which electromagnetic behaviors does not vary substantially from image to image. Hooper *et al.* (2004) developed a new method for identifying and processing PS applicable to low-amplitude natural targets without any prior

model of deformation; they extracted the temporal and spatial pattern of deformation even where conventional interferograms showed almost complete decorrelation.

Berardino *et al.* (2002) extended the Least Squares approach to the case of multiple small baseline acquisition subsets proposing the Small Baseline Subset (SBAS) approach. The method is based on the point that the interferograms are generated from image pairs carefully selected in order to minimize the spatial baseline with the aim to reduce the spatial decorrelation and the topography contribution. In order to link SAR datasets separated by large baselines (otherwise independent) the authors used the Singular Value Decomposition (SVD) method. Originally, the SBAS method was used to investigate large scale deformations at spatial resolution of about 100x100m, calculating the time-series of deformation and estimating the DEM error and the atmospheric artifacts in a similar way as in the PS-InSAR technique. A complementary approach, utilizing two different sets of data generated at low (multi-look) and full resolution (single-look) respectively, to monitor localized deformation, was developed by Mora *et al.*, (2002).

In 2003, Werner *et al.* proposed a new method to build time series called Interferometric Point Target Analysis (IPTA). They use interferometric pairs with long baselines, in a similar approach as for the PS-InSAR.

There has been some debate about the relative merits of PS and SBAS approaches. However, because they are optimized for different models of ground scattering, the two approaches are complementary, as a minimum in the usual case where a data set contains pixels with a range of scattering characteristics. For this reason, in 2008, Hooper presented a new algorithm that combines both PS and SBAS approaches to maximize the spatial sampling of useable signal. Increase of the spatial sampling is important at least for two reasons: first of all, there is an increasing of the resolution of any deformation signal; second, it allows for a more reliable estimation of integer phase-cycle ambiguities present in the data (phase unwrapping). The author developed a free software package to apply the PS, SBAS and combined MT-InSAR algorithms (StaMPS/MTI).

In 2003 Mora *et al.* developed a Coherent Pixels Technique (CPT) choosing the temporal coherence as criterion for permanent scatterers selection, only to make flexible the SAR image requirement in PS analysis.

Blanco *et al.* (2007) and Duque *et al.* (2007) improved the CPT into an operational advanced technique for terrain deformation mapping, in terms of linear and nonlinear deformation extraction, robustness with DEM error, thus allowing DEM refining, and atmospheric phase screen (APS) removal. Main steps of this technique are optimal interferogram set selection, coherent pixels selection, linear and nonlinear blocks for a full deformation extraction (Blanco *et al.*, 2008). They used a Delaunay triangulation and Minimum Spanning Tree (MST) for the best combination of interferograms, Conjugate Gradient Method (CGM) for Phase Unwrapping, multi-layer for liable estimation of linear deformation. CPT can provide full-resolution deformation by integrating the amplitude-based criterion for pixels selection and it is considered a well-integrated technique of the main PSI techniques.

2.2.2 Differences and similarity among methods

The techniques mentioned above are characterized by several differences, mainly relying in data requirements (minimum number of SAR images, i.e. more than thirty needed for PS for a well constrained statistics of phase stability), the limitations on baseline length (SBAS, LS, CPT), the need for multilooking (SBAS, LS, CPT), the multi-pair approach (SBAS, LS, CPT) for interferogram formation. On the other hand, all approaches use a two-step method, linear and nonlinear, to extract information about the ground deformation, although the linear model is a way to clean the phase to make nonlinear estimation easier.

In all multitemporal DInSAR methods, the final products separate the contributions coming from deformation signal, DEM errors and atmospheric artifacts. In general the topographic and atmospheric errors are bigger than the ground deformation signal, compared with classical SAR interferometry. For this reason these techniques need a large number of images. After the estimation and removal of the linear phase (linear deformation and DEM error phases), we still

have the contributions of the Atmospheric Phase Screen (APS), of the nonlinear deformation and of the noise. The multilooking process in SBAS and CPT or the neighboring differencing in PS and CPT, mitigates the noise. The atmospheric phase component is characterized by a well defined spatial correlation and exhibits a significantly low temporal correlation (nearly random behaviour); starting from this observation, the APS is isolated using a spatial low-pass, and a temporal high-pass filtering (Ferretti *et al.*, 2001; Berardino *et al.*, 2002; Mora *et al.*, 2003)

Concerning the multi platform interferometry, I analyzed the possibility of integration of data from ERS and ENVISAT satellite. In fact, both satellites work with C-band, but there is a frequency difference that, although small, limits the generation of useful cross-interferograms (Monti *et al.*, 2000). The SBAS multitemporal InSAR techniques get around the problem by considering ERS and ENVISAT as independent subsets, searching for a least squares solution with a minimum norm deformation velocity constraint (Berardino *et al.*, 2004; Pepe *et al.*, 2005; Mallorquí *et al.*, 2005; Blanco *et al.*, 2006)

2.3 The SBAS technique

In this work, to analyze the interseismic ground deformation in the two test areas of the Gargano Promontory and Central Iran, I used the DInSAR-SBAS approach of Berardino *et al.* (2002). These areas show many differences in terms of coherence and number of available images. The first area is characterized by a good ERS-ENVISAT image database, but because of the vegetation and large cultivated areas, the coherence is limited. Whereas the second one is characterized by a limited ENVISAT image database, but a very good coherence, being the area almost entirely desert.

The Berardino *et al.* (2002) approach extends the technique presented in Lundgren *et al.* (2001) and Usai (2001) to the case of multiple Small Baseline (SB) acquisition subsets via an easy and effective combination of all the available SB interferograms. They based this combination on a minimum-norm criterion of the deformation velocity, applying the singular value decomposition (SVD) method. The technique satisfies two key requirements: 1) the “temporal sampling rate” is

increased using all the acquisitions included in the different SB subsets; 2) the method preserves the system capabilities to provide spatially dense deformation maps. This approach can be easily implemented as a postprocessing step applied to the set of differential SAR interferograms generated with classical tools of interferometry. In this approach unwrapped interferograms are used with a two-step processing procedure extending the sparse-grid approach presented by Costantini and Rosen (1999). In the used SBAS algorithm are also present an estimate of the topographic error and the filtering of the atmospheric phase artifacts on the computed space–time deformation measurements, following the solution developed for the PS technique (Ferretti *et al.*, 2000; 2001).

The first operation of DIFSAR processing algorithm, whose overall block diagram is shown in figure 2.10, carries out an unwrapping step on the (small baseline) wrapped interferograms computed from the available SAR images, the latter assumed all co-registered with respect to a master scene which identifies a common output azimuth/slant-range grid; the unwrapping operation is applied to each DIFSAR phase pattern but only involves those pixels that exhibit an estimated coherence value higher than an assumed threshold, for this reason, the coherence-driven pixel selection must be implemented on a data set lying on a sparse grid. A refinement of the results obtained from the first unwrapping step is generally needed because the unwrapping operation can be rather critical in the DIFSAR case. A low-pass (LP) phase component, with respect to time, is estimated for each interferogram, starting from the stack of the different unwrapped phase patterns, that are subtracted modulo- 2π from the corresponding input interferograms, thus typically leading to a rate reduction of the residual fringes. a new unwrapping step can be applied to the residual wrapped phase patterns and, thus, the retrieval operation is significantly simplified and allows to achieve, by adding back the subtracted LP phase component, a refined unwrapped DIFSAR phase pattern.

Refined unwrapped DIFSAR phase signals are obtained as a consequence of the topography artifacts mitigation and of the two-step unwrapping operation, and the SVD-based inversion can be finally applied. The obtained results do not only

account for the wanted deformation signal, but also for the decorrelation effects and for possible topographic and atmospheric artifacts; the complex multilook operation carried out within the DIFSAR interferograms generation process and by the coherence-driven pixels selection can significantly mitigate the decorrelation phenomena. the presence of an atmospheric phase component represents a critical issue because it may significantly reduce the accuracy of the detected deformations; thus, a filtering operation (derived from the PS approach) must be performed on the output of the SVD-based procedure in order to mitigate the effect of these atmospheric artifacts. The filtering is based under the assumption that the atmospheric signal phase component is characterized by a high spatial-correlation and low time-correlation. The evaluated atmospheric phase component is finally subtracted from the estimated phase signal.

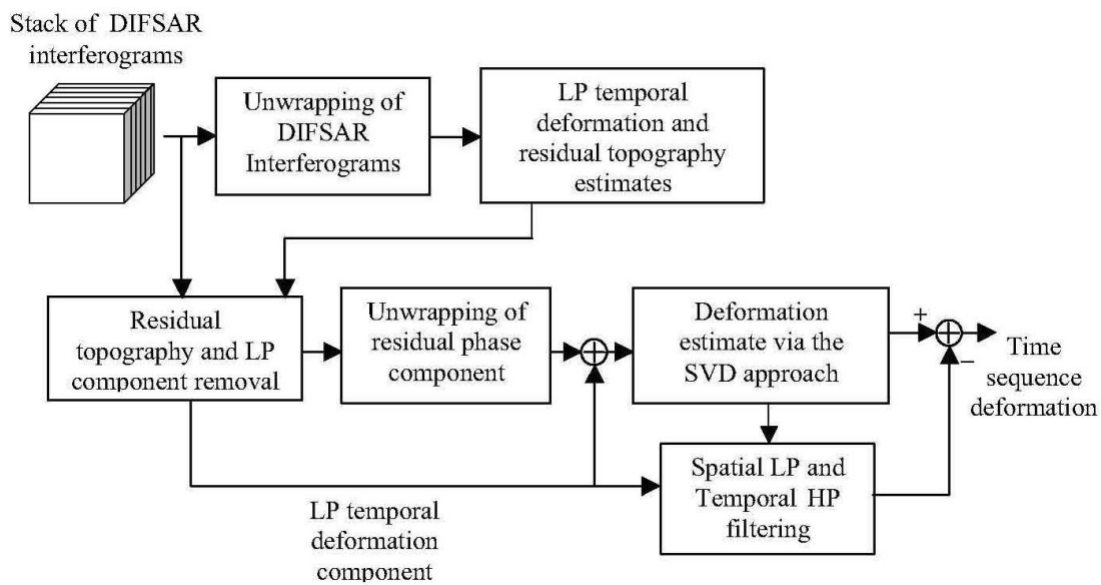


Figure 2.10: flow diagram of the SBAS processing chain (from Berardino *et al.*, 2002).

For a more complete discussion of the principles of SBAS, see Berardino *et al.* (2002).

At the end of the SBAS processing chain, we obtain three final products: 1) a multilook amplitude image of the area; 2) a ground displacement time series for each pixel whose coherence value is over a determinate threshold; 3) a mean

velocity map of the study area. The accuracy of the latter has been evaluated in a comprehensive study to be about $\pm 1 \text{ mm yr}^{-1}$ (Casu *et al.* 2006). The velocity map and the time series are referred to a conventional stable point: for example a zero velocity point in a SAR map means that it has the same velocity of the reference point. In addition, the velocity map and the time series are expressed in Line of Sight (LoS) velocity: positive values indicate approach to the satellite, whereas negative ones indicate moving away from the satellite. In this work I used the SAR images from ERS and ENVISAT satellites, whose acquisition geometry is very similar. The two orbits can be considered quasi polar: the azimuth angle is only 8.5° with respect to the North; the LoS is inclined about 23° with respect to the vertical, looking right along the orbit direction (Figure 2.11).

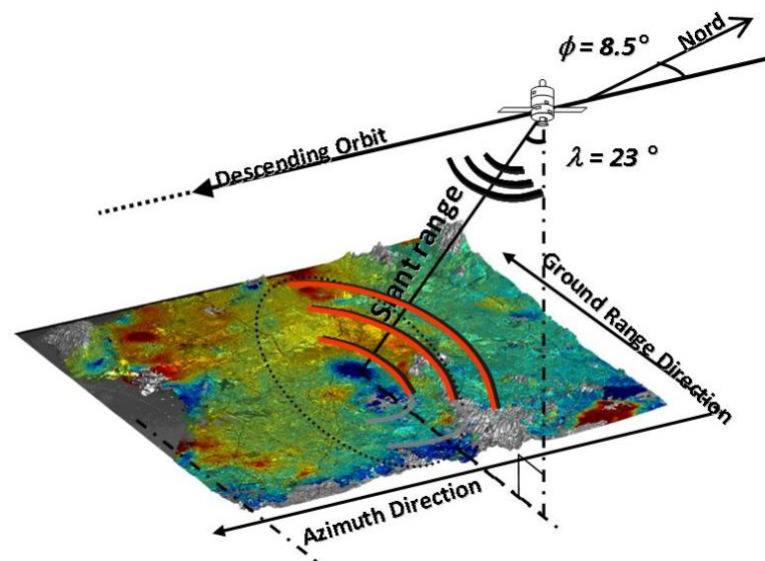


Figure 2.11: Simplified illustration of the acquisition geometry for ERS and ENVISAT satellites. The satellite orbits are characterized by an azimuth angle of about $\Phi \approx 8.5^\circ$, whereas the LoS is $\lambda \approx 23^\circ$ dipping respect to the vertical.

2.4 Post-processing techniques

With the expression “post-processing techniques”, I mean all operations made, following the SBAS processing, over the final products of the multitemporal analysis.

2.4.1 Data validation

First of all, I seek to validate the InSAR results with other geodetic data, as GPS and/or other InSAR results. Information provided by GPS is used to relate InSAR measurements within a reference frame. Atmospheric and orbital effects distributed over hundreds or thousands of square kilometers can be difficult to discriminate without independent information, thus justifying the complementary between GPS and DInSAR data (Prati *et al.*, 2008).

First Bock *et al.* (1997; 1998) suggested the idea of InSAR and GPS integration. A Double Interpolation and Double Prediction (DIDP) approach for this integration was proposed by Ge *et al.* (1997, 2000). Gudmundsson (2000) proposed a methodology using Markov Random Field (MRF) regularization and simulated annealing optimization, to unwrap InSAR images, obtaining a high-resolution 3-D motion field from combined GPS and interferometric observations. Using GPS, MODIS and MORIS data, Li (2005) and Li *et al.* (2005) produced regional water vapor model with a spatial resolution of 1x1 km, which, applied to the ERS-2 repeat-pass data, assisted in discriminating geophysical signals from atmospheric artifacts. By use of global atmospheric models (GAM) Doin *et al.* (2009), proposed another approach to model and remove the stratified tropospheric delay efficiently.

In this work I simply used the GPS velocities to compare to the InSAR results. Because of the scarcity of GPS station, I could only compare SAR and GPS velocities for the Gargano. In the other test cases no GPS stations are present in the SAR dataframes, thus I compared the InSAR velocity with the regional velocity field from GPS.

2.4.2 Residual ramp removal

Because of the errors in the DEM, of incomplete orbital signal removal, or residual atmospheric signal, it is possible that, at the end of the SBAS processing, some artifacts are still present. In most cases, some residual orbital ramps (mainly in the range direction) are present. Their order of magnitude is often comparable to the expected tectonic signal, so that a residual ramp removal is necessary to improve

the accuracy of the ground deformation signal. Where the tectonic signal is nearly linear, particular care must be taken to avoid its partial or total elimination during the ramp removal. The best solution again would be to use CGPS site velocities, which cannot contain InSAR orbital ramps, to estimate the tectonic signal trend. When CGPS are not available, one can use a priori information on the expected tectonic signal trends, and make a qualitative estimate of possible deformation signal removal. For example, the interseismic velocity field on an E-W oriented strike slip fault, should show variations mostly along the N-S direction (at least for large faults and to the first order); if the residual ramp estimated from the final velocity field is oriented ~E-W (i.e. indicating variations in the azimuth direction) its removal from the velocity map will probably eliminate some part of the interseismic tectonic signal. Whereas, if the ramp is oriented at a high angle, and is of larger magnitude than the expected tectonic signal, one can safely assume that only a limited part of it has been removed.

One can safely remove ramps also when studying localized deformation patterns, as coseismic deformation or subsidence fields, since their limited extension and peculiar spatial patterns (i.e. different from a simple linear gradient), mean that a very limited amount of signal can be removed along with a regional ramp.

2.4.3 North and up component analysis

Displacement is in general a 3D vector that I have used to imagine decomposed in three orthogonal direction, that can be East, North and Up for my goal.

One of the InSAR limitations is, however, its ability in detecting only the displacement component in the satellite-ground direction, i.e. the LoS that is not horizontal nor vertical. Regardless the direction of the measurements, the availability of only one component prevents the description of the full 3D displacement (or velocity field, is working with the results of a time-series approach).

SAR satellites have nearly polar orbits; therefore most of the earth surface is imaged from two different points of view: ascending, i.e. from south to north, and

descending. It is therefore likely that I can combine, for the same area, at least 2 different measurements.

Assuming, at a first order, that the direction is perfectly polar, i.e. following a geographic meridian, the side looking acquisition allows to completely describe the displacement occurred in a EW, vertical plane (Figure 2.11). Under this assumption, the system is completely blind to every north-south component of the displacement. Actually, a small divergence from the north direction ($\sim 10^\circ$) allows to have a small sensibility to the north-south direction, but mathematically the problem is still under-determined, with only 2 measurements (the two line-of-sight) to describe a 3D displacement. This can be described as a linear system of two equations with three unknowns (Hunstad *et al.*, 2009):

$$\begin{aligned} Ascending(i, j) &= East(i, j) \cdot coeff_{E_A}(i, j) + North(i, j) \cdot coeff_{N_A}(i, j) + Up(i, j) \cdot coeff_{U_A}(i, j) \\ Descending(i, j) &= East(i, j) \cdot coeff_{E_D}(i, j) + North(i, j) \cdot coeff_{N_D}(i, j) + Up(i, j) \cdot coeff_{U_D}(i, j) \end{aligned} \quad (2.25)$$

where (i, j) identifies the discrete pixel coordinates, $East(i, j)$, $North(i, j)$ and $Up(i, j)$ are the unknown components of the velocity field, $Ascending(i, j)$ and $Descending(i, j)$ are values retrieved through the SBAS-DInSAR algorithm and $coeff_{E_{A/D}}(i, j)$, $coeff_{N_{A/D}}(i, j)$, $coeff_{U_{A/D}}(i, j)$ are the coefficients (subscripts A and D state for Ascending and Descending) defining the two LOS geometries (Price & Sandwell, 1998) computed from precise satellite orbits (Parsons *et al.* 2006).

A possible way to get through this under-determination is the adoption of a north-south displacement value from external measurement, e.g. from GPS.

It is worth observing that SAR measurements have little sensitivity to the north-south component of the displacement, with average absolute values for $coeff_U$, $coeff_E$ and $coeff_N$ being 0.93, 0.38, 0.08, respectively. Therefore, I can assume even a single mean value for the north component to get the system (2.25) perfectly determined.

In my work I calculated the north-south component of the velocity interpolating all the available GPS measurement. First I calculated, for each pixel, the North, East

and Up coefficients relative to the two ascending and descending line of sight, on the base of the satellite position derived from precise orbits. Then I estimated the East and Vertical component of the deformation from the Ascending and Descending mean velocity data, solving the following linear system 2.25.

Chapter3

Modeling of crustal deformation

3.1 Modeling approaches

As seen in Chapter 1, in order to better understand natural phenomena we need to build a conceptual model and, by comparing the model results with natural data, we can understand the underlying process. In addition to a conceptual model, that only provides a qualitative answer to the problems, we need to quantify the physical quantity and measure the natural processes. We can roughly schematize the model into three big families: analytical models, numerical models and analog models.

3.1.1 Analytical models

Analytical models are mathematical models that have a closed form solution: the solution to the equations used to describe changes in a system can be expressed as a mathematical analytic function. A model of personal savings (<http://serc.carleton.edu/introgeo/mathstatmodels/Analytical.html>) that assumes a fixed yearly growth rate, r , in savings (S) implies that time rate of change in saving $d(S)/dt$ is given by

$$d(S) / dt = r (S) \tag{3.1}$$

The analytical solution is:

$$S = S_0 \text{EXP}(r t) \quad (3.2)$$

wherein S_0 is the initial savings, t is the time, and $\text{EXP}(x)$ is Euler's number, e , raised to the power x . This equation is the analytical model of personal savings with fixed growth rate. We can consider the analytical models more aesthetically pleasing because they give information about the system's behavior only with an inspection of the mathematical function without the need for graphing or generating a table of values, like in numerical models. Even though the solution to the above simple system is quite simple, more analytical solutions that resolve equation describing more complex systems, could be more difficult; an analytical solution does provide a concise preview of a model behavior that is not as readily available with a numerical solution. The main disadvantage of analytical solutions is that they are often very mathematically challenging to obtain.

In Chapter 1, I presented some important analytical model applied to the earthquake cycle (e.g. Savage and Burford, 1973; Okada, 1985); more details about the elastic dislocation model (Okada, 1985) are reported in paragraph 3.2.

3.1.2 Numerical models

Numerical models are mathematical models that use some sort of numerical time-stepping procedure to obtain the models behavior over time. A generated table and/or graph represent the mathematical solution.

The same example of personal savings is here reported to compare analytical and numerical solution to the problem. The differential equation is the same as 3.1. An example of a numerical solution to this fundamental differential equation is shown in Table 3.1 along with the corresponding values from the analytical solution (3.2): $S = S_0 \text{EXP}(rt)$.

T (yr)	Snum (€)	Sanal (€)
0.000	100.00	100.00
0.083	100.83	100.84
0.167	101.67	101.68
0.250	102.52	102.53
0.333	103.38	103.39
0.417	104.24	104.25
0.500	105.11	105.13
0.583	105.98	106.01
0.667	106.86	106.89
0.750	107.75	107.79
0.833	108.65	108.69
0.917	109.56	109.60
1.000	110.47	110.52

Table 3.1: example of a numerical solution with $r = 0.1$ (1/yr) and $dt = 0.083$ yr.

Using the difference equation, generates the numerical values in the Table 3.1:

$$S(t+dt) = S(t) + d(S) = S(t) + r S(t) dt = S(t) [1 + r dt] \quad (3.3)$$

Because the change in savings, $d(S)$, is quite small each time step in this numerical solution agrees fairly well with the analytical solution. This is not true for the solution in table 3.2, calculated for $r = 2.0$ (1/yr) and $dt = 0.083$ yr), where a significant discrepancy between the numerical solution and the analytical (exact) solution occurs after only one year. To get a better agreement between the numerical solution and the analytical solution, a smaller time step would be required: for a time step of 0.01 yr gave a savings value of €724.46 with 100 numerical calculations compared with the exact result of €738.

T (yr)	Snum (€)	Sanal (€)
0.000	100.00	100.00
0.083	116.67	118.14
0.167	136.11	139.56
0.250	158.80	164.87
0.333	185.26	194.77
0.417	216.14	230.10
0.500	252.16	271.83
0.583	294.19	321.13
0.667	343.22	379.37
0.750	400.42	448.17
0.833	467.16	529.45
0.917	545.02	625.47
1.000	635.86	738.91

Table 3.2: example of a numerical solution with $r = 2.0$ (1/yr) and $dt = 0.083$ yr.

This example shows a clear disadvantage of numerical solutions to model equations: many iterative calculations are required to arrive to good results; however, today the computational cost may not be a problem; additionally, the precision of the model can be greatly improved by using a more sophisticated numerical procedure than the rather simple Euler's method described in 3.3. Excluding the computation cost, numerical models show several advantages compared to the analytical ones. Following the previous example, we can note that the equations are much more intuitive; anyone can understand and reproduce the equation 3.3 by hand or Excel, while an analytical solution needs a background in mathematics. Additionally, despite on how complicated the formulas are described $d(S)$, the basic procedure $S(t+dt) = S(t) + d(S)$ is always the same; on the contrary for analytical model as it is relatively easy to get into mathematics which is much too complicated to obtain in analytical solutions; consequently to obtain more realistic models of very complex natural processing, we need to investigate it by using numerical models.

Finite element method (FEM), also known as finite element analysis (FEA) is a numerical method for finding approximate solutions of partial differential equations (PDE) as well as integral equations. It has been applied to a number of physical problems, where the governing differential equations are available. The method essentially consists of assuming the piecewise continuous function for the solution and obtaining the parameters of the functions in a manner that reduces the error in the solution. Moreover, the technique is founded on eliminating the differential equation completely (steady state problems) or reproducing the PDE into an approximating system of ordinary differential equations; these are then numerically integrated using standard techniques such as Euler's method, Runge-Kutta, etc. The primary challenge to solving partial differential equations approximates the equation to be studied, but is numerically stable, meaning that errors in the input and intermediate calculations do not accumulate and cause the resulting output to be meaningless. FEM is a good choice for solving partial differential equations over complicated domains or when there are changes in the domain; it is a good solution also when the desired resolution change over the entire domain or when the solution lacks smoothness.

FE Models have been largely used to solving geophysical problems; for example, Trasatti *et al.* (2011) developed a procedure to perform inversion of geodetic data based on the finite element method, accounting for a more realistic description of the local crust. They applied this method to the 2009 L'Aquila earthquake (Mw 6.3), using DInSAR images of the coseismic displacement (Figure 3.1).

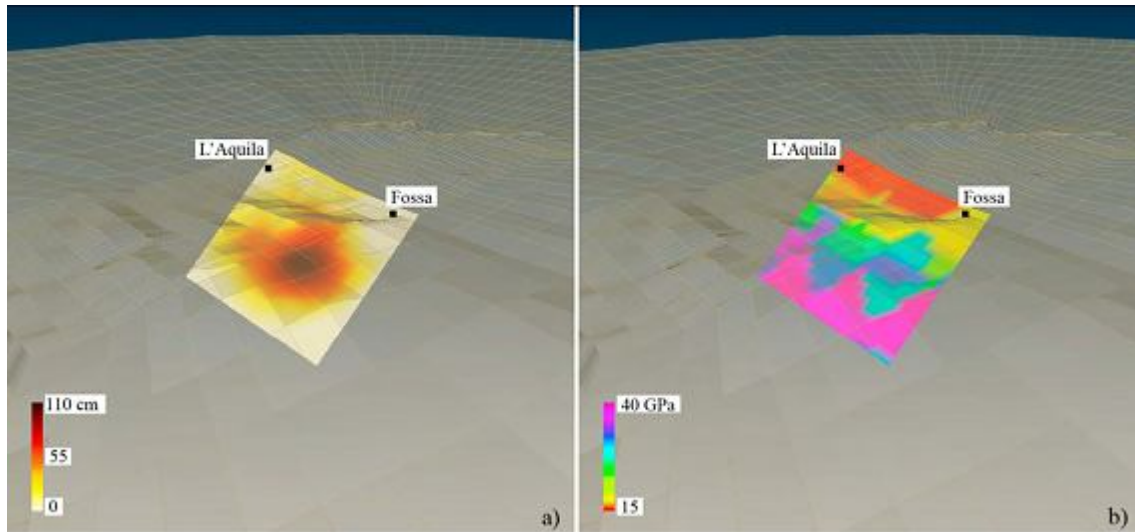


Figure 3.1: (a) Fault slip distribution within the FE HET model; (b) elastic properties (shear modulus) next to the fault plane, as implemented in the model. (Figure from Trasatti *et al.*, 2011)

On one hand, FE Models provide a very refined solution to geophysical problems; on the other hand they need ancillary information about rheology, slip distribution, crust stratification etc. that are not always available

3.1.3 Analog modeling

An analog model is a simplified scaled representation of nature. Physical parameters are chosen to mimic geometrical (i.e. lengths), kinematical (i.e. velocities) and dynamical (i.e. forces) natural conditions in order to reproduce a specific natural process, usually developing over long times and lengths, adopting more convenient geometric and temporal scales.

It is possible to realize an analog model following the evolution of the studied natural process (i.e. the physical response of the system to the applied experimental conditions) and studying complex three- dimensional processes for which governing equations are still poorly known or too complicated to be numerically solved.

The use of experimental tectonics to study tectonic processes is long-lasting in Earth Science. After the pioneering work of Sir James Hall (1815), who studied folding under compressive tectonic regime, many scientists (e.g. Hubbert, 1937; Ramberg, 1967; Weijermars & Schmeling, 1986) introduced proper scaling

relationships in order to transform the originally qualitative analog modeling approach into a solid method for studying a wide range of geodynamic processes. As shown in chapter 7, I developed a new analog model able to reproduce laboratory earthquakes following in continuum the deformation evolution during the seismic cycle, knowing the parameter values at every time step, passing from interseismic to coseismic phase of the earthquakes cycle; I used alimentary gelatins characterized by viscoelastic rheology as analog material for the crust.

3.2 Seismic source inversion

I started the earthquake-cycle analysis studying the coseismic phase of the cycle. This represents the first step of my work because to model the deformation due to an earthquake is a relatively simple cause, working at short-term scale, I can consider the earth like pure elastic medium (see Chapter 6).

The ground deformation pattern due to an earthquake can be used to determine the parameters of the seismic source (e.g. fault geometry and location, slip, rake angle, etc.) based on the elastic dislocation theory (see Chapter 1), firstly argued by Hooke. Now I show the basis for coseismic fault slip modeling as dislocations in an elastic half-space and the inversion model for the source parameters determination from InSAR data.

The models start from the idea that the strain release is concentrated on discrete fault planes during an earthquake and that the resultant energy is released through the seismic waves propagation. On short-term scale, the earth show elastic behaviors and, consequently, the seismic waves can only propagate; thus, under short-term scale condition, I can reasonably model the coseismic deformation by use of static-elastic dislocation theory (Wright, 2000).

Steketee (1958), that first introduced the elastic theory of Volterra (1907) to the field of seismology, demonstrated that the dislocation $\Delta u_j = (\xi_1, \xi_2, \xi_3)$, in a isotropic medium, across a plane rectangular surface, Σ , results in displacement field $u_i = (x_1, x_2, x_3)$ expressed as:

$$u_i = (1 / F) \iint \Delta u_j \{ \lambda \delta_{jk} (\partial u_i^n / \partial \xi_n) + \mu [(\partial u_i^j / \partial \xi_k) + (\partial u_i^k / \partial \xi_j)] \} v_k d\Sigma \quad (3.4)$$

where λ and μ are the Lamé's constant (bulk and shear moduli, respectively); δ_{jk} is the Kronecker delta; ν_k is the direction cosine of the normal to the surface element $d\Sigma$; u_i^j is the i th component of the displacement at $(x_1; x_2; x_3)$ due to the j th direction point force of magnitude F at (ξ_1, ξ_2, ξ_3) . The explicit solution to this integral equation was found by Okada (1985). Under the hypothesis of an elastic half-space, he enabled the efficient analytical calculation of displacements, strains and tilts due to shear and tensile displacements on faults. Figure 3.2 shows the geometry and coordinate space used by Okada:

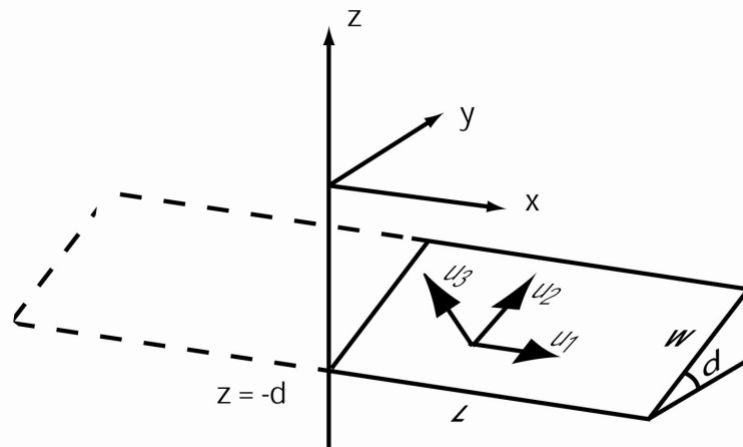


Figure 3.2: Geometry of elastic dislocation source model (after Okada, 1985).

In this reference frame, the two sides of the fault move by equal amounts, but in opposite directions, in absolute terms; this means that the total average displacement on the fault plane is equal to zero. As shown in chapter 2, when we talk about deformation from InSAR technique, the scalar displacement measured by satellite, given a surface displacement vector u , is given by $\hat{n} \cdot u$, which \hat{n} is the unit vector in the satellite line of sight. Thus, we can create synthetic interferograms starting from the Okada formulations, given a set of faults parameters that are: location, fault length, depth range, slip, strike, dip, and rake. Now we have an inverse problem: how to determine the fault parameters from the interferogram; this is not a simple problem because the calculated displacements

do not linearly depend on the fault parameters, with the exception of fault slip. To invert the elastic models which best fit the interferometric data, in this work I used the least-squares inversion algorithm based on the Levenberg-Marquardt approach, as described by Atzori *et al.*, (2009). The inversion is based on the minimization of a cost function expressed as:

$$CF = \frac{1}{N} \sum_i^N \frac{(d_{i,obs} - d_{i,mod})^2}{\sigma_i} \quad (3.5)$$

where $d_{i,obs}$ and $d_{i,mod}$ are the observed and modeled displacement of the i th point, σ_i is the standard deviation for the N points. The analysis of the uncertainty and the trade-offs affecting the source parameters is performed by perturbing the DInSAR data with a spatially correlated source of noise according to the approach of Atzori *et al.* (2008).

Despite the large number of assumption, like the elastic, isotropic, homogeneous, infinite half-space, and despite the Okada model that doesn't consider any kind of earth stratification, a wide literature exists showing its reliability. The successful of the Okada model is essentially due to the good fit of coseismic ground signal respect to the simplicity of the model. Moreover, such a model can be used within the inversion scheme, either non-linear or linear, to find the best-fit solution. That's a big advantage, if compared with the more sophisticated finite element model whose calculation is time consuming so that its use in the inversion is, at the present, prohibitive.

3.3 Interseismic deformation modeling

As discussed in the first chapter, the evolution in the concept of seismic cycle is related to the development of new conceptual model of the earthquake cycle and, therefore, to the quantitative models. I use geodetic data to study the surface deformation due to the earthquake cycle; in particular, the multitemporal DInSAR–SBAS technique allows to detect the ground deformation related to the interseismic phase of the seismic cycle.

The geodetic surface velocities are the expression of an interseismic accumulation of stress, while fault slip reflects the release of this stress, and the consequent strain, during a frictional failure. Under this hypothesis the long-term fault slip rates must be modeled only based on limited snapshots of strain accumulation. It is possible to classify the models thus far employed into three different groups. (1) Thatcher (2007) assumes the interiors of tectonic blocks far from fault boundaries undergo rigid-body rotation. (2) Savage and Burford (1973) propose also a rigid-block rotation far from fault boundaries and they model steady interseismic elastic strain accumulation with dislocations in an elastic half-space. Meade (2007) assumes that the elastic strain accrual is completely recovered during earthquakes. (3) Other models introduce a distributed viscous flow within the lithosphere whose surface expression is the current deformation field (Bendick and Flesch, 2007; England and Molnar, 2005). With different approximations these models describe the processes that occur at different depth in the lithosphere. In fact, primarily, the upper crust deforms by brittle faulting; during the earthquakes the elastic strain accumulation along block boundaries is released. In depth, in the middle to lower crust and in the mantle lithosphere, a viscoelastic flow is probably present (e.g., Nur and Mavko, 1974; Savage and Prescott, 1978). Thus, the interseismic surface velocity could be strongly biased by the coupling of the time-variable elastic deformation of the upper crust with the viscoelastic lithosphere flow. During most of the earthquake-cycle, the far-field surface velocity may be reduced and then recovered by the rapid relaxation in the middle to lower crust and upper mantle under earthquake-generated stresses. This is how the apparent discrepancy between the present day surface velocity and the geologic record is explained. Many authors (e.g., Johnson and Segall, 2004) assert that deep afterslip or localized shear zone within the middle to lower crust could also contribute to accelerate surface deformation rates early in the earthquake cycle. It is also fundamental the role played by the time-dependent viscous flow at depth: at large distance from the strike-slip deformation zone, it could potentially reduce the velocity. This is the requisite condition to accommodate both rapid, long-term strike-slip rates and low interseismic surface velocities.

As above mentioned, the fault slip rates inferred from geodesy sometimes disagree with those determined from geologic markers (e.g. Hilley *et al.*, 2010), which has led some authors to question whether fault slip rate deduced from geodetic surface velocities are representative of those averaged over longer time scales (Mériaux *et al.*, 2004). For example in the northern Tibet geodetic data estimate a relative low slip rate of 4-10 mm yr⁻¹ across an ~250 Km swath perpendicular to the Altyn Tagh fault (Bendick *et al.*, 2000; Wallace *et al.*, 2004) respect a slip rates of 20-34 mm yr⁻¹ from geologic data, in the last 6 Ka (Mériaux *et al.*, 2004; Peltzer *et al.*, 1989). Systematic errors in geologically determined fault slip rates could be the cause of this discrepancy, like some authors have hypothesized (e.g. Cowgill, 2007). On the other hand, estimates of fault slip rate from geodetic data may be biased by models that neglect the episodic loading and viscous relaxation of the middle to lower crust and mantle lithosphere that would cause surface deformation rates to vary throughout the earthquake cycle (Hetland and Hager, 2006; Hilley *et al.*, 2005; Johnson and Segall, 2004; Pollitz, 2001; Savage and Prescott, 1978).

Here I used an analytical approach the study of interseismic signal; in particular I inverted the multitemporal InSAR data by use of dislocation model (Okada, 1985). As mentioned in the previous paragraph, many authors have used this model to invert the coseismic ground deformation field under the assumption of an elastic, isotropic, homogeneous, infinite half-space. This condition is roughly true at short-term time scale, as in the coseismic condition, but it is not true concerning the interseismic phase. However, many authors (e.g. Wright, 2001; Fialko, 2006; Biggs *et al.*, 2007) applied successfully elastic dislocation models (e.g. Savage and Burford, 1973) to invert ground dislocation field, related to the interseismic signal of strike slip faults in intra-plate geodynamical contexts, characterized by high strain rate (e.g. North Anatolian Fault, Turkey; San Andreas Fault, California; Denali Fault, Alaska; respectively). The screw dislocation model (Savage and Burford, 1973) is only applicable to vertical pure strike slip fault; thus this model is not suitable in my case study, where, in addition to the main strike slip kinematic, I also hypothesize a considerable vertical component along a not perfect vertical fault plane. Hence, I tried to apply an elastic dislocation model to invert

the interseismic deformation field related to not pure strike slip faults characterized by low deformation rate in intra-plate geodynamical contexts.

The use of such a model shows several advantages respect to more complex numerical or Finite Elements models. The main one is the possibility of a fast calculation of a forward model, that allows the finding of a best-fit solution of some observed data with iterative approaches (i.e. Montecarlo, Simulated Annealing, etc.). This is, instead, unfeasible with finite element models that require a complex and time consuming. In addition, this approach often needs ancillary information on the crust rheology that is not always available. In my case, I used the analytic elastic solution within an inversion scheme based on the Levenberg-Marquardt algorithm (Levenberg, 1944, Marquardt, 1963). By means of this approach, I am able to provide a first order result relative to the interseismic source.

Chapter 4

Interseismic deformation analysis of the Gargano area (Southern Italy)

4.1 Introduction

The 50-km-long, east-west oriented Mattinata fault marks the topographic feature of the Gargano Promontory in the foreland of the Southern Apennines, Italy.

The NE-SW crustal extension, perpendicular to the axis of the Apennines, is well described by recent and historical earthquakes (Selvaggi, 1998) and by geodetic estimation of the extension rates (Hunstad *et al.*, 2003), whereas the tectonic features of the Gargano Promontory and the role of the Mattinata fault within the regional kinematics are still under debate.

Relative plates motion tends to be focused on discrete faults but, where one or both plates are continental, a significant fraction could be also accommodated on diffuse fault systems hundreds kilometers wide (England *et al.*, 1987). The relative motion between Eurasia and Africa gives rise to a broad deforming zone including the Italian peninsula.

Slip vectors of earthquakes around the Adriatic Sea, and space geodetic data have been used to establish a counterclockwise rotation of the Italian peninsula relative

to Eurasia, around an Eulerian pole located between the Po Valley and the French Alps (Anderson and Jackson, 1987; Ward, 1994; Calais *et al.*, 2002). D'Agostino *et al.* (2008) proposes an interpretation of GPS solutions and earthquake slip vectors using a block model where active deformation in the central Adriatic is controlled by the relative motion between the Adria and the Apulia micro plates. In this view, the $\sim 1.5 \text{ mm yr}^{-1}$ of NW-SE shortening in the Gargano Promontory is consistent with seismological observation showing NW-SE and E-W faults. Assuming that all the relative convergence is absorbed within the Gargano Promontory, D'Agostino *et al.* (2008) also argues that the upper bound of right-lateral strike slip $1.1 - 1.4 \text{ mm yr}^{-1}$ can be taken up by the Mattinata Fault.

In contrast, starting from structural field data, other authors (e.g. Billi *et al.*, 2007) support the hypotheses of left-lateral strike slip motion on the Mattinata Fault.

Using the SBAS multitemporal DInSAR technique (Berardino *et al.* 2002) I analyzed a SAR dataset composed of 68 descending and 47 ascending ERS and ENVISAT images with a temporal span of 9 years (from 1992 to 2001) and 16 years (from 1992 to 2008) respectively.

I used elastic dislocation model (Okada, 1985) to investigate the rate of interseismic loading, the geometry and the kinematics of the Mattinata Fault, inverting the Line of Sight (LoS) velocity field of the Gargano Promontory.

4.2 Geological and seismotectonic framework

The Gargano Promontory (southern Italy) is an ENE-WSW oriented topographical and structural high (Figure 4.1) (Finetti, 1982; Anderson and Jackson, 1987; Bosellini *et al.*, 1993; De Alteriis and Aiello, 1993); in particular it represents a portion of the Apulian foreland extending into the Adriatic Sea. The Gargano is located within the Adriatic continental block, which has played the role of foreland for both the E-verging Apennine (Miocene-Pleistocene) and the W-verging Dinaride (Eocene–Miocene) thrust-and-fold belts (Parotto and Pratlurion, 1981).

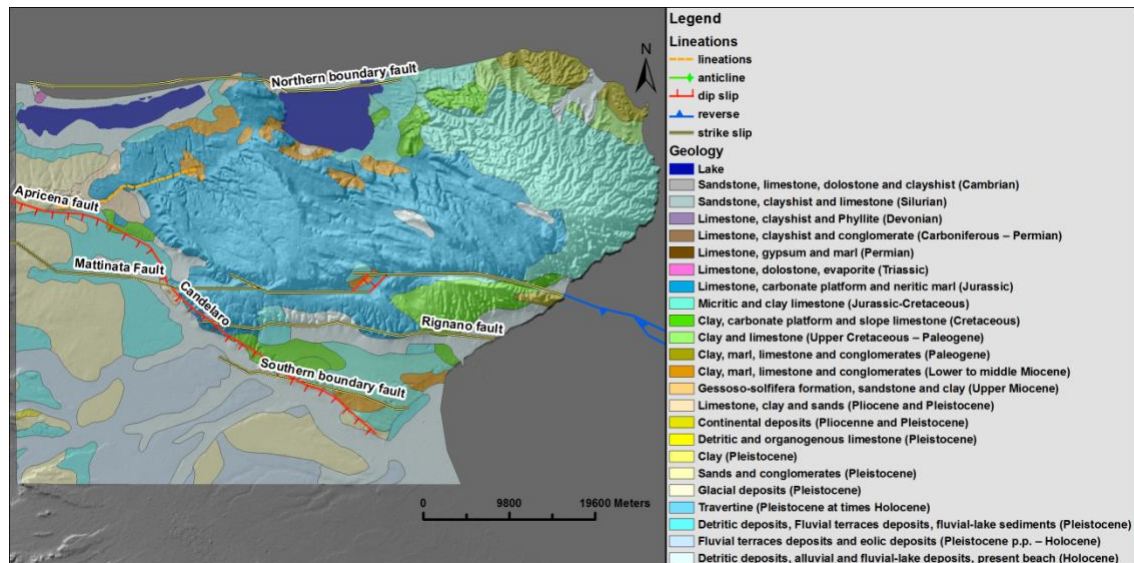


Figure 4.1: Geological map of the Gargano promontory with the main fault systems of the area.

The Gargano promontory is characterized a) by a maximum altitude of 1000 m *a.s.l.*, with respect to the maximum elevations of 200–300 m of the contest (Giorgetti and Mosetti, 1969), b) by an inland and offshore seismicity (Suhadolc and Panza, 1989), c) by the presence of gravimetric and magnetic positive anomalies (Finetti *et al.*, 1987), d) by a heat flow of 60 mW/m², which is higher than the southern Apulian region (40 mW/m²) (Mongelli and Ricchetti, 1970), and e) by a crustal thickness smaller (25 km) than the average thickness estimated for the Apulian region (35–40 km) (Console *et al.*, 1989, 1993; Favali *et al.*, 1993; Lombardi *et al.*, 1998) These features distinguish this sector from the rest of the Apulian Foreland.

A 4000m thick sequence of carbonate rocks (Jurassic - Middle Miocene) (AGIP wells: Foresta Umbra 1 and Gargano 1) characterizes the structural high of the Gargano promontory. These deposits show variable lithologic features, related to different depositional environments: the southwestern sector contains mainly shallow-water carbonates outcrops, while slope and basinal deposits bound these sequences eastward. At the southern margin of the promontory, two evident morphologic and tectonic escarpments (the Candelaro and Rignano faults, Figure 4.1) separate the rugged landforms and high topography of the carbonate successions from the Foggia plain (Ciaranfi and Riccetti, 1980). Terrigenous sediments of the Apennine foredeep basin, overlaid by recent continental and

marine deposits, characterize the plain. With regard to the structural setting, the Gargano promontory appears as a broad anticline elongated E-W, and affected by faults trending NW-SE, E-W, and, to a minor extent, NE-SW.

The spatial and temporal changes in the depositional environments and the consequent lithological differentiation has been related to different causes: tectonic events, according to Masse and Borgomano (1987) and Masse and Luperto Sinni (1987), or simple platform dismantling, according to Bosellini and Ferioli (1988) and Bosellini *et al.* (1993).

Other important tectonic structures are present in the area: the Apricena-San Nicandro morphotectonic landform is located in the epicentral area of the destructive 1627 earthquake ($I_0 = X$ MCS), which shows an E-W isoseismal field compatible with this fault. Field investigations, and unpublished INGV paleoseismologic and seismic refraction data confirm the presence of a dip-slip fault, downthrowing the Pleistocene sediments of the upper Foggia Plain to the south (Salvi *et al.*, 2000). Mainly on the basis of deep seismic profiles, Patacca and Scandone (2004) define instead the Apricena fault as a WNW-ESE structure, dipping towards SSW, and extending for about 30 kilometres from Serracapriola to Santa Maria di Stignano. The fault cuts the entire series of Plio-Pleistocene deposits. Although the kinematics of this fault is unknown, a rollover anticline that developed in the hangingwall block shows an important component of dip-slip motion in the cumulative displacement.

The most evident structure of the Gargano area is the E-W Mattinata fault (hereinafter MF). The inland extent of the MF is ~50Km long, but it reaches ~150 Km including its continuation offshore into the Gondola line (Figure 4.1). Some authors (e.g. Funicello *et al.*, 1988) consider the MF a left lateral strike-slip fault and others as a dextral one (Guerricchio and Wasowski, 1988). The offshore prolongation of the MF has been explained differently: De Alteris and Aiello (1993) indicate a transcurrent structure, active in recent times, with a right E-W shear. Transpressive motions, acting along this structure, and a trarstension, occurring in the southeastern part of the fault, have generated a pull-apart basin to the south of the ridge. Colantoni *et al.* (1990) implicated a diapiric tectonics,

whereas Argnani *et al.* (1993) suggest a fold tectonics caused by compressive shear. A ~ 200 m wide and 40 km long fault damage zone is recognizable along the onshore portion of the fault; here the kinematic indicators show a strike-slip mechanism with a left-lateral sense of slip (Billi *et al.*, 2003). The age of this tectonics is not well constrained, but is probably related to the formation of the Sant'Egidio pull-apart basin (Miocene–Pleistocene) (Funiciello *et al.*, 1988; Billi *et al.*, 2007).

Some authors (e.g., Funiciello *et al.*, 1988) suggest a pure strike-slip motion along the E-W MF system, or along a system of E-W trending left-lateral strike-slip faults (Brankman and Aydin, 2004), whereas others authors (e.g., Ortolani and Pagliuca, 1988; Bertotti *et al.*, 1999; Casolari *et al.*, 2000) support the contribution of compressive deformation resulting from N-S and NE-SW compression, and consider the crustal deformation in the Gargano Promontory to be related to remote stresses from the Dinarides.

4.3 Seismicity

The Gargano is well known as a seismically active zone (Peronaci, 1980; Suhadolc *et al.*, 1983). Destructive earthquakes have occurred in historical times, with felt effects in the area up to XI MCS (Guidoboni and Tinti, 1988; Boschi *et al.*, 1997; Console *et al.*, 1993; Tinti *et al.*, 1995). Extensive damage and casualties were referred to these events, but the exact location of their seismogenic and, in some cases, tsunamigenic sources (Tinti *et al.*, 1997) is still uncertain. Since 1975, the instrumental catalogue (Castello *et al.*, 2005, Seis. Bull. INGV-RSNC) shows that the Gargano area is characterized by a background seismicity with isolated low magnitude events ($M_{\max} = 3.5$) (Figure 4.2), but a major activity occurred in 1995 when a seismic sequence started with an $M_w = 5.2$ main shock (Figure 4.2), for which Del Gaudio *et al.* (2007) show a dextral focal mechanism and hypocenter location dept of 25 km.

The analysis of focal mechanisms shows that the seismogenic structures in the foreland sector of northern Apulia should be sought among transpressive faults with an approximately east–west strike angle, characterized by right lateral

movement, or among north–south striking faults with left lateral movement. The Mattinata Fault and the Tremiti Islands deformation belts have been frequently proposed as natural candidate to represent major seismogenic structures in the Gargano area; however the spatial distribution of the recorded seismicity does not concentrate around these structures (Del Gaudio *et al.* 2007).

Valensise *et al.* (2004) suggested that the Mattinata fault system should be considered as part of a very extended E–W right lateral strike–slip fault system connecting the eastern offshore Gondola-Grifone line to the source of the 2002 Molise earthquakes, passing through a possible location of the 1627 north Capitanata major earthquake (Figure 4.2). In general the kinematics of the E–W MF is compatible with the NW-SE regional stress field (σ_1), if a prevailing dextral strike–slip character is assumed for it (Del Gaudio *et al.* 2007).

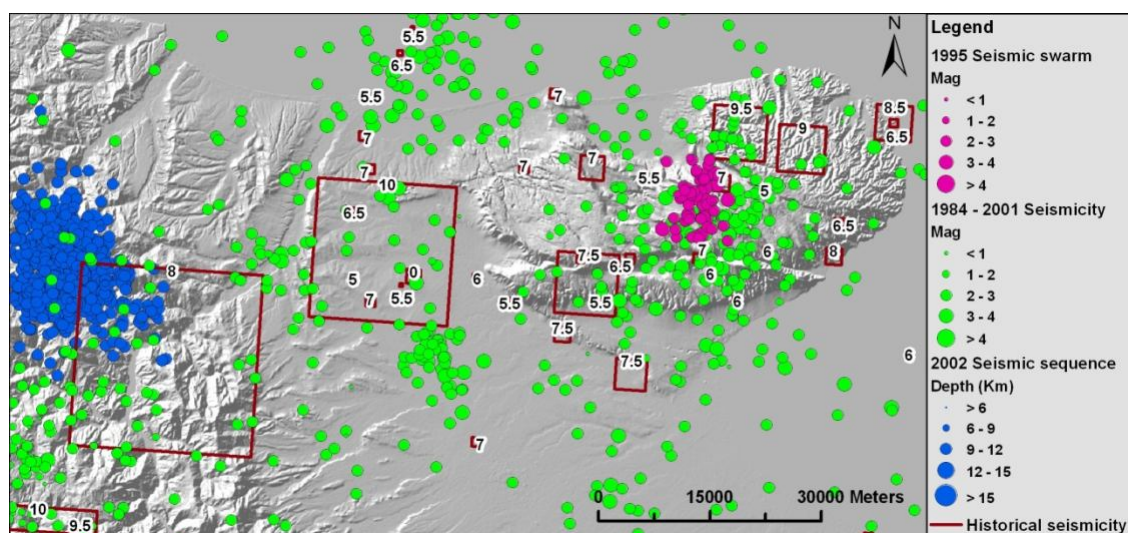


Figure 4.2: Historical and instrumental seismicity of the Gargano area. The map shows in green the 1984 - 2001 seismicity and in blue the 2002 seismic sequence of the Molise region. In purple the 1995 seismic swarm is highlighted.

In the last decades, the Mattinata Fault has been the subject of several studies by both stratigraphers and structural geologists, who debated about the strike-slip kinematics of this fault. The sense of the present strike-slip regime on the Mattinata Fault is still the subject of a heated debate (Billi *et al.*, 2003). Some authors suggest that the sense of the movement inverted at the end of the Pliocene (Argnani *et al.* 2009)

4.4 DInSAR Data Processing

In this work I applied the multitemporal SBAS DInSAR technique (Berardino *et al.* 2002) to retrieve the mean velocity and the evolution in time of the ground displacement field for the Gargano area. By means of the ascending and descending orbits we measured the components of the displacement in the radar Line-of-Sight (LOS), i.e. the ground-to-satellite direction, with an estimated accuracy of about 5 mm and 1 mm yr⁻¹ for the time-series displacement and mean velocity, respectively (Casu *et al.*, 2006). I used 68 ERS images acquired from the descending orbit and 47 ERS and ENVISAT from the ascending orbit; they span 9 years (from 1992 to 2001) and 16 years (from 1992 to 2008), respectively. In the SBAS processing I set a maximum temporal baseline of 1200 days, with a maximum spatial baseline of 200 m; the SRTM digital elevation model was used to remove the topographic contribution from the 109 ascending and 115 descending interferograms (Berardino *et al.* 2002). The geocoded velocity maps have an output resolution of 80m, that I further reduced to 400m in order to increase the signal-to-noise ratio (Figure 4.3 and 4.4).

I removed residual orbital signals (planar "ramps") using the procedure described in (Casu *et al.*, 2006). The expected tectonic interseismic signal could be roughly represented as N-S planar ramp across the E-W oriented tectonic source, whereas the removed orbital ramp shows a NE to SE strike direction. Thus, I assumed that only a small fraction of tectonic signal has been removed. All dataset information is summarized in table 4.1.

Dataset	Track	Frame	N° of images	Time span	Residual orbital ramp (strike)	Residual orbital ramp (slope)
Asc.	86	825	47	1992-2008	131°	0.10 mm km ⁻¹
Dsc.	494	2768	68	1992-2002	51°	0.07 mm km ⁻¹

Table 4.1: Multitemporal InSAR datasets.

I used two permanent GPS stations (MSAG and SGRT) to validate InSAR data; I evaluated the differential East velocities between the GPS benchmarks; then I calculated the corresponding InSAR differential East velocities (2x2km around the GPS stations) and I estimated the GPS – SAR differences, as it is shown in table 4.2.

	GPS	InSAR	GPS - InSAR
MSAG-SGRT	0.71	1.12	-0.41

Table 4.2: Differential east velocities between two GPS benchmarks and corresponding InSAR velocities. Last column shows the velocity difference between GPS and InSAR. InSAR velocities have been calculated using 2x2km boxes around the GPS stations.

The differential velocity fits into the $\pm 1 \text{ mm yr}^{-1}$ uncertainties interval, demonstrating a good agreement between the two geodetic methods.

Combining the ascending and the descending orbits, I was able to retrieve the horizontal (East) and vertical components of the displacement, according to the approach of Wright *et al.*, 2004.

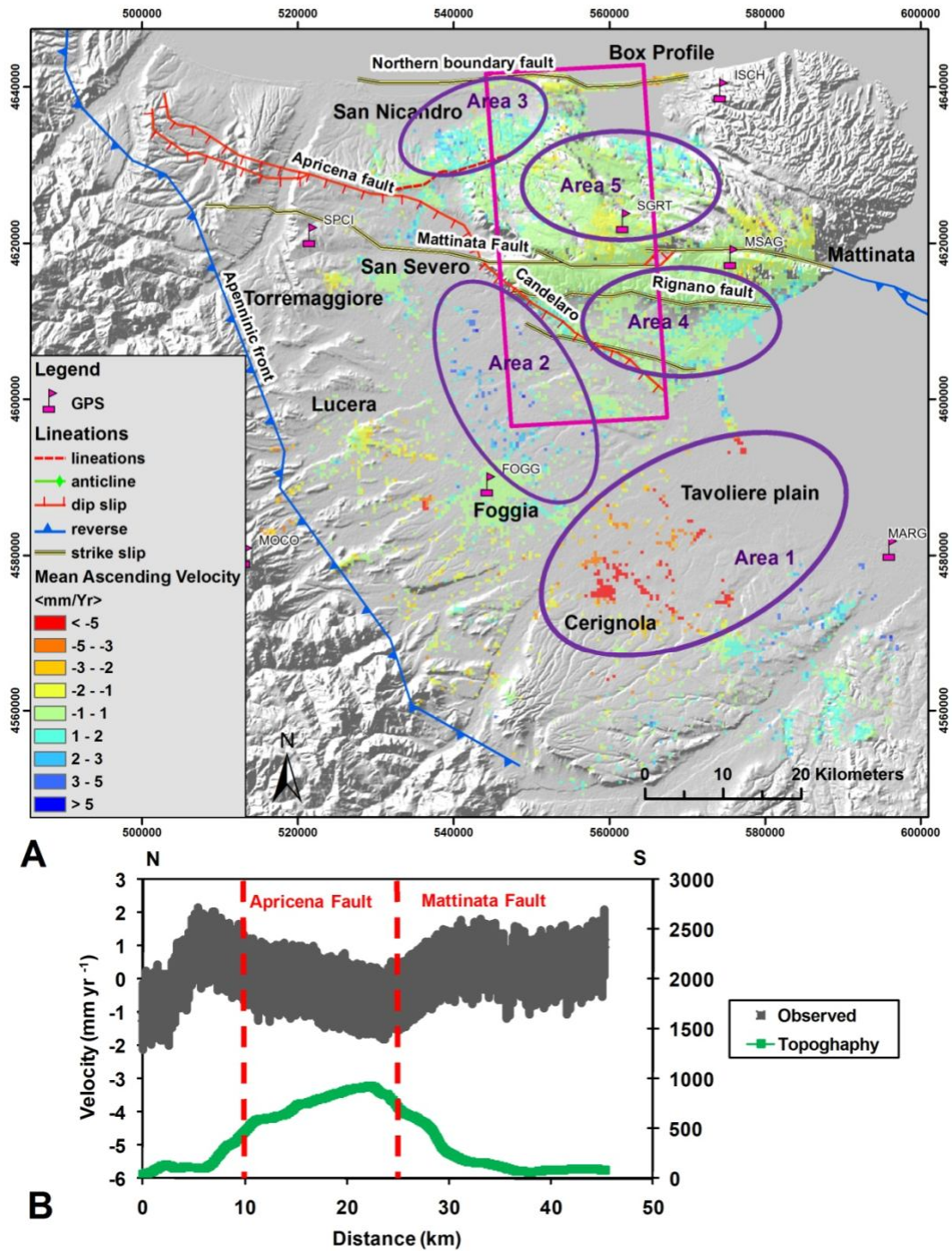
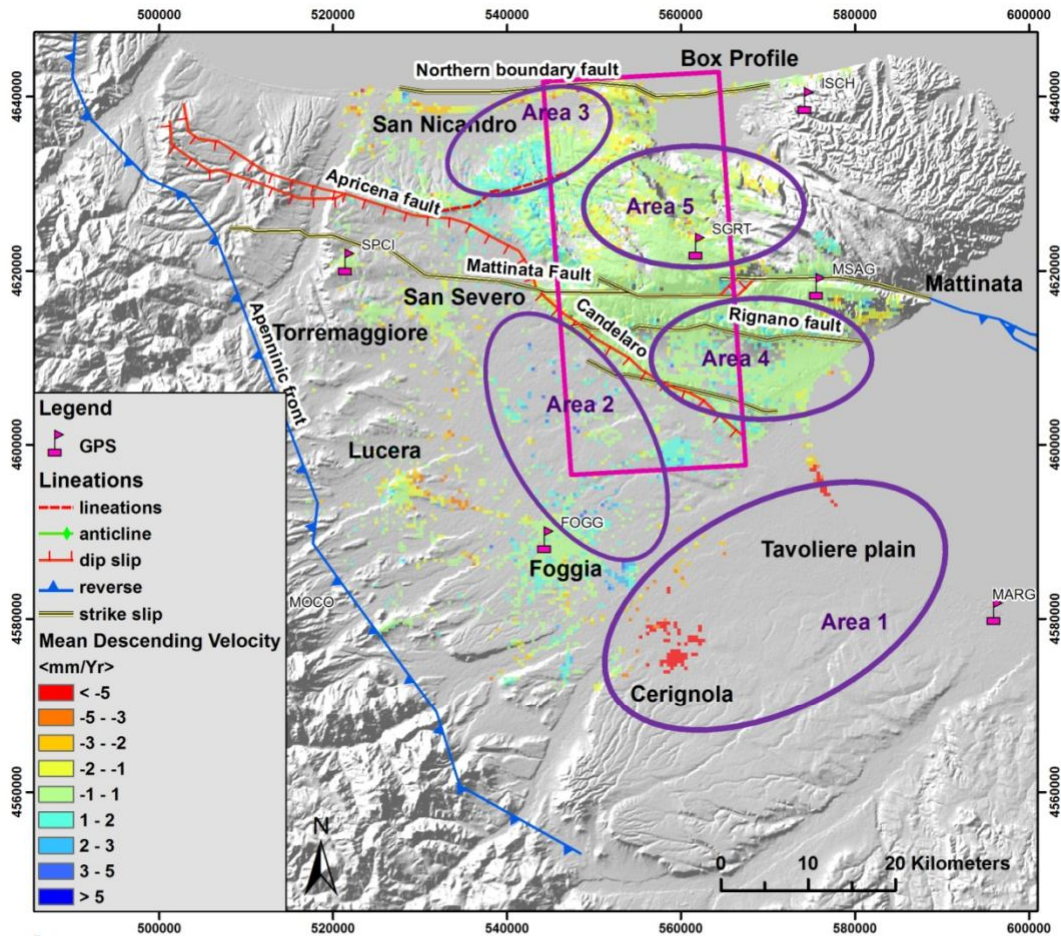
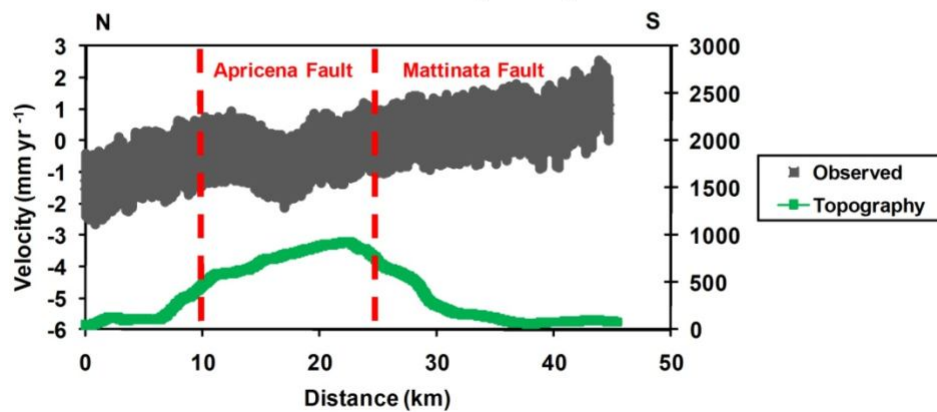


Figure 4.3: A) Mean ascending LoS velocity map. In blue we show positive values of displacement (approaching to satellite) and in red the negative values (increasing the distance from the satellite). Purple flags represent the GPS permanent stations. The violet ellipses highlight the different trend areas. In the figure are also shown the principal tectonic features of the area. B) N-S 10 km buffered velocity profile corresponding to the box in A).



A

Descending velocity



B

Figure 4.4: A) Mean descending LoS velocity map. In blue we show positive values of displacement (approaching to satellite) and in red the negative values (increasing the distance from the satellite). Purple flags represent the GPS permanent stations. The violet ellipses highlight the different trend areas. In the figure are also shown the principal tectonic features of the area. B) N-S 10 km buffered velocity profile corresponding to the box in A).

In figures 4.3 and 4.4, I show the LoS mean ground velocity maps for the ascending and descending case respectively. Both maps show similar patterns and it is possible to identify 5 homogeneous areas.

An evident sector (Area 1 in figures 4.3 and 4.4) with negative values of both ascending and descending LoS mean velocities is present between the towns of Foggia and Cerignola and it continues NE towards the coast. The main component of ground motion is vertical, although some East velocity is present, as shown in Figures 4.5 and 4.6.

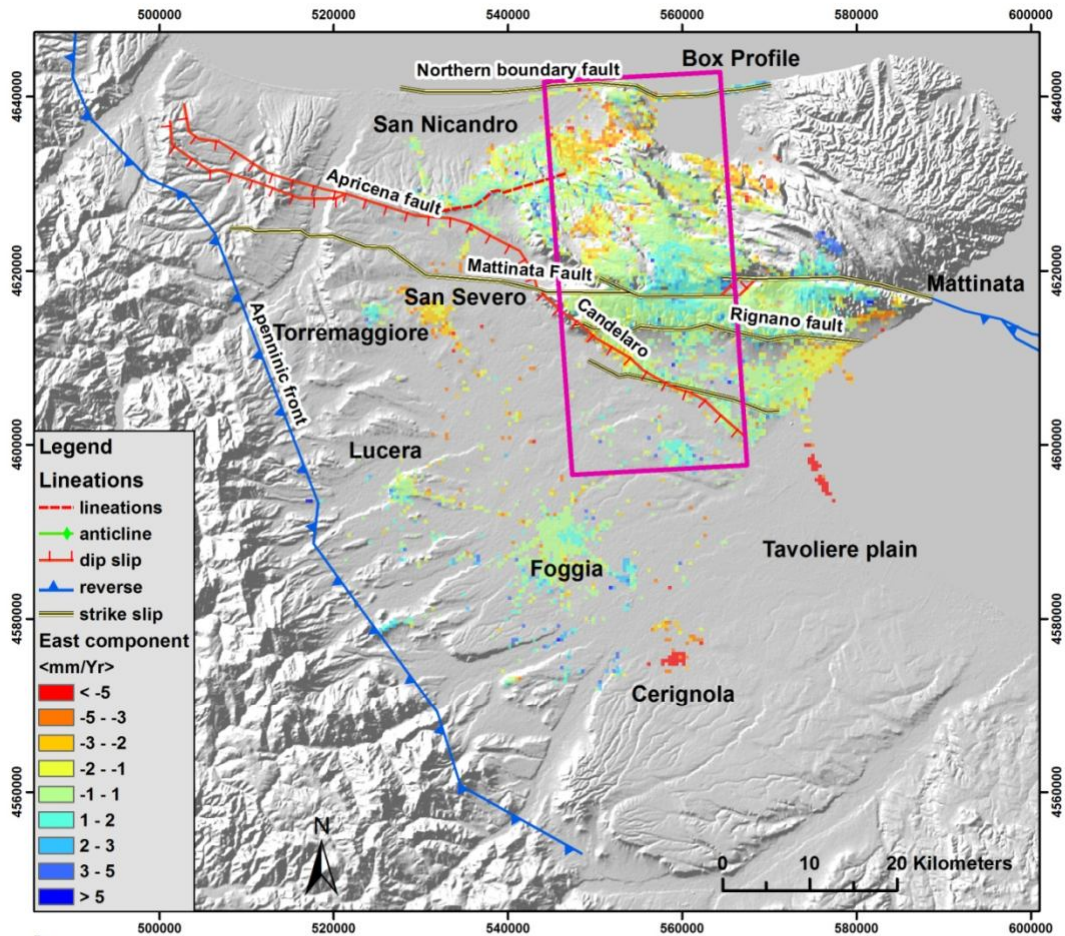
The zone between Foggia and the Apricena fault is also characterized by a similar pattern for the two maps: a general positive velocity trend is present between Foggia and San Severo (Area 2 in figures 4.3 and 4.4), whereas the area included between Lucera and Torremaggiore shows negative values.

The northern sector of the Apricena fault presents a generally positive pattern in ascending map (Area 3 in figures 4.3 and 4.4), whereas a positive SW to negative NE gradient is present in the descending map.

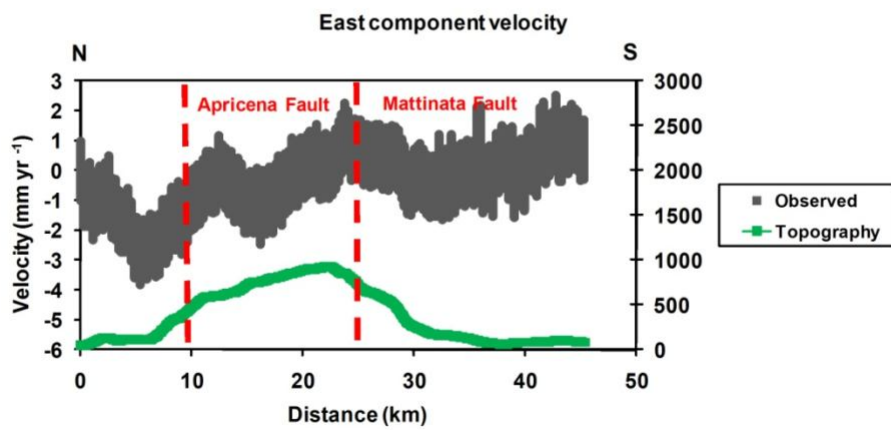
Low values of mean velocity with almost slightly positive trend are present in both geometries in the southern sector of the Mattinata fault (Area 4 in figures 4.3 and 4.4). This suggests a main vertical component of ground motion as display in figure 4.6.

Also the northern sector of the Mattinata fault shows low values of mean velocity in both maps (Area 5 in figures 4.3 and 4.4). In the ascending map is recognizable a general negative trend with a cluster of positive values in correspondence to the 1995 seismic swarm. Low and slightly negative values are present in descending map.

The maps of the East and Up components (Figures 4.5 and 4.6) show different spatial correlation patterns; the vertical component appears more uniform and spatially correlated than the East component. This is due to the different sensitivity of the SAR LoS measurements with respect to motion in the Up, East and North directions. The average absolute values for the Up, East, and North directions in the LoS direction cosine vector are about 0.93, 0.38 and 0.08, respectively.

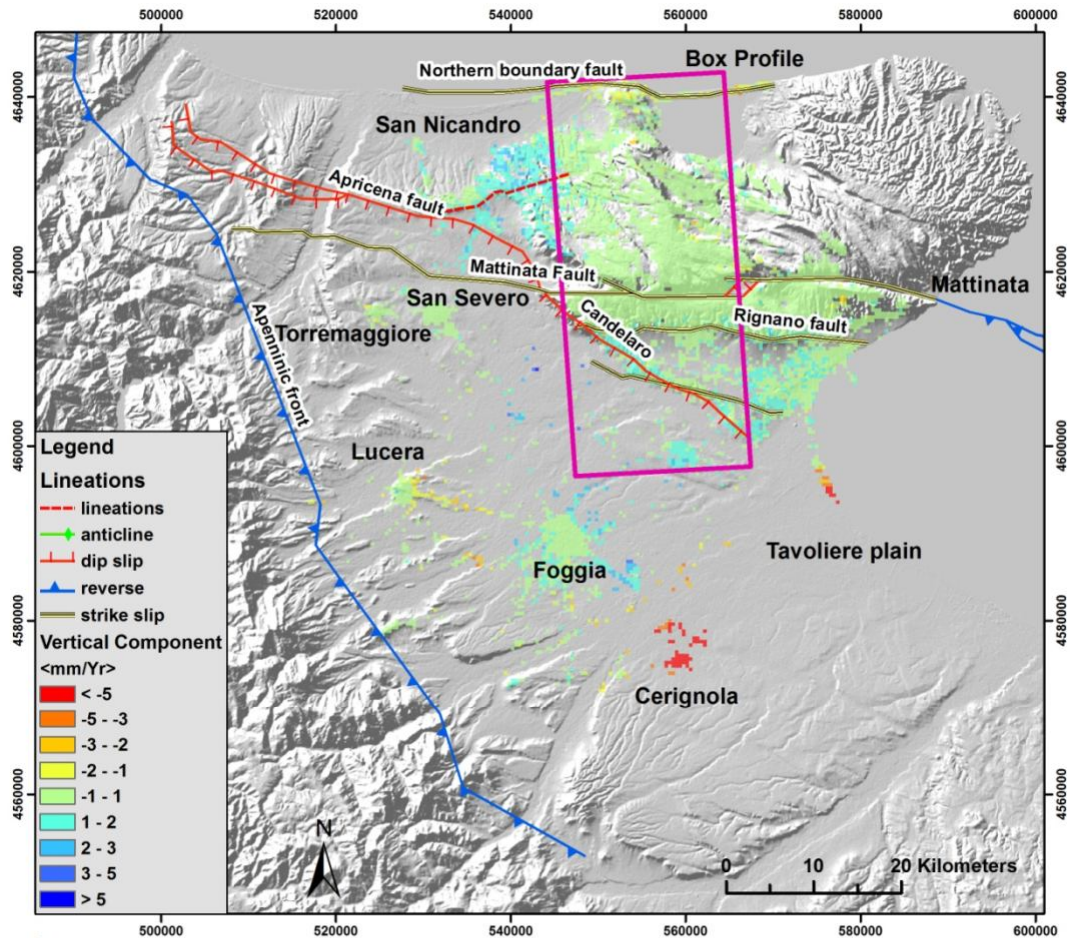


A



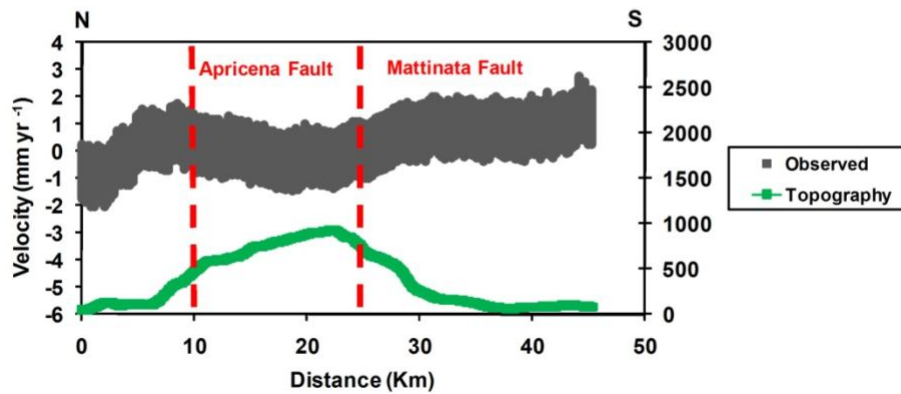
B

Figure 4.5: A) Mean velocity map – East component. In blue we show positive values of displacement (to the east) and in red the negative values (to the west). In the figure are also shown the principal tectonic features of the area. B) N-S 10 km buffered velocity profile corresponding to the box in A).



A

Up component velocity



B

Figure 4.6: A) Mean velocity map – Up component. In blue we show positive values of displacement (uplift) and in red the negative values (subsidence). In the figure are also shown the principal tectonic features of the area. B) N-S 10 km buffered velocity profile corresponding to the box in A).

The east velocity (Figure 4.5) shows an E-W compression between the eastern limit of the appenninic chain and the Gargano promontory, across an alignment connecting the towns of Torremaggiore, Lucera and Foggia; the area near the town

of San Nicandro also shows an evident pattern of E-W compression. The N-S velocity profile (Figure 4.5b) shows the velocity pattern of the East component across the MF.

The Up velocity (Figure 4.6) shows a stable area in the central part of the Gargano promontory, whereas south of the Mattinata fault a positive trend is apparent. Positive values are also present near the town of San Nicandro in the footwall of the Apricena fault. Strong negative values occur in the southernmost sector of the area due to groundwater depletion. The N-S velocity profile (Figure 4.6b) shows the velocity pattern across the Mattinata fault.

4.5 Modeling

The regional crustal deformation signal in the Gargano Promontory is weak, but shows some well defined patterns above the noise level (Figure 4.5b and 4.6b). I used simple analytical dislocation modelling to simulate the observed deformation, trying to obtain information on the seismic cycle in the area. For large strike slip faults, I used a widely accepted conceptual model based on a thick lithosphere with an embedded fault. During the interseismic phase, the fault is locked from the surface to a depth d (locking depth). The fault plane below this depth slips (creeps) at a constant rate, which can be determined through data inversion. This model is highly attractive as an entire set of velocities may be fitted by adjusting the locking depth and the fault slip rate. Again, interseismic velocities can be fit by least square inversion for fault slip rate and locking depth.

The inversion technique used here is based on the Levenberg-Marquardt algorithm (Levenberg, 1944, Marquardt, 1963) and the modelling of the interseismic signal has its rationale in the work of Wright *et al.* (2001) and D'Agostino *et al.*, (2005). The inversion is based on the minimization of a cost function expressed as

$$CF = \frac{1}{N} \sum_i^N \frac{(d_{i,obs} - d_{i,mod})^2}{\sigma_i} \quad (4.1)$$

where $d_{i,obs}$ and $d_{i,mod}$ are the observed and modeled displacements of the i -th point, σ_i is the standard deviation for the N points. A further step is the analysis of the uncertainty and the trade-offs affecting the source parameters, performed by perturbing the DInSAR data with a spatially correlated source of noise according to the approach of Atzori *et al.* (2008).

To investigate the active faults in the Gargano Promontory, I have performed several inversions of the observed DInSAR velocities. I have modeled the velocity data using the elastic dislocation solutions of Okada (1985), applied to the creeping part of the fault plane, below a locking depth defined a priori.

I have run several tests over the data, with either single and multiple fault models. In particular I considered the most important tectonic structures of the area for which a recent activity has been proposed: the Apricena fault (Patacca & Scandone, 2004), the Apricena-San Nicandro fault (Salvi *et al.*, 2000) and the Mattinata fault. In order to test the models I also considered these other large faults. These faults are 20 km (as the MF) to 40 km (as the Apricena fault) long and the locking depth interval is about 10-20 km. Inversions do not show remarkable solutions and they are characterized by bad fitting and unrealistic rake and dip angles. Using local scale surface geometric constrains, the interseismic sources appears too deep and short to fit a very low surface signal; this is, probably, related to larger scale deep creeping phenomena below the entire Gargano promontory.

Thus, I assume a nearly infinite fault extent (500 km) in order to minimize the fault edge effects. After some attempts of inverting for all the 9 fault parameters (Length, Width, Depth, Strike, Dip, East and North position, Rake, Slip), I introduced some constraints on strike, position and width of the model, based on geological evidences for the Mattinata fault.

In table 4.3 I report the parameters of the best single fault solution, obtained with an inversion where top depth (i.e. locking depth), dip, rake and slip of the fault are unconstrained (parameter uncertainties are in parenthesis).

Length (Km)	Width (Km)	Top Depth (Km)	Strike (deg)	Dip (deg)	East Coordinate (UTM WGS84)	North Coordinate (UTM WGS84)	Rake (deg)	Slip (cm)
500	100	12.2 (0.4)	90°	70.0 (5.5)	542616	4618683	175.1 (4.4)	1.4 (0.1)

Table 4.3: Best fitting fault parameters relative to the single fault inversion. In parenthesis the parameter uncertainties. The values are referred to the Mattinata fault.

The values of the constrained parameters are derived from geological and seismological considerations. The uncertainty of the parameters retrieved by inversion is shown in figure 4.7.

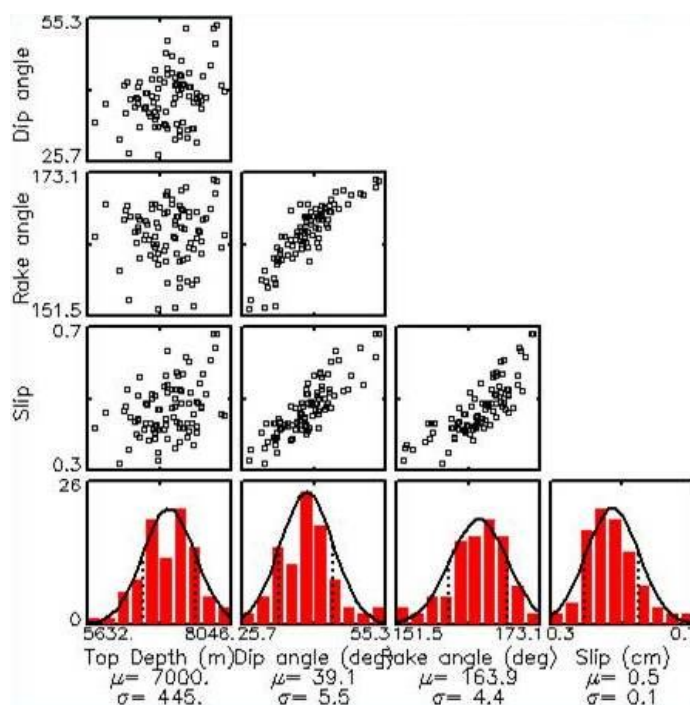


Figure 4.7 Statistic of the Mattinata fault.

Figures 4.8 and 4.9 show the modelled velocity field in ascending and descending LoS respectively, whereas the residual velocities are shown in figures 4.10 and 4.11 for the ascending and descending geometries.

The modelled LoS velocities show very low values in both geometries with two different pattern of velocity distribution: the ascending velocity map (Figure 4.8a) shows negative values in the central part of the Gargano and positive in the rest of the area, increasing northward; the modelled velocity profile (Figure 4.8b) fits the

observed one along the entire profile excluding the northernmost area. Here the interaction with other unmodelled tectonic structures, like the Apricena-San Nicandro fault, could play an important role in the velocity pattern.

The descending velocity map (Figure 4.9a) shows roughly positive values south of the Mattinata fault and negative in the north. The modelled and the observed velocity profiles (Figure 4.9b) show as the model does not fit the SAR data well.

The residual maps show misfit areas near the town of Apricena and near the Varano Lake for the ascending case and south of the Mattinata fault for the descending one. A critical discussion of the model is proposed in the next paragraph. In table 4.4 a goodness of fit in terms of RMS is reported for the two datasets.

Dataset	RMS (null solution)	RMS (non linear)
Envisat Ascending	0.106	0.100
Envisat Descending	0.113	0.111

Table 4.4: RMS table for ascending and descending dataset. The RMS (in cm) of the null solution corresponds to the RMS of the data themselves.

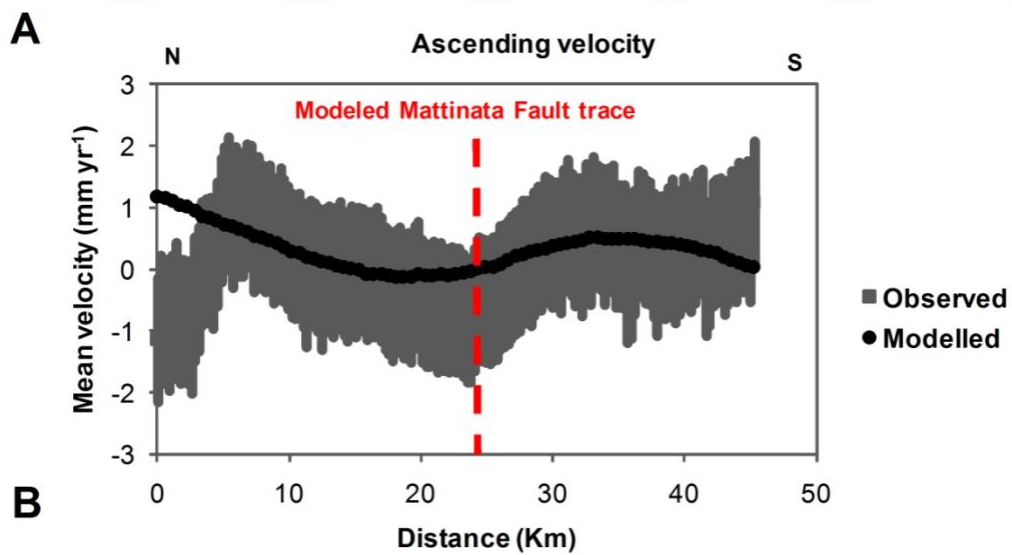
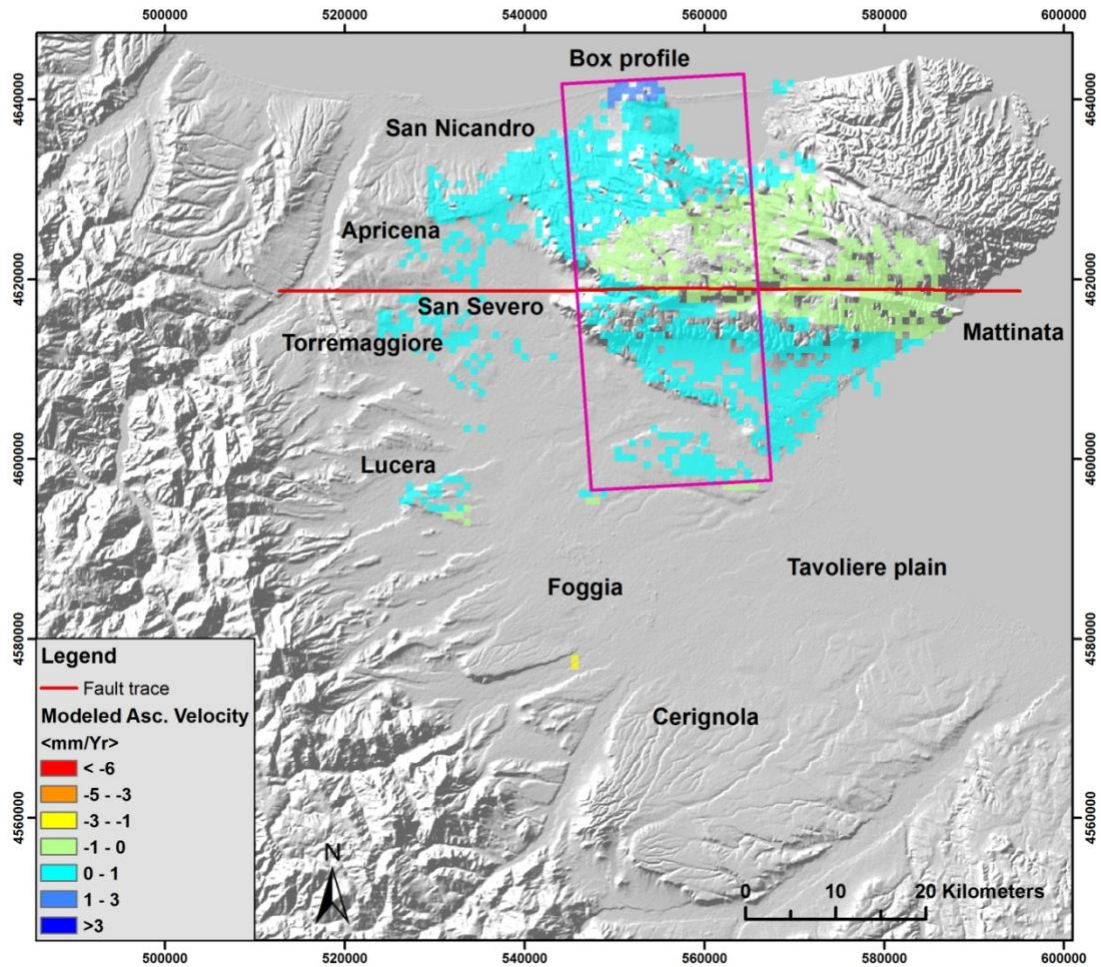


Figure 4.8: A) Modelled velocity field in the ascending LoS. B) N-S 10 km buffered velocity profile corresponding to the box in A).

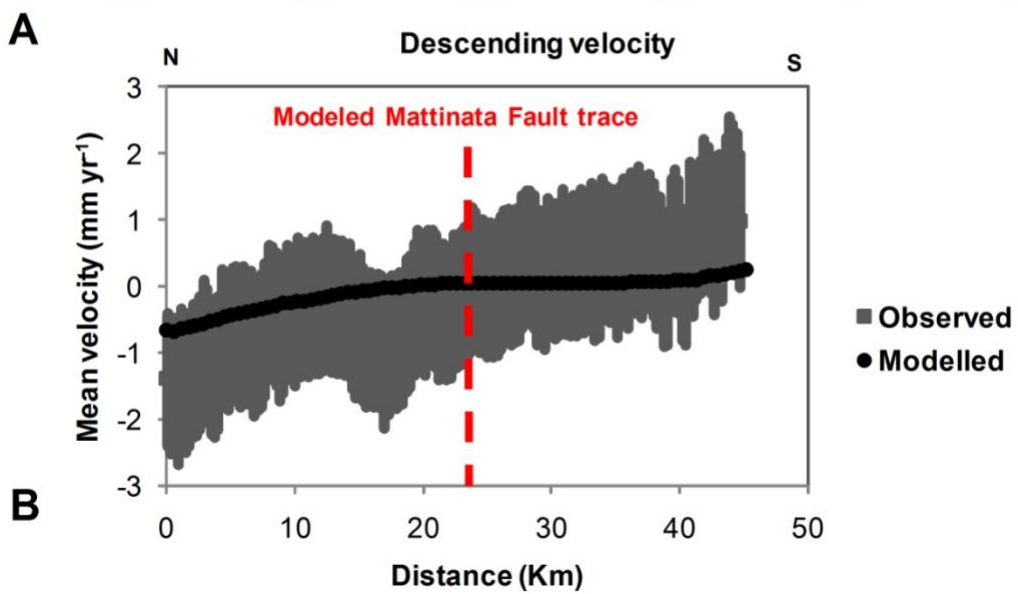
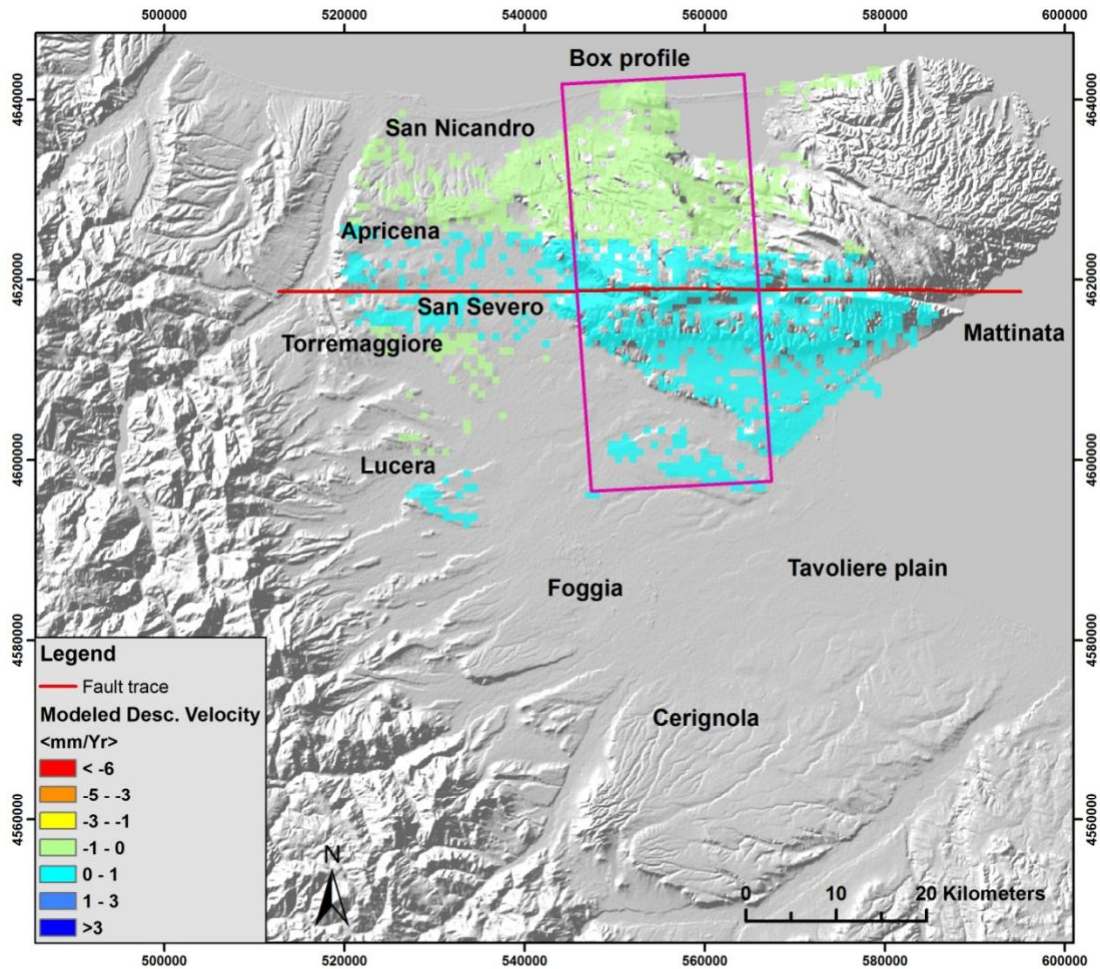


Figure 4.9: A) Modelled velocity field in the descending LoS. B) N-S 10 km buffered velocity profile corresponding to the box in A).

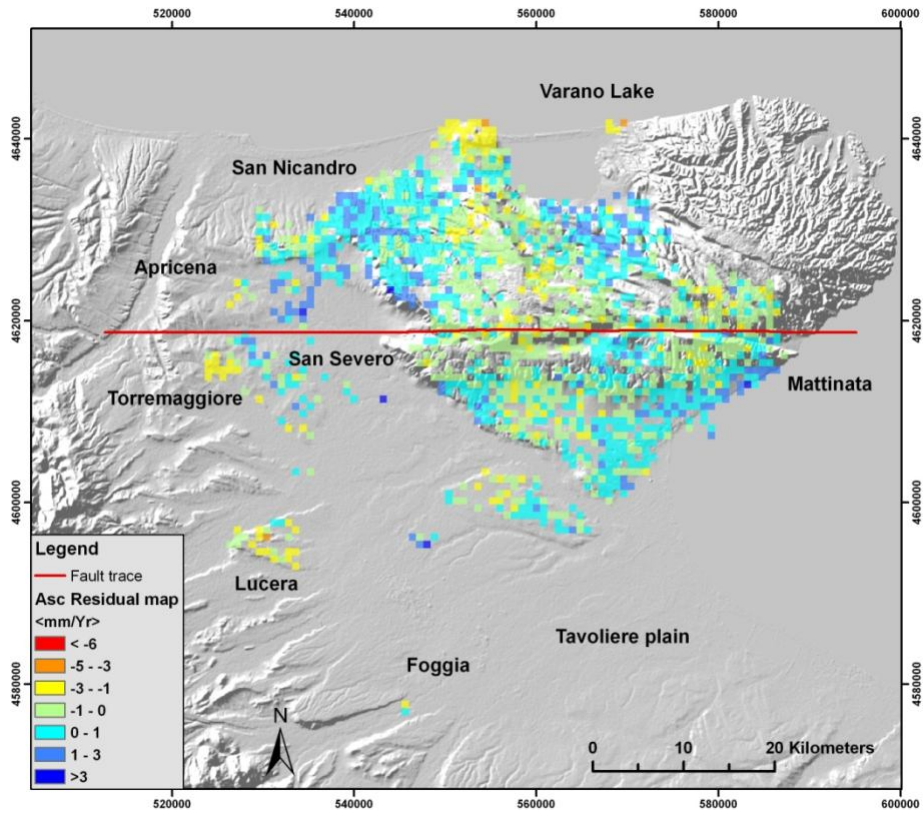


Figure 4.10: Residual Modelled Vs Observed velocity field in ascending geometry

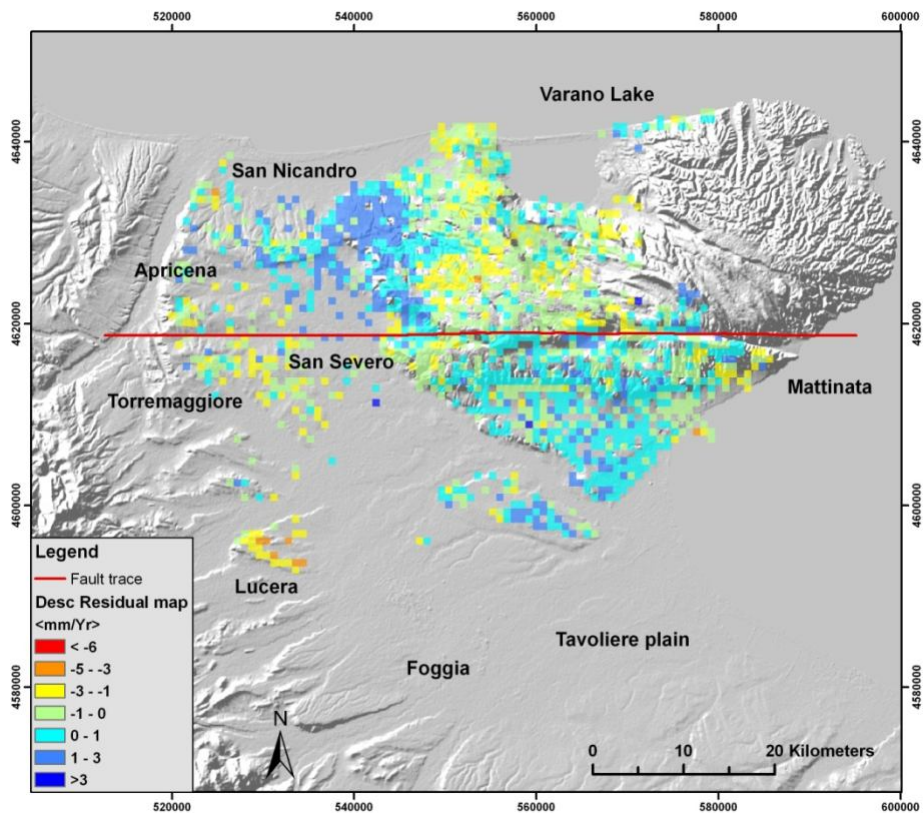


Figure 4.11: Residual Modelled Vs Observed velocity field in descending geometry

4.6 Discussion

The area between the towns of Foggia, Cerignola and the coast is affected by strong subsidence as shown in the ascending and descending LoS ground velocity maps (Figures 4.3 and 4.4) and in the Up component (Figure 4.6). The underground water pumping by farms, largely present in the south-east area of Foggia, is the probable cause of this deformation. On the other hand, the dimensions and the shape of the subsiding zone are constrained by other phenomena, as the presence of tectonic discontinuities or the extension of compressible sediments. In this area crop out detritic deposits, alluvial and fluvial-lake deposits of the Holocene, that could be subject to compaction. Moreover the subsidence pattern may be influenced by the presence of a fault buried under the Holocene sediments, along the south-west continuation of the NE-SW scarp that limits the Gargano promontory to the south. In the literature, two regional strike slip faults, bounding a large *graben*, are mentioned: the Manfredonia-Sorrento fault and the Foce Ofanto-Paestum fault (Ricchetti *et al.*, 1992). The subsiding area is well overlapped to such graben (Figure 4.12). The presence of these structures could control the underground water motion and divide sectors with different thickness of soft sediments and therefore influence the compaction rate.

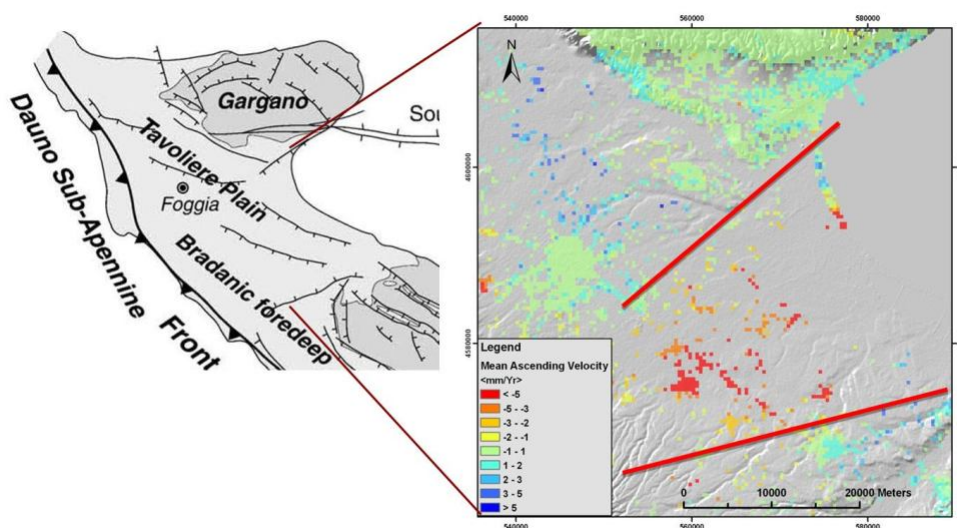


Figure 4.12: The subsidence in the Tavoliere plain. Left: structural framework of the appenninic foredeep. Right: ascending mean velocity map of the area. In red the main faults controlling the Tavoliere graben (faults after Ricchetti *et al.*, 1992).

The northern sector of the area, near the town of Apricena and San Nicandro, shows an uplift pattern that could be related to the strain accumulation along the Apricena-San Nicandro fault. In particular it is possible to speculate a transpressive kinematics of this fault with a left lateral strike slip principal component and a secondary compressive component of the motion. SAR velocities not exclude the Patacca and Scandone (2004) hypothesis; in fact the velocity field is also compatible with the Apricena fault as a WNW-ESE structure, dipping towards SSW, and extending for about 30 kilometres from Serracapriola to Santa Maria di Stignano. Both hypotheses are in a quite good agreement with geological and seismological data: both structures are located in the epicentral area of the destructive 1627, $I_0 = X$ MCS, earthquake showing an E-W isoseismal compatible with these lines. Field investigations confirmed the presence of an oblique-slip fault, downthrowing to the south the Pleistocene sediments of the upper Foggia Plain (M. Lenoci, unpublished seismic refraction data), (Salvi *et al.*, 2000) (Figure 4.13).

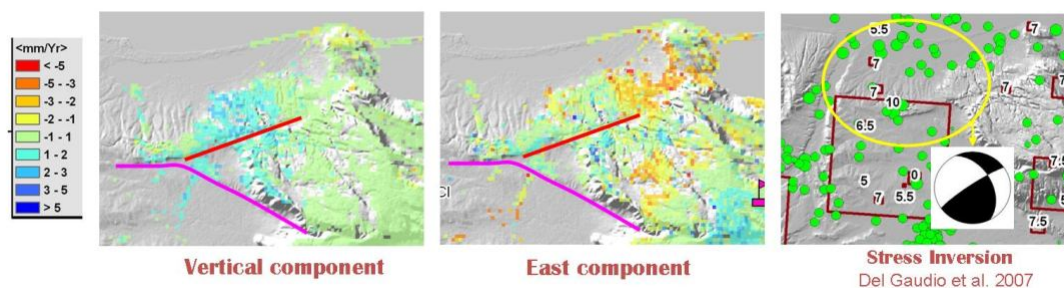


Figure 4.13: The uplift pattern near the Apricena fault. The figure highlights the Up and East component velocities and the stress inversion from instrumental seismicity (Del Gaudio *et al.*, 2007). In red the hypothetical Apricena-San Nicandro fault trace (Salvi *et al.*, 2000); in violet the Apricena fault trace (Patacca and Scandone, 2004).

The area north-east of the Gargano (NE of the SGRT GPS benchmark, see figure 4.2) shows a different pattern of deformation with respect to the central part of the area: this sector moves westward faster than the central one and show a low, but evident uplift. This suggests an active compression in the area, with a σ_1 orientation variable from NW, in agreement with Argnani *et al.* 2009, to NE. This hypothesis is confirmed by the compressional seismicity recorded in the Gargano

region and extending with similar features into the central Adriatic, i.e. NE of the Gargano Promontory (Vannucci *et al.*, 2004; Pondrelli *et al.*, 2006), where recent deformation is also observed on seismic profiles (Argnani *et al.*, 1993, Argnani and Frugoni, 1997; Bertotti *et al.*, 2001). Moreover, in the same area, a seismic swarm occurred in 1995 with a maximum magnitude $M_w = 5.2$ and a right lateral focal mechanism (Figure 4.14). In an analysis of local seismicity, Del Gaudio *et al.* 2007 show a clear prevalence of strike–slip solutions, with nodal planes close to north–south/east–west directions, with a pressure axis P and a tension axis T respectively oriented in a NW–SE and in a NE–SW direction. This is consistent with the InSAR results and our hypothesis.

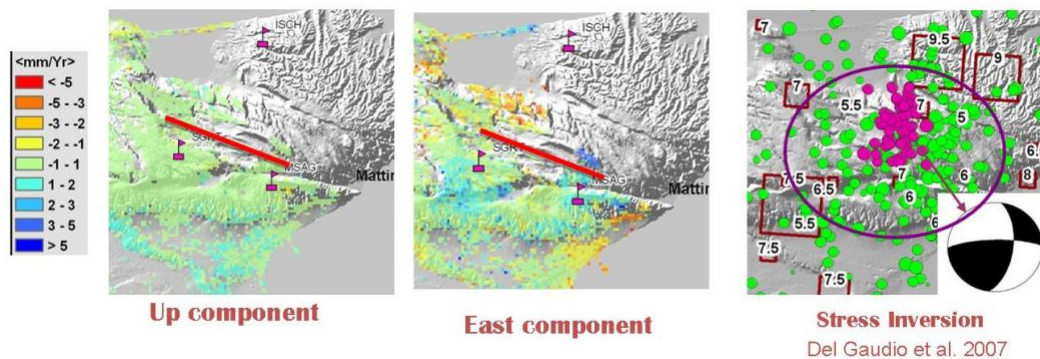


Figure 4.14: the 1995 seismic swarm. The figure highlights the Up and East velocities and the stress inversion from instrumental seismicity (Del Gaudio *et al.*, 2007). Purple epicentres are referred to the 1995 seismic sequence. In red the hypothetical seismic source surface trace of the 1995 seismic sequence mainshock.

An interesting velocity trend is present in the west of the area. A low velocity gradient ($0.2\text{-}0.3 \text{ mm} \cdot \text{yr}^{-1}\text{km}^{-1}$) in the East component is present between the town of Torre Maggiore and San Severo and between Lucera and the north of Foggia (Figure 4.5). This low signal, indicating active shortening, could be attributed to the eastward force of the orogenic wedge due to the active extensional tectonic of the Central-Southern Apennines.

Observing the Ascending and Descending LoS velocity maps a relative uplift zone it is recognizable in the Northern Tavoliere, between the Gargano promontory and the towns of Foggia and San Severo. This signal apparently corresponds to a

buried structural high. Moreover, this zone shows geomorphological evidences of recent uplift, as a more evident fluvial incision with respect to the other parts of the Tavoliere.

With regard to the modelling it is possible to make some considerations.

- The model fits the dataset only to the first order, and it is not able to model the deformation pattern at higher orders. For example it does not fit the compressive deformation present near the town of Apricena and in the north-east.
- The shape, downdip dimension, and orientation of the modelled fault are in good agreement with the mapped Mattinata fault, confirming that it has an important role in the crustal deformation of the area.
- The rake angle (179°) shows a pure dextral solution for the modelled fault, in agreement with most of the bibliographic literature. The inverted data do not admit a left lateral solution for the Mattinata fault despite the weak goodness of fit. This is a contribution to the open discussion over the kinematics of the MF, and for the development of a geodynamical model of the area.
- Very little seismicity is associated with the Mattinata fault, despite the best fit model suggests that the MF is the principal deformation feature of the area. For example the seismic swarm occurred in 1995 had a maximum magnitude $M_w = 5.2$ and a right lateral focal mechanism, in agreement with the model right lateral rake, but is located few kilometres north.

Another important open discussion is the relationship between the Mattinata fault and the 31 October 2002 Molise earthquake. Valensise *et al.* 2004 suggest that the Mattinata fault may continue westward up to the seismic source of the 2002 seismic swarm. The right lateral solutions and the very deep localization for the two main shocks are consistent with this hypothesis. In fact a pure strike slip solution is not well explainable in the Southern apenninic context, dominated by extensional tectonics; moreover the main shock hypocenters fall into the Apulian Platform, under the apenninic orogenic wedge (located above 10 km depth), where no significant aftershock activity was observed. The SAR data do not allow us to

confirm or deny this hypothesis because of the unclear deformation pattern around the westward continuation of the Mattinata fault and the large distance between the westernmost morphological evidence of the fault and the 2002 Molise sequence.

4.7 Conclusion

In this work I determined a further constraint to the kinematics of the Mattinata fault. The InSAR data inversion, even with an RMS near the null solution, shows a best fit right lateral strike slip solution for the Mattinata fault; the same dataset does not admit a left lateral solution.

The best model does not fit all the local signals; two of the misfit areas are located in the north-east and north-west, where a compressive deformation is evident and is confirmed by seismological data; in fact this work has revealed a clear uplift pattern (about $2\text{-}3 \text{ mm} \cdot \text{yr}^{-1}$) localized along the Apricena Fault where geological and seismological data point out recent seismic activity, characterized by compressive tectonic regime.

The southern area of the analyzed frame shows a strong subsidence probably due to the high compaction rates of the south part of the Tavoliere, where the sediment thickness is large. This area is characterized by an important graben that divides the northern part of the Tavoliere to the Murge southward. The bounding faults seem to limit the extent of the aforementioned subsidence.

The application of an analytical dislocation model to fit an interseismic signal allows to fit the deformation velocities at regional scale, but it is inadequate to fit the local deformations and to account for the interactions between different tectonic structures in a complex area like the Gargano promontory.

Chapter 5

Interseismic deformation analysis of the Doruneh fault (Central Iran)

5.1 Introduction

One of the longest and best identifiable tectonic structures of the northern Iran is the Doruneh Fault System (hereinafter DFS). This 600 km strike-slip fault system was first described by Welman (1966) and it E-W crosses the entire region from Central Iran to the Afghanistan. Doruneh Fault plays a very important role in the general tectonics context of the North-Iranian area, accommodating part of the 15 mm yr^{-1} N-S right lateral shear observed at the eastern boundary of the Iranian block (Vernant *et al.*, 2004; Fattahi *et al.*, 2007). Many authors hypothesize a clockwise rotation of the southern block of the Doruneh fault involved by the accommodation of this strain (e.g. Jackson & McKenzie, 1984; Jackson *et al.* 1995; Walker & Jackson 2004).

Recent geomorphological study on the Quaternary deposit along the surface trace of the fault, evaluate 2.5 mm yr^{-1} mean velocity and pure left-lateral kinematics (Fattahi *et al.*, 2007). Despite of clear geomorphological evidences of active faulting, the size and the central role that seems to play in the geodynamic of the area, the Doruneh shows a low rate of seismicity. Few earthquakes have been recorded in the area (Ambraseys and Malville, 1977) in contrast to the neighbouring Dasht-e Bayaz region, which appears to play a similar role in the regional tectonics (Walker *et al.*, 2004) but which has suffered from many earthquakes recorded both instrumentally and historically (e.g. Berberian and Yeats, 1999, 2001; Walker *et al.*, 2004). Thus, the question is: is the Doruneh fault capable to generate strong earthquakes similar to the Dasht-e Bayaz region events or is it characterized by a principle aseismic creeping associated with low seismicity? In others words, are we observing only a small portion of a hypothetical total deformation that will be recovered during a future strong earthquake or any stress accrual is today acting? In both cases, which is the role of the Doruneh fault in the geodynamical framework of the Arabia-Eurasia collision? To answer these questions first of all it is necessary to compare the present day deformation velocity with the long-term velocity obtained from geologic records. With this aim, I consecutively present an interseismic deformation study of the western termination of the Doruneh fault performed by the multitemporal InSAR-SBAS methodology (Berardino *et al.*, 2002). Four ENVISAT SAR images datasets have been processed acquired from 2002 to 2010. A data modelling has been also performed using an analytical elastic model (Okada, 1985).

5.2 Tectonic framework

The study area is located in the Northern Iran, at the border with Afghanistan and Turkmenistan (Figure 5.1).

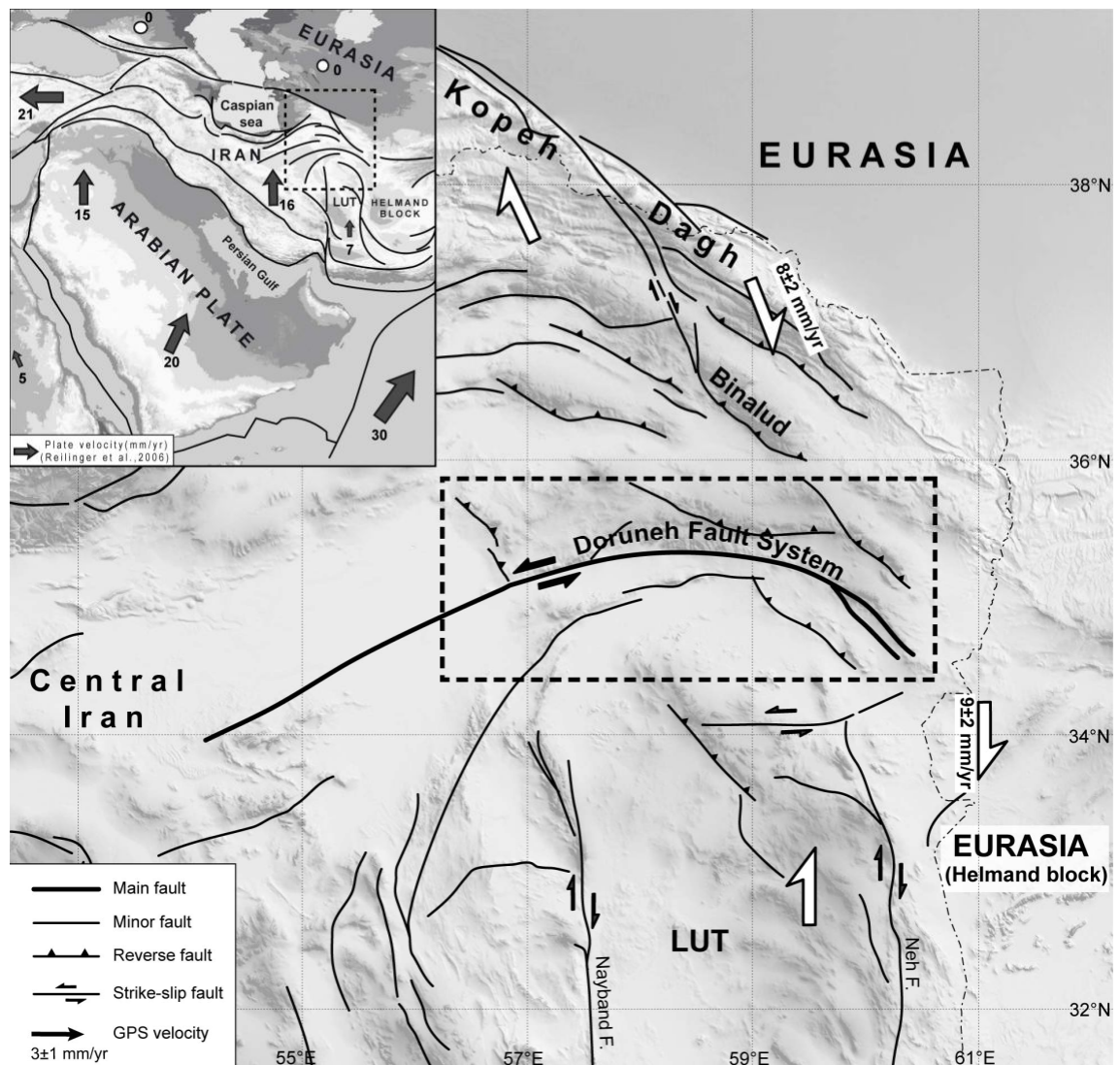


Figure 5.1: Top right: tectonic framework of the DFS in the major context of the Arabia-Eurasia collision. Gray arrows and associated numbers indicate the GPS plate velocity respect stable Eurasia (Reilinger *et al.*, 2006). Big centre: GTOPO30 image of Central and North-Eastern Iran showing the Doruneh fault and the principles tectonic structures of the area. White arrows indicate horizontal GPS velocity respect stable Eurasia (Masson *et al.*, 2007). (from Farbod *et al.*, 2011).

Active tectonic of this block is controlled by an average northward movement of about 25 mm yr^{-1} of the Arabic plate respect Eurasia (Vernant *et al.*, 2004). This movement is gradually absorbed from South to North and is about totally confined in the Iran boundary. In detail, the northern motion seems to be mainly absorbed in the seismically active regions of the Zagros Mountains in south of the country and in Alborz-Kopet Dagh area to the North. These areas are separated by virtually aseismic regions of the Dasht-e Kavir and Dasht-e Lut depressions. On the

contrary, the Afghan block and Turkmen block seem to be stable part of the Eurasian plate (Figure 5.2).

The central part of Iran is 15 mm yr^{-1} northward moving respect the Afghan one (Vernant *et al.*, 2004). This movement is accommodate by a N-S right lateral fault system located at the Iran-Afghanistan border (Regard *et al.*, 2004; Walker and Jackson, 2004)

Available geodetic data on the Eastern Iran (Vernant *et al.*, 2004; Masson *et al.*, 2007; Tavakoli, 2007) indicate an N-S accommodation rate of 9 mm yr^{-1} , in good agreement with geologic long-term velocities of Shabanian *et al.* (2009a) that shows 8 mm yr^{-1} mean velocity between the Central Iran block and Eurasia (Figure 5.1). The Doruneh Fault System (DFS) is located between this block and the above mentioned N-S right lateral fault system.

The term “Doruneh fault” was coined by Wellman in the 1966 to identify the longest strike-slip fault of the Iranian plateau 600 km running in E-W direction from 54° to $60^\circ 30'$ of longitude. The DFS shows a bow-shape northward convex structure like evidenced in the regional geological maps (Stocklin and Nabavi, 1973; Eftekhar-Nezhad *et al.*, 1972; Huber, 1977). At the beginning it was ideally split in two different blocks mainly on the base of the strike change at the Doruneh town longitude (Tchalenko *et al.*, 1973b; Mohajer-Ashjai, 1975).

Actually, new geomorphic and structural data complemented with pre-existing ones shows that the structural boundary between the western and eastern parts does not closely coincide with the location of the Doruneh village. Instead, at a longitude of $56^\circ 45'E$ there is an evident change in the geologic, geomorphologic and structural expression of the fault itself: there is an about 40 km-long structural gap in along which Quaternary deposits have not been affected by the fault activity (Farbod *et al.*, 2011).

Based on geomorphological data, Farbod *et al.* (2011) subdivides the DFS in three distinct blocks: the Western Fault Zone (WFZ); the Central Fault Zone (CFZ) and the Eastern Fault Zone (EFZ) (Figure 5.3)

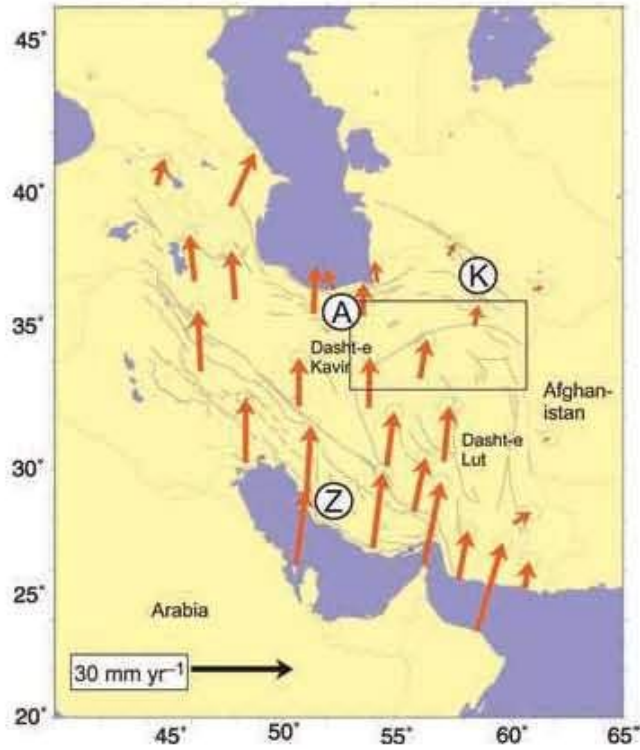


Figure 5.2: GPS velocity map respect to the stable Eurasia, from Vernant *et al.*, 2004. The Northward decreasing trend up to zero at the northern Iranian boundary shows like the Arabia-Eurasia convergence is total accommodate into the state border.

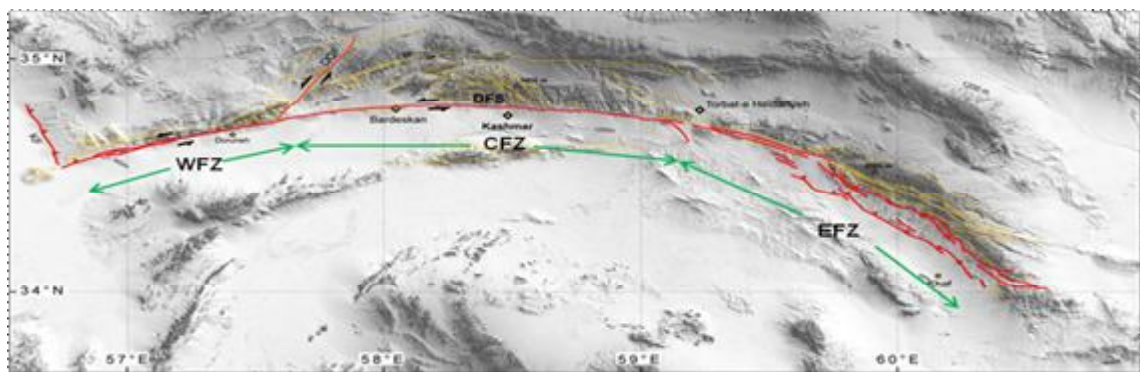


Figure 5.3: The DFS partition based on the geologic and structural field evidences. The image shows the different orientations of the Western fault zone (WFZ), Central fault zone (CFZ) and Eastern fault zone (EFZ) (from Farbod *et al.*, 2011)

Whereas the EFZ is characterized by an imbricate reverse fault system and NW-SE anticline, that evidence a clear and exclusive compressive component, the CFZ shows a left lateral kinematics without any evidence of vertical component

(Farbod *et al.*, 2011). Different tectonic behaviours are distinctive of the WFZ. Indeed, a transpressive tectonic regime is affecting the WFZ: reverse and strike-slip component are almost equivalent.

In fact the WFZ (Figure 5.4) is characterized by transpressive tectonic regime where the reverse and transcurrent component are almost equivalent, in apparent contrast with the SW-NE fault orientation and the general transcurrent left lateral kinematic of the DFZ. This apparent disagreement is justified by the interaction of the WFZ with the left lateral strike slip motion of the Dahan-Qaleh fault (DQF). Indeed, the western block of the DQF shows a relative motion towards SW, that implies a transpressive tectonic regime along the WFZ (with WSE-ENE orientation). This movement is evident along the entire fault segment located west of the DQF-DFZ intersection. The westward motion of the WFZ northern block is accommodated by the NNW-SSE Kharturan reverse fault (KF), that marks the limit from the DFZ at East and the Great Kavir Fault at West (Farbod *et al.*, 2011).

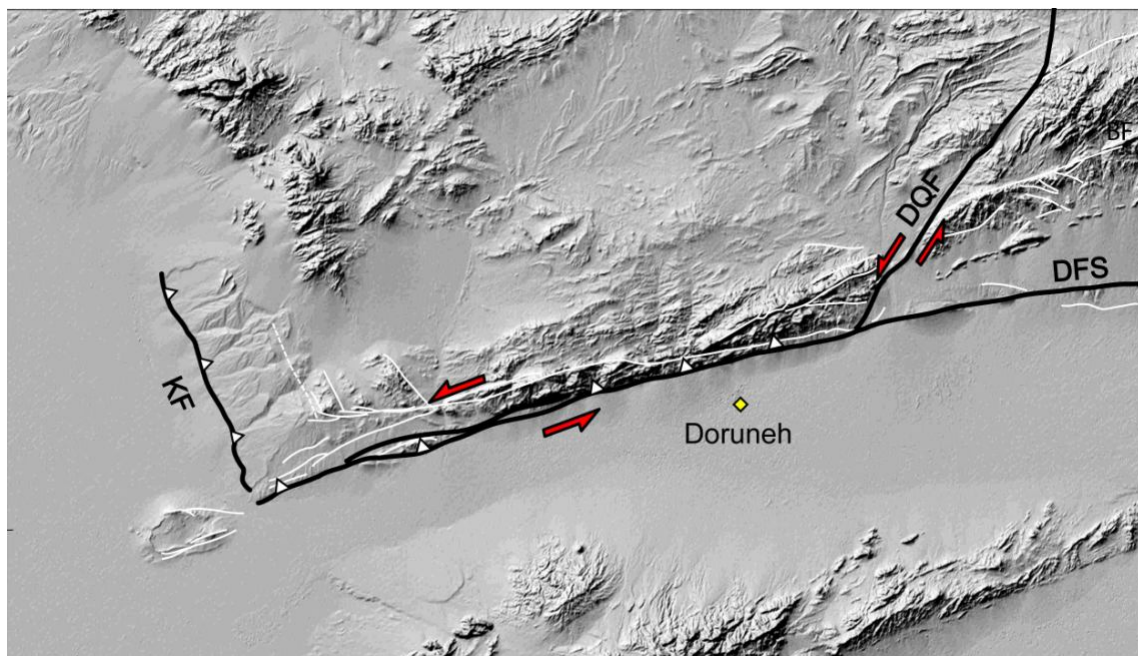


Figure 5.4: The western fault zone of the DFZ. The WFZ trace intersects the left lateral DQF trace at the latitude of 50°N. The western tip of the WFZ is characterized by the intersection with reverse NNW-SSE Kharturan fault. This tectonic structure accommodates the westward motion of the northern block of the WFZ and marks a topographic escarpment, representing the limit with the Great Kavir Desert.

5.3 Seismicity

In the morning of 21th October 1336 occurred the earliest recorded event in the Doruneh region, the Khwaf earthquake. It caused destruction over a wide area in the region southeast of Torbat-e Heydarieh and east of Khwaf (e.g. Ambraseys and Melville 1977). The meizoseismal area was about 110 km long and oriented roughly NW–SE (Ambraseys and Melville 1982). Given the location and orientation of the damaged zone, the earthquake is likely to have ruptured thrust faults within the Jangal thrust fault system, which runs parallel and to the south of the Kuh-e Sorkh range-front and Doruneh fault.

The village of Doghabad was destroyed during the May 1619 earthquake, with about 800 fatalities (Ambraseys and Melville 1982). Doghbad village is located south of Doruneh close to a E-W oriented reverse fault system; despite no information about the damaged area are available, it is reasonable to ascribe this earthquake to the above mentioned reverse fault system.

Ambraseys and Moinfar (1975) and Ambraseys & Melville (1982) describe the 25th September 1903 Turshiz earthquake; the earthquake caused extensive damage in an east–west region extending about 40 km west from Kashmar (then known as Turshiz) to the village of Kishmar. Although the distribution of damage is parallel to the Doruneh fault trace, the meizoseismal zone is not centred on the Doruneh fault.

The most recent destructive earthquake occurred in the Doruneh region is the 1923 May 25th Kaj-Darakht event (Ambraseys and Moinfar 1977). The major damage occurred in a ~20 km long region, directly southwest of Torbat Heydarieh. From the damage distribution it is likely that the earthquake occurred on the Doruneh fault. The relatively small epicentral zone and the absence of surface rupturing, suggests a reasonably small magnitude (estimated at Ms 5.8 by Ambraseys and Moinfar 1977).

In figure 5.5 I show the focal solutions of magnitude $M_w > 4.5$ events; excluding the pure reverse 02/02/2002 earthquake, all events show a very important left lateral strike slip component on E-W oriented fault plane. In general, because of

the big uncertainty in the events localization (Engdhal *et al.*, 1998), the relationship between the instrumental seismicity and the tectonic structures is not very obvious and few earthquakes could be directly related to the DFS.

The 9th December 1979 event was localized close the DFS, about 50 Km west respect the Doruneh village. In this case, the Harvard CMT focal solution shows a pure reverse mechanism. Jackson and McKenzie (1984) proposed an alternative solution with transcurrent mechanism on an ENE oriented fault plane. They supported this hypothesis on the base of major congruency on the focal mechanism with the tectonic structures orientation of the WFZ.

However detailed field works (e.g. Farbod *et al.*, 2011) show a good agreement between the Harvard CMT solution, the structural pattern and the fault system geometry.

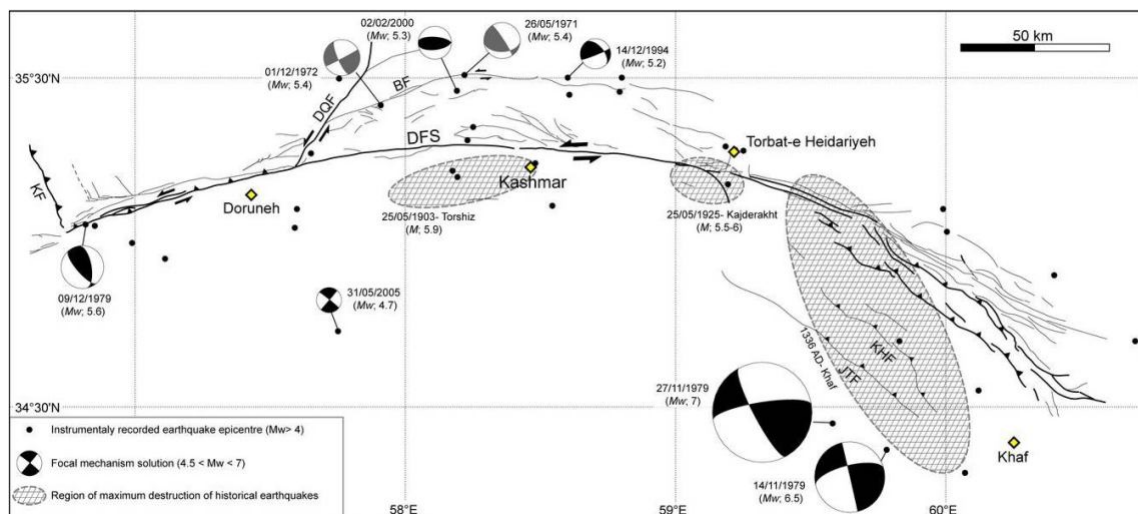


Figure 5.5: Historical and instrumental seismicity along the DFS. We show major damaged zone from Ambraseys and Melville (1982), the focal solution from Harvard seismic catalog (<http://www.globalcmt.org/CMTsearch.html>) and the epicenter from NEIC (http://neic.usgs.gov/neis/epic/epic_global.html) (from Farbod *et al.*, 2011)

From this short seismic analysis I can note that, in spite of destructive earthquakes occurred in this area, only the 1923 Kaj Darakht earthquake and, maybe, the 1903 Turchiz earthquake can be ascribe to the Doruneh fault. In addition these events

seem not to show high magnitude. Instead, more earthquakes could be ascribed to the active tectonic structures located north and south of the DFS.

In general, both historical and instrumental events show moderate seismicity along the Doruneh fault, especially if I compare this area with the close areas of Kopneh Dagh (Tchalenko, 1973a; Berberian and Yeats, 1999, 2001; Shabanian *et al.*, 2009b) and the northern border of the Lut block (Berberian and Yeats, 1999).

In this geodynamical context it is very important to understand if the moderate seismicity of the area is related to an aseismic motion between northern and southern block of the DFS or if this tectonic structure is potentially able to cause destructive earthquake in the future.

5.4 Multitemporal DInSAR data processing

5.4.1 Mean ground velocity maps

I processed 25 ascending (track 156, Frame 692) and 19 descending (Track 206, Frame 2902) ENVISAT images using multitemporal DInSAR–SBAS approach (Berardino *et al.*, 2002); both ascending and descending datasets cover 8 years of temporal span, from 2002 to 2010. A summarizing panel of data frame processed is shown in table 5.1. This method allows to obtain mean ground velocity maps and displacement time series for each pixel of the maps. In figure 5.5 and 5.6 I show the preliminary mean velocity maps; I decreased the ground resolution of the velocities maps from the original 80 m to 400 m, to improve the signal to noise ratio, and masked some strong subsidence signals observed in the large plain South of the DFS, related to water table overpumping (Anderssohn *et al.*, 2008). I further removed some residual orbital signal (planar "ramps") using the procedure described in Casu *et al.* (2006) since the modeled profiles are nearly perpendicular to the ramp directions, I assumed that a small fraction of tectonic signal may have been removed. The final velocity maps are shown in figure 5.8 and 5.9.

Using the same procedure I studied the eastward continuation of the WFZ (from WFZ to CFZ); I processed 38 descending ENVISAT images of track 435 (frame

2902) with temporal span from 2003 to 2010 (Table 5.1): a preliminary map is shown in figure 5.10. Also in this case I removed some residual orbital signal and, to improve the signal to noise ratio I decreased the ground resolution from 80 m to 400 m. The final velocity map is shown in figure 5.11; I also masked some strong subsidence signals observed in the large plain South of the DFS, related to water table overpumping (Anderssohn *et al.*, 2008).

Datase t	Track	Fram e	N° of images	Time span	Residual orbital ramp (strike)	Residual orbital ramp (slope)
Asc.	156	692	25	2004-2010	140°	0.08 mm km ⁻¹
Asc.	385	692	8	2003-2010	207°	0.09 mm km ⁻¹
Desc.	206	2902	19	2003-2010	15°	0.17 mm km ⁻¹
Desc.	435	2902	38	2003-2010	27°	0.13 mm km ⁻¹

Table 5.1: Multitemporal InSAR datasets.

Ascending mean velocity map (Figure 5.8) shows an important deformation pattern in the northern block of the WFZ: excluding the northern border of the data frame this area shows positive values up to velocity of 3 mm yr⁻¹. Instead southern block of the WFZ is characterized by general negative values. This trend is easily identifiable in the NNW-SSE profile of the same figure and it seems to be in agreement with a general left lateral transcurrent kinematic of the fault.

On the velocity map from the descending track 206 (Figure 5.9) a very low signal is present; this may arise from an excessive fraction of tectonic signal removed with the correction of the orbital signal. Indeed track 206 has the steepest slope

among the three data sets, and its strike is the closest (22°) to the DFS trace (Table 5.1).

Concerning descending dataset (Track 435) (Figure 5.11), I observe diffuse low velocity excluding the northwestern block of the area delimited by the DFS to the South and DQF to the East. In this region positive high velocity of displacement are present up to $3\text{-}4\text{ mm yr}^{-1}$.

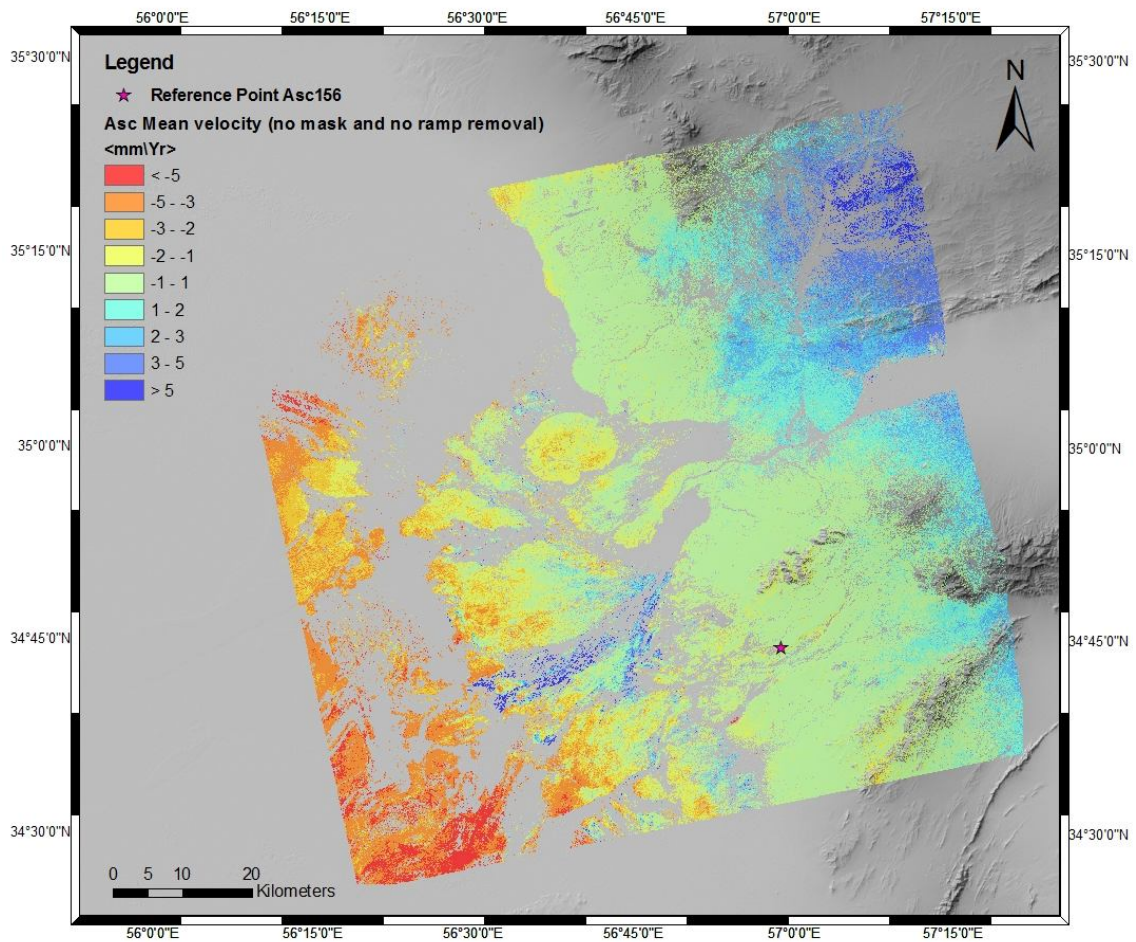


Figure 5.6: Preliminary mean velocity map in satellite line of sight relative to ascending track 156. In blue I show positive values of displacement (approaching to satellite) and in red the negative values (removal to satellite). Star represents the reference point, that is the point I consider stable (mean velocity equal to zero); single pixel velocities are referred to reference point; thus, all pixel velocities are not absolutely, but relative. A SW-NE oriented linear trend is clearly visible and likely due to residual orbital ramp.

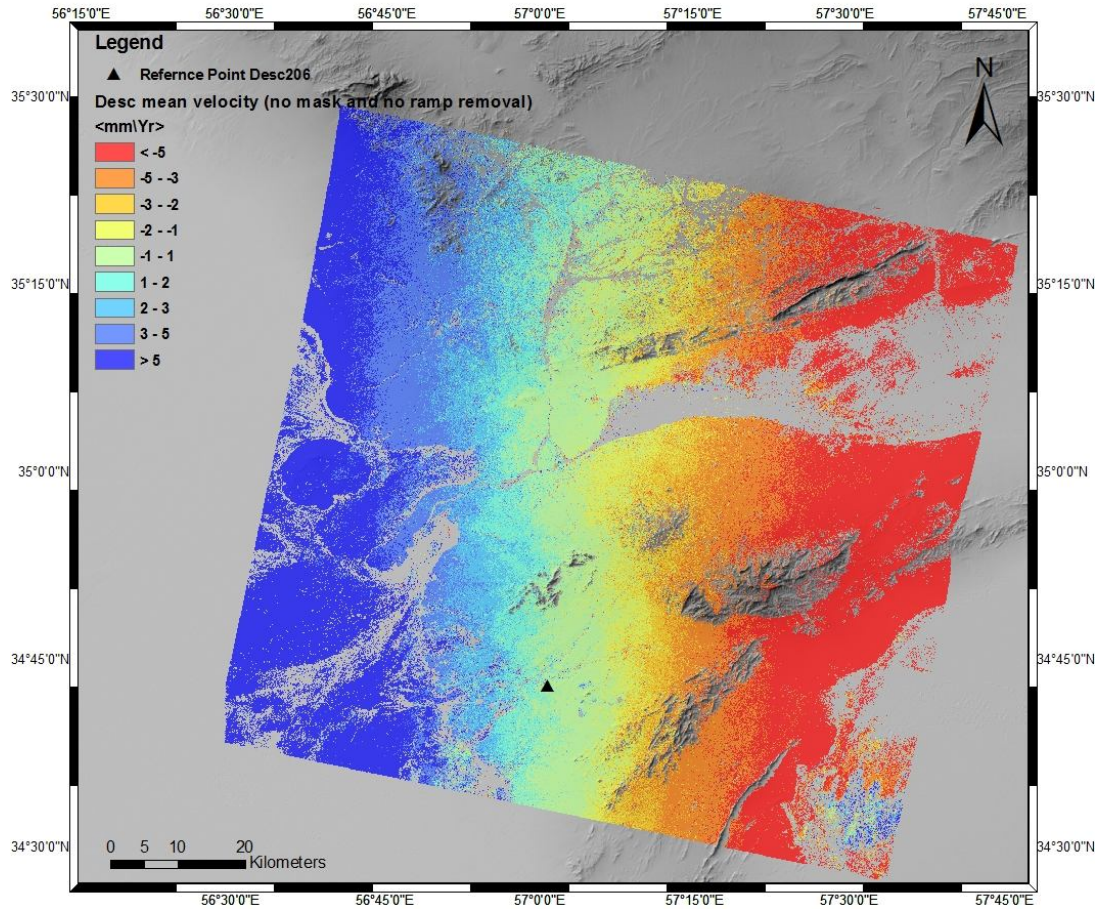


Figure 5.7: Preliminary mean velocity map in satellite line of sight relative to descending track 206. In blue I show positive values of displacement (approaching to satellite) and in red the negative values (removal to satellite). Star represents the reference point, that is the point I consider stable (mean velocity equal to zero); single pixel velocities are referred to reference point; thus, all pixel velocities are not absolutely, but relative. As for the ascending map, it shows an orbital ramp oriented E-W

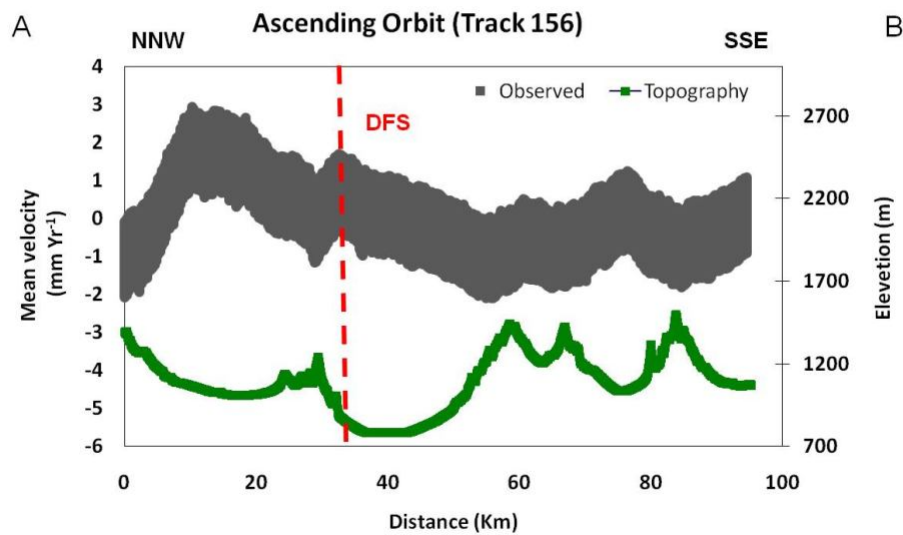
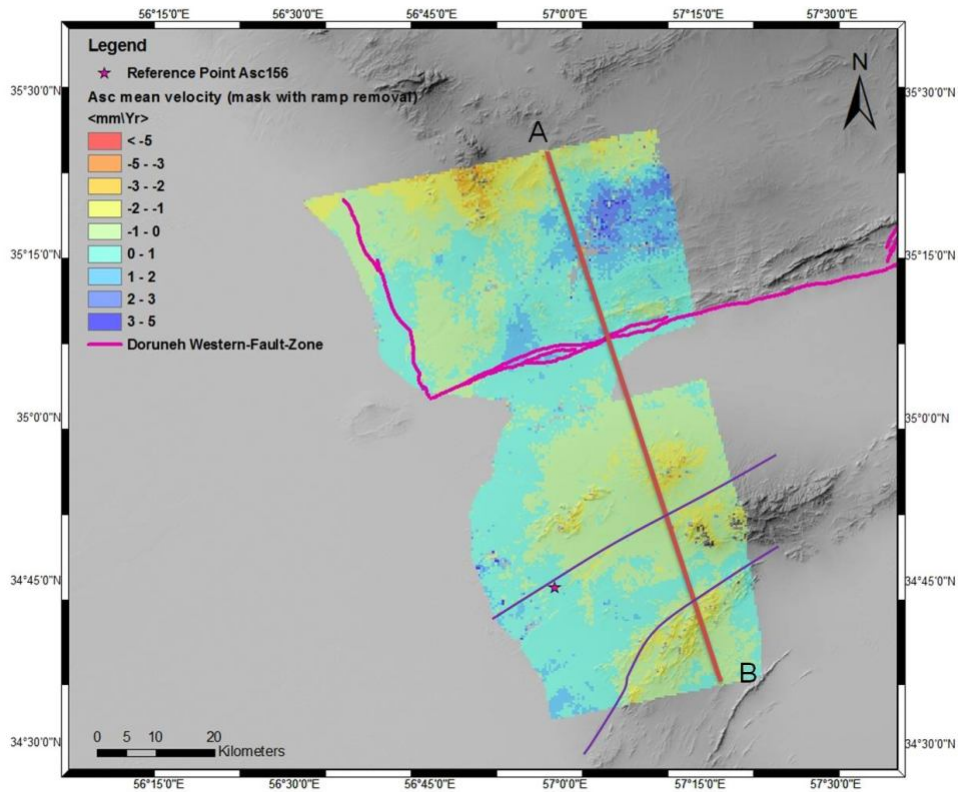


Figure 5.8: Top: final mean velocity map in satellite line of sight relative to ascending track 156. Also in this case in blue I show positive values of displacement (approaching to satellite) and in red the negative values (removal to satellite). Star represents the reference point, that is the point I consider stable (mean velocity equal to zero). In purple the Doruneh fault system surface trace; in dark purple the more evident fault trace of the area that I not consider in this study. Continue red line with the letters A and B represents the NNW-SSE oriented profile trace shown below. Bottom: in gray the mean velocity profile (1200 buffered); in green I show the topographic profile; in red the position of the DFS.

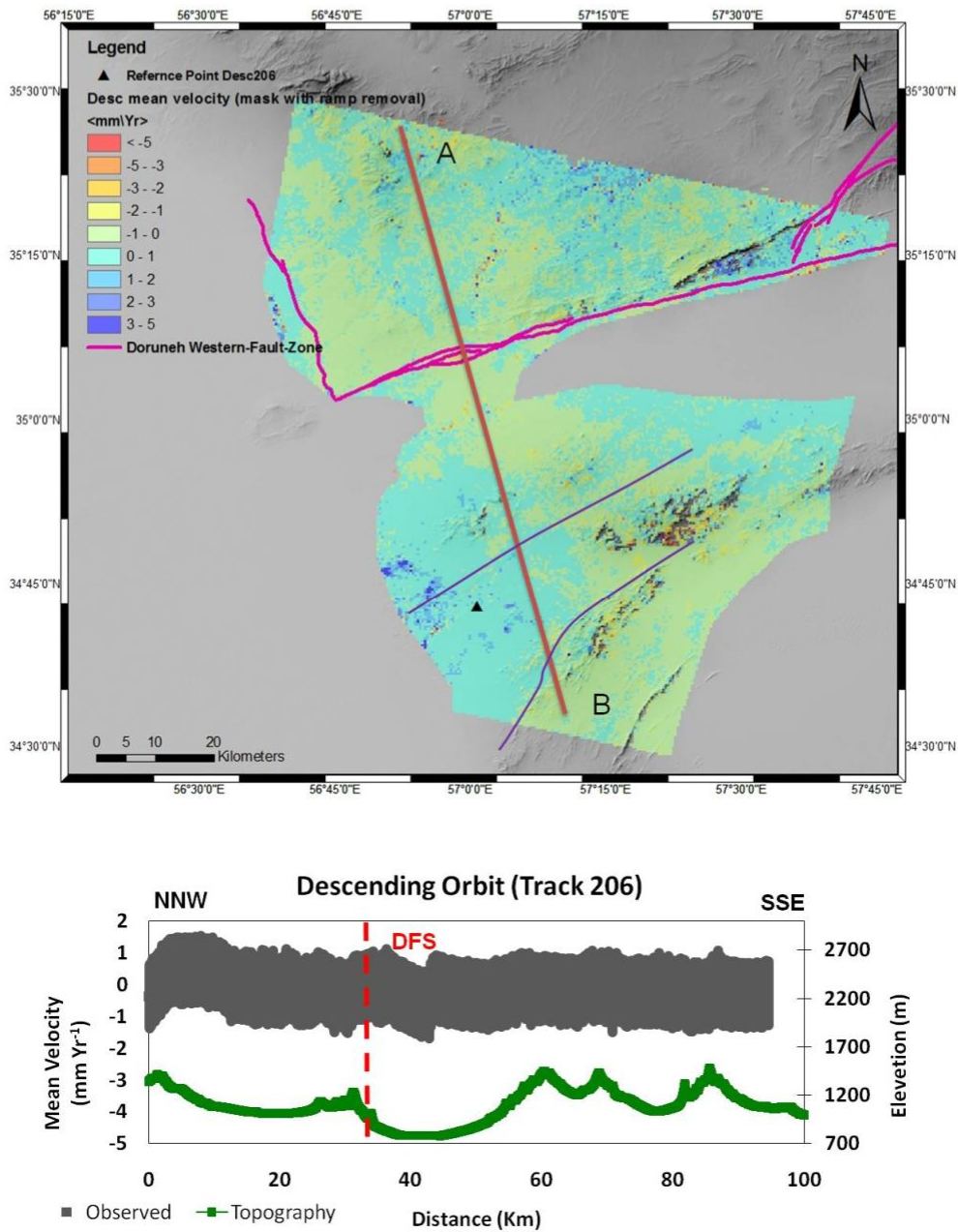


Figure 5.9: Top: final mean velocity map in satellite line of sight relative to descending track 206. In blue I show positive values of displacement (approaching to satellite) and in red the negative values (removal to satellite). Triangle represents the reference point, that is the point I consider stable (mean velocity equal to zero). In purple the Doruneh fault system surface trace; in dark purple the more evident fault trace of the area that I not consider in this study. Continue red line with the letters A and B represents the NNW-SSE oriented profile trace shown below. Bottom: in gray the mean velocity profile (1200 buffered); in green I show the topographic profile; in red the position of the DFS.

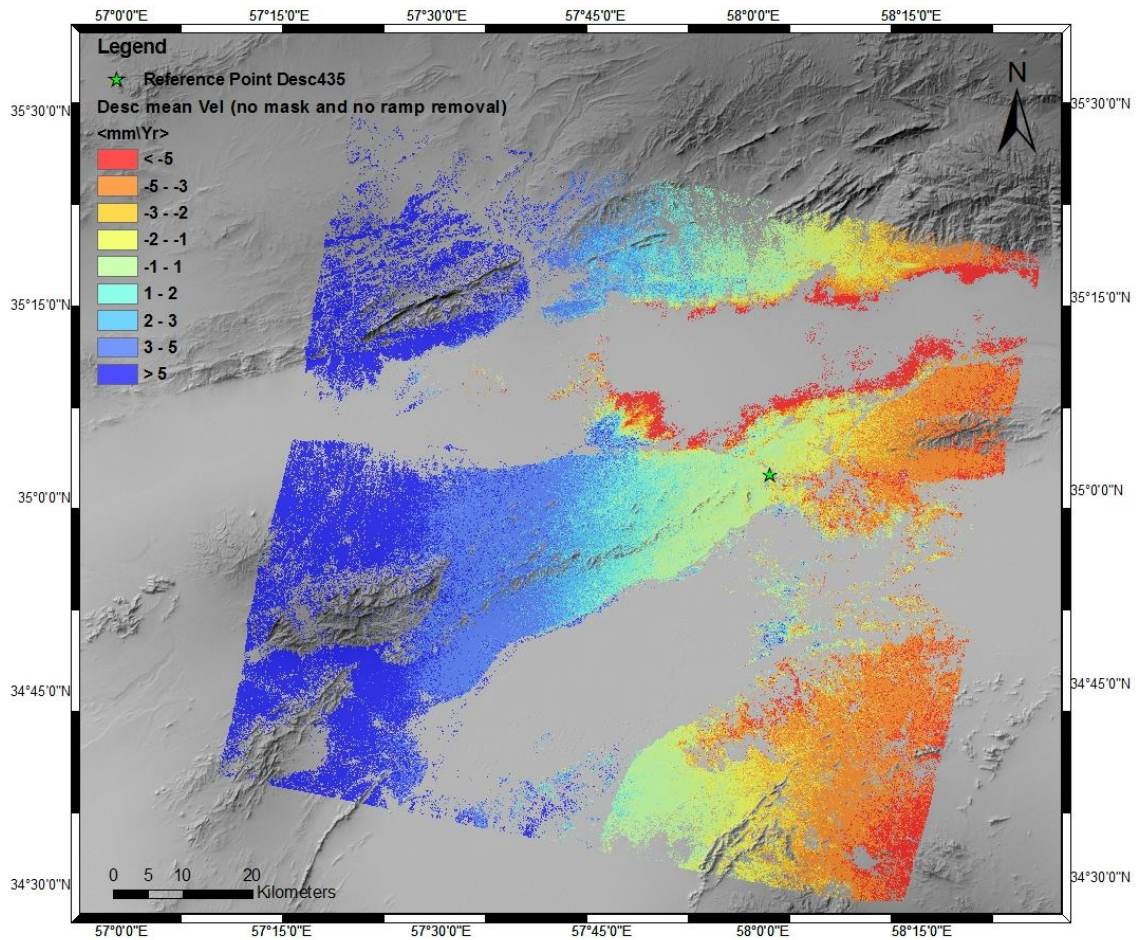


Figure 5.10: Preliminary mean velocity map in satellite line of sight relative to descending track 435. In blue I show positive values of displacement (approaching to satellite) and in red the negative values (removal to satellite). Star represents the reference point, that is the point I consider stable (mean velocity equal to zero); single pixel velocities are referred to reference point; thus, all pixel velocities are not absolutely, but relative. A SW-NE oriented linear trend is recognizable in the map; this is probably due to residual orbital ramp.

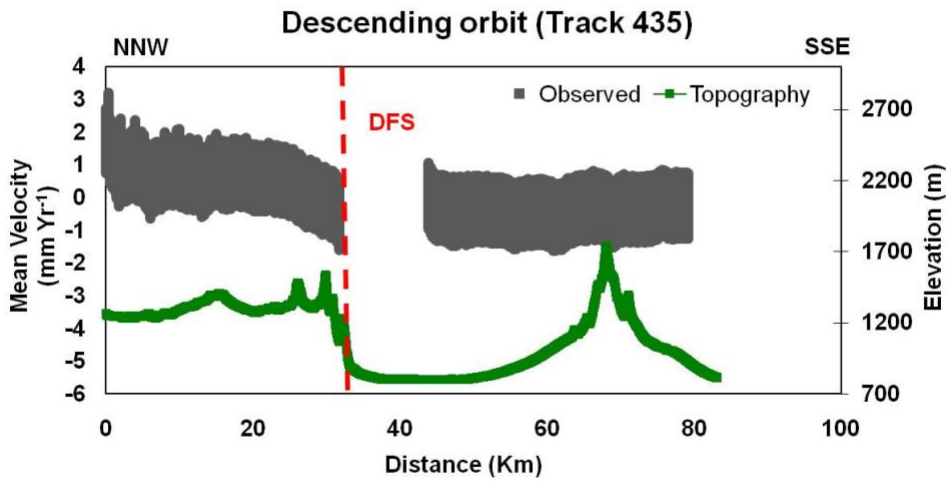
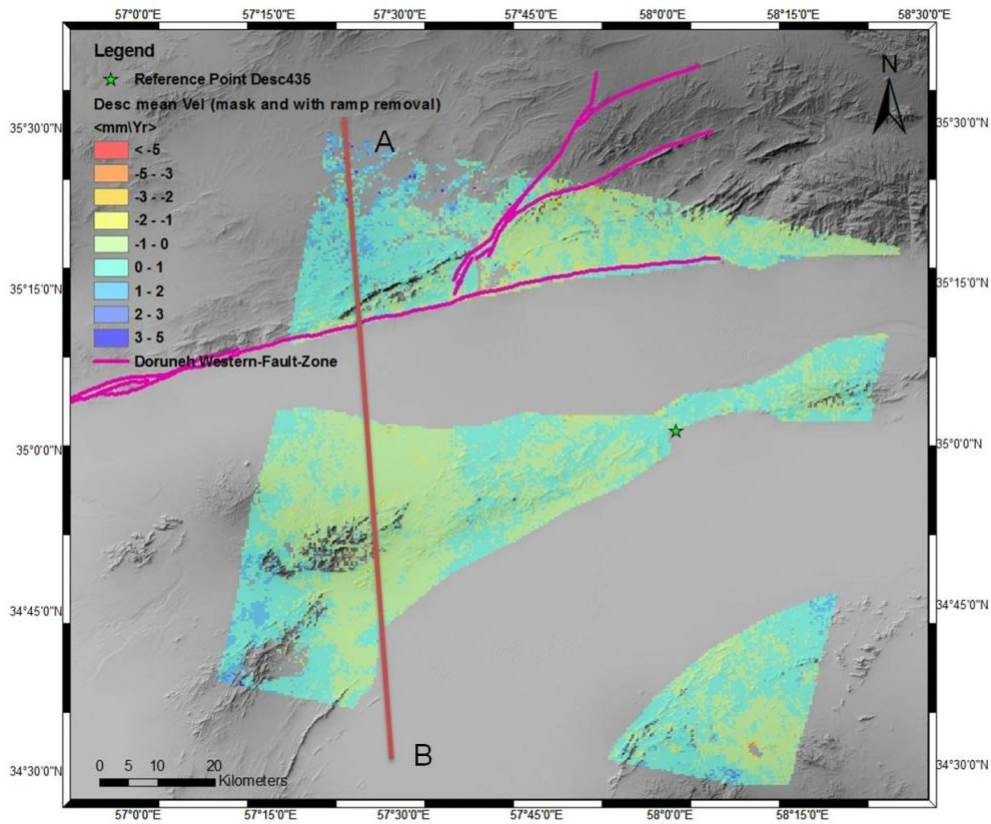


Figure 5.11: Top: final mean velocity map in satellite line of sight relative to descending track 435. In blue I show positive values of displacement (approaching to satellite) and in red the negative values (removal to satellite). Star represents the reference point, that is the point I consider stable (mean velocity equal to zero). In purple the Doruneh fault system surface trace. Continue red line with the letters A and B represents the N-S oriented profile trace shown below. Bottom: in gray the mean velocity profile (1200 buffered); in green I show the topographic profile; in red the position of the DFS.

Despite only 8 ENVISAT images are available for the ascending track 385 dataset (Table 5.1) I completed the processing, adopting the same processing parameters and the same methodology of the other datasets; preliminary results are shown in figure 5.12a. I removed a linear trend probably due to the residual orbital ramp. Also in this case I decreased the ground resolution of the velocities maps from the original 80 m to 400 m, to improve the signal to noise ratio, and masked some strong subsidence signals observed in the large plain South of the DFS, related to water table lowering (Anderssohn *et al.*, 2008). Final mean velocity map is shown in figure 5.12b. The map is clearly correlated with the topography (high topography corresponds with low velocity values) ascribable to residual topographic error or atmospheric artifacts. For such reason this dataset was discarded.

Summarizing, I observe a clear pattern of accumulation of interseismic deformation across the WFZ. The velocity maps show predominantly higher velocities north of the fault, with a relative difference of $\sim 2 \text{ mm yr}^{-1}$ over a distance of 30-40 km from the fault (Figure 5.8, 5.9 and 5.11). There is no discontinuity in the velocities across the Doruneh fault trace, indicating that no surface creep is presently acting on the WFZ. Two ENVISAT datasets (ascending track 156 and descending track 435) show velocity patterns with approximate wavelengths of 30-40 km, both across and along the fault. On the velocity map from the descending track 206 (Figure 5.9) a very low signal is present; this may arise from an excessive fraction of tectonic signal removed with the correction of the orbital signal. Indeed track 206 has the steepest slope among the three data sets, and its strike is the closest (22°) to the DFS trace. I excluded ascending track 385 dataset because of the little number of available images.

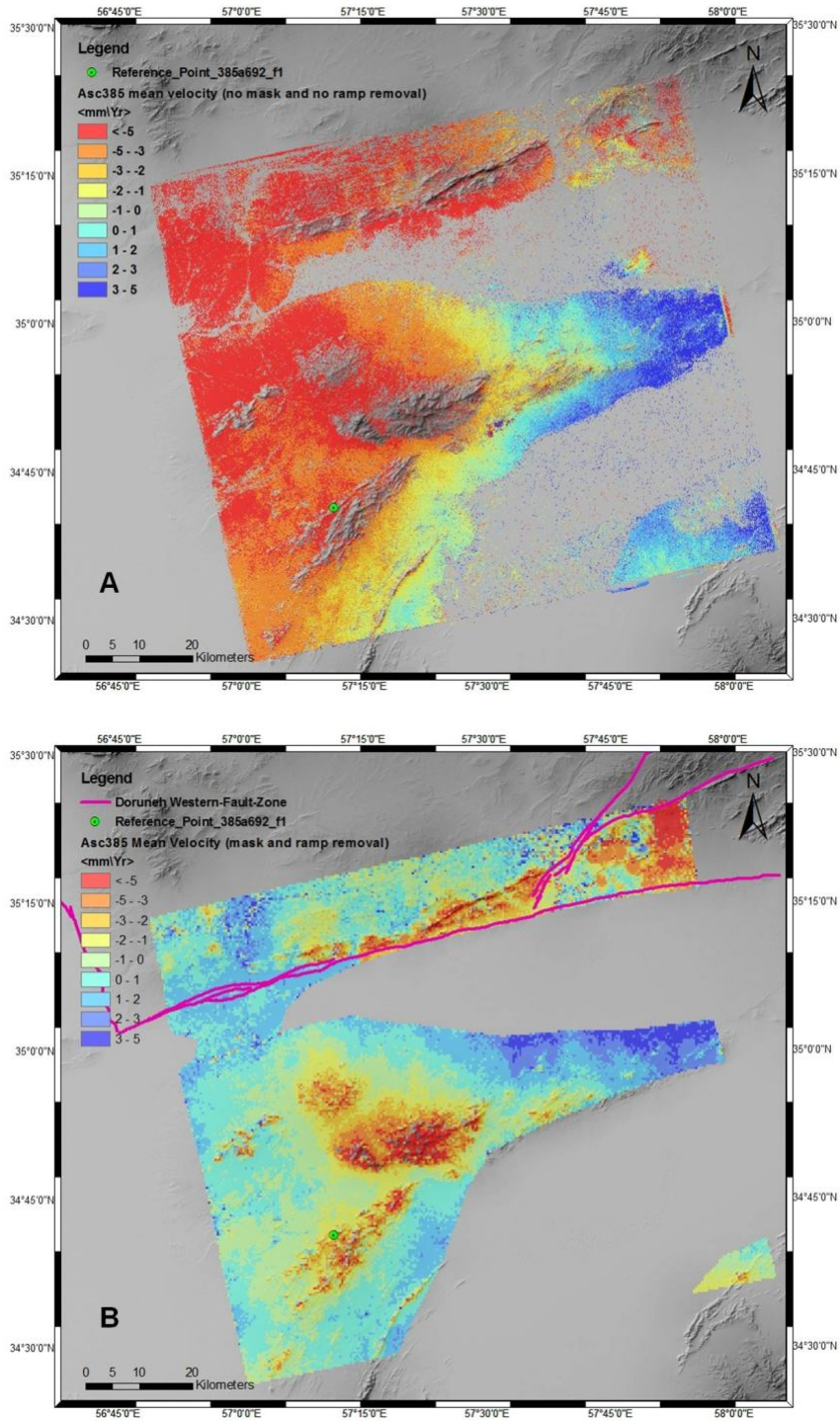


Figure 5.12: A: Preliminary mean velocity map in satellite line of sight relative to ascending track 385. In blue I show positive values of displacement (approaching to satellite) and in red the negative values (removal to satellite). Circle represents the reference point, that is the point I consider stable (mean velocity equal to zero); B: final mean velocity map in satellite line of sight relative to ascending track 385. In purple the Doruneh fault system surface trace.

5.4.2 Displacement time series.

Previous velocity maps are derived from the single pixel mean velocity of displacement. I calculate the mean velocity from the displacement time series available for every pixel at the end of SBAS process chain. Time series analysis allows to study the displacement evolution during the time span covered by images dataset. Thus, it is possible to highlight both the general trend of displacement and potential jumps related, for example, to earthquakes. In the same way I can analyze seasonally cycle related to the ground water variation.

During the 2002-2010 dataset time span no relevant earthquakes are recorded; I therefore do not expect discontinuities in the time series or post-seismic relaxation, letting to hypothesize a nearly linear deformation trend. Figure 5.13 shows three displacement time series of a pixel located in the northern block of the Doruneh fault system for the datasets ascending (track 156), descending (track 206) and descending (track 435) respectively. In this figure I observe a linear trend displacement; little oscillations are essentially related to seasonally oscillation linked with ground water variation or atmospheric artifact.

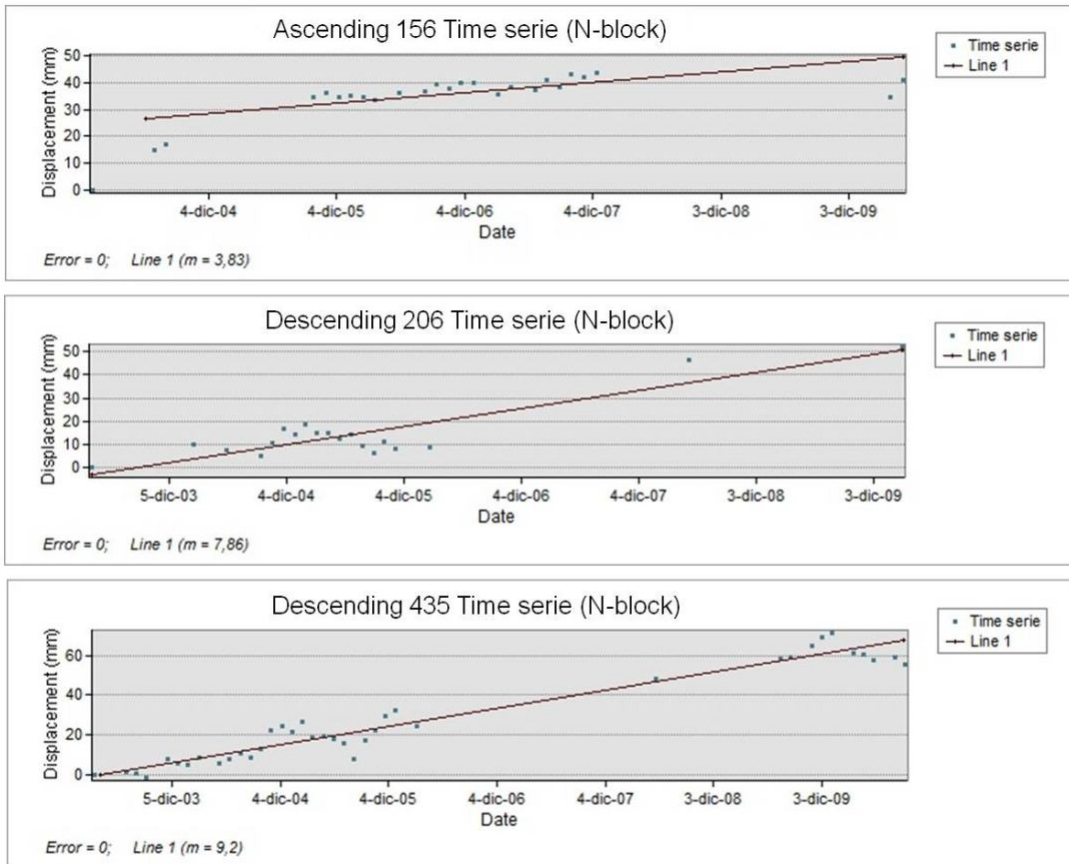


Figure 5.13: Displacement time series of a pixel located in the northern block of the Doruneh fault system for the datasets ascending (track 156), descending (track 206) and descending (track 435) respectively. Red line is the linear regression which slope represents the pixel displacement mean velocity. No displacement jumps are recognizable in the time series, but only seasonally displacement variation.

5.4.3 North and up component analysis

In the areas covered by both ascending and descending SAR data, I evaluated the horizontal and up velocity components using the approach of Hunstad *et al.*, 2009. First I calculated, for each pixel, the North, East and up coefficients relative to the two ascending and descending line of sight starting from the state vector of satellite orbits. Using trigonometric calculate, I combined ascending and descending velocity with North, East and Up coefficients and evaluate the East and Up components of motion. Because of the acquisition geometry I am not able to estimate the North component. Because only the ascending track 156 and

descending track 206 are superimposed, I only can discern the two components for the overlapping areas of these datasets.

The Up component map (Figure 5.14) shows an evident uplift pattern located in the north-eastern zone of the map, with a negative gradient toward NW.

South, low velocity is present with a small negative gradient toward NE. This velocity distribution, highlighted in the NNW-SSE profile, seems to be compatible with left lateral kinematic of the area. Also east component map and related NNW-SSE profile (Figure 5.15) confirms this kind of kinematic: I observe positive values in the south side of the WFZ, whereas the northern one is characterized by negative velocities; the positive value of the northernmost segment should not be related to the DFS kinematic; here the East velocity distribution shows a clear compressive pattern between the two areas.

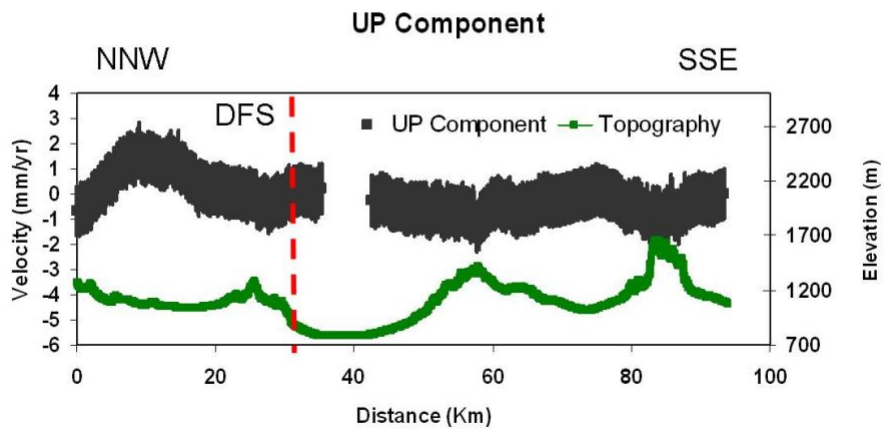
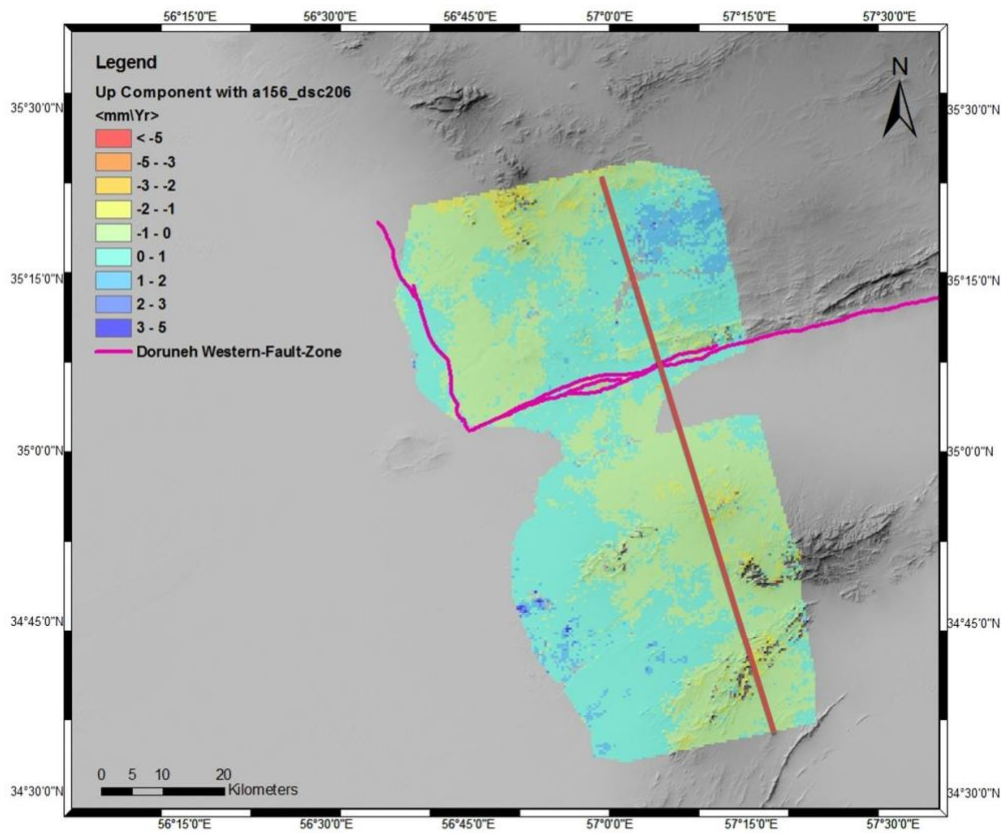


Figure 5.14: Top: up component velocity map. In blue I show positive values of displacement (uplift) and in red the negative values (subsiding). In purple the Doruneh fault system surface trace. Continue red line with the letters A and B represents the N-S oriented profile trace shown below. Bottom: in gray the mean velocity profile (1200 buffered); in green I show the topographic profile; in red the position of the DFS.

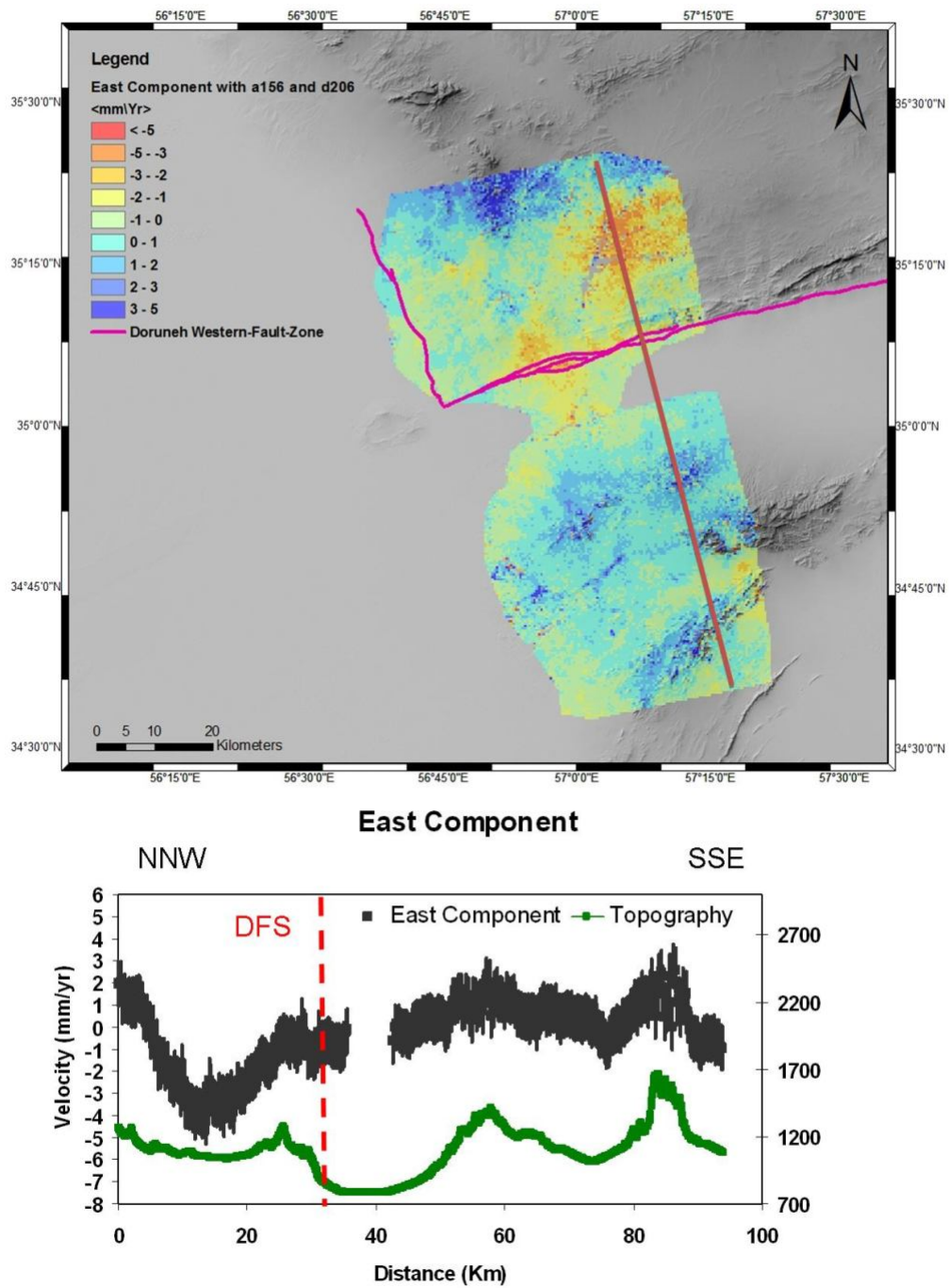


Figure 5.15: Top: East component velocity map. In blue I show positive values of displacement (eastward moving) and in red the negative values (westward moving). In purple the Doruneh fault system surface trace. Continue red line with the letters A and B represents the N-S oriented profile trace shown below. Bottom: mean velocity profile (1200 buffered); in green I show the topographic profile; in red the position of the DFS.

5.5 3D analytical modeling

I performed the data inversion to determine the source parameters, using three datasets: ascending track 156, descending track 206 and 435. I performed the inversion using the Okada (1985) analytical solutions for a dislocation in an elastic, homogenous and isotropic half-space. I progressively refined the inversion starting from a three fault unconstrained inversion. I then gradually reduced the range variability of each parameter using geological constraints; I performed a last inversion with two faults, introducing constraints based on geomorphological data by Farbod *et al.*, (2011).

During the inversion, we simultaneously assessed the tectonic signal due to the source and the linear ramp introduced by orbital inaccuracy. I used the masked map to isolate areas whose signal is only related to tectonic activity.

The inversion started with three different sources: the Western fault zone (WFZ) of the Doruneh fault, the Dahan-Qaleh fault (DQF) and the Kharturan fault (KF). I observed the low contribution of the modeled KF to the velocity field; this is probably due to the marginal position of the fault with respect the data coverage (KF border the ascending track 156 and descending track 206 dataset and is out of descending track 435 dataset distribution) and to its small dimension. I therefore discarded this source from the modeling.

Concerning the DQF, I reached to similar conclusions; however we remark that two of the three datasets cover the fault area and the descending track 435 shows a high velocity area delimited from the DFS to the South and from the DQF at East. Since most of the DQF is not covered by data, to avoid large uncertainty on the parameters I fixed them and let only the slip rate to vary.

Concerning the DFS, I fixed all the fault parameters with the exception of the slip rate and the fault top depth, i.e. the locking depth. I set for the sources a width equal to half of length, adopting a rake angle derived from field observation by Farbod *et al.* (2011).

Table 5.2 shows the best fit solution and figures 5.17, 5.18 and 5.19 show the modeled velocity field in LoS of ascending track 156, descending track 206 and

435, respectively. In figure 5.17 I observe positive velocities in the northern block of DFS, where an ESE-WNW oriented positive trend is present. Southern block is characterized by negative velocities and ESE-WNW oriented negative trend is also detected.

Figure 5.18 (Descending track 206) shows positive pattern in northern block; higher velocities are concentrated close the across between the DQF and DFS, resulting from the two left lateral motions of the faults and of the compressive component on the DFS fault plane.

The same area shows positive values also for the descending track 435 (Figure 5.19). In this case a positive areas at East of the DQF and a negative one in the southern block of the DFS are also visible.

Modeled fault parameter

DQ Fault

Length	40000. (m)	fixed
Width	20000. (m)	fixed
Top Depth	15000. (m)	[5000 , 15000]
Strike angle	225. (deg)	fixed
Dip angle	90 (deg) in	fixed
Fault east	566855. (m)	fixed
Fault north	3916917. (m)	fixed
Rake angle	0 (deg) in	fixed
Slip	1.2 (cm) in	[0.0 , 1.2]

D. Fault

Length	80000. (m)	fixed
Width	40000. (m)	fixed
Top Depth	6728 (m)	[5000 , 15000]
Strike angle	255.0 (deg)	fixed
Dip angle	90.0 (deg)	fixed
Fault east	515691. (m)	fixed
Fault north	3889045. (m)	fixed
Rake angle	30.0 (deg)	fixed
Slip	0.2 (cm) in	[0.0 , 1.2]

Asc156: Constant shift -0.45 (cm) in [-1,1]
East ramp 0.008 (cm/km) North ramp 0.004 (cm/km)
 final cost: 0.08 (null solution: 0.18)

Dsc206: Constant shift 0.6 (cm) in [-1,1]
East ramp -0.017 (cm/km) North ramp 0.001 (cm/km)
 final cost: 0.07 (null solution: 0.44)

Dsc435: Constant shift 0.9 (cm) in [-1,1]
East ramp -0.014 (cm/km) North ramp 0.003 (cm/km)
 final cost: 0.07 (null solution: 0.50)

FINAL COST: 0.24 (Null solution: 7.01)

Table 5.2: Top: Fault parameters of best fitting solution with range variability for each parameter. Bottom: for three dataset inverted I show residual orbital ramps subtracted during the processing, cost functions respect to the null solution and rigid shifts. DF is Doruneh Fault and DQF is the Dahan-Qaleh fault.

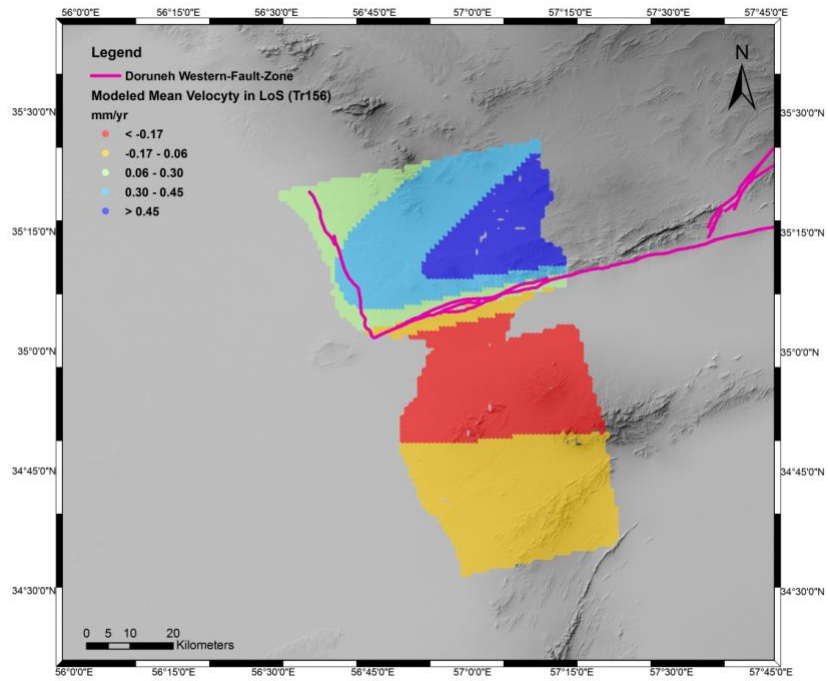


Figure 5.16: Modelled velocity field in ascending track 156 LoS. In blue I show positive values and in red the negative. In purple the DFS trace.

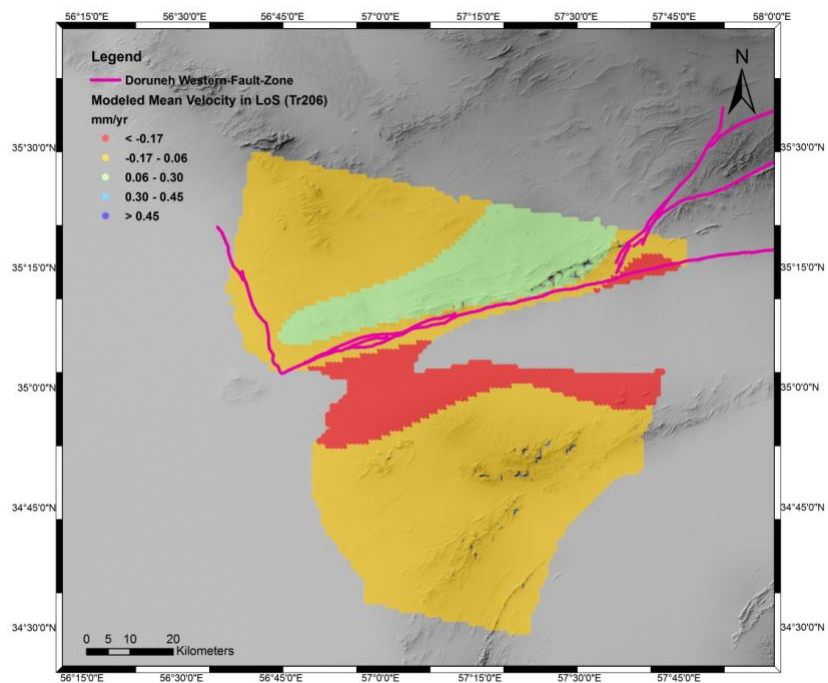


Figure 5.17: Modelled velocity field in descending track 206 LoS. In blue I show positive values and in red the negative. In purple the DFS trace.

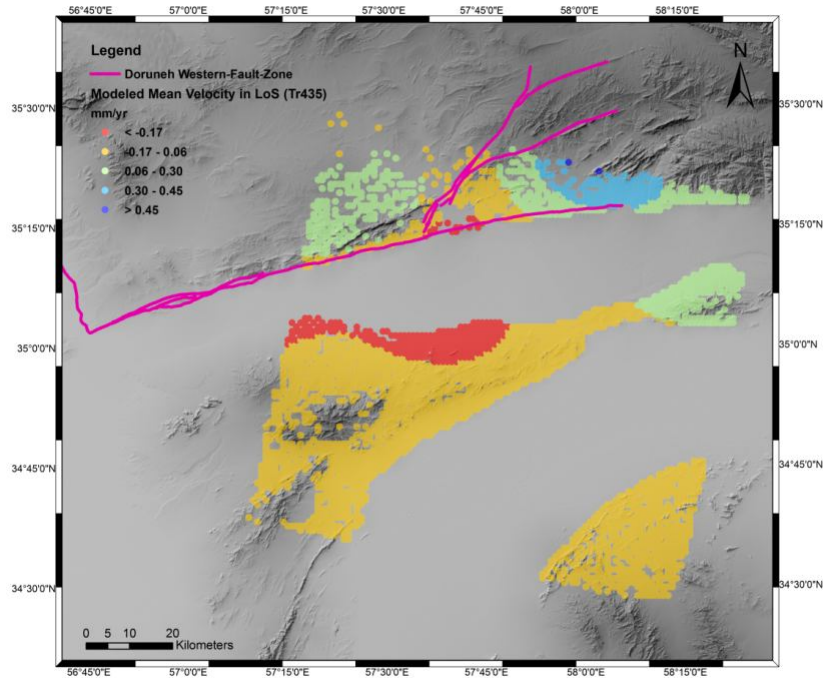


Figure 5.18: Modelled velocity field in descending track 435 LoS. In blue I show positive values and in red the negative. In purple the DFS trace.

In summary, the 3D best fit model is only roughly able to reproduce DInSAR data, as shown by the residual maps of Figure 5.19. For the DQF I obtained a slip rate and a top depth not very reliable, at the edge of the permitted range. Moreover, a slip rate of 12 mm yr^{-1} appears too high for this area. Concerning the DFS, I obtained a realistic locking depth of 7 km with a slip rate of 2 mm yr^{-1} . This velocity is in good agreement with geological velocity of Fattahi *et al.* (2007) and the locking depth is consistent with seismological data available for this area (i.e. Engdhal *et al.*, 1998). This result lead us to abandon the hypothesis of a 3D modelling, moving to a more reliable 2D modelling, described in the next section.

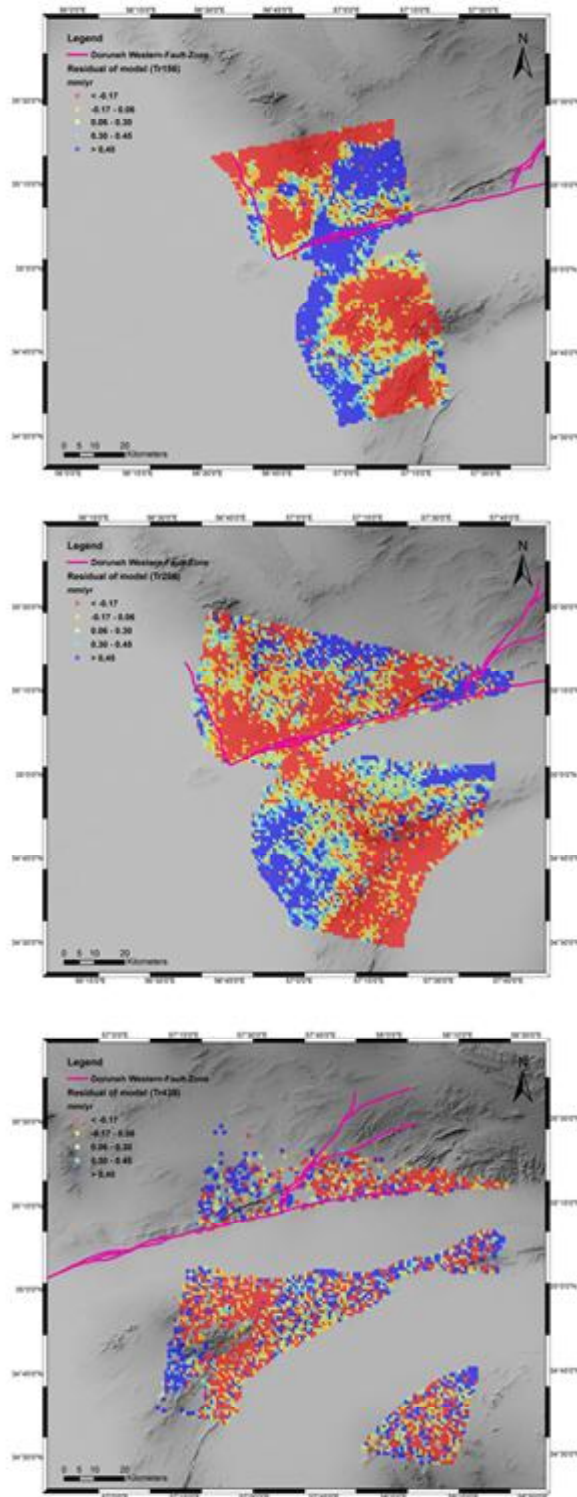


Figure 5.19: Residual maps of modelled ascending track 156, descending track 206 and 435 (from top to bottom).

5.6 2D analytical model approach

Here I investigated some of the characteristics of the Doruneh fault by a 2D non-linear modeling of our geodetic observations. Such a simplified model implies a constant deformation along strike. This assumption is confirmed by the low-varying signal along strike for the two descending data sets up to the DQF intersection to the East. The velocity from ascending orbit decreases about 3 mm yr^{-1} along the northern side of the DFS, from East to West (Figure 5.8). This is compatible with the presence of a fault discontinuity, and the western limit of the WFZ, as defined by Farbod *et al.* (2011), is here limited by the transversal KF. To avoid any border effect, I inverted only data extracted over box profiles calculated for the central part of the Western DFS (Figure 5.20a-c). I approximated the DFS as an infinitely long dislocation occurring on a defined fault plane extending from the surface to an infinite depth. The model assumes that the fault part extending below a certain depth is freely slipping and is loading the brittle, upper crustal layer, locked in the interseismic period (Savage and Burford, 1973). The deformation rates observed at the surface are inverted to retrieve the fault parameters at depth. The locking depth is determined by the thickness of the brittle seismogenic layer, where elastic deformation dominates (Savage and Burford, 1973). When modeling interseismic deformation across large areas, the presence of parallel faults and across-strike variations of crust rigidity may complicate the deformation pattern up to a point where simple elastic models cannot provide a reasonable fit to the data (Fialko, 2006). While no information exists on possible crust rigidity variations in the area, the presence of a nearly parallel, $\sim 100 \text{ km}$ long fault to the South of the WFZ, bordering to the North the Kavir-e Namak basin, is reported (Fattahi *et al.*, 2007).

North of the WFZ there are no major mapped faults, but the presence of ENE-WSW basins and ridges and sharp geological boundaries suggests that a similarly oriented active fault is present here too, at a distance of $\sim 40 \text{ km}$. To minimize possible contributions of interseismic crustal velocities from nearby faults, I

truncated the profiles at a distance where I expect that the observed signal is attributed to WFZ.

I constrained my model source by fixing the strike to 255° , as the WFZ trace, and setting a locking depth of 12 km, according to the average depth of the seismicity (Engdahl *et al.*, 2006). Using the Okada (1985) analytical solutions, I solved for the fault dip, rake and slip rate, by means of a non-linear, least-squares inversion algorithm based on the Levenberg-Marquardt approach, as described by Atzori *et al.*, (2009). The comparison between observed and predicted data is shown in Figure 5.21 for the three velocity maps. The parameter uncertainty and trade-offs (Figure 5.21d) show that rake and slip are not correlated and are well resolved, while the dip has a higher uncertainty.

According to my modeling the WFZ fault plane is constrained by the InSAR observations to be North-dipping, with dip values in the interval $60^\circ \pm 11^\circ$, a locking depth of 12 km and slip rates of about $4\text{-}6 \text{ mm yr}^{-1}$. The rake angle between 30° and 38° defines a left-lateral strike-slip, with slightly transpressive kinematics, with an anti-correlation between slip and rake, though confined in a small interval.

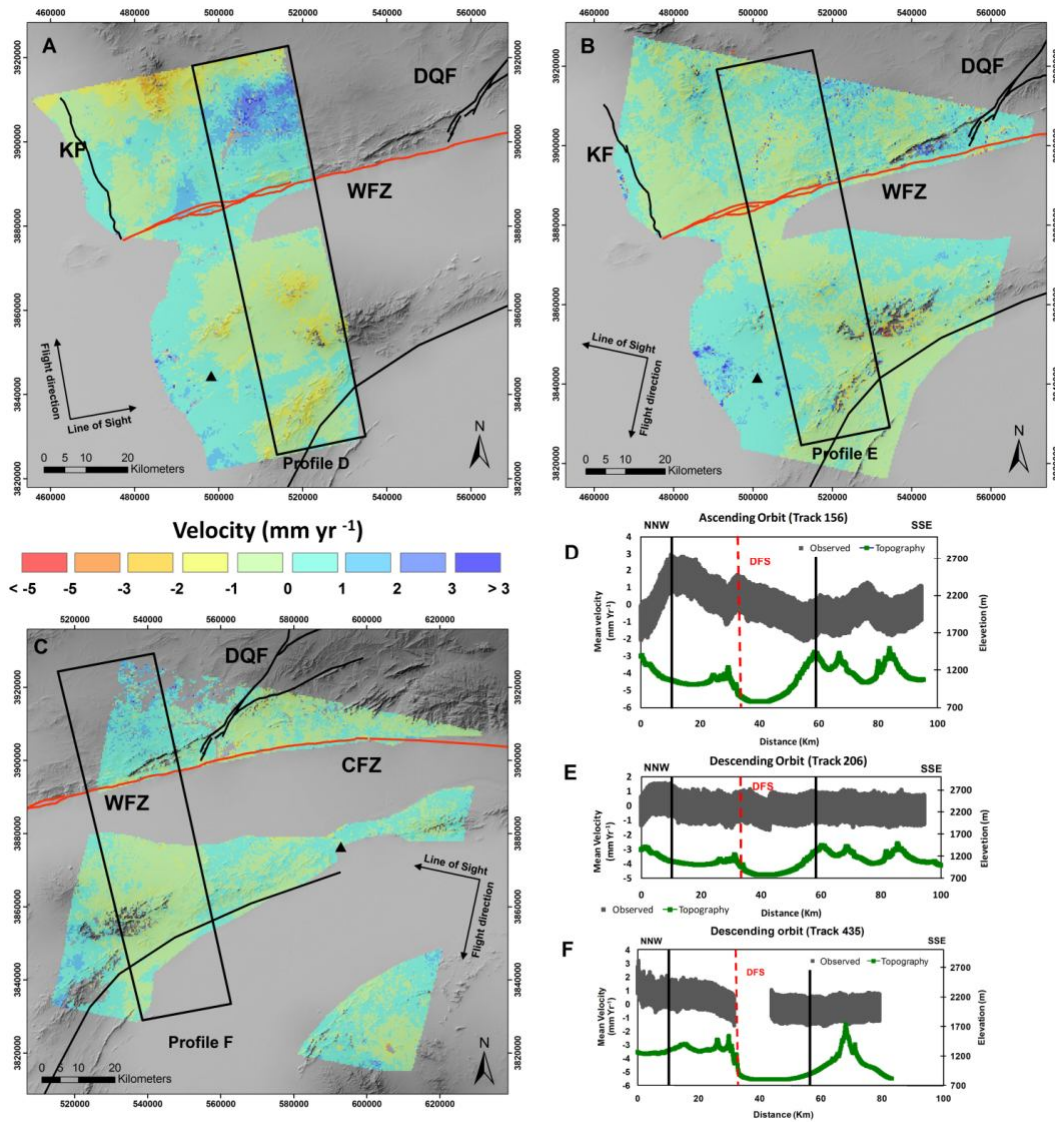


Figure 5.20: Mean Line of Sight velocity maps from (A) ascending track 156, (B) descending track 206 and (C) descending track 435. In red I show the DFS system trace; other faults in the region are in black. Black boxes mark the ~20 km buffered velocity profiles reported with the profile (D), (E) and (F), where the topography is also reported in green; dashed red lines mark the intersection with the DFS trace. Black triangles indicate the reference point whereas solid black line mark the truncation of profile, around the DFS trace, used in the inversion processing.

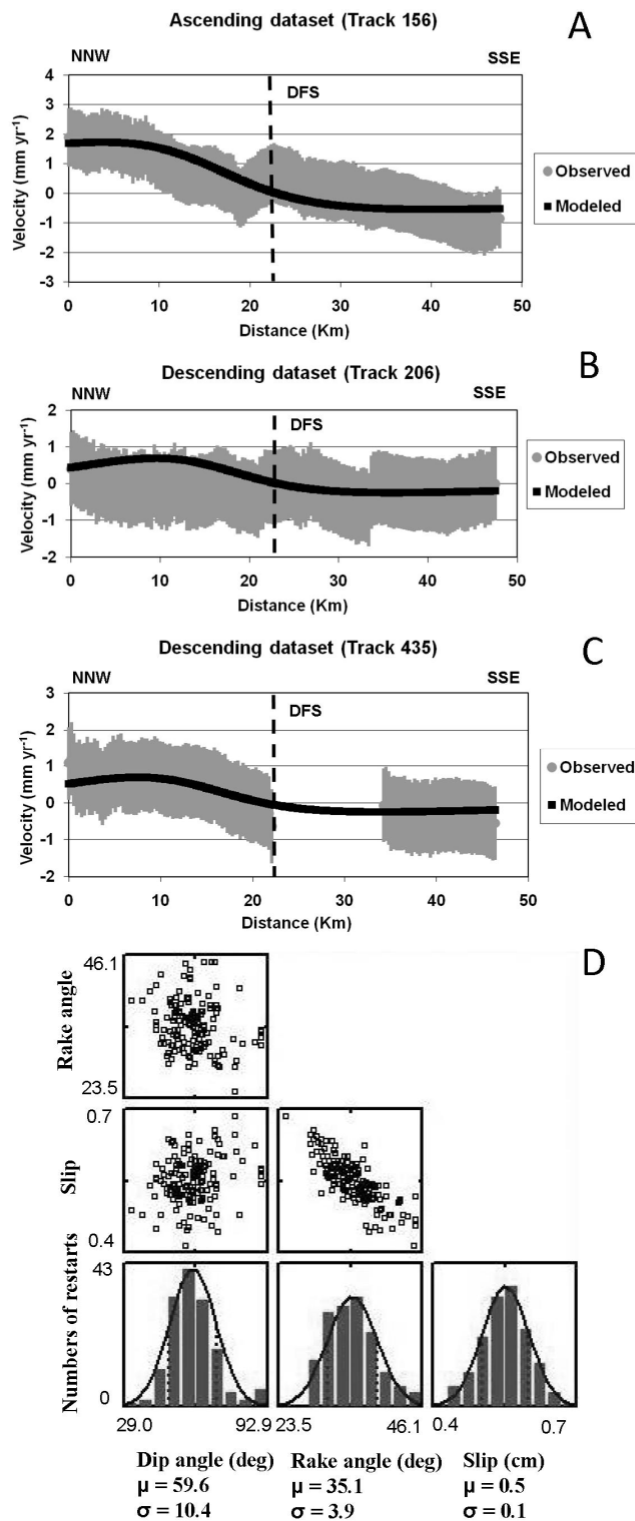


Figure 5.21: Observed (gray) vs. Modeled (black) velocity profiles for (A) ascending track 156, (B) descending track 206 and (C) descending track 435; Dashed lines mark the intersection with the DFS trace. D) Uncertainty and trade-offs for inverted parameters, calculated with 50 restarts according the work of Atzori *et al.* (2009); mean value (μ) and standard deviation (σ) are also reported.

5.7 Discussion and Conclusion

My simple 2-D model is able to fit the observations quite well (Figure 5.21). The inverted model parameters, confirms the main characteristics of this sector of the DFS, give new pieces of information into the seismic potential of the fault. My model confirms the left lateral kinematics of the DFS, as first defined by Wellman (1966), but an additional important thrust component is introduced to fit the observations (Rake angle of 34 ± 4). The modeled rake results in the left-lateral component being about 2/3 of the total slip rate, which is in agreement with the long term record as reconstructed by structural and geomorphic observations. A steep fault dip to the North ($\sim 60^\circ$) is well constrained by the observations, and is in agreement with field observations on the Western and Central DFS.

My modeled slip rate of $\sim 5 \text{ mm yr}^{-1}$ is the first quantitative estimate of strain accumulation for the Western DFS, corresponding to $\sim 4 \text{ mm yr}^{-1}$ of pure horizontal movement and 2.5 mm yr^{-1} of pure vertical displacement. In the long term, Fattahi *et al.* (2007) estimates $\sim 2.4 \text{ mm yr}^{-1}$ of left lateral slip rate on the CFZ, by Infrared Stimulated Luminescence Dating (ISLD) dating of sediments sampled on one Holocene alluvial fan, at longitude $58^\circ 10'$. Although this is so far the only geological slip rate available for the DFS, it cannot be extended to the entire 360 km length of the DFS. In fact, there are many geological and geomorphological evidences that the DFS is segmented and the evidence of paleo-earthquakes (Fattahi *et al.* 2007), suggests that the maximum rupture length of a single earthquake along the DFS system is $\sim 100 \text{ km}$.

The transpressive character of the WFZ resulting from my model is in agreement with the kinematic model proposed by (Farbod *et al.*, 2011), in which the WFZ slip vector is compatible with those of the left-lateral strike slip Daleh-Qahan fault and of the reverse KF (Figure 5.4).

At the regional scale, my slip rate and slip vector for the WFZ are in agreement with the sparse quantitative data available on the present deformation field (Vernant *et al.*, 2004). My model implies a shortening rate across the DFS of $\sim 1.3 \text{ mm yr}^{-1}$, which is 1/4-1/5 of the total shortening accommodated between the Lut

block and Eurasia, as measured by GPS networks (Vernant *et al.*, 2004). Although in this area the DFS is the most prominent active tectonic structure, it is certainly not the only one, and our data imply that other faults with similar rates of activity are needed north of the Lut block to accommodate the mentioned shortening rates. If I consider a single earthquake rupturing the entire ~80 km of the WFZ, I can expect a surface slip per event of about 2 m (Wells and Coppersmith, 1994); in this case, assuming that all interseismic deformation is recovered with a single event, I would estimate a characteristic recurrence interval of about ~400 yr. The lack of such strong seismicity in the historical record is not surprising at all, since this part of Iran has been devoid of major centers and communication lines for over 1500 years of the Persian history (Ambraseys and Melville, 1982). Alternative explanations for the lack of strong historical records may be found in peculiar seismicity patterns occurring along the WFZ, as for instance when the seismic moment is released during frequent moderate magnitude earthquakes (Hergert and Heidbach, 2010).

Chapter 6

Coseismic deformation analysis for the 2008 Balochistan seismic sequence

6.1 Introduction

In this study I analyzed the 2008 Balochistan (western Pakistan) seismic sequence by means of DInSAR technique, focusing the attention on the source modeling and the stress transfer between adjacent faults. This sequence is characterized by two Mw 6.4 events on October 28 and 29 and a Mw 5.7 foreshock on December 9. The most seismically active regions of Balochistan are Quetta Syntaxis and the Sulaiman Lobe. These areas are tectonically located between the Indian Plate and the Afghan block of the Eurasian Plate. The Indian plate moves northward at the rate of 38 mm yr^{-1} and the collision with the Afghan block generates the tectonic features in northern and western Pakistan. The complex converging movements of the two plates reflect in a wide range of fault mechanisms, with a major role played by the left lateral Chaman Fault System, west of Quetta. The Sulaiman

Lobe shows a diffuse deformation due to a southward motion; this extrusion is accommodated along its eastern margin by the left-lateral Kingri fault system. On the other side, in the Quetta Syntaxis, a right-lateral tectonic regime characterizes the western margin of the Lobe. Seismicity in the Quetta Syntaxis occurs in a NW-SE oriented band of about 25x100 Km, with a predominant NW-SE transcurrent kinematics. Therefore the tectonic regime is supposed to be accommodated by NW-SE oriented strike-slip structures; however, no surface evidences support such assumption.

I analyzed the coseismic deformation of the October/December 2008 events by means of DInSAR technique. Images from the C-band ENVISAT and from the L-band ALOS satellites are available, with different looking geometries and coverage: ascending and descending orbits, wide swath and fine beams, incidence angles from 23 to 41 degrees. The time distribution of the images allows to discriminate the contribution of the October and December events, so that a precise modeling of the seismic sequence is possible. I tried to define the source geometries with a non-linear inversion, followed by a linear inversion to retrieve the slip distribution.

Finally, I analyzed the static stress transfer using the Coulomb Failure Function, in order to understand the interaction of nearby faults and the tectonic implications for this sector of the Himalayan converging margin.

6.2 Geodynamical and seismotectonic frameworks

6.2.1 Geodynamical context

The Indian-Eurasian plate convergence is estimated to be $\sim 38 \text{ mm yr}^{-1}$ at the location of Hyderabad, India (Altamimi *et al.*, 2007) (Figure 6.1a). The most evident onset of this convergence along the western boundary of the Indian Plate is the left lateral Chaman Fault System (CFS) (Figure 6.1b). Szeliga (2010), based on the seismicity investigation along the CFS, suggests that the deformation along the fault system is partitioned between left motion and range- normal convergence;

furthermore, based on geodetic estimates, he suggests that the overall left lateral rates are near the lower bound of geologic slip estimates (19.5 mm yr^{-1}).

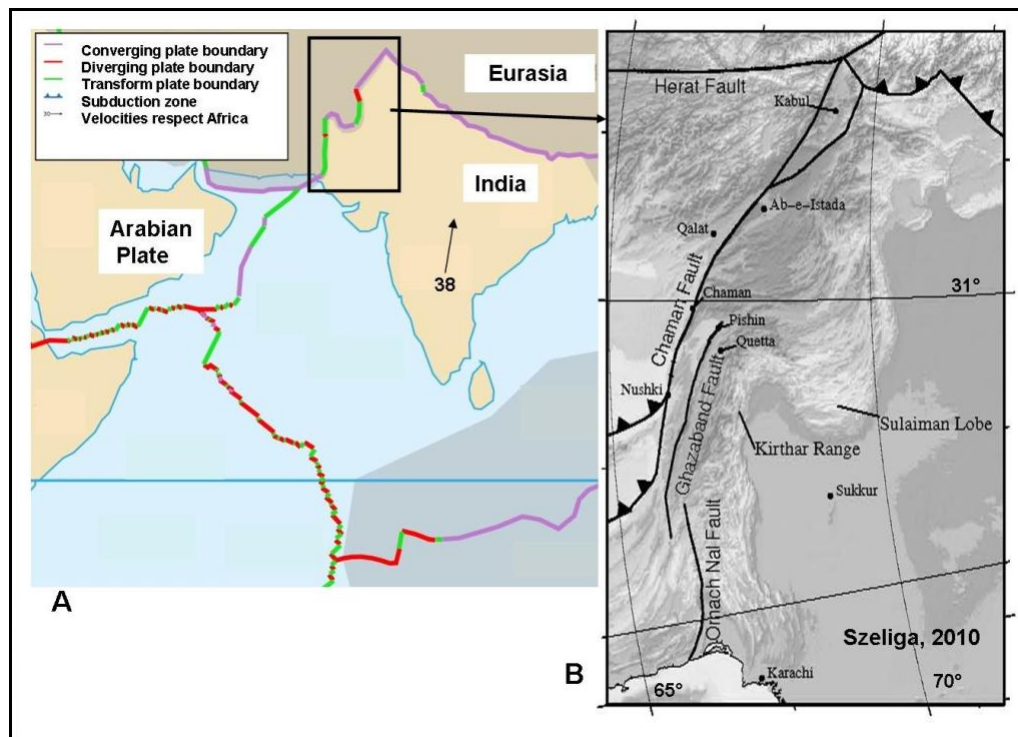


Figure 6.1: A) Geodynamic context of the India-Eurasia convergence with plate velocities respect to Eurasia (Altamimi *et al.*, 2007). B) Map of the western boundary of the Indian plate (from Szeliga, 2010) where are shown the main tectonic structures; dashed black line indicate strike slip faults, whereas the triangles indicate the hanging wall of thrust faults.

Along the plate boundary, some of this motion is absorbed in diffuse deformation into the Sulaiman Lobe; this is a south verging salient produced by the northward translation of the semi-rigid Katawaz block by CFS (Figure 6.2) (Haq and Davis, 1997; Bernard *et al.* 2000). At the eastern margin of the Sulaiman Lobe, the left-lateral Kingri fault system accommodates the southern extrusion of the Lobe (Rowlands, 1978). Although the seismicity of the western margin of the Sulaiman Lobe could indicate the presence of a right lateral fault system analogous to the Kingri fault system, no faults are mapped in this area (Banks and Warburton, 1986; Bannert *et al.*, 1992; Schelling, 1999).

The fold-and-thrust belts of Western Pakistan show a lobate shape studied by many authors (Jones, 1961; Rowlands, 1978; Quittmeyer *et al.*, 1984; Banks and

Warburton, 1986; Humayon *et al.*, 1991; Jadoon *et al.*, 1993, 1994; Jadoon and Kurshid, 1996; Haq and Davis, 1997; Bernard *et al.*, 2000). The lobate structure and the strike of both Kirthar and Sulaiman Ranges could be due to the northward translation of the semi-rigid Katawaz block along the eastern border of the Chaman Fault System (CFS) as demonstrate by analog and viscoelastic modeling (Haq and Davis, 1997; Bernard *et al.*, 2000). Simple strike slip faults (e.g. the Kingri Fault) along the eastern boundary of the Sulaiman Lobe accommodate the southward extrusion of the Lobe itself (Figure 6.4; Rowlands, 1978). The convergence velocities and directions between the Sulaiman Lobe and the northern Kirthar Range suggest that dextral shear accommodates their differential shortening rates, along the western margin of the Sulaiman Lobe, (Figure 6.4). At the transition between the Kirthar Range and the southern verging Sulaiman Lobe, is located the Quetta Syntaxis. The Indian plate is moving northward 29 mm yr^{-1} with respect to the Eurasia plate (Altamimi *et al.*, 2007) as shown in figure 6.2; this velocity is about parallel to the N-S strike of the Kirthar Range and the Sulaiman Range. In figure 6.2 is highlighted as the trend of the mapped structures, proceeding to the east from the Kirthar Range, rotates to nearly NW-SE azimuth at the summit of the Quetta Syntaxis and arrives to be orthogonal to the India-Eurasia convergence direction before rotating back to N-S direction in the Sulaiman Lobe. Between the Kirthar Range and the Sulaiman Lobe, at the apex of the Quetta Syntaxis, there is the most seismically active area of the western Indian Plate margin.

6.2.2 Seismicity

A NW-SE oriented band approximately 25 km wide and stretching 100 km (from Pishin in the NW to near Harnai in the SE) contains the highest seismicity in the Quetta Syntaxis (Figure 6.3 and Table 6.1). On the contrary, the Katawaz Block is seismically quiet; at the south of the block, the town of Pishin marks the limit of the seismic zone of the Quetta Syntaxis; toward SE, the seismicity becomes more diffuse and the thrust faults mechanisms become dominant (Figure 6.4; Bernard *et*

al., 2000). In this seismic belt, during the past century, at least four earthquakes with magnitude $> M_w 6$ have occurred (Table 6.1): the Sharigh earthquake ($M_w = 6.8$), occurred in 1931 (Szeliga, 2010); the Harnai earthquake ($M_w = 7.1$) occurred in 1997 (Khan, 1998; Bernard *et al.*, 2000) and the two Ziarat events of 2008 ($M_w = 6.4$) (Szeliga, 2010) object of this study. Additionally, during the past century, numerous $M_w > 5$ earthquakes have occurred in this area (Figures 6.3 and 6.4). Engdahl and Villasenor (2002) hypothesize that the 1909 Kachhi earthquake, which magnitude was estimated about seven, occurred near to the 1997 Harnai earthquake.

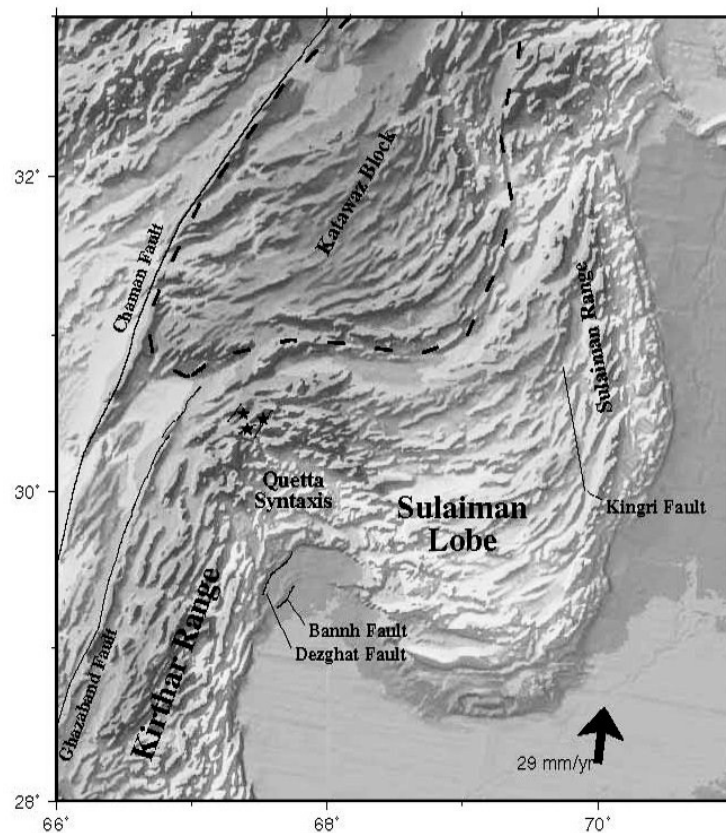


Figure 6.2: The Sulaiman Lobe, the Kirthar Range and the Katawaz Block of Pakistan with main faults of the area (Figure from Szeliga, 2010). In figure are reported the Bannh and Dezhgat faults that last ruptured during the Mach earthquake of the 1931. During the Qatta earthquake occurred in 1935, the Ghazaband Fault ruptured, while in 1892 and 1976 last ruptured the Chaman Fault. In figure is reported the Katawaz Block, as localized by Haq and Davis (1997). The two main shocks (October 2008) and the largest aftershock (December 2008) of the 2008 Pishin Earthquake sequence are indicated with stars. In the figure is also reported the left lateral Kingri fault (Rowlands, 1978) that is presumed to enable the southward extrusion of the Sulaiman Lobe. Black arrows indicates the plate velocity with respect to Eurasia (Altamimi *et al.*, 2007).

Number	Date	Epice nter	Epice nter Source	Magnitude	Magnitude Source
1	20 Oct. 1909	68.0E, 30.0N	ISC	7.2	ISC
2	24 Aug. 1931	67.7E, 30.2N	ISC	6.8	ISC
3	29 Sep. 1941	67.2E, 30.7N	ISC	5.4	ISC
4	16 Jun. 1976	67.2E, 30.7N	ISC	5.1	ISC
5	16 Nov. 1993	67.0891E, 30.8024N	Szeliga, 2010	5.6	Szeliga, 2010
6	27 Feb. 1997	67.9875E, 29.9932N	Szeliga, 2010	7.2	ISC
7	28 Oct. 2008	67.3825E, 30.5012N	Szeliga, 2010	6.4	Szeliga, 2010
8	29 Oct. 2008	67.5297E, 30.4659N	Szeliga, 2010	6.4	Szeliga, 2010
9	9 Dec. 2008	67.4416E, 30.4024N	Szeliga, 2010	5.7	Szeliga, 2010

Table 6.1: Historical earthquakes in the Quetta Syntaxis. During the October–December 2008 aftershock sequence other 5 earthquakes ($5.1 < M_w < 5.4$) occurred in the same area.

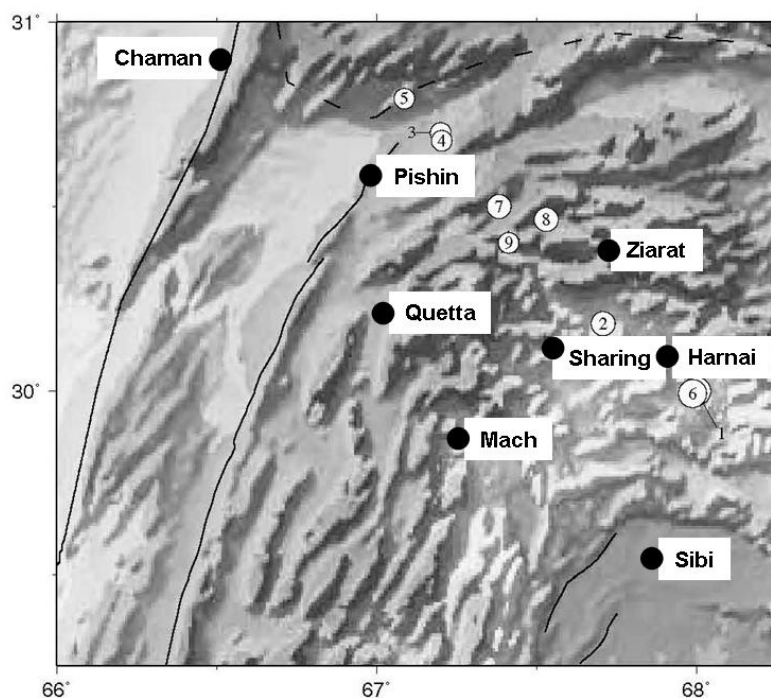


Figure 6.3: Map of Quetta Syntaxis. The epicenters of the earthquakes in table 6.1 (Historical earthquakes in the Quetta Seismic zone, 1900–2010) and the principal towns, are reported.

One of the main problems of the earthquake source determinations in the Quetta Syntaxis arises from the contrast existing between the expected (right lateral) sense of deformation, the tectonic structure trend at the surface, and the fault plane ambiguity determined by moment tensors. In the NW-SE seismic area north of Quetta, focal mechanisms show a prevalent N-S trending P-axes, in agreement with the Indian plate present day velocity with respect to Eurasia (figure 6.4, Altamimi *et al.*, 2007). Moving from NW to SE along this seismicity band, a progressive change in focal mechanism is present: in the NW a dominantly strike slip mechanism is present, whereas a normal thrusting in the SE is dominant; in this area the orientation of the main mapped faults becomes compatible with the activation of thrust faults (Bernard *et al.*, 2000).

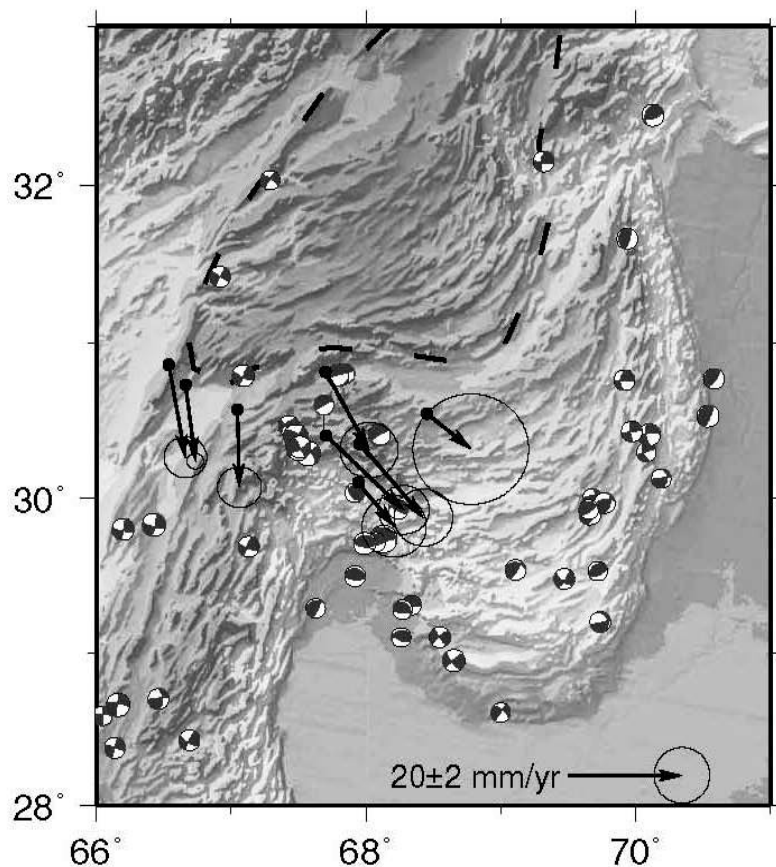


Figure 6.4: GPS velocity spatially averaged with respect to the stable Indian Plate (Szeliga, 2010): velocities are calculated as the weighted spatial average of all regional GPS velocities within a 30' grid and the location of each velocity average is calculated as the mean of the locations within each grid (Szeliga, 2010). In the map are also presented the CMT centroid moment tensors ($M_w > 5$ since 1976) (Dziewonski *et al.*, 1981). No seismicity is present within the Katawaz Block (place names are reported in figure 6.2)

6.2.3 The October 2008 Balochistan seismic sequence

An M_w 5.2 foreshock preceded by only thirty-six minutes the first of the two mainshocks of the October 2008 sequence, occurred at 23:10:2.0 GMT on 28 October 2008 at the Latitude of 30.40° and Longitude of 67.48° (Global CMT catalog). The catalog localizes the hypocenter at 17.2 Km depth and proposes two fault planes, as shown in table 6.2. The M_w 6.4 earthquake struck the region 40 km NE of Quetta and was followed by a similarly sized earthquake (Table 6.3) 11 hours later, 15 km SE of the first shock (Figure 6.5).


200810282309A PAKISTAN			
Date: 2008/10/28		Centroid Time: 23:10:2.0 GMT	
Latitude = 30.40°		Longitude = 67.48°	
Depth = 17.2 Km		Half duration = 3.9	
Centroid time minus hypocenter time: 4.3			
Moment Tensor: Expo = 25 0.896 - 5.010 4.110 0.424 1.380 - 1.590			
$M_w = 6.4$	$m_b = 6.3$	Scalar Moment = $5.08e+25$	$M_s = 6.6$
Fault plane: strike = 304 dip = 73 slip = 171			
Fault plane: strike = 37 dip = 81 slip = 18			

Table 6.2: The 28 October 2008 earthquake (Global CMT catalog).


200810291132A PAKISTAN			
Date: 2008/10/29		Centroid Time: 11:32:48.6 GMT	
Latitude = 30.29°		Longitude = 67.57°	
Depth = 12.0 Km		Half duration = 4.0	
Centroid time minus hypocenter time: 5.5			
Moment Tensor: Expo = 25 1.000 - 5.310 4.300 2.210 0.497 1.290			
$M_w = 6.4$	$m_b = 6.2$	Scalar Moment = $5.39e+25$	$M_s = 6.6$
Fault plane: strike = 324 dip = 68 slip = -178			
Fault plane: strike = 233 dip = 88 slip = -22			

Table 6.3: The 29 October 2008 earthquake (Global CMT catalog).

The October 2008 earthquakes show similar magnitudes and focal mechanisms; both earthquakes have strike slip solutions, along two NW-SE and NE-SW oriented fault planes. Whereas the 28 October 2008 earthquake occurred at 17.2 km of depth, the 29 October, 2008 was located at 12 kilometers (Global CMT catalog); hereinafter I will consider both earthquakes as “mainshocks”, talking about “first” and “second” mainshock, when I need to distinguish the two earthquakes. The aftershock sequence from these two earthquakes consisted of more than 50 earthquakes larger than Mw 4, with a total additional seismic moment equivalent to a Mw 6.0 and lasted until mid-December 2008 (Szeliga, 2010). In particular the aftershock sequence was characterized by three Mw > 5 aftershocks occurred on December 9, 2008: two within three hours (Mw 5.2 and 5.3), and a third after 17 hours (Mw 5.3). In table 6.4 the details of this aftershock are reported, while in figure 6.5 the entire seismic sequence is shown.


200812092252A PAKISTAN			
Date: 2008/12/09		Centroid Time: 22:52:39.3 GMT	
Latitude = 30.33°		Longitude = 67.51°	
Depth = 15.9 Km		Half duration = 1.7	
Centroid time minus hypocenter time: 1.7			
Moment Tensor: Expo = 24 -0.397 -3.030 3.430 -0.348 0.968 2.100			
Mw = 5.7	mb = 5.7	Scalar Moment = 3.98e+24	Ms = 5.7
Fault plane: strike=62 dip=75 slip=0			
Fault plane: strike=152 dip=90 slip=-165			

Table 6.4: The 09 December 2008 earthquake (Global CMT catalog).

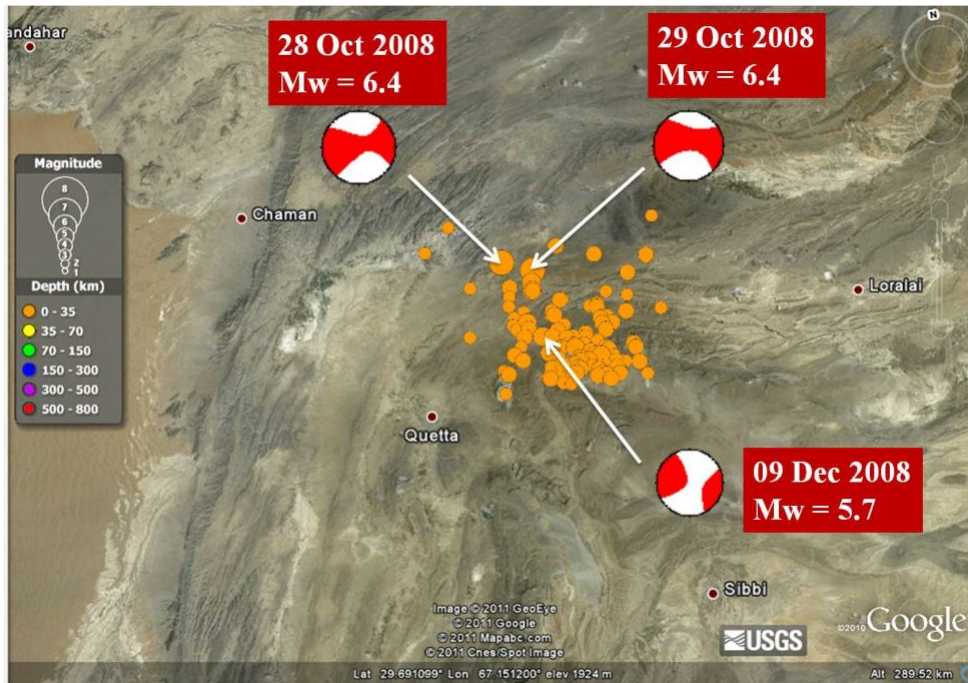


Figure 6.5: The October 2008 – January 2009 Balochistan seismic sequence; in the Google map are reported the epicenters (from USGS web-site catalog) and the focal mechanism of the two mainshocks and the Mw = 5.7 aftershock of the 09 Dec. 2008 (from Global CMT catalog).

In this work I tried to model the ground deformation due to the two mainshocks and the Mw = 5.7 aftershock occurred on 9 December 2008 using DInSAR. I tried to isolate the different contribution of the three earthquakes to the ground deformation, to better understand and resolve the ambiguity between different possible solutions. In the complex tectonic framework of the Quetta Syntaxis both NW-SE or NE-SW oriented fault plane solutions are compatible with the southward movement of the Sulaiman Lobe with respect to the Indian plate and the Katawaz block.

6.3 The DInSAR data

The SAR image dataset used to isolate the contribution of the different earthquakes is composed of images from the ENVISAT and ALOS satellites.

For ENVISAT, catalog images from three different tracks are available: 231, 363 and the wide swath 170. In table 6.5 I report the spatial baselines among the

different ENVISAT images relative to the track 231 (ascending pass), frame 597 (North) and 581 (South).

TRK 231	06/05/2008	19/08/2008	23/09/2008	02/12/2008	06/01/2009	10/02/2009	21/04/2009	26/05/2009	08/09/2009
06/05/2008		434	117	102	163	76	122	27	378
19/08/2008			545	533	272	498	557	461	60
23/09/2008				13	272	49	26	92	485
02/12/2008					260	44	35	79	476
06/01/2009						225	285	190	218
10/02/2009							68	55	442
21/04/2009								96	498
26/05/2009									404
08/09/2009									

Table 6.5: Spatial baselines (meters) among the ENVISAT images of track 231. Acquisition dates on the first column indicate the Master images, whereas on the first row are reported the slave images. Red lines highlight the two 2008 October mainshocks and the 2008 December aftershock.

Image pairs falling between the two vertical red lines isolate the contribution of the two mainshocks, whereas the pairs included between the horizontal red lines isolate the contribution of the 9 December aftershock. Pairs in the blue area of the table are affected by ground deformation due to the entire sequence. In the same manner in table 6.6 are reported the ENVISAT images of the track 363 (descending pass).

TRK 363	04/03/2006	17/06/2006	22/07/2006	04/11/2006	08/11/2008	13/12/2008	19/09/2009
04/03/2006		220	1098	531	80	159	457
17/06/2006			878	749	142	371	241
22/07/2006				1628	1022	1249	642
04/11/2006					606	379	989
08/11/2008						228	383
13/12/2008							612
19/09/2009							

Table 6.6: Spatial baselines (meters) among the ENVISAT images of track 363. Acquisition dates on the first column indicate the Master images, whereas on the first row are reported the slave images. Red lines highlight the two 2008 October mainshocks and the 2008 December aftershock.

Two images of the ENVISAT Wide Swath track 170 were used in this study, corresponding to the date 16 August 2008 and 3 January 2009, with perpendicular spatial baseline of 183 m.

TRK 170	01/03/2003	20/03/2004	16/08/2008	29/11/2008	03/01/2009
01/03/2003		613	129	363	141
20/03/2004			662	265	497
16/08/2008				429	168
29/11/2008					258
03/01/2009					

Table 6.7: Spatial baseline (meters) among the Wide-Swath ENVISAT images of track 170. Acquisition dates on the first column indicate the Master images, whereas on the first row are reported the slave images. Red lines highlight the two 2008 October mainshocks and the 2008 December aftershock.

Regarding the ALOS satellite, three dates (ascending geometry) are considered, as shown in table 6.8.

TRK 542	11/03/2008	12/12/2008	27/01/2009
11/03/2008		3251	3065
12/12/2008			203
27/01/2009			

Table 6.8: Spatial baseline (meters) among the ALOS images of track 542. Acquisition dates on the first column indicate the master images, whereas on the first row are reported the slave images. Red lines highlight the two 2008 October mainshocks and the 2008 December aftershock.

As shown in table 6.8, it was not possible discern the contributions of the three earthquakes with only ALOS interferograms.

To remove topography, I used the 90 m resolution Digital Elevation Model from the Shuttle Radar Topography Mission (SRTM). I produced the interferograms using the SARscape software package, running on the ENVI platform. Interferograms were sampled with 4 looks in range and 20 looks in azimuth to produce 80x80 m resolution cells for the ENVISAT images (track 231 and 363), 6 looks in range and 1 looks in azimuth to produce 80x80m resolution cells for the Wide Swath ENVISAT images (track 170) and 11 looks in range and 27 looks in azimuth to produce 80x80m resolution cells for the ALOS-PALSAR images (track 542). Then, I filtered the interferograms by using a power spectral method (Goldstein and Werner, 1998) and unwrapped then using a least squares methodology (MCF algorithm).

6.3.1 The ALOS interferograms

Using the images reported in table 6.7, I produced two ALOS-PALSAR interferograms relative to the track 542, frame 600. In order to cover the entire deformed area of the seismic sequence, I should have processed also the westward adjacent track, but because of the poor results in terms of coherence shown by first interferogram (Figure 6.6), I decided to stop the ALOS processing.

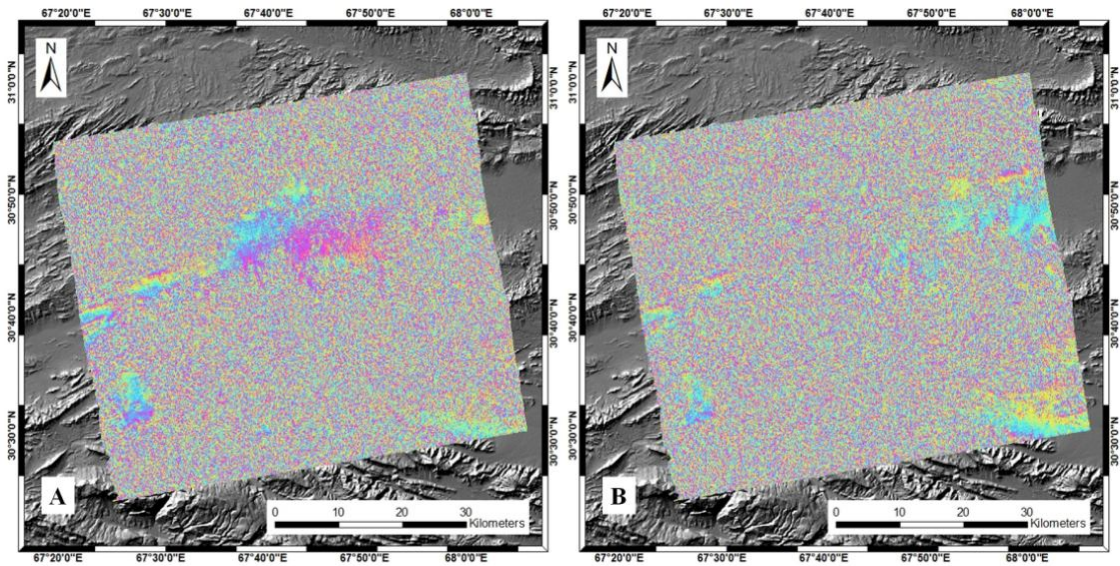


Figure 6.6: ALOS-PALSAR interferograms relative to the ascending pass (track 542, frame 600); A) 11032008-12122008 interferogram; B) 11032008-27012009 interferogram.

6.3.2 The ENVISAT wide-swath interferogram

As discussed in the previous paragraph, two ENVISAT wide-swath images relative to the ascending track 170 were used to study the October 2008 – January 2009 seismic sequence. In figure 6.7 I report the 16082008-03012009 interferogram focused on the seismic sequence area.

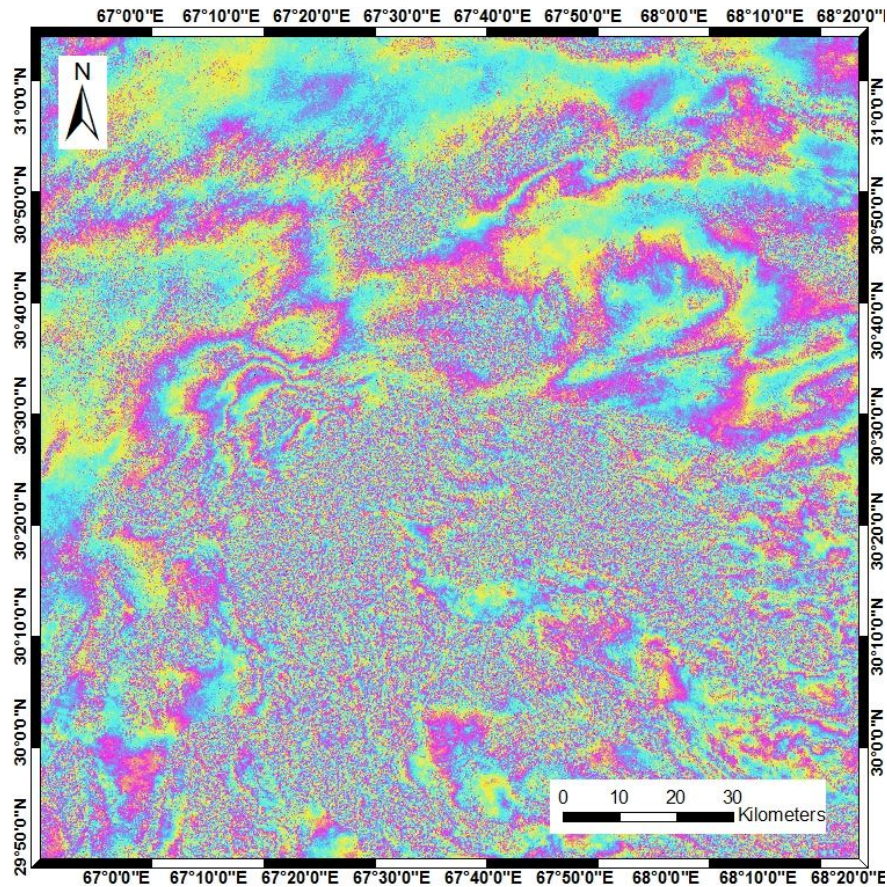


Figure 6.7: ENVISAT wide-swath interferogram relative to the ascending pass (track 170); the interferogram corresponds to the dates 16082008-03012009.

6.3.3 The ENVISAT image mode interferograms

Concerning the ENVISAT images I present here the results of two datasets as previously mentioned: the ascending track 213 and the descending track 363.

For the ascending pass many pairs with good spatial and temporal baselines were available (Table 6.5). During the processing of these pairs I realized that every pair involving the acquisition of the September 23, 2008, was affected by residuals strongly correlated to the topography and making the interferograms unsuitable for modeling. I therefore was forced to discard these interferograms despite their favorable temporal and spatial baselines. With the aim to isolate the ground deformation pattern of the three main events, I elaborated three interferograms. The first one (hereinafter “Interf1”), corresponds to the dates 02 December 2008 -

10 February 2009, and highlights the surface coseismic deformation of the 09 December 2008 aftershock (Figure 6.8).

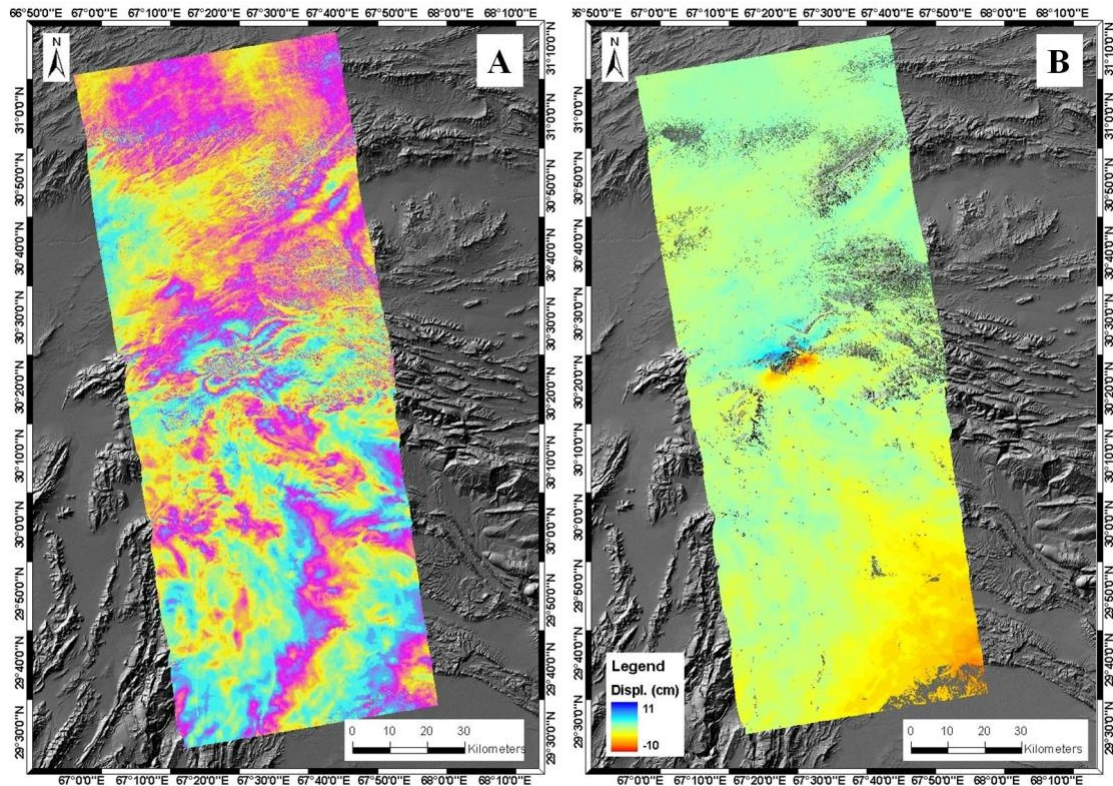


Figure 6.8: 02122008-10022009 ENVISAT interferogram (track 213, ascending pass). In A) I show the wrapped phase and in B) the unwrapped one.

Considering the small baseline of the pair 02122008-21042009, I generated also this interferogram (hereinafter “Interf3”), that also highlights the coseismic deformation of the 09 December 2008. It is well consistent with the 02122008-10022009 interferogram. Interf3 is shown in figure 6.9.

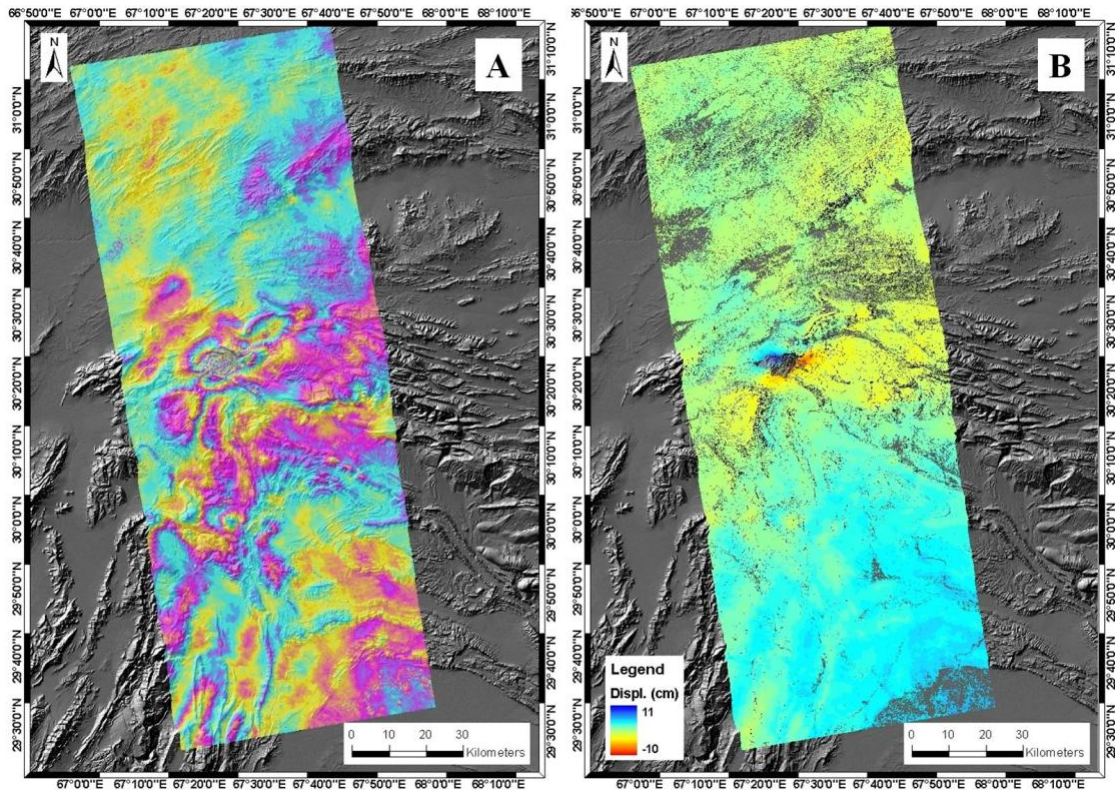


Figure 6.9: 02122008-21042009 ENVISAT interferogram (track 213, ascending pass) interferogram. In A) I show the wrapped phase and in B) the unwrapped one.

The two interferograms show the same displacement pattern, although both seem affected by orbital errors. In fact they show a displacement gradient in the azimuth direction: Interf1 shows a positive gradient from south to north, whereas Interf3 shows an opposite one. However, these gradients add only a very limited "noise" to the localized fringes of the coseismic deformation (Figure 6.9).

In order to discern the ground deformation due to the 28 and 29 October 2008 mainshocks I produced the interferogram using the images corresponding to the dates 06 May 2008 and 02 Dec. 2008 (hereinafter ‘Interf2’). In figure 6.10 I show the wrapped and the unwrapped phase. The unwrapped interferogram is characterized by positive values (in blue) from 30°20’ to 30°30’ of latitude north, in the eastern part of the interferogram, and by two areas of relative minimum values that border the positive area to the west and to the south. This complex displacement pattern is related to the presence of two overlapped displacement

fields. No pairs characterized by a temporal baseline able to isolate these earthquakes is available, thus I used this interferogram to model and study the sources of these events.

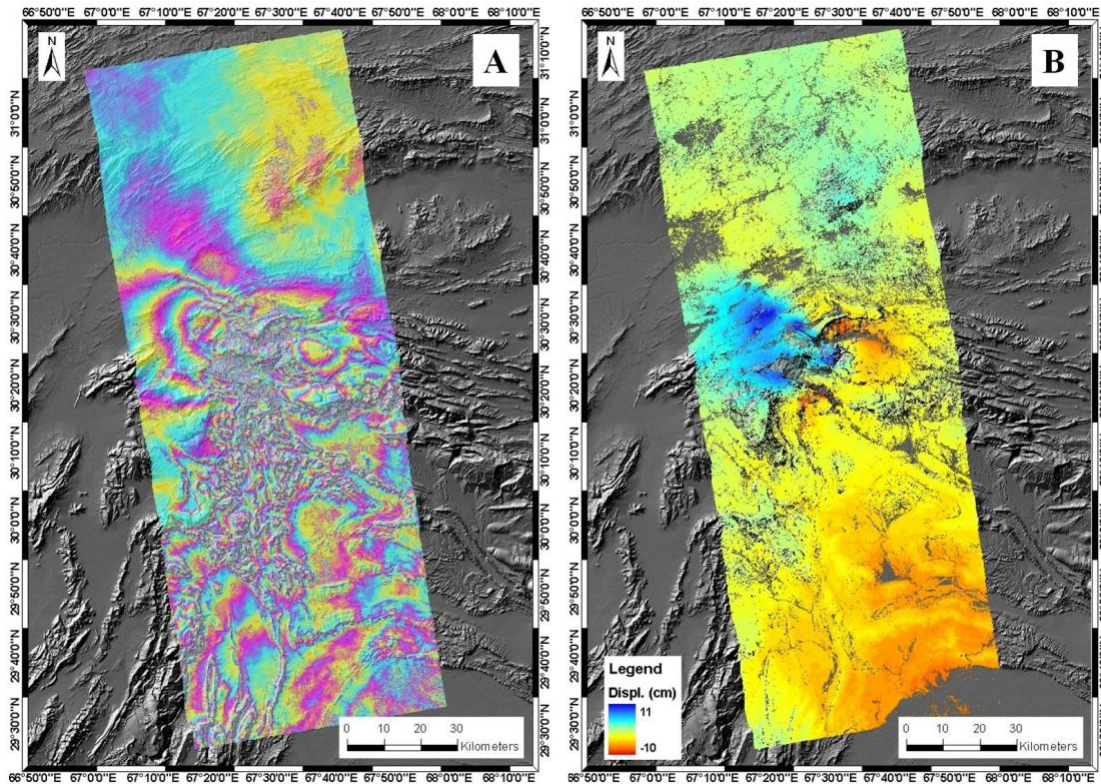


Figure 6.10: 06052008-02122008 ENVISAT track 213 (ascending pass) interferogram. In A) we show the wrapped phase and in B) the unwrapped one.

Thus I have two pairs relative to the 09 December aftershock and one pair for the two mainshocks. I can now elaborate a new interferogram covering a temporal span including the entire seismic sequence: in the next paragraph I will try to model the two mainshocks and the aftershock using Interf2 and Interf1/Interf3 respectively. I also processed an interferogram (19082008-08092009) covering the entire sequence, which could have been used to verify the inversion of the seismic sources carried out using Interf1-3.

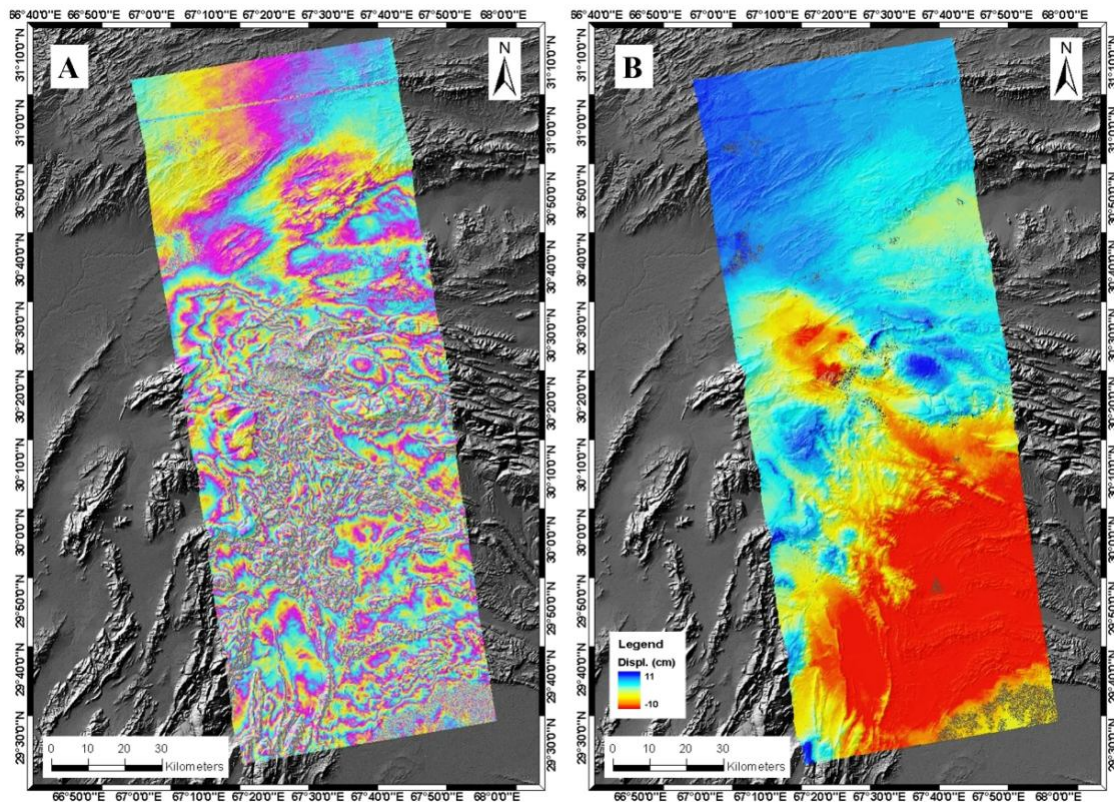


Figure 6.11: 190808-080909 ENVISAT track 213 (ascending pass) interferogram. In A) we show the wrapped phase and in B) the unwrapped one.

Unfortunately the 190808-080909 interferogram shows some problems of topographic residual signal, as visible in wrapped phase (Figure 6.11a), and this does not allow to unwrap the phase correctly (Figure 6.11b).

For the descending pass (track 363) I proceeded as for the ascending one: I first produced the interferograms covering a temporal span useful to isolate the different contribution of the mainshocks and the aftershock, and then I generated an interferogram covering the entire seismic sequence. In figure 6.12 I show the wrapped phases of the 04032006-08112008 and 17062006-08112008 pairs. In the first case (Figure 6.12a), despite the noise in the interferogram, some coseismic fringes are recognizable, but the unwrapping cannot be completed successfully because of the high number of unwrapping errors. The second interferogram (Figure 6.12b) is even noisier, and the coseismic signal is not detectable.

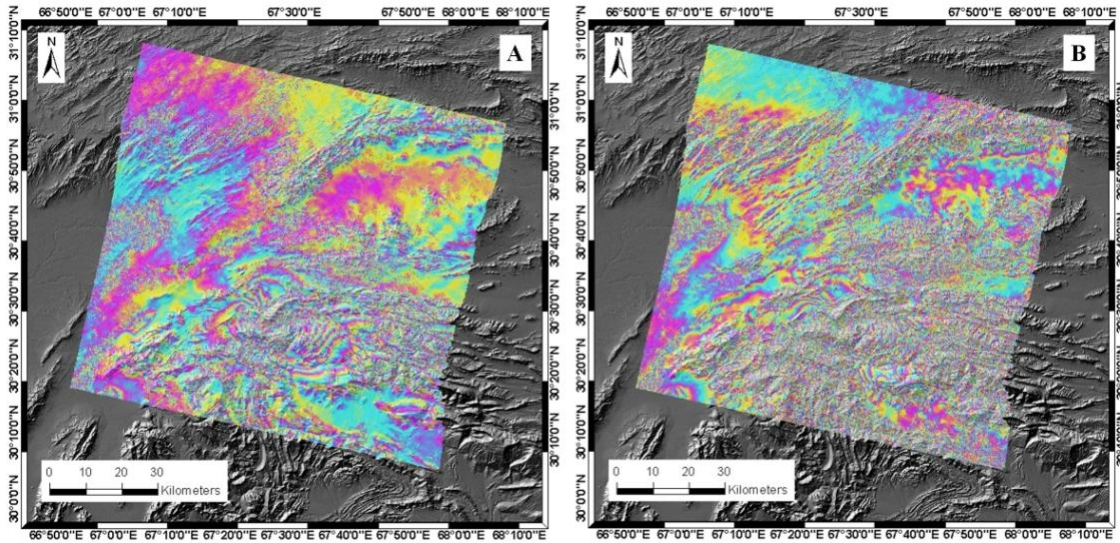


Figure 6.12: A) 04032006-08112008 and B) 17062006-08112008 ENVISAT track 363 (descending pass) interferograms.

In figure 6.13 A and B I show the ENVISAT track 363 interferograms relative to the pairs 08112008-13122008 and 04032006-13122008, respectively. In the first case the interferogram covers the time span of the two mainshocks, whereas the second one covers the entire October 2008 - January 2009 seismic sequence. Both interferograms are very noisy and only in the 04032006-13122008 pair coseismic fringes are identifiable.

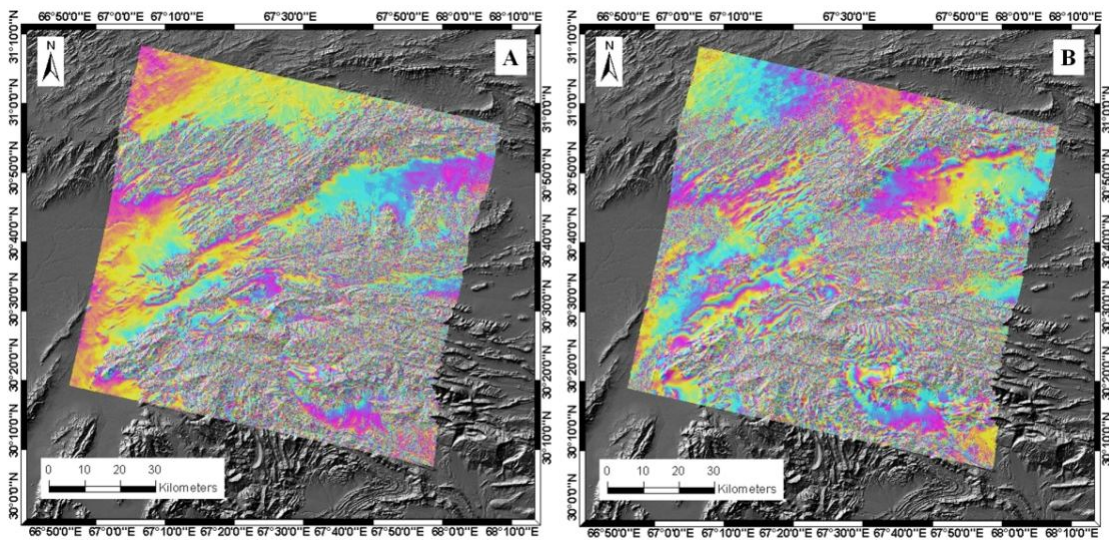


Figure 6.13: A) 08112008-13122008 and B) 04032006-13122008 ENVISAT track 363 (descending pass) interferograms.

I also produce the interferograms relative to the date 04112006-13122008 and 17062006-19092009, but the signal to noise ratio is very bad again.

6.4 Non Linear Inversions

I used a non linear inversion of the DInSAR data to define the three main seismic sources of the October 2008- January 2009 seismic sequence. In particular I wanted to determine the following parameters of the fault plane: position (Latitude and Longitude); Length; Width; Strike angle; Dip angle; Top depth; Rake angle and Slip. In order to obtain these parameters I used the inversion technique based on the Levenberg-Marquardt algorithm (Levenberg, 1944, Marquardt, 1963), based on the minimization of a cost function expressed as

$$CF = \frac{1}{N} \sum_i^N \frac{(d_{i,obs} - d_{i,mod})^2}{\sigma_i} \quad (6.1)$$

where $d_{i,obs}$ and $d_{i,mod}$ are the observed and modeled displacement of the i -th point, σ_i is the standard deviation for the N points. I simulated the ground displacements using the elastic dislocation formulations of Okada (1985), as shown in previous chapters.

I modeled two interferograms: Interf3 and Interf2; the first one to model the 09 December 2008 earthquake, and the second to model the 28 and 29 October 2008 mainshocks.

6.4.1 DInSAR data inversion for the 09/12/2008 earthquake

The coseismic dislocation pattern for this earthquake seems to be relatively simple. After some attempts of inverting for all the 9 fault parameters (Length, Width, Depth, Strike, Dip, East and North position, Rake, Slip), I introduced some constraints on strike angle, dip angle and rake angle based on the Global CMT solutions: first one (hereinafter CMT1) is characterized by NE-SW strike; $\sim 80^\circ$ of dip angle and right lateral kinematic; second one (hereinafter CMT2) shows left

lateral kinematic along a vertical NW-SE oriented fault plane. Thus, I performed many inversions changing the range of each parameter to define the best fitting solution (Table 6.9). In this case no ambiguity is found between two solutions from Global CMT; in figure 6.14 we show the coseismic modeled displacement field for the CMT1 solution. In fact the displacement field modeled using the CMT2 (Figure 6.15) and corresponding source parameters (Table 6.10) appears not reliable; moreover the RMS of residuals is higher (0.91 cm of CMT1 solution vs. 1.05 cm of CMT2 solution).

Fault Parameter	Best Fitting value
Length	16823 m
Width	4000 m
Depth	0 m
Strike angle	64°
Dip angle	79°
Longitude	349965 (UTM)
Latitude	3366413 (UTM)
Rake angle	7°
Slip	69 cm
RMS of residuals	0.91 cm

Table 6.9: Best fitting solution for the 09 Dec. 2008 Balochistan earthquake obtained by inversion of the 02122008-21042009 interferogram (ENVISAT, track 213, ascending pass). Strike angle, dip angle and slip are being fixed from one of the two solutions of the Global CMT (CMT1).

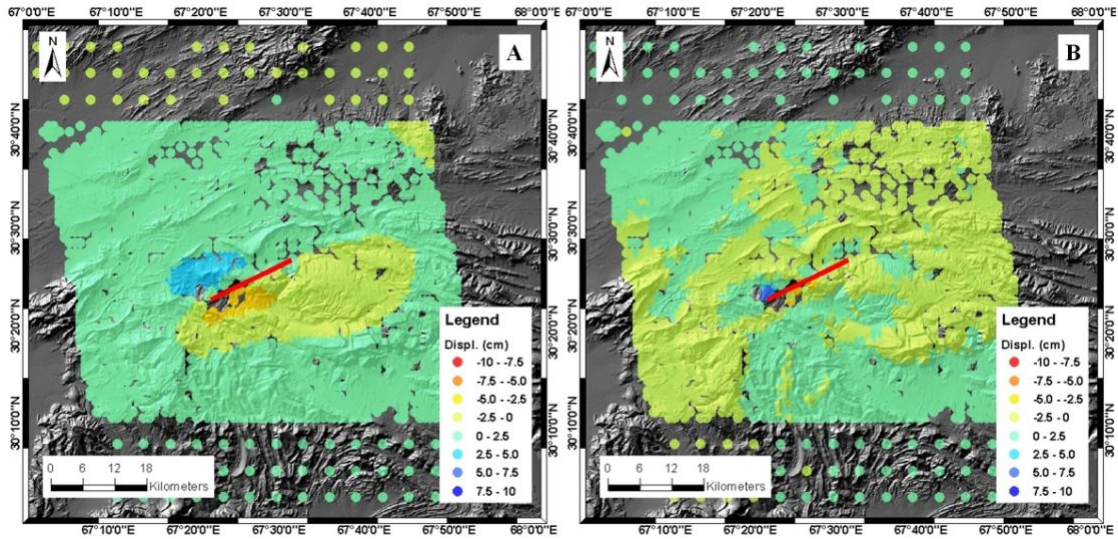


Figure 6.14: A) Coseismic displacement field modeled inverting the 02122008-21042009 interferogram (ENVISAT, track 213, ascending pass); strike angle, dip angle and slip are being fixed from one of the two solutions of the Global CMT (CMT 1). B) Residual displacements between the modeled displacement field and the observed one. The red line is the modeled fault trace.

Fault Parameter	Best Fitting value
Length	5000 m
Width	4000 m
Depth	0 m
Strike angle	152°
Dip angle	90°
Longitude	346093 (UTM)
Latitude	3364496 (UTM)
Rake angle	165°
Slip	101 cm
RMS of residuals	1.05 cm

Table 6.10: Best fitting solution for the 09 Dec. 2008 Balochistan earthquake obtained by inversion of the 02122008-21042009 interferogram (ENVISAT, track 213, ascending pass). Strike angle, dip angle and slip are being fixed from one of the two solutions of the Global CMT (CMT2).

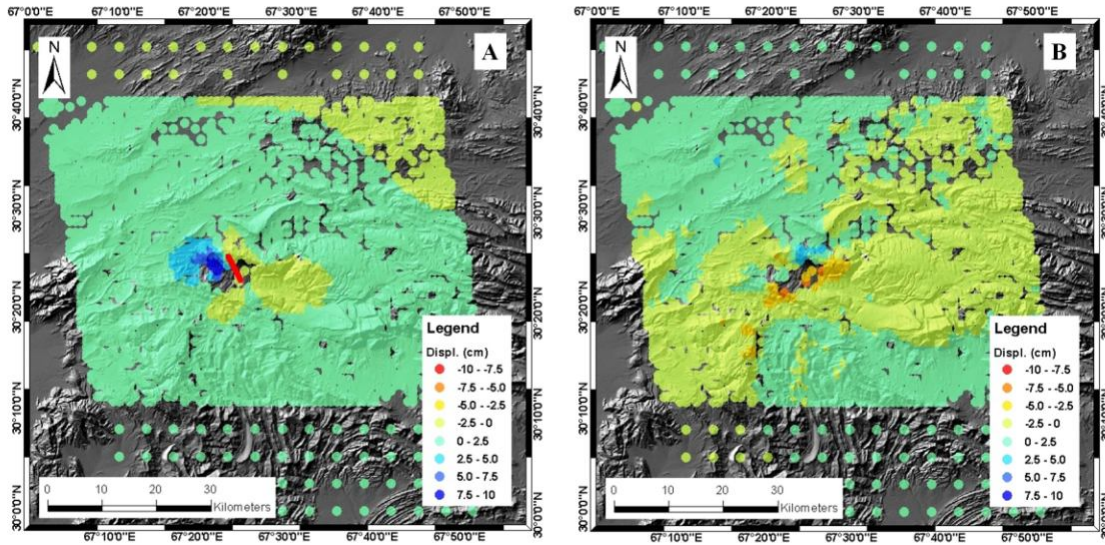


Figure 6.15: A) Coseismic displacement field modeled inverting the 02122008-21042009 interferogram (ENVISAT, track 213, ascending pass); strike angle, dip angle and slip are being fixed from one of the two solutions of the Global CMT (CMT2). B) Residual displacements between the modeled displacement field and the observed one. The red line is the modeled fault trace.

6.4.2 DInSAR data inversion of the 28 and 29/10/2008 earthquakes

Also for this earthquake I constrained the DInSAR inversions using the Global CMT nodal planes. There is no surface expression for these faults, and no surface faulting has been reported either; thus I tested two possible fault geometries. First I tried to invert the DInSAR data using the CMT fault planes which are NE-SW oriented (hereinafter called CMT1 solution); then I used the CMT fault planes NW-SE oriented (hereinafter called CMT2 solution). The fault parameters determined using the CMT1 solution are shown in Table 6.11 and the displacement field and the corresponding residual between modeled and observed data is shown in figure 6.16.

Fault Parameter	28 Oct. 2008 seismic source	29 Oct. 2008 seismic source
Length	25000 m	22477 m
Width	20000 m	14605 m
Depth	5000 m	0 m
Strike angle	37°	233°
Dip angle	81°	88°
Longitude	355767 (UTM)	357536 (UTM)
Latitude	3384045 (UTM)	3368740(UTM)
Rake angle	18°	-22°
Slip	48 cm	97 cm
RMS of residuals	1.85 cm	

Table 6.11: Best fitting solution for the 28 and 29 Oct. 2008 Balochistan earthquakes. Fault parameters are defined by inversion of the 06052008-02122008 interferograms (ENVISAT, track 213, ascending pass). Strike angle, dip angle and slip are fixed from the CMT1 solution.

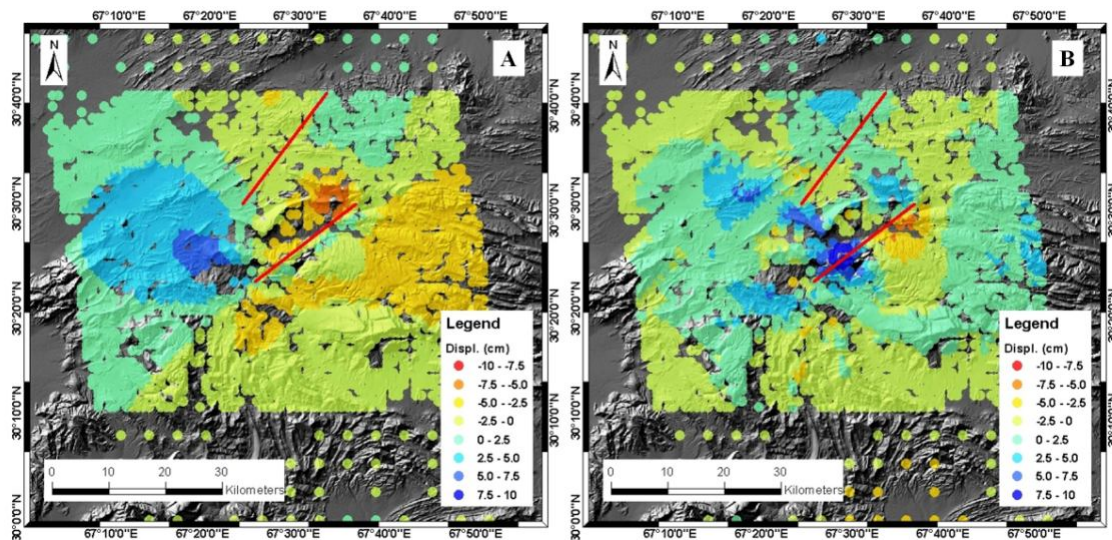


Figure 6.16: A) Coseismic displacement field modeled fitting the 06052008-02122008 interferogram (ENVISAT, track 213, ascending pass); B) Residual displacement between the modeled displacement field and the observed one. Strike angle, dip angle and slip are fixed from the CMT1 solution. The red lines are the modeled fault traces.

In Table 6.12 are reported the source parameters determined for the CMT2 solution, and in figure 6.17 the modeled displacement field, and the corresponding residual map.

Fault Parameter	28 Oct. 2008 seismic source	29 Oct. 2008 seismic source
Length	10464 m	22800 m
Width	15000 m	20000 m
Depth	5000 m	0 m
Strike angle	304°	324°
Dip angle	73°	68°
Longitude	350284 (UTM)	361988 (UTM)
Latitude	3379681 (UTM)	3367118 (UTM)
Rake angle	171°	-178°
Slip	122 cm	79 cm
RMS of residuals	1.73 cm	

Table 6.12: Best fitting solution for the 28 and 29 Oct. 2008 Balochistan earthquakes. Fault parameters are defined by inversion of the 06052008-02122008 interferograms (ENVISAT, track 213, ascending pass). Strike angle, dip angle and slip are fixed from the CMT2 solution.

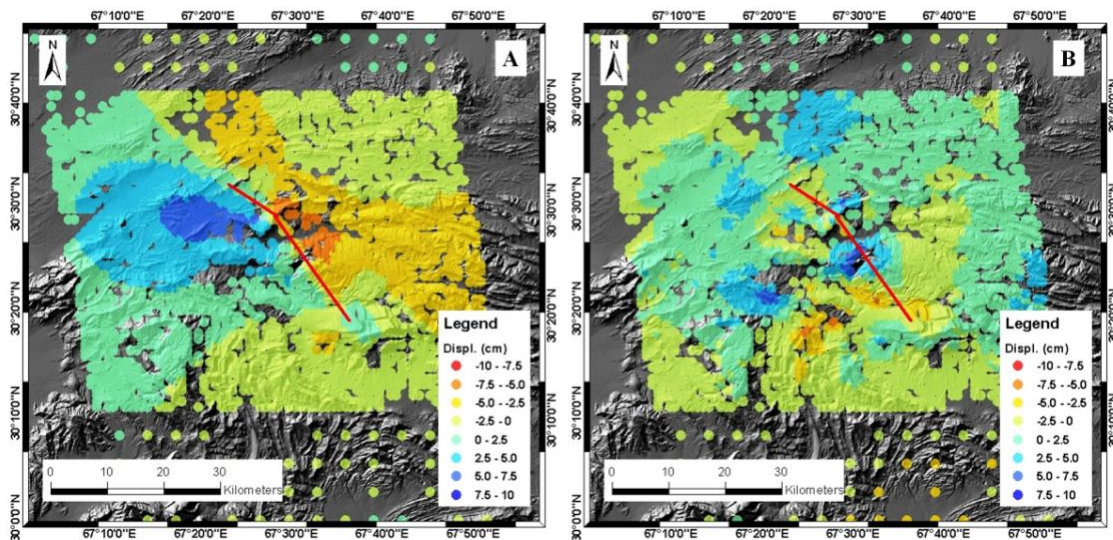


Figure 6.17: A) Coseismic displacement field modeled fitting the 06052008-02122008 interferogram (ENVISAT, track 213, ascending pass); B) Residual displacement between the modeled displacement field and the observed one. Strike angle, dip angle and slip are fixed from the CMT2 solution. The red lines are the modeled fault traces.

Comparing the modeled displacement fields and the RMS values for both models, it is clear that no substantial differences are present for the two solutions. Thus,

considering only the ground displacement observation, it is not possible to resolve this ambiguity.

Starting from the left lateral solution for the 9 December 2008 aftershock, I supposed that this earthquake sequence involved sinistral faulting along NE-SW trending faults; this interpretation is compatible with dextral shear in the Quetta Syntaxis accommodated along en-echelon NE-SW trending sinistral faults through “bookshelf faulting” as shown in Figure 6.18.

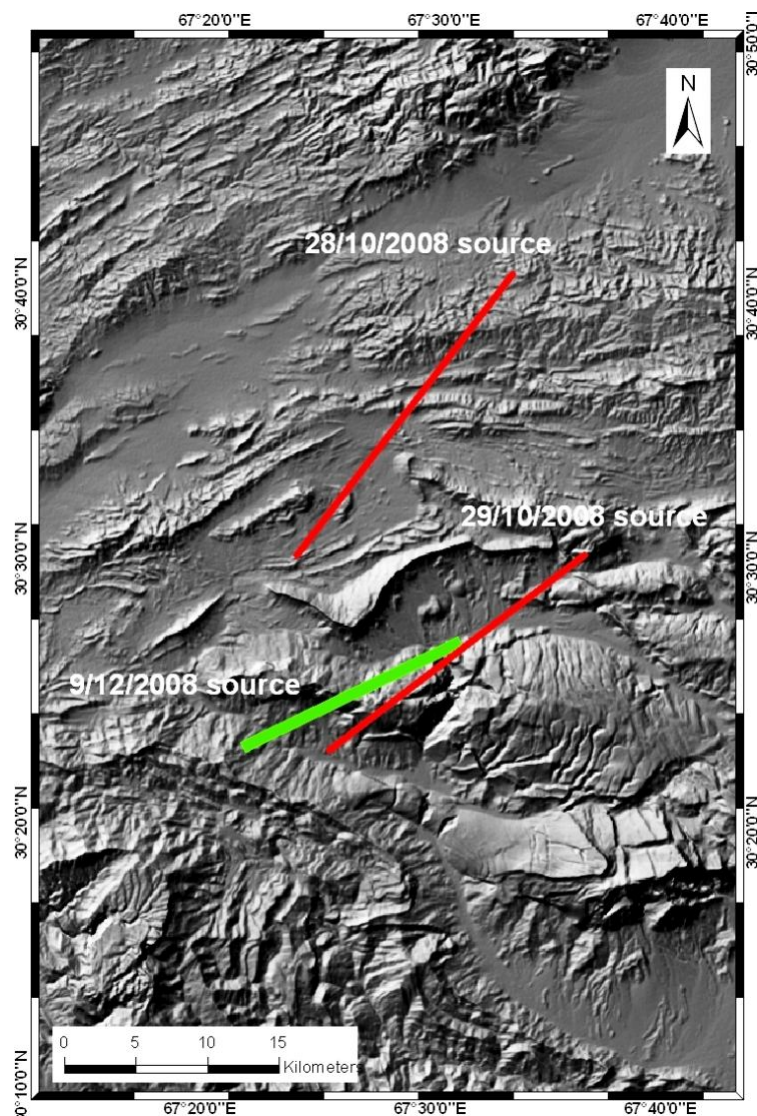


Figure 6.18: The modeled sources of the October 2008 and December 2008 earthquakes. Red lines show the fault traces of the 28 and 29 October 2008 mainshocks; the green line shows the fault trace of the 9 December 2008 aftershock.

6.5 Linear inversions

Using non linear inversions I determined the source slip distributions of the three principal seismic events of the October 2008 - January 2009 seismic sequence. I performed linear inversions of the DInSAR data with all source parameters (except the slip) fixed, according to the CMT1 solution determined in the previous section. The fault plane was subdivided in regular size patches of 2 x 2 km; the unknown quantity of our inversions is the slip of each patch. In this case too, I used the inversion technique based on the Levenberg-Marquardt algorithm (Levenberg, 1944, Marquardt, 1963), based on the minimization of a cost function (expression 6.1) and I simulated the ground displacements using the elastic dislocation formulations of Okada (1985), as shown in previous chapters.

Figure 6.19 shows the slip distributions along the fault planes of the 28 and 29 October 2008 earthquakes. Higher values of slip (blue color) are clustered in the deepest part of the faults and they decrease towards the fault tip and the surface, where they assume values near to zero (red color).

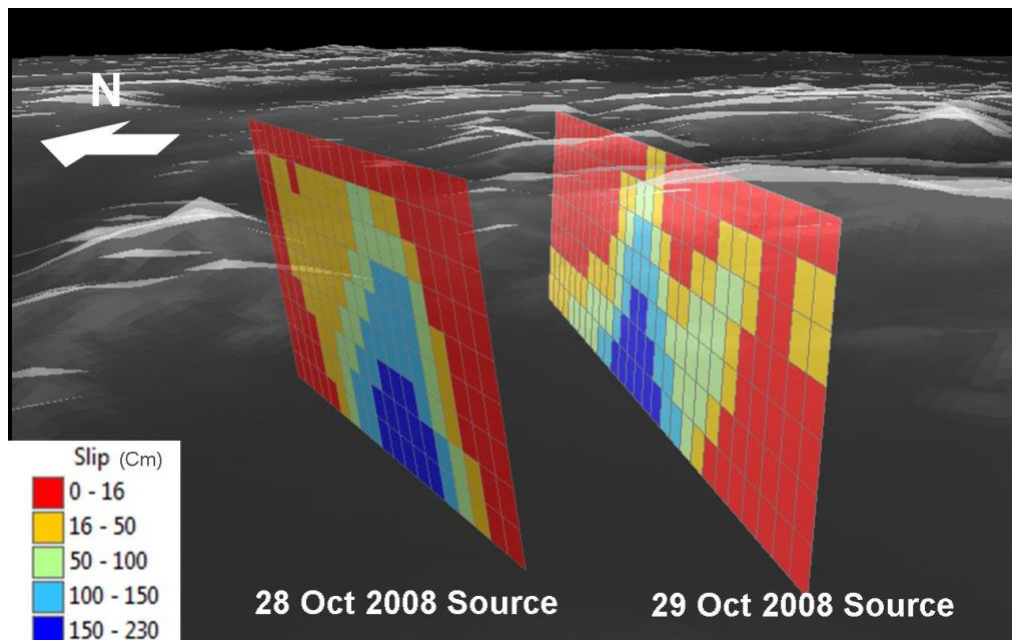


Figure 6.19: 3D view (from SW) of slip distributions along the fault planes of the 28 and 29 October 2008 earthquakes.

Similarly I performed a linear inversion to investigate the slip distribution on the 09 December 2008 earthquake. The result is shown in figure 6.20.

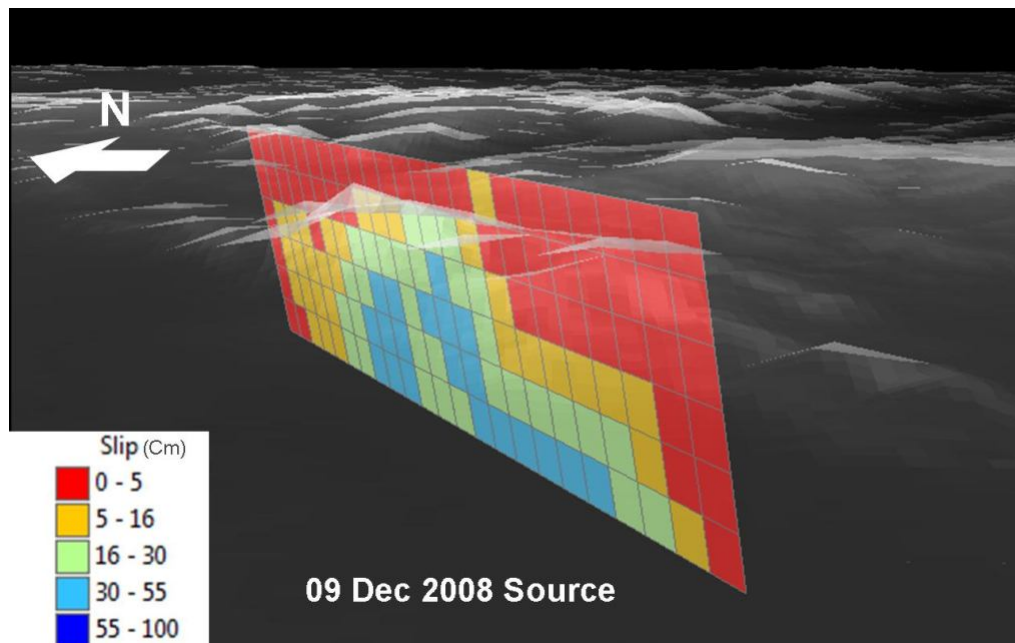


Figure 6.20: 3D view (from SW) of slip distributions along the fault planes of the 09 December 2008 earthquake.

In this case too, higher values (blue color) of slip are clustered in the deepest part of the fault; they decrease towards the fault tip and the surface where they assume values near to zero (red color).

6.6 Coulomb Failure Function

In order to study the seismic sequence evolution in terms of stress changes and possibly in terms of stress triggering, I applied the Coulomb Failure Function (CFF) technique to the principal seismic events of the sequence. When an earthquake occurs on a particular fault segment, it perturbs the stress state on adjacent faults and may favor or inhibit subsequent earthquake ruptures. Because these changes in the state of stress could affect the likelihood of future earthquakes, their determination is important for the assessment of earthquake hazard. If the time-dependent stress concentrations generated during the

propagation of the coseismic rupture are not significant, theoretically we can investigate the fault interaction by use of static analysis; on the contrary, the stress field produced by the propagation of the dynamic rupture controls the fault interaction belonging to the same segment and the coseismic rupture during an earthquake. Harris and Day (1993) infer that the time-dependent stress field, generated by the propagating rupture on the first segment, would not permit the rupture to jump to a secondary parallel non-collinear fault before it reaches the end of the first fault segment. As found by Cotton *et al.* (1995) and Cotton and Coutant (1996), they establish that the dynamic stress reaches its static value 10 to 15 seconds after the rupture arrest. The most important implication of this is that the dynamic interaction due to the time-dependent stress field occurs within a few tens of seconds; after this time the stress field assumes the static configuration. This means that we can use the static stress changes to study the interactions between fault segments that rupture during different seismic events, or the interaction between segments of the same fault whose ruptures are separated in time by more than several tens of seconds or minutes (Harris and Simpson, 1992; King *et al.*, 1994; Harris *et al.*, 1995).

The analysis of static stress changes due to co-seismic dislocations has been commonly applied to study the variations in Coulomb stress on well-known fault segments, such as those belonging to the San Andreas Fault system, and the response of local and regional seismicity (Das and Scholz, 1981; Reasenber and Simpson, 1992; Du and Aydin, 1993; King *et al.*, 1994). Many studies on the Southern California faults (Reasenber and Simpson, 1992; Harris and Simpson, 1992; Stein *et al.*, 1992; Simpson and Reasenber, 1994; Harris *et al.*, 1995) suggest that earthquakes induce changes in static stress on neighbouring faults that may delay, hasten, or trigger subsequent earthquakes.

In this study, I applied the numerical procedure proposed by Nostro *et al.* (1997) to evaluate the static stress changes due to co-seismic dislocations on strike slip faults based on the solutions obtained by Okada (1985). The Coulomb Failure Function, CFF (Harris and Simpson, 1992; Reasenber and Simpson, 1992; Stein *et al.*,

1992, 1994; Simpson and Reasenberg, 1994; King *et al.*, 1994; Harris *et al.*, 1995) is defined as:

$$\text{CFF} = |\tau| + \mu (\sigma_n + P) = |\tau| + \mu' \sigma_n \quad (6.2)$$

Which $|\tau|$ is the shear stress magnitude; σ_n is the normal stress (positive for extension), P is the pore fluid pressure:

$$P = -B \sigma_n \quad \text{with } B = \text{Skempton coefficient} \quad (6.3)$$

And μ' is the effective friction coefficient, defined by

$$\mu' = (1 - B) \mu \quad (6.4)$$

where B is used to take into account the modifications of the effective normal stress caused by pore fluid pressure. Variations of the CFF values are defined, following the Coulomb criterion for shear failure (e.g., Jaeger and Cook, 1979), as:

$$\Delta \text{CFF} = \Delta \tau + \mu' \Delta \sigma_n \quad (6.5)$$

Where $\Delta \tau$ and $\Delta \sigma_n$ are the changes in shear and normal stresses respectively; shear stress changes are calculated in the fault slip direction. Thus, strike and dip component variations of shear traction have to be considered to compute the shear stress changes. For an oblique-slip faulting mechanism, all three components of static traction changes contribute to the changes of the CFF.

In this study I used the source parameters defined by linear and non linear inversions (see previous sections) to compute the CFF along the fault planes. In particular I calculated the CFF on the 29 October 2008 earthquake fault plane induced by the previous 28 October 2008 seismic event (Figure 6.21). Then I

evaluated the CFF on the 9 December 2008 earthquake fault plane produced by both 28 and 29 October events (Figure 6.22).

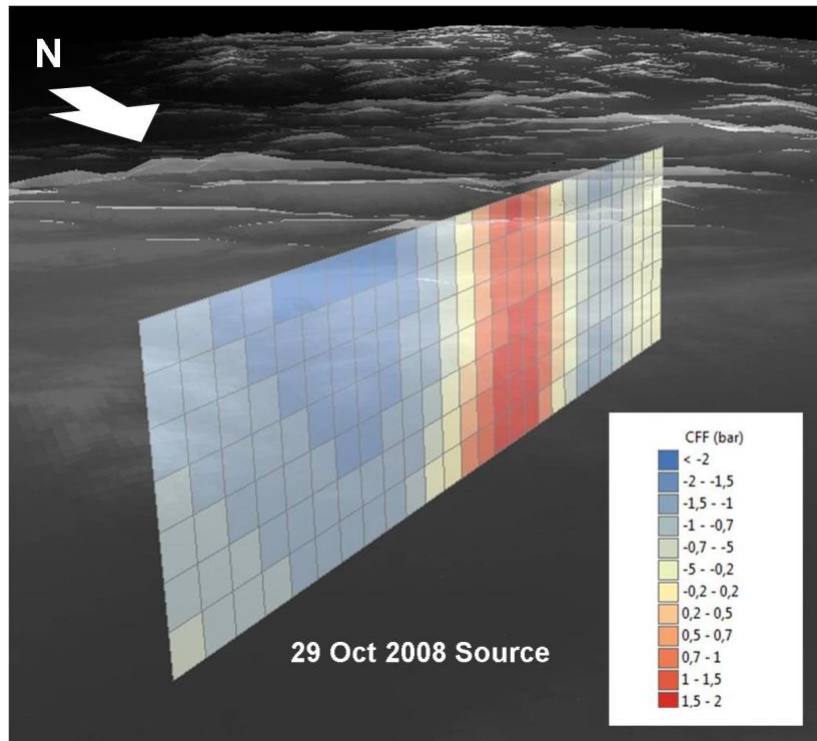


Figure 6.21: 3D view (from NE) of CFF (bar) on the 29 Oct. 2008 earthquake fault plane induced by the 28 Oct. 2008 earthquake. The CFF values are calculated for each patch on a 2x2 km grid. Red colors correspond to increase of stress, whereas blue colors correspond to decrease of CFF.

The CFF distribution on the 29 Oct. 2008 fault plane (Figure 6.21) highlights a zone of high values located at the centre of the fault. This zone is characterized by values up to 2 bar and is homogeneous from the fault bottom up to the surface. Away from the fault centre two negative areas are present, with values up to about -2 bar; near zero values are present near to the fault tips. The positive area roughly corresponds to the major slip area defined by the linear inversion.

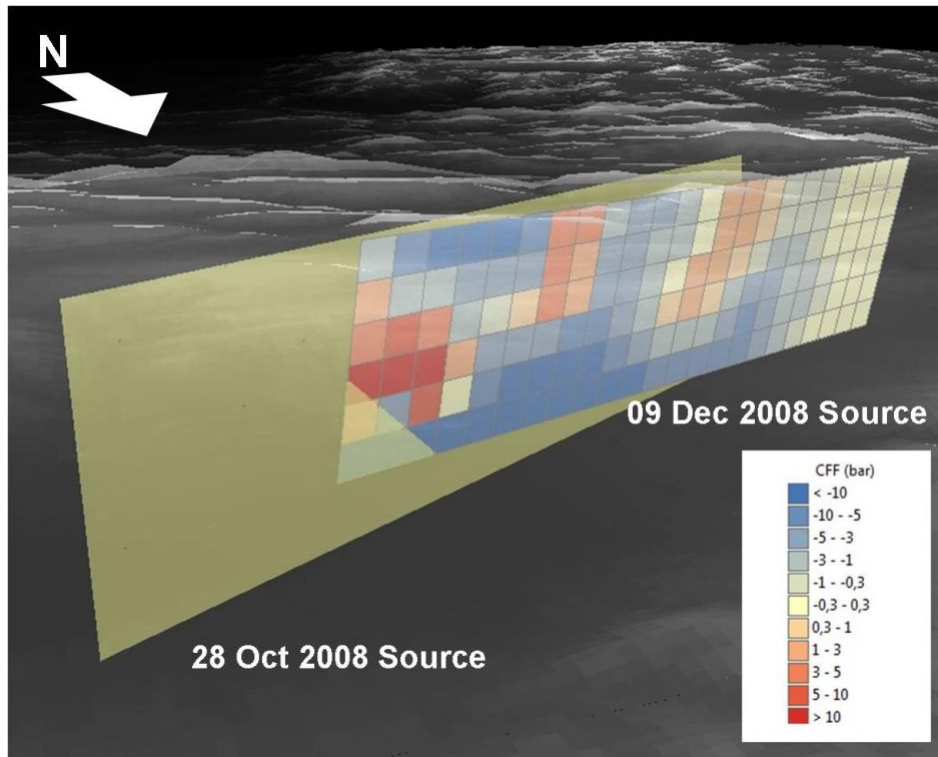


Figure 6.22: 3D view (from NE) of CFF (bar) on the 09 Dec. 2008 earthquake fault plane induced by the 28 and 29 Oct. 2008 earthquakes. The CFF values are calculated for each patch on a 2x2 km grid. Red colors correspond to increase of stress, whereas blue colors correspond to decrease of CFF.

The CFF distribution on the 09 December 2008 fault plane (Figure 6.22) shows a more complex situation with respect to the 29 October 2008 one, and the CFF values are more scattered. However, it is possible to discern three positive areas: two areas are located at 1/3 and 2/3 of the fault length and are characterized by values up to 5 bar, in the upper part of the fault plane. A third positive area is placed at the north-eastern fault tip, where the fault plane intersects the 28 Oct. 2008 earthquake fault plane; in this case the CFF reaches about 10 bar. Almost the entire lower part of the fault plane shows negative values up to about -10 bar. In this case no evident correlation pattern between the CFF and slip distribution is present except for the lower part of the fault plane where major slip values correspond to negative CFF values.

6.7 Discussion

The computed Coulomb Failure Function on the structures of impending events of the sequence shows well identified areas of increased CFF. Stress variations are of the order of about 10-20% of the seismic stress drop. For the 29 October 2008 source there is a rough correspondence between major slip areas and CFF positive values; whereas for the 09 December 2008 no evident correlation pattern between the CFF and slip distribution is present except for the lower part of the fault plane where major slip values correspond to negative CFF values. These results validate the hypothesis that a static elastic triggering could be invoked to explain the sequence evolution.

Concerning the study of the seismic cycle, aim of this thesis, I can formulate some general considerations, although a better analysis could result after the study of the interseismic deformation of this area. I can compare the use of the elastic dislocation model of Okada (1985) to invert the coseismic ground dislocation field, to the modelling of the interseismic velocity field. In this work we have seen how the lack of external geological or seismological constraints prevents the univocal determination of the seismic source. In fact, I defined two possible fault solutions for the two mainshocks of the Balochistan seismic sequence, using as constraints the two possible solution defined by the Global CMT catalogue. The ground displacement fields relative to the two solutions are very similar, as well as the RMS of the model residuals (1.73 cm vs. 1.85 cm). Thus, it is not possible to discern from the two solutions without further constraints derived from geological data, defining the fault position, strike angle or dip angle, or from a well localised aftershock distribution, constraining the strike and dip angles.

On the other hand, an almost total lack of constraints as for the Balochistan case, completely bans the use of numerical models, and the Okada-based inversion is still the best method to explore a variety of possible source solutions without entering a subjective judgment into the modeling process.

Concerning the interseismic phase of the earthquake cycle, I note that, without the 2008 seismic swarm, any study of the interseismic ground deformation in this area

would have probably concentrated on the Chaman Fault, the longest and most evident fault in this area. It would have been impossible to model any interseismic signal caused by the blind earthquake sources studied here, without the knowledge of their geometries. This highlights the importance of geological and morphotectonic information when interpreting the interseismic strain accumulation in a seismic area.

Now that the 2008 seismic sources are approximately known, I can try, in a future work using ERS and ENVISAT data, to investigate how they can explain the interseismic deformation.

Chapter 7

Analog model of earthquake-cycle in transcurrent tectonic domains

7.1 Analog modelling of tectonic process: an overview.

7.1.1 What is an analog model and why should we use it?

A model, and in particular an analog model, is a simplified scaled representation of nature. Physical parameters are chosen to mimic geometrical (i.e. lengths), kinematical (i.e. velocities) and dynamical (i.e. forces) natural conditions in order to reproduce a specific natural process, usually developing over long times and large lengths, adopting more convenient geometric and temporal scales.

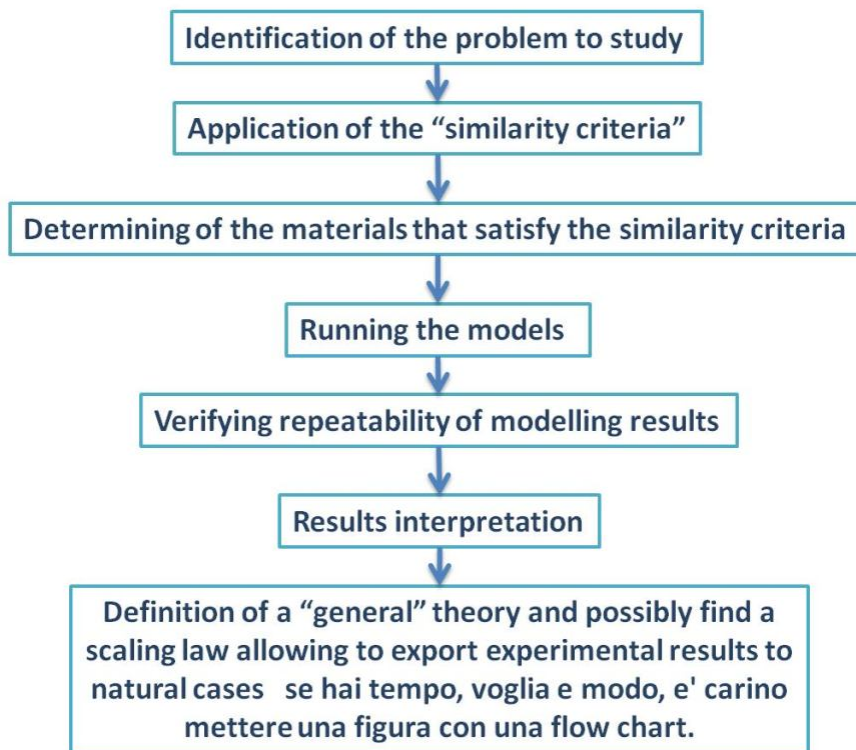
Realizing an analog model is possible to follow the evolution of the studied natural process (i.e. the physical response of the system to the applied experimental conditions) and to study complex three-dimensional processes for which governing equations are still poorly known or too complex to be numerically solved.

The use of experimental tectonics to study tectonic processes is long-lasting in Earth Science. After the pioneering work of Sir James Hall (1815), who studied folding under compressive tectonic regime; many scientists (e.g. Hubbert, 1937; Ramberg,

1967; Weijermars & Schmeling, 1986) introduced proper scaling relationships in order to transform the originally qualitative analog modelling approach into a solid method for studying a wide range of geodynamic processes.

7.1.2 Designing an analog model

To build a robust laboratory model is important to follow a precise procedure as shown in the following flow chart.



“Identification of the problem to study” means to identify a phenomenon and, in turn, the scale of the work. Up to now, experimental tectonics has examples both in large-scale geodynamic applications (i.e. subduction, evolution of thrust belts, formation of basins, pluton emplacement, mantle and crustal convection) and in smaller scale structural geology (i.e. faults, folds, diapirism, boudinage).

Multiscale phenomena like earthquakes are also modelled adopting specific assumptions and simplifications.

The second step “application of the similarity criteria” is the key-phase of model building. It is a fundamental requirement to scale the studied natural processes to the laboratory environment. In order to scale an analog model to a natural process, the model should be geometrically, kinematically, dynamically and rheologically similar to the natural prototype (Hubbert, 1937, Ramberg, 1981). The application of the similarity theory begins with the identification of the most relevant physical parameters active into the studied natural system. Each variable (length, velocity, force and material specific parameters) is thus normalized by means of a dimensionless number. Each set of dimensionless parameters defines a family of equivalent solutions, which only differs by a scale factor. If the governing equations are known, they can be nondimensionalized to make the key parameters appear explicitly in the equations. Otherwise it is used the Buckingham- π theorem (Buckingham, 1914; Boutelier and Cruden, 2008; Boutelier *et al.*, 2008) following which a model described by N-dimensional parameters of which M have independent physical dimensions, can be completely described by (N-M) combinations of the dimensional parameters.

Geometric parameters	$l_0 = l_m / l_n$	(length scale factor)	
Rheologic parameters	$E_0 = E_m / E_n$	(Young modulus scale factor)	
	$\rho_0 = \rho_m / \rho_n$	(density scale factor)	
	$\eta_0 = \eta_m / \eta_n$	(viscosity scale factor)	
Kinematic parameters	$t_0 = t_m / t_n = \eta_0 / \sigma_0$	(time scale factor)	
	$v_0 = v_m / v_n = \sigma_0 l_0 / \eta_0$	(velocity scale factor)	
	$g_0 = g_m / g_n$	(gravity scale factor)	
Dynamic parameters	$\sigma_0 = \sigma_m / \sigma_n$	(stress scale factor)	
	Ar	forces density contrast/total strength	<i>Argand number</i>
	$F = g l^2 \Delta \rho / \eta v$	(buoyancy force/viscous force)	<i>Buoyancy number</i>
	$Re = vl\rho / \eta = vl / \mu$	(inertial force/viscous force)	<i>Reynold number</i>
	$Ra = D^3 g \rho \alpha \Delta T / \kappa \eta = D^3 g \eta / \kappa$		<i>Rayleigh number</i>
	$Pr = \mu / k$	(viscous/thermal diffusivity)	<i>Prandtl number</i>
	$Pe = vl / \kappa$	(advection of heat/conduction of heat)	<i>Peclet number</i>
	$Nu = Hl / \kappa(T_2 - T_1)$	(heat transfer/heat transfer which would occur by conduction)	<i>Nusselt Number</i>
	$Ca = \rho v^2 / K$	(inertial force/elastic force)	<i>Cauchy number</i>

Table 7.1: List of the most common dimensionless parameters used in the similarity analysis for laboratory experiments. Robust scaling implies that characteristic dimensionless ratios are the same for the model (subscript m) and its prototype (subscript n). l is length, ρ is density, η is viscosity, μ is kinematic viscosity, g is gravity acceleration, t is time, v is velocity, σ is stress, E is Young's modulus, D is depth of convective mantle, $\Delta\rho$ is pressure difference, κ is thermal diffusivity, k the thermal conductivity, H is the heat transfer per unit area, T is the temperature, α is the thermal expansion coefficient and K is the bulk modulus of elasticity.

The application of similarity criteria allows to identify the proper analog materials to realize scaled models. Unfortunately, available materials to satisfy similarity criteria are limited. Moreover the selected material has to be inexpensive and manageable in sufficient quantities. Commonly, brittle behaviours are modeled by uniform size quartz sand (e.g. Hubbert, 1937; Horsfield, 1977; Naylor *et al.*, 1986; Vendeville *et al.*, 1987; Davy and Cobbold, 1988, 1991; McClay, 1990; Ratschbacher *et al.*, 1991;

Richard, 1991; Richard and Krantz, 1991; Richard *et al.*, 1991, 1995; Lallemand *et al.*, 1992; Nieuwland and Walters, 1993; Brun *et al.*, 1994; Faccenna *et al.*, 1996, 1999; Bonini *et al.*, 1997; Hatzfeld *et al.*, 1997; Keep and McClay, 1997; Basile and Brun, 1998) or artificial well classed microspheres (e.g. Rossi & Storti, 2003). These Coulomb materials are characterized by an internal frictional coefficient similar to nature ($\phi \sim 0.6$) and a negligible value of cohesion (e.g. McClay, 1990; Krantz, 1991; Faccenna *et al.*, 1996; Acocella *et al.*, 2000; Bonini *et al.*, 1997; Mart and Dautevil, 2000; Schellart, 2000; Rossi and Storti, 2003). To simulate ductile behaviours, characteristic of the lower crust, the lithosphere, magma and evaporitic/clay levels, many authors use silicone putties or plasticines. These are viscoelastic materials but the elastic component is usually suppressed in scaled geological models adopting experimental times always larger than the characteristic Maxwell time of the material. The asthenosphere and the mantle are often simulated using honey or syrups (glucose, corn, maple). These materials are classified as Newtonian low viscosity and high density fluids (e.g. Funicello *et al.*, 2003; 2006; Bellahsen *et al.*, 2005; Heuret *et al.*, 2007; Guillaume *et al.*, 2009; 2010; Schellart, 2000; 2004).

The next phase consists in running the models. As a rule of thumb, it is necessary to perform a sufficient number of runs to reasonably explore the parameter space of the analyzed problem. In order to isolate and understand possible cause-effect relationships between parameters, it is suggested to vary only a single parameter every run, keeping constant all the others constraints. The documentation of the history of the model is crucial to qualitatively and quantitatively describe the studied process. Photographs and/or video cameras permit to monitor and record the time-evolution of the model. Nowadays the quantitative description of the evolution of a laboratory model can also use more sophisticated tools to be added to the set-up to monitor specific quantities (i.e. high-precision laser scanning profiler, interferometer, high-frequency induction coil proximity probe: topography; Particle Image Velocimeter, Feature Tracking, Particle Tracking Velocity: flow field analysis; X-ray tomography: non destructive analysis of internal deformation; thermochromic liquid

crystal: temperature field; schlieren and shadowgraph: temperature and compositional field). To be sure to work with robust results, one must ensure that modelling outcomes are repeatable. Hence, it is important to run the same model several times under the same boundary condition.

Finally, at the end of this step it is possible to interpret the obtained results and to define a “general” theory able to interpret natural cases. It is fundamental to remind that scaled models should be only considered as an idealized and simplified physical guideline from which a theory (geometrical, kinematical or dynamical relationships) can be deduced for interpreting tectonic processes. A direct export of experimental results to interpret natural data is a wrong and dangerous procedure.

7.2 Laboratory model of transcurrent tectonic domain

In the previous section I have briefly seen what is an analog model, how it is possible to build up it and which are potentialities of experimentation. In this section, these foundations will be extended to approach the geodynamic problem central to this thesis: the study of earthquake-cycle in transcurrent tectonic domains. The goal is thus to build a laboratory model capable to properly reproduce the whole earthquake-cycle of a hypothetical generic strike slip fault. This requires building up an ad hoc apparatus and, in turn, a novel procedure able to scale down for earthquakes and interseismic deformations. Hence, these models offer the unique possibility to analyze and quantify both the coseismic and the interseismic deformations of a single strike slip fault area and to shed new lights on their mutual relationships which tune the seismogenetic behaviours of transcurrent faults.

Because of limited number of materials used in analog modelling, first works do not arrive to correctly reproduce the seismic cycle (e.g. Atmaoui *et al.*, 2006) because the unique reproducible deformation was the plastic one (e.g. sandbox models). In this study I used an analog material (Pig Skin 2.5% gelatine like characterized by Di Giuseppe *et al.*, 2009) characterized by viscoelastic rheology, a frictional interface

able to reproduce stick slip behaviours (Sandpaper like characterized by Corbi *et al.*, 2011) and an images processing able to monitoring very small deformation rate.

7.2.1 Properties of materials and scaling

In order to realize models of the transcurrent tectonic domain, the fundamental requirement is represented by the selection of viscoelastic analog materials able to reproduce the viscous deformation of the interseismic phase and the quasi-elastic behaviours of the coseismic phase. The choice of the analog material has been oriented toward gelatins, whose rheological and physical properties have been already extensively studied (Di Giuseppe *et al.*, 2009) and which have been already adopted to realize analog models of seismic sources (Corbi *et al.*, 2011).

Elastic solids follow Hooke's law which strain (γ) is always proportional to stress (σ) and the stress is independent of strain rate ($\dot{\gamma}$). Viscous liquid not store energy, but dissipate it and there exists a proportionality between the stress and the strain rate, linear (Newtonian) or nonlinear. Di Giuseppe *et al.* 2009 shows like gelatins in gel-state are characterized by an elastic response when high stress is quickly applied and a viscous response when low stress is applied for long time; in general, under a constant imposed strain, at the beginning the gelatins show elastic deformation, that is converted into permanent viscous deformation in time and the corresponding stress decay. Materials which the strain is depending of the time are called viscoelastic (e.g. Ferry, 1980).

Di Giuseppe *et al.* 2009 characterized different gelatins in terms of the storage (G') and loss moduli (G'') (Ferry, 1980); these parameters are determinate as a functions of strain, strain rate, temperature and time providing a full characterization of the materials behavior. If $G' \gg G''$, the material is described by Hook's law and the elastic shear modulus, G_0 is given by (Bagdassarov and Dorfman, 1998)

$$G_0 = \lim_{\omega \rightarrow \infty} G'(\omega) \quad (7.1)$$

Where ω is the experimental frequency (strain rate) in the oscillatory test performed using a rheometer. If $G' \ll G''$, the material shows viscous behavior and the complex viscosity (η^*) is defined by (Nowick and Berry, 1972; Barnes *et al.*, 1989)

$$\eta^*(\omega) = (G' + iG'') / i\omega \quad (7.2)$$

And the dynamic viscosity is given by (Marin, 1998):

$$\eta_0 = \lim_{\omega \rightarrow 0} \eta^*(\omega) = \lim_{\omega \rightarrow 0} G'' / \omega \quad (7.3)$$

If $G' \approx G''$ the material shows viscoelastic behavior. The ration between the elastic and viscous behavior is called “loss factor”. “damping factor” or “internal friction”:

$$G''/G' = \tan \delta \quad (7.4)$$

δ is called “loss angle” and is used as criterion in determining gel formation (Mezger, 2002). The gel state is characterized by $\delta < 45^\circ$ ($G' > G''$).

The viscoelastic gelatines are thus used as analog of the upper crust, where the strike slip faults usually cluster. In particular, it has been adopted the gelatin s.s., also known as "Pig Skin". Pig skin is an animal biopolymer available in tasteless and odourless powder form. Pig skin diluted in water at the concentration of 2.5 % and used at the gel state under the constant temperature of 10°C responds to the $G' \approx G''$ (viscoelastic interval) and $G' > G''$ (gel-state) and have been proven to downscale for length, density, stress and viscosity upper crustal rock in the natural gravity field (Di Giuseppe *et al.* 2009). These kind of material shows density of $\sim 1 \text{ g/cm}^3$, a viscosity of about $4.7 \cdot 10^5 \text{ Pa s}$ and a shear modulus of $10^3 - 10^4 \text{ Pa}$ depending on the gelatins ageing.

The use of the Pig Skin 2.5 wt offers several advantages. First of all, it is a reasonably cheap material, manageable in sufficient quantities. Second, as all the gelatins, Pig Skin 2.5 wt is viscoelastic allowing to properly to simulate the rheological behaviour of the natural prototype, including its strain time dependency. Third, Pig Skin 2.5 wt is transparent allowing to detect internal deformations occurring during the evolution of the model, eventually thanks to the inclusion of passive tracers and the adoption of image analysis techniques.

Thus, I used gelatin Pig Skin 2.5%_{wt} to model the upper crust. I assumed, for the upper crust, a thickness $h=15$ km, density $\rho = 2700$ Kg m⁻³ and viscosity $\eta = 10^{20}$ Pa s. The model has been designed using a model/nature length scaling factor of $L^* = 3.33 \cdot 10^{-6}$ (i.e. 1 cm in model corresponds to 5 Km in the nature) (Table 7.2). This scaling factor has been derived by assuming that viscous stress in the analog material scales with lithostatic pressure (see eq. 7 in Di Giuseppe *et al.*, 2009). In natural gravity field ($g_n = g_m$), the stress scaling factor is given by

$$\sigma^* = \rho^* \cdot L^* \quad (7.5)$$

Where ρ^* is model / nature density scaling factor. Since pig skin 2.5%wt gelatin density is about 1000 kg m⁻³ and the average upper crustal density is 2700 kg m⁻³, I have $\sigma^* = 1.23 \cdot 10^{-6}$ (1 Pa in the model corresponds to 1.23 MPa in nature).

The stress scaling factor is about $1.23 \cdot 10^{-6}$ with experimental shear modulus ranging between $10^2 - 10^4$ Pa and depending on material ageing, and the natural prototype of ($10^8 - 10^{10}$ Pa). The experiments are therefore appropriate to model the elastic component of the lithosphere.

Time has been scaled with the relation where t^* is nature/model time scale factor:

$$t^* = t_m/t_n = (\sigma_m/\sigma_n) / (\eta_n/\eta_m) = [(\rho gh)_m / (\rho gh)_n] / (\eta_n / \eta_m) \quad (7.6)$$

t^* is $3.81 \cdot 10^{-9}$ (one minute in the model is about 370 yr in nature), considering a viscosity of $4.7 \cdot 10^5$ Pa s. The resulting velocity scaling factor, V^* (derived as the length scaling factor L^* divided by the time scaling factor t^*), is $8.76 \cdot 10^2$ so that the experimental loading rate (0.26 cm/min) scale to approximately $1.5 \cdot 10^2$ cm/yr in nature. This value appears too high respect to the real plate velocity in nature. Thus, I need in future experimental setting to reduce the imposed velocity of two orders of magnitude.

My subject of study is characterized by a big variability of strain rate, thus it has not been possible to use a unique timescale for both coseismic and interseismic phase. I uses a double timescale like proposed by Rosenau *et al.* (2009). The gelatin is characterized by a Maxwell time of ~ 45 s. The material thus responds as a viscoelastic solid during the interseismic phase, and it is mainly elastic during the few seconds characterizing the slip phase. The rheological properties of gelatin are a fundamental factor to obtain a comprehensive model throughout the entire earthquake cycle including the interseismic viscoelastic deformation [e.g. Rice, 1993; Lapusta, et al. 2000]. Thus the coseismic time scale factor is (Hubbert, 1937; Rosenau, 2009):

$$t^* = \sqrt{L^*} \quad (7.7)$$

Thus $t^* = 1.8 \cdot 10^{-3}$ (one second in the model is about 9 minutes in nature). The resulting velocity scaling factor, V^* (derived as the length scaling factor L^* divided by the time scaling factor t^*), is $1.8 \cdot 10^{-3}$: it means that 1 m s^{-1} in laboratory corresponds to approximately 600 m s^{-1} in nature.

Model parameters	Unit	Quantity	Model	Nature (SI)	Nature (handy units)		Scaling factor (M/N)
gravitational acceleration	$m \cdot s^{-2}$	g	9.80	9.80			1.00
length	m	depth	$7.50 \cdot 10^{-2}$	$2.25 \cdot 10^4$	22.5	km	$3.33 \cdot 10^{-6}$
time (coseismic)	s	rupture duration	6	$3.29 \cdot 10^3$	54.8	min	$1.83 \cdot 10^{-3}$
time (interseismic)	s	mean recurrence interval	45	$1.18 \cdot 10^{10}$	374.56	yr	$3.81 \cdot 10^{-9}$
velocity (coseismic)	$m \cdot s^{-1}$	mean rupture velocity	$4.17 \cdot 10^{-5}$	$2.28 \cdot 10^{-2}$			$1.83 \cdot 10^{-3}$
velocity (interseismic)	$m \cdot s^{-1}$	plate velocity	$4.33 \cdot 10^{-5}$	$4.95 \cdot 10^{-8}$	$1.56 \cdot 10^2$	$cm \cdot yr^{-1}$	$8.76 \cdot 10^2$
stress	Pa	stress	$1 \cdot 10^7$	$8 \cdot 10^7$	81	Mpa	$1.23 \cdot 10^0$
Material parameters							
density	$kg \cdot m^{-3}$		$1.00 \cdot 10^3$	$2.70 \cdot 10^3$			$3.70 \cdot 10^{-1}$
viscosity	Pa s		$4.70 \cdot 10^5$	$1.00 \cdot 10^{20}$			$4.70 \cdot 10^{-15}$

Table 7.2: Resuming scaling table of the model and material parameters. The table shows the model quantities, nature quantities and the scaling factors.

To model the strike slip fault zone, it was necessary to reproduce a depth seismic profile wherein seismogenic and aseismic zones have been properly distinguished. In this work, the seismogenic and the aseismic portion of the transcurrent fault have been simulated using sandpaper and Plexiglas, respectively. Corbi *et al.* (2011) investigated the frictional properties of the gelatin-sandpaper interface by using a linear spring block-like device. In particular, they explored the static friction coefficient, μ_s , and the friction rate parameter, $a-b$, of the gelatins-sandpaper interface as function of the sliding velocity, normal pressure and roughness of the contact surface (expressed in terms of amplitude and wavelength). Nine sandpapers have been tested with different grit sizes. The models presented in this thesis have been performed using the P220 sandpaper characterized by Roughness mean height (RMH) of 0.068 mm, $\lambda = 0.202$ mm, $a-b = 0.025$ (Corbi *et al.*, 2011). To simulate the

aseismic sliding condition, Plexiglas is used since the frictional behaviour of gelatin-Plexiglas interface shows stable sliding.

7.2.2 Strike-Slip-Fault-Box

A new box has been designed to respond to specific requirements:

1. Box materials and shape: the selected analog material is the Pig Skin 2.5% wt. This material shows photoelastic behaviour useful to determine the stress field in model. This property will be not explored in this preliminary work. However, it will be a must for future applications which, in turn, will require detecting the whole volume of the system. Furthermore, sandpaper has been used to simulate the fault plane. How can sandpaper be included into the gelatin model?
2. Box dimension: it was necessary to choose "workable" lengths of the experimental system, compromise between the necessity to minimize unavoidable border effects and the requirement to have a handy apparatus able to be easily moved even by a single operator. The latter point is due to the fact that the box with the gelatins must be put into the fridge in order to finalize the gelatin preparation (see "gelatins cooking" in Di Giuseppe *et al.*, 2009).
3. Deformation velocity control: usual deformation velocities for laboratory models range between some millimetres to some centimetres a minute (e.g. Corbi *et al.*, 2011), thus, I needed a device able to move into this velocity interval.
4. Experimental monitoring: it was necessary to supervise the whole model surface deformation during both interseismic and coseismic experimental phases. These phases have very different time-length.

To supply at all these requirements I chose the following technical solution during the box building (Figure 7.1):

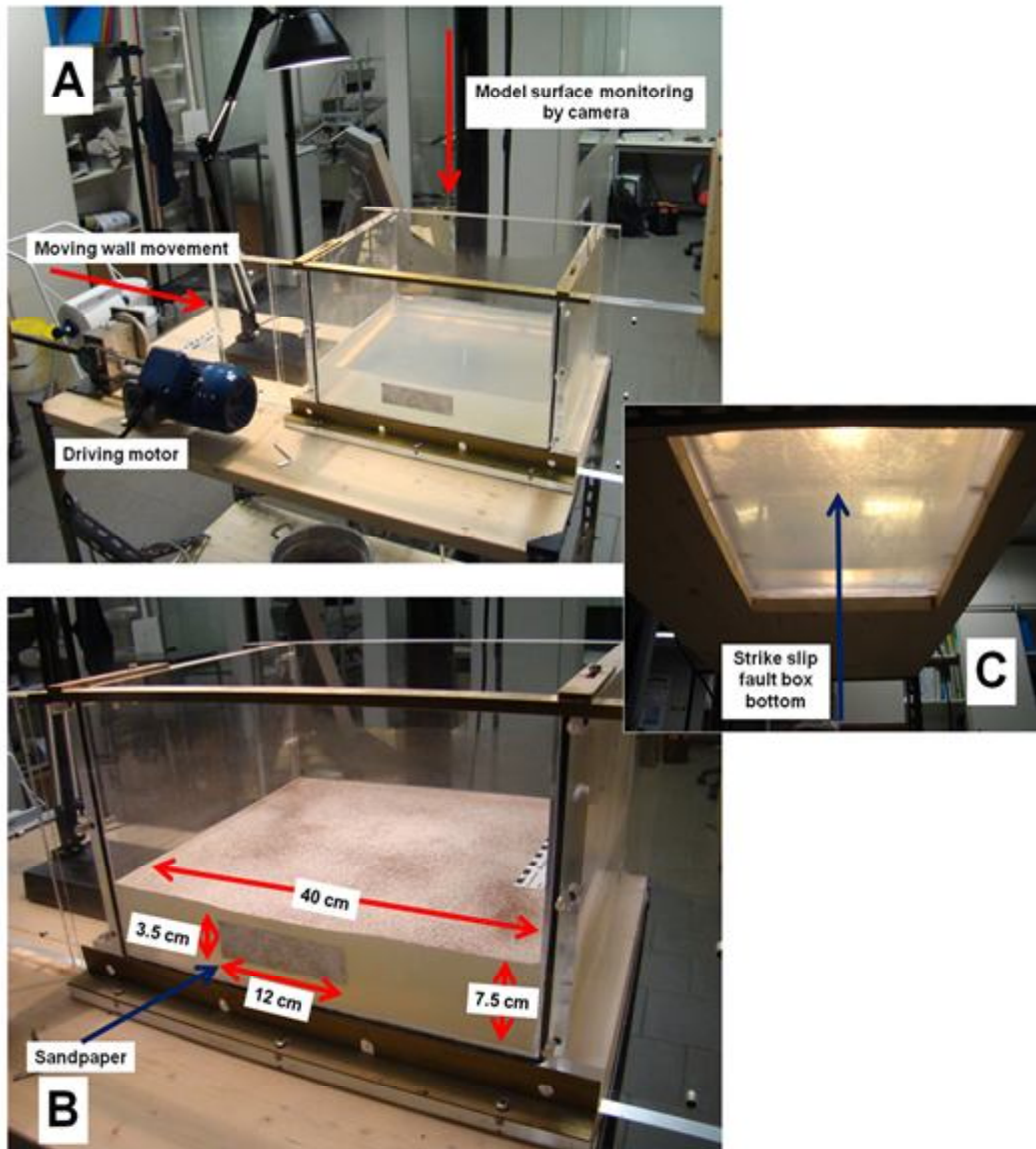


Figure 71: Strike slip fault box. A: overall view of the instrumentation; driving motor push the moving wall like shown by the red arrow. I monitor the surface model by a camera located over the box. B: the core of the strike slip fault box; blue arrow shows the sandpaper location on the moving wall. C: Bottom view of the box; the box is put on a table that allow us to light the gelatins from bottom to up through the bottom of the box.

1. **Box materials and shape:** I have built the entire box in transparent rigid Plexiglas that can be crossed by polarized light. The box was put on a table that allows us to light the gelatins from bottom to up through the bottom of the box (Figure 1c). Concerning the box shape, I put the sandpaper along a moving screen of the box that deforms the gelatins. In practice, I have a transparent box with a wall free to move longer than others. The motor push one end the moving wall with sandpaper in the same direction of the screen orientation (Figure 1a and b). The sandpaper slide on the gelatins and deform it. The sandpaper position cover the depth between 1.5 cm and 5 cm from the gelatine surface, corresponding to the instable depth interval (depth from 4 to 15 Km) (Scholz, 1998). In this setting I can only analyze the strain field of one fault block and hypothesize a symmetrical deformation of the two fault block respect to the fault.

2. **Box dimension:** the box is 40 cm length and 35 cm width. It is 24 cm height, but I normally had a gelatine height not bigger than 10 cm (Figure 1b). These values refer to the interior of the box. The free to move wall is 80 cm long to have the maximum freedom in the acquisition time windows and velocity setting of the experiments.

3. **Deformation velocity control:** I used an electric motor equipped with many gear ratios (Figure 1a). Using an inverter of the electric alimentation, I was able to set the right deformation velocity of the model. In the figure 7.2 the relation between the electric alimentation frequency and the plunger velocity.

4. **Experimental monitoring:** a sequence of images taken by a camera in time intervals are used to monitor the gelatin surface of the strike slip fault model. I used a Pike F421C IRF24 (Allied Vision Technologies) camera with a maximum frame rate of $30 \text{ frame} \cdot \text{s}^{-1}$. The gel-quakes are detection using the Particle Imaging Velocimetry; this technique is a robust tool used to measure deformation and flow pattern in nature

and analog models (e.g. Funicello *et al.*, 2006; Moroni and Cenedese, 2006). In my experiments I acquired at 7.5 frame/s; subsequently all images are processed by use the MatPIV modulus of Matlab to calculate single interrogation window displacement at every frame (a basic cross correlation accounting for optical deformation monitoring)

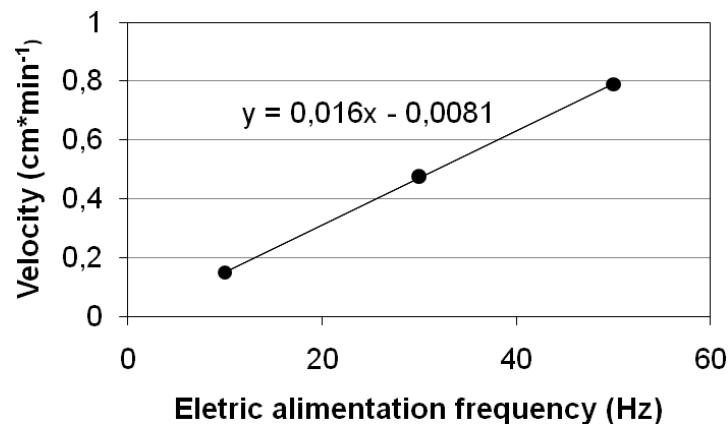


Figure 7.2: Relation between the electric alimentation frequency and the plunger velocity

7.3 Preliminary results

In this section I present the preliminary results and future opportunity of applications of gelatin strike-slip fault modelling.

The preliminary tests have been performed using a very simplified configuration. The model topography is a flat surface obtained spilling the liquid state gelatine in the box and, subsequently, laying the box into the fridge to obtain the solid state. After 12 hours I take the box out of the fridge; I remove the moving wall and I put on the sandpaper; subsequently I re-put the moving wall adherent to the gelatins using a system of rails. I performed several runs of the same model setting to verify the repeatability of the experiments.

Using Matlab, an open source code (running on matlab platform) which provides velocity field of a couple of frames, I plotted a time series of horizontal displacement

of an interrogation window (64x64 pixels) (Figure 7.3). At the beginning, the model starts moving and the wall starts to load elastically the gelatins. In this step no sliding along the wall is recorded because the sandpaper-gelatin interface is fully coupled: this is the beginning of the interseismic phase. This step which gelatin is accumulating elastic strain is very long and variable in terms of total displacement and duration. During this phase the gelatin are moving at the same direction and with the same velocity of the screen velocity (corresponding to the interseismic velocity in nature), this means that the fault is locked at the surface and the deformation decrease away the fault plane. When the stress accumulated is close to the yield stress, no more elastic deformation can be stored. From this point the system is ready to produce a fracture (a decoupling between moving wall and gelatin): thus, I have the first sliding along the fault plane and therefore the first modeled earthquake.

From this point (at about 380s), it is starting the coseismic phase in which the system try to recover the displacement stored during the interseismic phase. Under perfectly elastic rheology condition, the entire deformation is instantaneously recuperated and the displacement values down to zero; whereas, if the system is perfectly viscous, no earthquakes are recorded. My model works under viscoelastic condition; thus, only part of deformation is recovered. In fact, the gelatin rapidly move in opposite direction respect to the interseismic one (Cf. figure 4a to figure 4b) and then it start again to store interseismic deformation (at about $t = 390s$). New elastic load is accumulating in gelatin up to a new stress drop: a new earthquake cycle is started. Small slides are recorded before the first true earthquake.

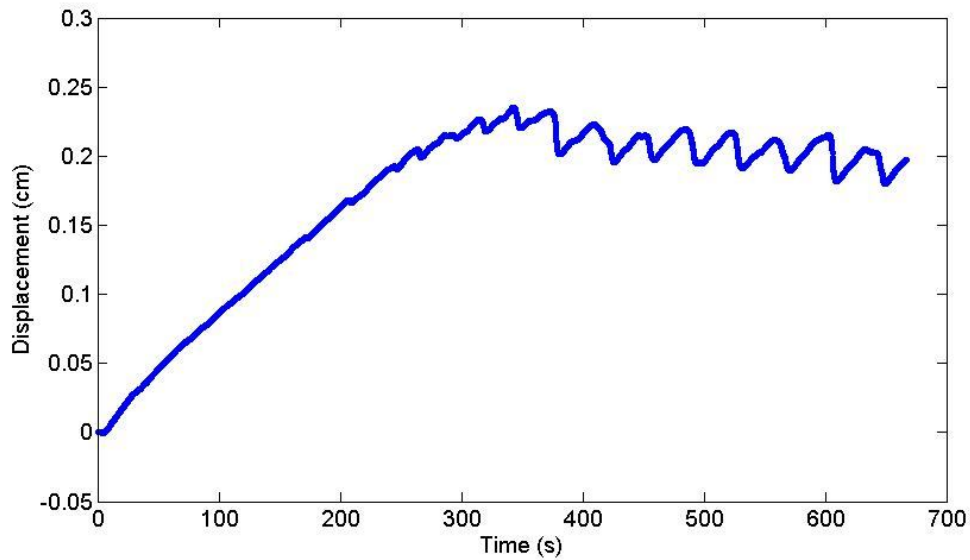


Figure 73: Horizontal displacement time series relative to an interrogation window of 64x64 pixels. The pixel is located 1 cm from the fault in the gelatins portion deformed by the sandpaper.

At every earthquake-cycle the stored deformation is progressively reduced up to level off at stable values (~ 0.025 cm). At the same time the coseismic slip is progressively stabilized at characteristic displacement and slip rate (slope of the curve during the coseismic phase). This means that the system is characterized by well-defined maximum displacement and characteristic earthquakes after a variable time and a certain number of earthquake-cycle.

In my experiments, “Normal” earthquake cycles shows an interseismic phase characterized by displacement of about 0.025 cm, a period of about 45 seconds and interseismic velocity of about $5.5 \cdot 10^{-4}$ cm s⁻¹, like shown in figure 7.3. Starting from the scale factors in table 7.2, I can evaluate the corresponding dimensions in nature. Thus, our interseismic phases show mean displacement of about 75 m in 370 years and an interseismic velocity of 20 cm yr⁻¹. This appears very high velocity respect to the natural velocity that normally are about some millimetres for year or at least few centimetres for year, our velocity seems to be an upper boundary of the natural range, whereas the interseismic period seems to be more reliable.

Concerning the coseismic events I have a displacement of about 0.025 cm in about 6 seconds corresponding to 75 m in 54 minutes, respectively. In the model I have a coseismic velocity of $4.17 \cdot 10^{-5} \text{ m s}^{-1}$, which is equal to 0.02 m s^{-1} in nature. This value is about two orders of magnitude smaller than the real one.

Figure 7.4a and b show the displacement field (top view) during the interseismic and coseismic phase respectively.

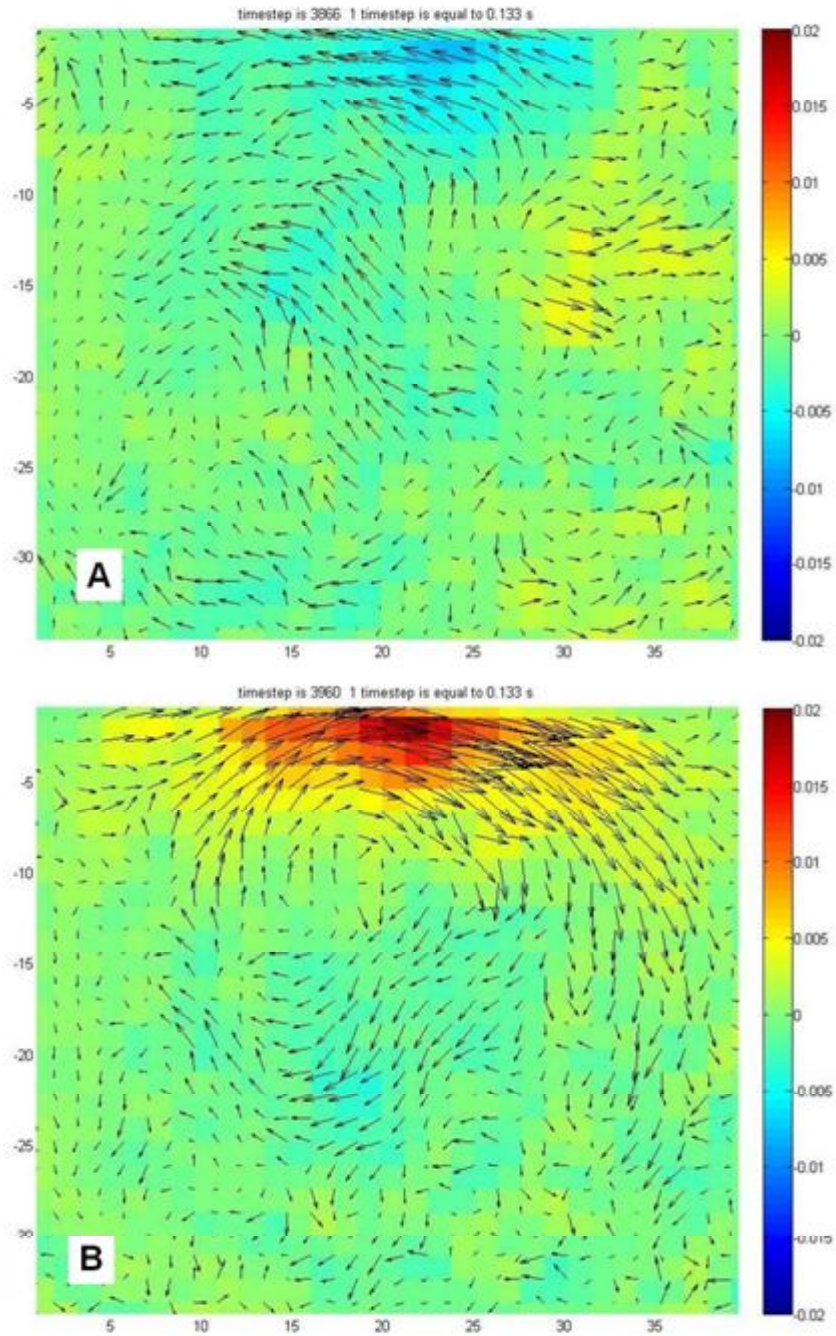


Figure 74: Top view of the modeled velocity field (relative to two consecutive images) during the interseismic (A) and coseismic (B) phase. Fault is localized at the top of each map, at Y coordinate = 0. Fault is moving along the X axis from right to left. Blue colour indicates pixel moving toward right, whereas red one toward left. The pixel movement is also highlight by the velocity vector field. Vector length is proportional to the interrogation windows velocity.

Summarizing, in this chapter I show the preliminary results of an analog model of seismic cycle. This is a very important result because I was able to follow the deformation evolution during the seismic cycle in continuum: every model parameter is known at every time step. I shown like the strike slip fault box with a Pig Skin like crust analog material can reproduce both the viscoelastic deformation acting during the interseismic phase and the elastic deformation release during the coseismic step. Figure 7.3 shows a large number of seismic cycles where a characteristic earthquake is recognizable. In fact the displacement drop during the earthquake is similar for all of seism, as well the coseismic velocity and the recurrence time. It means that, after a starting phase where the gelatin stores deformation, the system releases elastic deformation regularly.

Concluding, I associated at the study of the finite deformation in the transcurrent tectonic domain with the study of the earthquake cycle in the same model. I monitored, at the same time, the long and short term effect of the seismic cycle and the earthquakes. This is a very important result because I was able to reproduce the natural process, despite of the scaling problems I met during the work like for the plate velocity and the coseismic rupture velocity. These problems could be solved by new experimental settings. In fact many variations in the laboratory setting are necessary to arrive at a satisfactory conclusion in terms of seismic cycle knowledge improvements, but I consider these results like the first step for a new important laboratory experience.

Conclusions

In this thesis I investigated the seismic cycle of strike slip faults in intra-plate geodynamical contexts, by measuring the associated crustal deformation using the SBAS InSAR technique, and then trying to simulate the observations using analytical and analogical modeling.

I used this approach for three test areas with different structural, seismotectonic and environmental settings: the Gargano Promontory, Italy, where the Mattinata fault is expected to dominate the seismic strain release, the Doruneh fault, Central Iran, a much larger structure for which geological data point out a change in kinematics along its 300 km, and Central Pakistan, where three large earthquakes occurred in 2008 in the Balochistan region.

I also developed an analogical model for a more general approach to the seismic cycle simulation on strike slip faults.

Measurement of interseismic deformation in the Gargano Promontory

Using the SBAS InSAR technique I obtained the mean ground velocity maps of the Gargano promontory area. Overall, the deformation signal appears to be only slightly above the accuracy level of the SBAS technique and the velocities show that the inner Gargano area is subject to limited internal deformation; in spite of the low velocity values, SAR data allow to determine the right lateral kinematic pattern of the Mattinata Fault (MF), the most prominent tectonic structure of the Gargano. The InSAR results also highlight a compressional deformation pattern in the northern sector and an extensional one in the south. Moreover the InSAR velocities draw attention to some areas characterized by high deformation values and spatially limited patterns:

- The area around the town of Apricena is characterized by a well defined uplift (about 2-3 mm yr⁻¹ with respect to the central part of the promontory) probably related to the Apricena fault activity.
- The Tavoliere Graben is affected by strong subsidence due to water table depletion; the buried tectonic structures bordering the Graben control the underground water motion and define sectors with different soft sediments thicknesses, that are consequently affected by different compaction rates.
- On the contrary, in the northern Tavoliere, the footwall of the northernmost graben-bounding faults shows diffuse uplift, for which a tectonic explanation is probable.

All these phenomena are well recognized by the SBAS InSAR method because of the good spatial data coverage; they cannot be detected using GPS data given the sparse station density. On the other hand, the few permanent GPS stations located in the Gargano promontory enable to validate the InSAR results. As shown in chapter 4, I estimated the GPS – SAR differences for two GPS benchmarks: The differential velocity fall into the ± 1 mm yr⁻¹ uncertainty interval, demonstrating a good agreement between two geodetic methods.

Modeling of the interseismic deformation in the Gargano Promontory

The 1995 seismic sequence occurred few kilometers north of the MF; the low instrumental seismicity levels directly related to the MF suggest that although this fault is the most prominent (geologically and geomorphologically) tectonic structure of the area, it is not associated to frequent background seismicity, as seen for other large faults in the Apennines. Weighing the geological and geomorphological evidence more than the instrumental seismicity, I modeled the SBAS InSAR velocities assuming that the Mattinata fault is the principal structure driving strain accumulation in the area.

In Chapter 4 I show like the use of the Okada model allows to define some important constraints to the kinematics of the MF and, more in general, to the

entire Gargano area. Although our model fits the observed velocity field only roughly, the InSAR data inversions are only compatible with a right lateral strike slip solution for the MF: it is not possible to fit the same dataset using an interseismic source characterized by left lateral kinematics.

A problem with my model is that, even if it fits the DInSAR data within the uncertainties, the modeled slip rate of 13-15 mm yr⁻¹ seems too high with respect to the 0.8-0.9 mm yr⁻¹ velocities from the geological record. This overestimation arises from the depth of the creeping zone: a large slip rate is needed below 12 km depth to simulate even the little surface deformation observed at the surface. The use of a heterogeneous, non-isotropic medium would probably reduce this difference.

My model fits the observations to the first order: some misfit areas show deformation patterns which cannot be simulated, and which are well over the noise level. For example it was not possible to fit the compressional deformation present in the north of the area, near the town of Apricena and in the north-east (see Chapter 4).

The application of an analytical dislocation model to fit an interseismic signal allows to discern the deformation character at regional scale when it can be referred to a well defined tectonic structure, but it is inadequate to fit more local deformation, especially for poorly known sources. In the Gargano promontory, an univocal and reliable data interpretation is made difficult by the interaction between various tectonic structures and deformation trends characterized by different intensity and extension.

Measurement of interseismic deformation in Central Iran

The SBAS InSAR velocities evidence moderate deformation rates along the western termination of the main tectonic structure of the area: the E-W oriented Doruneh Fault System (DFS). The mean velocity maps of the three processed datasets highlight:

- The deformation pattern along the Western Fault Zone (WFZ) points out the left lateral transcurrent kinematics of this fault segment, in agreement with bibliographic references.
 - An Up component ($2-3 \text{ mm yr}^{-1}$) above the northern side of the WFZ has been brought to light by the SAR velocities and, following the data inversion, is in agreement with geomorphic and structural data that indicate a transpressional tectonic regime. In this geodynamical model, the left-lateral faulting along the NE-SW oriented Dahan-Qaleh Fault (DQF) implies a SW translation of its western block; this block corresponds to the northern block of the WFZ and its SW movement is resolved into reverse and left lateral components of faulting along the WFZ fault plane. At the western termination of the WFZ, the relative westward motion of the northern block is principally taken up by reverse faulting along the Kharturan Fault (KF) that marks a boundary between the DFS and the westward continuation of the DFS under the Great Kavir desert, called Great Kavir Fault (GKF).
 - Strong subsidence signal has been observed in the large plain South of the DFS ($\sim 15 \text{ mm yr}^{-1}$); as demonstrated by structural and hydrogeological study, this velocity pattern is related to water table overpumping acting into a tectonic controlled graben under the plain.
 - With the exception of the north-western area adjacent to the KF and the previous mentioned subsidence pattern in the plain, the SAR maps show spatially correlated velocity variations without much high frequency signals. With respect to what observed in the Gargano region, I explain this as meaning that the velocity maps are less affected by atmospheric and unwrapping artifacts, but also that the interseismic tectonic signal is mainly due to a single large source.
- Since no GPS stations are located into the study area, no InSAR data validation has been performed.

Modeling of the interseismic deformation in Central Iran

My analytical model confirms the left lateral kinematics of the Doruneh Fault System and adds an important thrust component (rake angle of $34^{\circ}\pm 4$), necessary to fit the observed SAR velocities. The left lateral strike slip component being about 2/3 of the total slip rate is in agreement with the long term record as reconstructed by structural and geomorphic observations; in addition the steep fault dip to the North ($\sim 63^{\circ}$) is well constrained by the observations, and is in agreement with field observations on the Western and Central DFS.

In this case the slip rate estimation from the elastic dislocation model is in good agreement with the geological record; indeed the 5 mm yr^{-1} slip rate, the first quantitative estimate of strain accumulation for the Western Doruneh Fault System, corresponds to $\sim 4 \text{ mm yr}^{-1}$ of pure horizontal movement and $\sim 2.5 \text{ mm yr}^{-1}$ of pure vertical displacement. While there are no independent estimates of the vertical component, the horizontal velocity is compatible (within errors) with the $\sim 2.4 \text{ mm yr}^{-1}$ of left lateral slip rate estimated by Fattahi *et al.* (2007) for the Central Fault Zone (CFZ).

The transpressive character of the Western Fault Zone (WFZ) defined from the model is in agreement with a recent kinematic model, in which the WFZ slip vector is compatible with those of the left-lateral strike slip Daleh-Qahan fault and of the reverse Kharturan Fault (Farbod *et al.*, 2011).

At the regional scale, the modeled slip rate and slip vector for the WFZ are compatible with the sparse quantitative data available on the present deformation field. In fact my model implies a shortening rate across the DFS of $\sim 1.3 \text{ mm yr}^{-1}$, which contributes to 1/4-1/5 of the total shortening accommodated between the Lut block and Eurasia, as measured by GPS networks.

Overall, the use of the elastic dislocation model of Okada has demonstrated to be a useful tool to investigate the interseismic source parameters where the majority of the ground deformation can be attributed to a geologically well defined fault.

The coseismic deformation of the 2008 seismic sequence in the Balochistan region (Eastern Pakistan)

I analyzed the 2008 Balochistan (western Pakistan) seismic sequence, characterized by two Mw 6.4 events on October 28 and 29, followed by a large, Mw 5.7 aftershock on December 9, by means of the classical DInSAR technique. I used ENVISAT and ALOS SAR image datasets to measure the coseismic ground deformation:

- the ALOS interferograms are affected by decorrelation problems and no useful information has been obtained.
- In ENVISAT Wide swath interferogram only few coseismic fringes are recognizable and the epicenter area appears affected by decorrelation problems; the phase unwrapping cannot be done.
- Although the ENVISAT descending pass dataset, corresponding to the track 363, is composed by a large number of useful images, the interferograms have been discarded because of the large number of topographic fringes and an unfavorable signal to noise ratio.
- A large number of ascending pass ENVISAT images (track 213) have been combined to obtain independent interferograms; I chose two pairs to discern the two Oct. 2008 mainshocks and the December 2008 aftershock contributions.

I used the 06/05/2008-02/12/2008 interferogram to measure the total coseismic+postseismic displacement field up to December 2, obtaining a maximum displacement of about 20 cm. For the 09 Dec. 2008 aftershock, I measured a maximum displacement of about 15cm using the 02/12/2008-21/04/2009 interferogram.

Source modeling of the 2008 seismic sequence in the Balochistan region (Eastern Pakistan)

I inverted the 06/05/2008-02/12/2008 and 02/12/2008-21/04/2009 interferograms using the elastic dislocation model of Okada, to determine the source parameters of the three main seismic events. I determined fault positions, lengths, widths, depths and slip distributions, constraining the other source parameters using the Global CMT solutions.

A well constrained solution has been obtained for the 09 December aftershock, as shown in Chapter 6: the modeled displacement field fits very well the observed one, although no geological or geomorphological constraint has been used.

Concerning the October 2008 seismic events, the source definition is more difficult without any geological or kinematic constraint; I tested two possible fault solutions derived from those proposed by the Global CMT catalogue. Because the RMS values and the displacement distributions are very similar, it is not possible to favor one of the solutions without independent constraints derived from geological data. Unfortunately few and sparse information about the geological and seismotectonic framework of the epicentral area are available, and none at all about the possible surface expression of the sources.

This site was initially selected as a candidate to study both the interseismic and post-seismic phases of the seismic cycle. The difficulty in the identification of the 2008 sources discouraged the analysis of the pre-event SAR data, since any interseismic signal detected in the area would have been even more difficult to model than the coseismic one. The modeling of the interseismic signal was then addressed for the Iran site, for which the causative source of interseismic deformation is clear.

In a future work, I want to carry out an analysis of the pre- and postseismic deformation also on these earthquakes, to verify if any interesting pattern of crustal deformation has preceded and followed the quakes, and try to extract some useful information to solve the ambiguities between the two possible sources.

Earthquake cycle measurements using InSAR methods: conclusions

I applied the SABS InSAR technology to two well defined strike slip faults characterized by quasi E-W azimuth and low slip rates: the Mattinata Fault and the Doruneh Fault. The first one is characterized by a $< 1 \text{ mm yr}^{-1}$ geological slip rate and by a still debated right lateral transcurrent kinematics, whereas the second one shows a well defined left lateral strike slip kinematics with a slip rate of 2-3 mm yr^{-1} .

The two test cases differ very much for climate conditions and percentage of vegetated area; consequently, different problems affect the two SBAS processings: temporal decorrelation and unwrapping problems represent an obstacle for the Gargano promontory because of the presence of agriculture and forested, steep slopes. The poorly vegetated landcover around the Doruneh Fault is affected by only limited temporal decorrelation, except for the cultivated fields in the alluvial plain, and the high SAR coherence allows to minimize the phase unwrapping errors. The dry climate of central Iran, with respect to the humid one of the Gargano, plays also an important role in the quality of the resulting velocity maps. In general the artifacts from turbulent atmosphere are more evident in the Gargano region, even though differences in the topography-correlated troposphere stratification probably generate some problems also in the quasi desertic Doruneh area (these artifacts are more difficult to detect). In addition, the higher tectonic signal for the DFS with respect to the MF facilitates the DFS data interpretation with respect to the MF.

In areas with low deformation rates, residual orbital ramps may represent a considerable problem: in both test sites, the expected interseismic deformation signal could be approximated as a planar ramp striking E-W, as the presumed tectonic source. For all datasets I removed residual orbital ramps striking about N-S; since the largest variations of the tectonic signal are expected nearly parallel to the ramp directions, I assumed that only a small fraction of tectonic signal may have been removed. A more accurate removal of residual ramp can only be

obtained using independent measurements of ground velocity, as those provided by CGPS data.

Analytical models applied to the InSAR data inversions: conclusions

Analytical dislocation models provide a fast and simple way to simulate coseismic and interseismic ground deformation arising from fault dislocation, in a simplified medium. However, to generate significant results they require geological, morphotectonic or seismological constraints of some source parameters; the model is not able to solve the ambiguities related to different possible solutions if no external constraints are available. Even for the coseismic case, for which the elastic dislocation theory is appropriate, the lack of external information may prevent a significant solution to be obtained, especially when only a single LoS interferogram is available.

When used to simulate low deformation rates occurring in intra-plate geodynamical contexts, the Okada dislocation model provides reliable source solutions only when geological or seismological data are available to identify the probable source, as demonstrated for the western termination of the DFS.

An attractive feature of this model is that it does not require specific knowledge on the crustal properties, that are generally not available; the a priori conditions are everywhere the same and results for different test sites are comparable. The Okada model assumes elastic, isotropic, homogeneous half-space conditions, which are certainly not verified for slow movements, and especially below the locking depth; for this reason, when using this model for studying the interseismic phase, the results are only to the first order. Moreover this model is more consistent with the view that the continental lithosphere deformation is dominated by the strength of its brittle upper crust. Positive results of the Okada model application support this view, again, at least to the first order.

I consider the goodness of model fit and the differences between modeled and geological slip rate as quality results index. Thus:

1. In the Gargano site, the model fits the DInSAR data within the uncertainties, but for the Mattinata Fault, the modeled slip rate (13-15 mm yr⁻¹) is too high with respect to the geological rate (0.8-0.9 mm yr⁻¹). This discrepancy could mean that 1) the model assumptions are completely wrong, or that 2) the deformation is not accumulated along the Mattinata fault, or that 3) the fault is totally locked.
2. In the Iran case, the model fits the observations quite well, and the modeled horizontal slip rate (4 mm yr⁻¹) is compatible with the geological one (2.4 mm yr⁻¹). This model result seems to support the idea that in Central Iran the deformation of the continental lithosphere is dominated (at the first order) by the strength of its brittle upper crust.

Analog models applied to the study of the earthquake cycle in transcurrent tectonic domains

Novel analog models have been set up to constraint experimentally the evolution of the deformation during the seismic cycle of strike slip faults. These models, using gelatin as suitably rheological analog for the crust, offer the unique advantage to simulate elastic deformations, as occurring during the coseismic phase, introducing also a proper visco-elastic relaxation for post-seismic deformations. Hence, experimental results allow constraining both the short- and the long-term behavior of seismogenic strike slip faults. In particular, developed image analysis solutions (i.e. Particle Image Velocimetry technique, photoelastic technique) allow to easily compare modeling results to natural observables (i.e. velocity fields, interferometric images).

Preliminary experimental results are promising mimicking the main features of the seismic cycle characterizing natural strike slip faults (e.g. stick-slip behavior, characteristic earthquake, coseismic velocity and recurrence time). The goal of future work will be to explore systematically the parameter space controlling the strike slip fault behavior (e.g. slip rate, fault geometry, fault roughness, crustal rheology, crustal stratification), searching for possible cause-effect relationships.

Reference list

- Acocella, V., Faccenna, C., Funicello, R. and Rossetti, F., 2000. Analogue modelling of extensional transfer zones. *Bollettino Societa' Geologica Italiana* 119, 85–96, 2000.
- Altamimi, Z., Collilieux, X., Legrand, J., Garayt, B. and Boucher, C., 2007. ITRF 2005: A new release of the International Terrestrial Reference Frame based on time series of station positions and Earth Orientation Parameters, *J. Geophys. Res.*, 112, B09401, doi:10.1029/2007JB004949.
- Ambraseys, N. and Melville, C., 1977. The seismicity of Kuhistan, Iran. *The Geographical Journal*, 143, 179–199.
- Ambraseys, N. and Melville, C., 1982. A history of Persian earthquakes. *Cambridge University Press*, Cambridge.
- Ambraseys, N. and Moinfar, A., 1975. The seismicity of Iran; the Turshiz, Kashmar – Khorasan earthquake of 25th september 1903. *Annali di Geofisica*, 28, 253–269
- Ambraseys, N. and Moinfar, A., 1977. The seismicity of Iran. The Kaj Darakht, Khurasan, earthquake of 25th May, 1923. *Annali di Geofisica*, 30, 3–18.
- Amelung, F., Galloway, D.L., Bell, J.W., Zebker, H.A. and Lacznia, R.L., 1999. Sensing the ups and downs of Las Vegas – InSAR reveals structural control of land subsidence and aquifer-system deformation. *Geology*, 27: 483–486.
- Anderson, H. and Jackson, J., 1987. Active tectonics of the Adriatic region, *Geophys. J. R. Astron. Soc.* 91, 937–983.
- Anderssohn, J., Wetzel, H. U., Walter T. R., Motagh, M., Djamour, Y., and Kaufmann, H., 2008. Land subsidence pattern controlled by old alpine basement faults in the Kashmar Valley, northeast Iran: results from InSAR and levelling, *Geophys. J. Int.*, doi: 10.1111/j.1365-246X.2008.03805.x
- Argnani, A., Rovere M. and Bonazzi, C., 2009. Tectonics of the Mattinata fault, offshore south Gargano (southern Adriatic Sea, Italy): Implications for active deformation and seismotectonics in the foreland of the Southern Apennines, *Geol. Soc. Of America Bul.*, Sept/Oct 2009

- Argnani, A., Favali P., Frugoni M., Gasperini M., Ligi M., Marani M., Mattiotti G. and Mele G., 1993. Foreland deformation pattern in the Southern Adriatic Sea, *Annali di Geofisica*, 36, 229-247.
- Argnani, A. and Frugoni, F., 1997. Foreland deformation in the central adriatic and its bearing on the evolution of the northern apennines, *Ann. Geophys.*, 40(3), 77-780.
- Atzori, S., Hunstad, I., Chini, M., Salvi, S., Tolomei, C., Bignami, C., Stramondo, S., Trasatti, E., Antonioli, A. and Boschi E., 2009. Finite fault inversion of DInSAR coseismic displacement of the 2009 L'Aquila earthquake (Central Italy), *Geophys. Res. Lett.*, 36, 115305, doi:10.1029/2009GL039293.
- Atzori, S., Manunta, M., Fornaro, G., Ganas, A. and Salvi, S., 2008. Postseismic displacement of the 1999 Athens earthquake retrieved by the Differential Interferometry by Synthetic Aperture Radar time series, *J. Geophys. Res.*, 113, B09309, doi:10.1029/2007JB005504
- Bagdassarov, N. and Dorfman, A., 1998. Viscoelastic behavior of partially molten granites. *Tectonophysics*, 290, 27–45.
- Bakun, W. H., Langbein, J. O., Lindh, A. G. and Roeloffs, E. R., 2004. History of the Parkfield Prediction Experiment. *American Geophysical Union, Fall Meeting 2004*, abstract #S53D-01
- Bakun, W.H. and Lindh, A.G., 1985. The Parkfield, California earthquake prediction experiment, *Science*, 229, 619-624.
- Bakun, W.H. and McEvilly, T.V., 1979. Earthquakes near Parkfield, California: Comparing the 1934 and 1966 sequences, *Science*, 205, 1375-1377.
- Banks, C. J. and Warburton, J., 1986. 'Passive-roof' duplex geometry in the frontal structures of the Kirthar and Sulaiman mountain belts, Pakistan, *J. Struct. Geol.*, 8(3/4), 229–237.
- Bannert, D., Cheema, A., Ahmed, A. and Schaffer, U., 1992. The structural development of the Western Fold Belt, Pakistan, *Geol. Jahrb.*, 80, 3–60.
- Barnes, H.A., Hutton, J.F. and Walters, K., 1989. *An Introduction to Rheology*. Elsevier Science Publishing Company, New York. 212 pp.
- Basile, C. and Brun, J.P., 1998. Transtensional faulting patterns ranging from pull-apart basins to transform continental margins, an experimental investigation. *J. Struct. Geol.*, 21, 23–37.
- Bellahsen, N., Faccenna, C. and Funicello, F., 2005. Dynamics of subduction and plate motion in laboratory experiments: Insights into the "plate tectonics" behavior of the Earth. *J. Geophys. Res.*, 110. doi:10.1029/2004JB002999.
- Bendick, R. and Flesch, L., 2007. Reconciling lithospheric deformation and lower crustal flow beneath central Tibet; *Geology*, v. 35, p. 895–898, doi:10.1130/G23714A.1.

- Bendick, R., Bilham, R., Freymueller, J.T., Larson, K. and Yin, G., 2000. Geodetic evidence for a low slip rate in the Altyn Tagh fault system: *Nature*, v. 404, p. 69–72, doi: 10.1038/35003555.
- Ben-Zion, Y., Rice, J. R. and Dmowska, R., 1993. Interaction of the San Andreas Fault creeping segment with adjacent Great Rupture Zones and earthquake recurrence at Parkfield. *J. Geophys. Res.*, vol. 98, no. b2, 2135-2144.
- Berberian, M., & Yeats R., 1999. Patterns of Historical Earthquake rupture in the Iranian Plateau. *Bull. Seismol. Soc. Am.*, 89, 120-139.
- Berberian, M. and Yeats R., 2001. Contribution of archaeological data to studies of earthquake history in the Iranian Plateau. *J. Struct. Geol.*, 23, 563-584.
- Berardino, P., Fornaro, G., Lanari, R. and Sansosti, E., 2002. A new algorithm for surface deformation monitoring based on small baseline differential interferograms, *IEEE Trans. Geosci. Remote Sensing*, vol. 40, pp. 2375–2383.
- Berardino, P., Casu, F. and Lanari, R., 2004. On the exploitation of the SBAS algorithm for the analysis of the deformations detected from the ERS and ENVISAT D-InSAR data[C]. *ERSENVISAT Symposium*.
- Bernard, M., Shen-Tu, B., Holt, W. E. and Davis, D. M., 2000. Kinematics of active deformation in the Sulaiman lobe and range, Pakistan, *J. Geophys. Res.*, 105(6), 13,253–13,279.
- Bertotti, G., Picotti, V., Chilovi, C., Fantoni, R., Merlini, S., and Mosconi, A., 2001. Neogene to Quaternary sedimentary basins in the south Adriatic (Central Mediterranean):Foredeeps and lithospheric buckling, *Tectonics*, pp. 771-787.
- Bertotti, G., Casolari, E., and Picotti, V., 1999. The Gargano Promontory: A Neogene contractional belt within the Adriatic plate: *Terra Nova*, v. 11, p. 168–173, doi: 10.1046/j.1365-3121.1999.00243.x.
- Biggs, J., Wright, T., Lu, Z. and Parsons, B., 2007. Multi-interferogram method for measuring interseismic deformation: Denali Fault, Alaska. *Geophysical Journal International*, 170: 1165–1179. doi: 10.1111/j.1365-246X.2007.03415.x
- Billi, A., Salvini, F. and Storti, F., 2003. The damage zone–fault core transition in carbonate rocks: Implications for fault growth, structure and permeability, *Journal of Structural Geology*, v. 25, p. 1779–1794, doi: 10.1016/S0191-8141(03)00037-3.
- Billi, A., Gambini, R., Nicolai, C., and Storti, F., 2007. Neogene-Quaternary intraforeland transpression along a Mesozoic platform-basin margin: The Gargano fault system, Adria, Italy, *Geosphere*, v. 3, p. 1–15, doi: 10.1130/GES00057.1.

- Blanco, P., Mallorquí, J. J., Duque, S. and Navarrete, D., 2006. Advances on DInSAR with ERS and ENVISAT data using the Coherent Pixels Technique (CPT), *Proc. IGARSS 2006*, Denver (USA).
- Blanco-Sanchez, P., Deque, S., Mallorquí, J.J. and Monells, D., 2007. Analysis of highly non-linear deformation due to mininh activity with DInSAR: PSIC Test site. Proc. 'Envisat symposium 2007', Montreux, Switzerland, 23-27 April.
- Blanco-Sanchez, P., Mallorquí, J.J., Duque, S. and Monells, D., 2008. The Coherent Pixels Technique (CPT): An Advanced DInSAR Technique for Nonlinear Deformation Monitoring, *Pure Appl. Geophys.*, No. 165, pp. 1167-1194.
- Bock, Y. and Williams, S., 1997. Integrated satellite interferometry in southern California, *Eos Trans. AGU*, 78(29), 293.
- Bock, S.Y. and Pang, P., 1998. Integrated satellite interferometry: tropospheric noise, GPS estimates and implications for interferometric synthetic aperture radar products, *J. Geophys. Res.*, vol. 103, no. B11, pp. 27 051–27067.
- Bonini, M., Souriot, T., Boccaletti, M. and Brun, J.P., 1997. Successive orthogonal and oblique extension episodes in a rift zone, laboratory experiments with application to the Ethiopian Rift. *Tectonics* 16, 347–362.
- Boschi, E., Guidoboni, E., Ferrari, G., Valensise, G., and Gasperini, P., 1997. Catalogo dei forti terremoti in Italia dal 461a.C. al 1990, *ING-SGA Eds.*, Bologna, p. 644.
- Bosellini, A. and Ferioli, G. L., 1988. Sequenze deposizionali e discordanze nel Gargano meridionale, *Atti 748 Congresso Soc. Geol. It.*
- Bosellini, A., Neri, C., and Luciani, V., 1993. Platform Margin Collapses and Sequence Stratigraphic Organization of Carbonate Slopes: Cretaceous-Eocene, Gargano Promontory, Southern Italy, *Terra Nova*, Vol. 5, pp. 282–297.
- Boutelier, D., Schrank, C. and Cruden, A., 2008. Power-law viscous materials for analogue experiments: New data on the rheology of highly-filled silicone polymers, *J. Struct. Geol.*, 30, 341–353, doi:10.1016/j.jsg.2007.10.009.
- Boutelier, D. A. and Cruden, A., 2008. Impact of regional mantle flow on subducting plate geometry and interplate stress: insights from physical modelling, *Geophys. J. Int.*, 174, 719–732, doi:10.1111/j.1365-246X.2008.03826.x.
- Brankman, C.M. and Aydin, A., 2004. Reply to the comments by G. Bertotti and V. Picotti on: "Uplift and contractional deformation along a segmented strikeslip fault system: The Gargano Promontory, southern Italy": *Journal of Structural Geology*, v. 26, p. 2327–2329, doi: 10.1016/j.jsg.2004.06.007.

- Brun, J.P., Sokoutis, D. and Van Den Driessche, J., 1994. Analogue modeling of detachment fault systems and core complexes. *Geology* 22, 319–322.
- Buckingham, E., 1914. On physically similar systems; Illustrations of the use of dimensional equations, *Phys. Rev.*, 4, 345–376.
- Bürgmann, R., Rosen, P., and Fielding, E., 2000. Synthetic aperture radar interferometry to measure Earth's surface topography and its deformation. *Ann. Rev. Earth. Planet. Sci.*, 28, 169-209.
- Bufe, C. G., Harsh, P. W. and Burford, R. O., 1977. Steady-state seismic slip - a precise recurrence model, *Geophys. Res. Lett.*, 4, 91-94.
- Calais, E., Nocquet, J.M., Jouanne, F. and Tardy, M., 2002. Current strain regime in the Western Alps from continuous Global Positioning System measurements, 1996-2001, *Geology*, 7, 651- 654.
- Carlson, R., Kanamori, H. and McNally K., 1979. A survey of microearthquake activity along the San Andreas fault from Carrizo Plain to Lake Hughes, *Bull. Seismol. Soc.*, 69, 177-186.
- Casolari, E., Negri, A., Picotti, V. and Bertotti, G., 2000, Neogene stratigraphy and sedimentology of the Gargano Promontory (southern Italy): *Eclogae Geologicae Helvetiae*, v. 93, p. 7–23.
- Castello, B., Selvaggi, G., Chiarabba, C. and Amato, A., 2005. CSI *Catalogo della Sismicità Italiana 1981–2002*, Versione 1.0: Roma, Istituto Nazionale di Geofisica e Vulcanologia-Centro Nazionale Terremoti: <http://www.ingv.it/CSI/> (accessed 2006).
- Casu, F., Manzo, M. and Lanari, R., 2006. A quantitative assessment of the SBAS algorithm performance for surface deformation retrieval from DInSAR data, *Remote Sens. Environ.*, 102, no. 3/4, 195–210.
- Ciaranfi, N. and Riccietti, G., 1980. Considerazioni sulla neotettonica del Promontorio del Gargano, *Publ., CNR-PFG 356*, CNR-Roma.
- Colantoni P., Tramontana M. and Tedeschi R., 1990. Contributo alla conoscenza dell'avanpaese apulo: struttura del golfo di Manfredonia (Adriatico meridionale), *Giorn. Geolog.*, 52, 19-32.
- Console, R., Di Giovanbattista, R., Favali, P. and Smriglio, G., 1989. Lower Adriatic Sea seismic sequence (January 1986): spatial definition of the seismogenic structure, *Tectonophysics* 166, 235–246.
- Console, R., Di Giovanbattista, R., Favali, P., Presgrave, B. M. and Smriglio, G. 1993. Seismicity of the Adriatic microplate, *Tectonophysics* 218, 343–354.

- Corbi, F., Funicello, F., Faccenna, C., Ranalli, G. and Heuret, A., 2011. Seismic variability of subduction thrust faults: insights from laboratory models. *J. Geophys. Res.*, 116, B06304, doi:10.1029/2010JB007993.
- Costantini, M. and Rosen, P. A., 1999. A generalized phase unwrapping approach for sparse data, in *Proc. IAGRS*, Hamburg, Germany, June 1999, pp. 267–269.
- Cotton, F., Coutant, O., Scholz, C. and Campillo, M., 1995. Triggering of aftershocks: comparison between static and dynamic stress changes during the 1992 Landers earthquake. 1995 Fall Meeting of the American Geophysical Union, EOS, November 7, 559, 1995.
- Cotton, F. and Coutant, O. 1997. Dynamic stress variations due to shear faults in a plane-layered medium. *Geophysical Journal International*, 128. 676–688. doi: 10.1111/j.1365-246X.1997.tb05328.x
- Cowgill, E., 2007. Impact of riser reconstructions on estimation of secular variation in rates of strike-slip faulting: Revisiting the Cherchen River site along the Altyn Tagh fault, NW China: *Earth and Planetary Science Letters*, v. 254, p. 239–255, doi: 10.1016/j.epsl.2006.09.015.
- Curlander, J.C., and McDonough, R.N. 1991. *Synthetic Aperture Radar systems and signal processing*. New York: John Wiley & Sons.
- D'Agostino, N., Avallone, A., Cheloni, D., D'Anastasio, E., Mantenuto, S. and Selvaggi, G., 2008. Active tectonics of the Adriatic region from GPS and earthquake slip vectors, *J. Geophys. Res.*, 113, B12413, doi:10.1029/2008JB005860.
- D'Agostino, N., Cheloni, D., Mantenuto, S., Selvaggi, G., Michelini, A. and Zuliani, D., 2005. Strain accumulation in the southern Alps (NE Italy) and deformation at the northeastern boundary of Adria observed by CGPS measurements, *Geophys. Res. Lett.*, 32, L19306, doi:10.1029/2005GL024266.
- Das, S. and Scholz, C.H., 1981. Off-fault aftershock clusters caused by shear stress increase?, *Bull. Seism. Soc. Am.* 71, 1669-1675.
- Davy, P. and Cobbold, P.R., 1988. Indentation tectonics in nature and experiment. 1. Experiments scaled for gravity. *Bulletin of the Geological Institute of Uppsala, New Series* 14, 129–141.
- Davy, P. and Cobbold, P.R., 1991. Experiments on shortening of a 4-layer continental Lithosphere, *Tectonophysics*, 188, 1-25.
- De Alteriis, G. and Aiello, G., 1993. Stratigraphy and tectonics offshore of Puglia (Italy, Southern Adriatic Sea), *Mar. Geol.* 113, 233–253
- Delacourt, C., Briole, P. and Achache, J. 1998. Tropospheric corrections of SAR interferograms with strong topography. Application to Etna. *Geophys. Res. Lett.*, 25(15), 2,849-2,852.

- Del Gaudio, V., Pierri, P., Frepoli, A., Calcagnile, G., Venisti, N. and Cimini, G.B., 2007. A critical revision of the seismicity of northern Apulia (Adriatic microplate/ southern Italy) and implications for the identification of seismogenic structures: *Tectonophysics*, v. 436, p. 9–35, doi: 10.1016/j.tecto.2007.02.013.
- Deng, J., Gurnis, M., Kanamori, H. and Hauksson, E., 1998. Viscoelastic flow in the lower crust after the 1992 Landers, California, earthquake, *Science*, 282, 1689–1692.
- Di Giuseppe, E., Funiciello, F., Corbi, F., Ranalli, G. and Mojoli, G., 2009. Gelatins as rock analog: A systematic study of their rheological and physical properties, *Tectonophysics*, 473(3-4), 391-403, doi:10.1016/j.tecto.2009.03.012.
- Doin, M-P., Lasserre, C., Peltzer, G., Cavalié, O. and Doubre, C., 2009. Corrections of stratified tropospheric delays in SAR interferometry: Validation with global atmospheric models. *Journal of Applied Geophysics*, v. 69, iss. 1, p. 35-50.
- Du, Y. and Aydin, A., 1993. Stress transfer during three sequential moderate earthquakes along the Central Calaveras fault, California, *J. Geophys. Res.* 98, 9947-9962.
- Duque, S., Mallorquí, J.J., Blanco-Sanchez, P. and Monells, D., 2007. Application of the coherent pixels technique (CPT) to urban monitoring, *2007 Urban Remote Sensing Joint Event*, vol.2, Paris, France.
- Dziewonski, A.M., Chou, T.A. and Woodhouse, J.H., 1981. Determination of earthquake source parameters from waveform data for studies of global and regional seismicity, *J. Geophys. Res.*, 86(4), 2825–2852.
- Eftekhari-Nezhad, J., Aghanabati, A., Hamzehpour, B. and Baroyant, V., 1972. *Geological map of Iran, Ser. J5, Kashmar sheet, Scale 1: 250 000*. Geol. Surv. of Iran, Tehran.
- England, P.C., 1987. Diffuse continental deformation: length scale, rates and metamorphic evolution. *Phil. Trans. R. Soc. Lond. A*. 321, 3-22.
- England, P.C. and Molnar, P., 2005. Late Quaternary to decadal velocity fields in Asia: *Journal of Geophysical Research*, v. 110, B12401, doi: 10.1029/2004JB003541.
- Engdahl, E. R., Van der Hilst, R., and Buland R., 1998. Global teleseismic earthquake relocation with improved travel times and procedures for depth determination. *Bull. Seismol. Soc. Am.*, 88(3), 722-743.
- Engdahl, E.R., Jackson, J.A., Myers, S.C., Bergman, E.A. and Priestley, K., 2006. Relocation and assessment of seismicity in the Iran region. *Geophys. J. Int.*, 167, 761–778 doi: 10.1111/j.1365-246X.2006.03127.x
- Engdahl, E.R. and Villasenor, A., 2002. Global seismicity: 1900–1999, in *International Handbook of Earthquake and Engineering Seismology*, vol. A, edited by W. H. K. Lee, H. Kanamori, P. C. Jennings, and C. Kisslinger, chap. 41, pp. 665–690, Academic Press.

- Faccenna, C., Davy, P., Brun, J.P., Funicello, R., Giardini, D., Mattei, M. and Nalpas, T., 1996. The dynamic of backarc basins: an experimental approach to the opening of the Tyrrhenian Sea, *Geophysical Journal International*, 126, 781-795.
- Faccenna, C., Giardini, D., Davy, P. and Argentieri, A., 1999. Initiation of subduction at Atlantic-type margins: Insights from laboratory experiments, *Journal of Geophysical Research*, 104 (B2), 2749-2766.
- Farbod, Y., Bellier, O., Shabanian, E. and Abbassi, M. R., 2011. Geomorphic and structural variations along the Doruneh Fault System (Central Iran), *Tectonics*, doi:10.1029/2011TC002889, in press.
- Fattahi, M., Walker, R.T., Khatib, M.M., Dolati, A. and Bahroudi A., 2007. Slip-rate estimate and past earthquakes on the Doruneh fault, eastern Iran. *Geophys. J. Int.*, 168, 691–709
- Favali, P., Mele, G. and Mattiotti, G., 1993. Contribution to the study of the Apulian microplate geodynamics, *Mem. Soc. Geol. It.* 44, 71–80.
- Feigl, K. L., Agnew, D.C., Bock, Y., Dong, D., Donnellan, A., Hager, B.H, Herring, T.A., Jackson, D.D., Jordan T.H., King, R.W., Larsen, S., Larson, K.M., Murray, M.H., Shen, Z. and Webb, F.H., 1993. Space geodetic measurements of crustal deformation in central and southern California, 1984–1992, *J. Geophys. Res.*, 98, 21,677–21,712.
- Ferretti, A., Prati, C. and Rocca, F., 2001. Permanent scatterers in SAR interferometry. *IEEE Transactions on Geoscience and Remote Sensing*. 39(1):8–20.
- Ferretti, A., Prati, C. and Rocca, F., 2000. Nonlinear subsidence rate estimation using permanent scatterers in differential SAR interferometry, *IEEE Trans. Geosci. Remote Sensing*, vol. 38, pp. 2202–2212, Sept. 2000.
- Ferry, J.D., 1980. *Viscoelastic properties of Polymers*, 3rd ed. Wiley Blackwell. 672.
- Fialko, Y., 2006. Interseismic strain accumulation and the earthquake potential on the southern San Andreas fault system, *Nature*, 441, doi:10.1038/nature04797, 968-971.
- Finetti, I., 1982. Structure, stratigraphy and evolution of Central Mediterranean, *Boll. Geof. Teor. Appl.* 38, 75–155.
- Finetti, I., Bricchi, G., Del Ben, A., Pipan, M. and Xuan, Z., 1987. Geophysical study of the Adria Plate, *Mem. Soc. Geol. It.* 40, 335–344.
- Ford, J.P., Blom, R.G., Crisp, J.A., Elachi, C., Farr, T.G., Saunders, R.S., Theilig, E.E., Wall, S.D. and Yewell, S.B., 1989. *Spaceborne radar observations: a guide for Magellan radar-image analysis*. California Institute of Technology: Jet Propulsion Laboratory.

- Franceschetti, G. and Lanari, R., 1999. Synthetic Aperture RADAR PROCESSING, Electronic engineering system series.
- Funiciello, R., Montone, P., Salvini, F. and Tozzi, M., 1988. Caratteri strutturali del Promontorio del Gargano, *Mem. Soc. Geol. It.* 41, 1235–1243.
- Funiciello, F., Faccenna, C., Giardini, D. and Regenauer-Lieb, K., 2003. Dynamics of retreating slabs (part 2): Insights from 3-D laboratory experiments, *J. Geophys. Res.*
- Funiciello, F., Moroni, M., Piromallo, C., Faccenna, C., Cenedese, A. and Bui, H.A., 2006. Mapping the flow during retreating subduction: laboratory models analyzed by feature tracking. *J. Geophys. Res.* 111, B03402 03410.01029/02005JB003792.
- Ge, L., Ishikawa, Y., Fujiwara, S., Miyazaki, S. and Qiao, X., 1997. The Integration of InSAR and CGPS: A Solution to Efficient Deformation Monitoring on Current Crustal Movement and Hazard Reduction in East Asia and South-east Asia, *Wuhan, P.R. China*, 4-7 November.
- Ge, L, Han, S and Rizos, C., 2000. The Double Interpolation and Double Prediction (DIDP) Approach for INSAR and GPS Integration, *IAPRS*, XXXIII.
- Gilbert, L. E., Scholz, C. H. & Beavan, J., 1994. Strain localization along the San Andreas fault: consequences for loading mechanisms. *J. Geophys. Res.* 99, 23975–23984.
- Giorgetti, F. and Mosetti, F., 1969. General morphology of the Adriatic Sea, *Boll. Geof. Teor. Appl.* 11, 49–56.
- Goldstein, R., 1995. Atmospheric Limitations to repeat-track radar interferometry. *Geophys. Res. Lett.*, 22(18).
- Goldstein, R.M. and Werner, C.L., 1998. Radar interferogram filtering for geophysical applications, *Geophys. Res. Lett.*, 25(21), 4035–4038.
- Guerricchio, A. and Wasowski, J., 1988. Some remarks on the tectonic significance of the paleomagnetic data from Gargano, southern Italy, *Mem. Soc. Geol. It.*, 41, 1263-1269.
- Guidoboni, E. and Tinti, S., 1988. A review of the historical 1627 tsunami in the Southern Adriatic, *Science of Tsunami Hazard* 1, 11–16.
- Guillaume, B., Martinod, J. and Espurt, N., 2009. Variations of slab dip and overriding plate tectonics during subduction: insights from analogue modelling, *Tectonophysics* 463, 167–174.
- Guillaume, B., Funiciello, F., Faccenna, C., Martinod, J. and Olivetti, V., 2010. Spreading pulses of the Tyrrhenian Sea during the narrowing of the Calabrian subduction zone, *Geology*, 38(9), 819–822, doi:10.1130/G31038.1.

- Hanssen, R.F., Weckwerth, T.M., Zebker, H.A. and Klees, R. 1999. High-resolution water vapor mapping from interferometric radar measurements. *Science*, 283, 1,297-1,299.
- Haq, S.S.B. and Davis, D.M., 1997. Oblique convergence and the lobate mountain belts of western Pakistan, *Geology*, 25(1), 23–26.
- Harris, R. A. and Simpson, R., 1992. Changes in a static stress on southern California faults after the 1992 Landers earthquake, *Nature* 360, 251-254.
- Harris, R.A. and Day, S.M., 1993. Dynamics of fault interaction: parallel strike slip fault, *J. Geophys. Res.* 98, 4461-4472.
- Harris, R. A., Simpson, R. and Reasenber, P. A., 1995. Influence of static stress changes on earthquake locations in southern California, *Nature*, 375, 221-224.
- Hatzfeld, D., Martinod, J., Bastet, G. and Gautier, P., 1997. An analog experiment for the Aegean to describe the contribution of gravitational potential energy. *Journal of Geophysical Research* 102, 649–659.
- Hearn, E., Burgmann, R. and Reilinger, R., 2002. Dynamics of Izmit earthquake postseismic deformation and loading of the Duzce earthquake hypocenter, *Bull. Seismol. Soc. Am.*, 92(1), 172– 193.
- Henstock, T., Levander, A. and Hole, J., 1997. Deformation in the lower crust of the San Andreas fault system in northern California, *Science*, 278, 650– 653.
- Hergert, T. and Heidbach, O., 2010. Slip-rate variability and distributed deformation in the Marmara Sea fault system. *Nature Geoscience* 3, 132 - 135, doi:10.1038/ngeo739.
- Hetland, E.A. and Hager, B.H., 2006. The effects of rheological layering on postseismic deformation: *Geophysical Journal International*, v. 116, p. 277–292.
- Heuret, A., Funicello, F., Faccenna, C. and Lallemand, S., 2007. Plate kinematics, slab shape and back-arc stress: A comparison between laboratory models and current subduction zones: *Earth and Planetary Science Letters*, v. 256, p. 473–483, doi: 10.1016/j.epsl.2007.02.004.
- Hilley, G.E., Buergermann, R., Zhang, P.Z. and Molnar, P., 2005. Bayesian inference of plastosphere viscosities near the Kunlun fault, northern Tibet: *Geophysical Research Letters*, v. 32, L01302, doi: 10.1029/2004GL021658.
- Hilley G. E., Johnson, K.M., Wang, M., Shen, Z.-K. and Bürgmann, R., 2009. Earthquake-cycle deformation and fault slip rates in northern Tibet. *Geology* 2009;37;31-34 doi: 10.1130/G25157A.1
- Hoffmann, J. and Zebker, H.A., 2003. Prospecting for horizontal surface displacements in Antelope Valley, California, using satellite radar interferometry. *Journal of Geophysical Research*, 108(F1): 6011. DOI: 10.1029/2003JF000055

- Hooper, A., 2008. A multi-temporal InSAR method incorporating both persistent scatterer and small baseline approaches, *Geophys. Res. Lett.*, 35, L16302, doi:10.1029/2008GL034654.
- Hooper, A., Zebker, H., Segall, P. and Kampes, B., 2004. A new method for measuring deformation on volcanoes and other natural terrains using InSAR persistent scatterers, *Geophys. Res. Lett.*, 31, L23611, doi:10.1029/2004GL021737.
- Horsfield W.T., 1977. An experimental approach to basement controlled faulting, *Geologie en Mijnbouw*, 56, 363-370.
- Huber, H. 1977. *Geological map of Iran, Sheet, Ser. No.2 and 3, North Central Iran and North East Iran, Scale sheets, scale 1:1 000000*. National Iranian Oil company, Tehran.
- Hubbert, M.K., 1937. Theory of scale models as applied to the study of geologic structures. *Bull. Geol. Soc. Am.* 48, 1459–1520.
- Humayon, M., Lillie, R. and Lawrence, R., 1991. Structural interpretation of the eastern Sulaiman foldbelt and foredeep, Pakistan, *Tectonics*, 10(2), 299–324.
- Hunstad, I, Pepe, A., Atzori, S., Tolomei, C., Salvi, S., & Lanari, R., 2009. Surface deformation in the Abruzzi region, Central Italy, from multitemporal DInSAR analysis. *Geophys. J. Int.* /178, Doi: 10.1111/j.1365-246X.2009.04284.x
- Hunstad, I., Selvaggi, G., D'Agostino, N., England, P., Clarke, P. and Pierozzi, M., 2003. Geodetic strain in peninsular Italy between 1875 and 2001, *Geophys. Res. Lett.*, 30(4), 1181, doi: 10.1029/2002GL016447.
- Jackson, J. and Mckenzie D., 1984. Active tectonics of the Alpine-Himalayan Belt between Turkey and Pakistan. *Geophys. J. R. astr. Soc.*, 77(1), 214-245.
- Jackson, J., Haines, J. & Holt, W., 1995. The accommodation of Arabia–Eurasia plate convergence in Iran. *J. geophys. Res.*, 100(B8), 15 205–15 219.
- Jadoon, I.A.K. and Kurshid, A., 1996. Gravity and tectonic models across the Sulaiman fold belt and the Chaman fault zone in western Pakistan and eastern Afghanistan, *Tectonophysics*, 254, 89–109.
- Jadoon, I.A.K., Lawrence, R.D. and Lillie, R., 1993. Evolution of foreland structures: an example from the Sulaiman thrust lobe of Pakistan, southwest of the Himalayas, in *Himalayan Tectonics*, edited by Treloar P.J. and Searle M.P., no. 74 in Special Publications, pp. 589–602, Geological Society, London, London, UK, doi:10.1144/GSL.SP.1993.074.01.39.
- Jaeger, J.C. and Cook, N.G.W., 1979. *Fundamentals of Rock Mechanics*, Chapman and Hall, London.

- Johnson, K. M. and Segall, P., 2004. Viscoelastic earthquake cycle models with deep stress-driven creep along the San Andreas fault system *J. Geophys. Res.*, 109, B10403, doi:10.1029/2004JB003096.
- Jones, A., (Ed.), 1961. Reconnaissance Geology of part of West Pakistan, a Columbo Plan cooperative project, *Hunting Survey Report, Government of Pakistan*, Oshawa.
- Khan, K., 1998. Determination of focal mechanisms and hypocenters for the mainshock and aftershocks of the 1997 Quetta earthquake in Pakistan, *Individual Studies by Participants to the International Institute of Seismology and Earthquake Engineering*, 34, 131–139.
- Keep, M. and McClay, K.R., 1997. Analogue modelling of multiphase rift systems. *Tectonophysics* 273, 239–270.
- Kenner, S. J. and Segall, P., 2003. Lower crustal structure in northern California: Implications from strain rate variations following the 1906 San Francisco earthquake, *J. Geophys. Res.*, 108(B1), 2011, doi:10.1029/2001JB000189.
- King, N. E., and Savage, J. C., 1984. Regional deformation near Palmdale, California, 1973-1983, *J. Geophys. Res.*, 89, 2471-2477.
- King, G.C.P., Stein, R.S. and Lin, J., 1994. Static stress change and the triggering of earthquakes, *Bull Seism. Soc. Am.* 84, 935-953.
- Krantz, R.W., 1991. Measurements of friction coefficients and cohesion for faulting and fault reactivation in laboratory models using sand and sand mixtures. *Tectonophysics* 188, 203–207.
- Lallemand, S.E., Malavieille, J. and Calassou, S., 1992. Effects of oceanic ridge subduction on accretionary wedges: experimental modeling and marine observations. *Tectonics* 11, 1301–1313.
- Langbein, J., Borchardt, R., Dreger, D., Fletcher, J., Hardebeck, J.L., Hellweg, M., Ji, C., Johnston, M., Murray, J.R., Nadeau, R., Rymer, M. J. and Treiman, J.A., 2005. Preliminary report on the 28 September 2004, M 6.0 Parkfield, California Earthquake. *Seismol. Res. Lett.*, 76, 10-26.
- Lapusta, N., Rice, J.R., Ben-Zion, Y. and Zheng, G.T., 2000. Elastodynamic analysis for slow tectonic loading with spontaneous rupture episodes on faults with rate- and state-dependent friction, *J. Geophys. Res.*, 105(B10), 23765-23789.
- Levenberg, K., 1944. A Method for the Solution of Certain Non-Linear Problems in Least Squares, *The Quarterly of Applied Mathematics*, 2, 164–168.
- Li, V. C., Rice, J. R., 1987. Crustal Deformation in Great California Earthquake Cycles, *J. Geophys. Res.*, 92, 11,533-551.

- Li, Z., 2005. *Correction of atmospheric water vapor effects on repeat pass SAR interferometry using GPS, MODIS and MERIS data*, Ph.D. thesis, University College London, London.
- Li, Z., Muller, J., Cross, P. and Fielding, E. J., 2005. Interferometric synthetic aperture radar (InSAR) atmospheric correction: GPS, Moderate Resolution Imaging Spectroradiometer (MODIS), and InSAR integration, *J. Geophys. Res.*, 110, B03410, doi:10.1029/2004JB003446.
- Lindh, A.G., et al., 1978. *Parkfield Prediction Program, Branch of Seismology*, USGS, 8-9930-02098, P.B. 2, 276-280.
- Linker, M. and Rice, J., 1997. Models of postseismic deformation and stress transfer associated with the Loma Prieta earthquake, in *The Loma Prieta, California Earthquake of October 17, 1989: Aftershocks and Postseismic Effects*, *U.S. Geol. Surv. Prof. Pap.*, 1550-D, D253–D275.
- Lisowski, M., Savage, J.C. and Prescott, W.H., 1991. The velocity field along the San Andreas fault in central and southern California, *J. Geophys. Res.*, 96,
- Lombardi, S., Billi, A., Angelone, M., Brunori, C. A., Ciotoli, G., Di Filippo, M., Doumaz, F., Duddridge, G. A., Funicello, R., Fytikas, M., Grainger, P., Guerra, M., Marty, B., Orlandi, C., Papachristou, M., Pavlidis, S., Pizzino, L., Pongetti, F., Quattrocchi, F., Romeo, G., Sacchi, E., Salvi, S., Salvini, F., Scarlato, P., Sciacca, U., Soulakellis, N., Taccetti, Q., Urbini, G., Zouros, N., and Zuppi, G. M.: 1998, Final report of the “*Geochemical Seismic Zonation*” EC Program, EC Contract N. ENV4-CT96-0291, DG XII, Bruxelles, Belgium.
- Lundgren, P., Usai, S., Sansosti, E., Lanari, R., Tesauro, M., Fornaro, G. and Berardino, P., 2001. Modeling surface deformation observed with SAR interferometry at Campi Flegrei Caldera, *J. Geophys. Res.*, vol. 106, pp. 19 355–19 367.
- Mallorquí, J. J., Blanco, P., Sanz-Marcos, J., Duque, S. and Navarrete, D., 2005. Application of the coherent pixels technique (CPT) to large ERS and ENVISAT SAR images for deformation series retrieval, in *Proc. FRINGE*, Frascati, Italy, Nov. 28–Dec. 2,
- Marin, G., 1998. Oscillatory rheometry. In: Collyer, A.A., Clegg, D.W. (Eds.), *Rheological Measurements*. Chapman and Hall, London, pp. 5–46.
- Marquardt, D., 1963. An Algorithm for Least-Squares Estimation of Nonlinear Parameters, *SIAM J. on Applied Mathematics*, 11, 431–441
- Mart Y., Aharonov, E., Mulugeta, G., Ryan, W., Tentler, T. and Goren, L., 2005. Analogue modelling of the initiation of subduction, *Geophysical Journal International*, 160, (3), 1081–1091.
- Masse, J. P. and Borgomano, J., 1987. Un modele de la transtion plate-forme – bassin carbonates controle par des phenomenes tectoniques: le Cretace du Gargano (Italie meridionale), *C.R. Acad. Sc. Paris* 304(10), 521–526.

- Masse, J. P. and Luperto, Sinni, E., 1987. A platform to basin transition model: the lower Cretaceous carbonates of the Gargano Massif (Southern Italy), *Mem. Soc. Geol. It.* 40, 99–108.
- Masson, F., Anvari, M., Djamour, Y., Walpersdorf, A., Tavakoli, F., Daignieres, M., Nankali, H., Van Gorp, S. 2007. Large-scale velocity field and strain tensor in Iran inferred from GPS measurements: new insight for the present-day deformation pattern within NE Iran. *Geoph. Journ. Int.*, 170, 436-440, doi: 10.1111/j.1365- 246X.2007.03477.x.
- Massonnet, D. and Feigl, K. L. 1995a. Discrimination of geophysical phenomena in satellite radar interferograms. *Geophys. Res. Lett.*, 22(12), 1,537-1,540.
- Massonnet, D. and Feigl, K. L., 1998b. Radar Interferometry and its application to changes in the earth's surface. *Rev. Geophys.*, 36(4), 441-500.
- Massonnet, D., Rossi, M., Carmona, C., Adragna, F., Peltzer, G., Feigl, K., and Rabaute, T. 1993. The displacement field of the Landers earthquake mapped by radar interferometry. *Nature*, 364, 138-142.
- McClay, K.R., 1990. Deformation mechanics in analogue models of extensional fault systems. *Geological Society of London Special Publications* 54, 445–453.
- McGarr, A., Zoback, M.D. and Hanks, T. C., 1982. Implications of an elastic analysis of in-situ stress measurements near the San Andreas fault, *J. Geophys. Res.*, 87, 7797-7896.
- Meade, B.J., 2007. Present-day kinematics at the India-Asia collision zone; *Geology*, v. 35, p. 81–84, doi: 10.1130/G22924A.1.
- Meade, B J. and Hager B.H., 2005. Block models of crustal motion in southern California constrained by GPS measurements, *J. Geophys. Res.*, 110, B03403, doi:10.1029/2004JB003209.
- Meissner, R., and Strehlau J., 1982. Limits of stress in continental crusts and their relation to the depth-frequency distribution of shallow earthquakes, *Tectonics*, 1, 73-89.
- Mériaux, A.S., Ryerson, F.J., Tapponnier, P., Van der Woerd, J., Finkel, R.C., Xu, X., Xu, Z. and Caffee, M.W., 2004. Rapid slip along the central Altyn Tagh fault: Morphochronologic evidence from Cherchen He and Sulamu Tagh: *Journal of Geophysical Research*, v. 109, B06401, doi: 10.1029/2003JB002558.
- Mezger, T.G., 2002. In: Ulrich, Zorll (Ed.), *The Rheology Handbook: For Users of Rotational and Oscillatory Rheometers*. Hannover, Germany.
- Mohajer-Ashjai, A. 1975). *Recent and contemporary crustal deformation in eastern Iran*. Ph.D. thesis, Imperial college, London.

- Mongelli, F. and Ricchetti, G., 1970. Heat flow along the Candelaro Fault – Gargano Headland (Italy), *Geothermics* 2 (special issue), 450–458.
- Monti, G. A., Prati, C., 2000. ERS-ENVISAT Combination for Interferometry and Super-resolution, *ERSENVISAT Symposium*, Gothenburg, Sweden, 16-20.
- Mora, O., Mallorqui, J. J., Duro, J. and Broquetas, A., 2001. Long-term subsidence monitoring of urban areas using differential interferometric SAR techniques, in Proc. *IGARSS*, vol. 3, Sydney, Australia, pp.1104-1106.
- Mora, O., Lanari, R., Mallorqui, J.J., Berardino, P. and Sansosti, E., 2002. A new algorithm for monitoring localized deformation phenomena based on small baseline differential SAR interferograms. Proc. *IGARSS*, Toronto, ON, Canada, 1237-1239.
- Mora, O., Mallorquí, J.J. and Broquetas, A., 2003. Linear and nonlinear terrain deformation maps from a reduced set of interferometric SAR images, *IEEE Trans. Geosci. Remote Sensing*, vol. 41, pp. 2243-2253.
- Moroni, M. and Cenedese, A., 2005. Comparison among feature tracking and more consolidated velocimetry image analysis techniques in a fully developed turbulent channel flow, *Meas. Sci. Technol.* 16, 2307–2322.
- Murray, M. H. and Segall, P., 2001. Modeling broadscale deformation in northern California and Nevada from plate motions and elastic strain accumulation, *Geophys. Res. Lett.*, 28.
- Naylor M.A., Mandl, G. and Sijpesteijn, C.H., 1986. Fault geometries in basement-induced wrench faulting under different internal states, *J. Struct. Geol.*, 8 737- 752.
- Nieuwland, D.A. and Walters, J.V., 1993. Geomechanics of the South Furious field. An integrated approach towards solving complex structural geological problems, including analogue and finite-element modelling, *Tectonophysics* 226, pp. 143–166, 1993.
- Nostro, C, Cocco, M. and Belardinelli, M. E., 1997. Static Stress Changes in Extensional Regimes' An Application to Southern Apennines (Italy). *Bulletin of the Seismological Society of America*, Vol. 87, No. 1, pp. 234-248,
- Nowick, A.S. and Berry, B.S., 1972. Anelastic Relaxations in Crystalline Solids. *Academic, Press Inc.*, New York. 677 pp.
- Nur, A. and Mavko, G., 1974. Postseismic viscoelastic rebound, *Science*, v. 183, p. 204–206, doi: 10.1126/science.183.4121.204.
- Okada, Y., 1985. Surface deformation due to shear and tensile faults in a half-space. *Bull. Seismol. Soc. Am.*, 75, 1135–1154.
- Ortolani, F. and Pagliuca, S., 1988. Il Gargano (Italia meridionale): Un settore di “avampaese” deformato tra le catene Appenninica e Dinarica: *Mem. Soc. Geol. It.*, v. 41, p. 1245–1252.

- Pantosti, D., Schwartz, D.P., Valensise, G., 1993. Paleoseismology Along the 1980 Surface Rupture of the Irpinia Fault: Implications for Earthquake Recurrence in the Southern Apennines, Italy. *J. Geophys. Res.*, vol. 98, n. b4, pp. 6561-6577, doi:10.1029/92JB02277
- Parotto, M. and Praturlon, A., 1981. Structural Sketch of the Middle-Eastern Mediterranean Area. *CNR-PFG, Publ.* 269, G.E.O. Roma.
- Parsons, T., 1998. Seismic reflection evidence that the Hayward fault extends into the lower crust of the San Francisco Bay area, California, *Bull. Seismol. Soc. Am.*, 88, 1212– 1223.
- Parsons, T. 2002. Post-1906 stress recovery of the San Andreas fault system calculated from three-dimensional finite element analysis, *J. Geophys. Res.*, 107(B8), 2162, doi:10.1029/2001JB001051.
- Parsons, T. and Hart, P., 1992. Dipping San Andreas and Hayward fault revealed beneath San Francisco Bay, California, *Bull. Seismol. Soc. Am.*, 82, 454– 480.
- Parsons, B., Wright, T. J., Rowe, P., Andrews, J., Jackson, J., Walker, R., Khatib, M., Talebian, M., Bergman, E. and Engdahl, E. R., 2006. The 1994 Sefidabeh (eastern Iran) earthquakes revisited: new evidence from satellite radar interferometry and carbonate dating about the growth of an active fold above a blind thrust fault, *Geophys. J. Int.*, 164, 202-217, doi:10.1111/j.1365-246X.2005.02655.x.
- Patacca, E. and Scandone, P., 2004. The 1627 Gargano earthquake (southern Italy): Identification and characterization of the causative fault, *Journal of Seismology*, v. 8, p. 259–273, doi: 10.1023/B:JOSE.0000021393.77543.1e.
- Peltzer, G., Tapponnier, P. and Armijo, R., 1989. Magnitude of late Quaternary left-lateral displacements along the north edge of Tibet: *Science*, v. 246, p. 1285–1289, doi: 10.1126/science.246.4935.1285.
- Pepe, A., Sansosti, E. and Berardino, P., 2005. On the generation of ERS/ ENVISAT DInSAR time series via the SBAS technique. *IEEE Geosci. and Remote Sensing Letters* , 2 (3) : 265-269.
- Peronaci, M., 1980. Zonizzazione sismica del Gargano: analisi statistiche, *Boll. Geof. Teor. Appl.* 22(85), 23–28.
- Pollitz, F.F., 2001. Mantle flow beneath a continental strike-slip fault: Postseismic deformation after the 1999 Hector Mine earthquake: *Science*, v. 293, p. 1814–1818, doi: 10.1126/science.1061361.
- Pollitz, F., Wicks, C. and Thatcher, W., 2001. Mantle flow beneath a continental strike-slip fault: Postseismic deformation after the 1999 Hector Mine earthquake, *Science*, 293, 1814– 1818.

- Pollitz, F.F., and Sacks, I.S., 1992. Modeling of postseismic relaxation following the great 1857 earthquake, southern California: *Seismological Society of America Bulletin*, v. 82, p. 454–480.
- Pondrelli, S., Salimbeni, S., Ekström, G., Morelli, A., Gasperini, P. and Vannucci, G., 2006. The Italian CMT dataset from 1977 to the present, *Phys. Earth Planet. Int.*, doi:10.1016/j.pepi.2006.07.008,159/3-4, pp. 286-303.
- Prati, C., Ferretti, A. and Perissin, D., 2008. Recent Advances on Surface Ground deformation measurement by means of repeated space-borne SAR observations, *Journal of Geodynamics*, doi:10.1016/j.jog.2009.10.011.
- Prescott, W. H., Savage, J. C. and Kinoshita, W. T., 1979. Strain accumulation rates in the western United States between 1970 and 1978, *J. Geophys. Res.*, 84, 5423-5435.
- Price, E. J. and Sandwell, D. T., 1998. Small-scale deformations associated with the 1992 Landers, California, earthquake mapped by synthetic aperture radar interferometry phase gradients, *J. Geophys. Res.*, 103, B27001-27016.
- Quittmeyer, R., Kafka, A.L. and Armbruster, J.G., 1984. Focal mechanisms and depths of earthquakes in central Pakistan: a tectonic interpretation, *J. Geophys. Res.*, 89, doi:10.1029/JB089iB04p02459.
- Ramberg, H., 1967. *Gravity, Deformation and the Earth's Crust*. Academic Press, London, 1967.
- Ramberg, H., 1981. *Gravity, Deformation and the Earth's crust*. New York, p. 452, 1981.
- Ratschbacher, L., Merle, O., Davy, P. and Cobbold, P., 1991. Lateral extrusion in the Eastern Alps, part 1: boundary conditions and experiments scaled for gravity. *Tectonics* 10, 245–256, 1991.
- Reasenber, P.A. and Simpson, R.W., 1992. Response of regional seismicity to the static stress change produced by the Loma Prieta earthquake, *Science* 255, 1687-1690.
- Reches, Z., Schubert, G. and Anderson, C., 1994. Modeling of periodic great earthquakes on the San Andreas fault: Effects of nonlinear crustal rheology, *J. Geophys. Res.*, 99, 21,983–22,000.
- Regard, V., Bellier, O., Thomas, J. C., Abbassi, M. R., Mercier, J., Shabanian, E., Fegghi, K., Soleymani, S., 2004. Accommodation of Arabia-Eurasia convergence in the Zagros - Makran transfer zone, SE Iran: A transition between collision and subduction through a young deforming system. *Tectonics*, 23, TC4007, doi: 10.1029/2003TC001599,.
- Reid, H.F., 1910. The mechanics of the earthquake. In: *The California Earthquake of 18 April, 1906: Report of the State Earthquake Investigation Commission, 2. Washington: Carnegie Institution.*

- Reilinger, R., *et al.*, 2006. GPS constraints on continental deformation in the Africa-Arabia-Eurasia continental collision zone and implications for the dynamics of plate interactions. *Journ. Geoph. res.*, 111, B05411, doi: 10.1029/2005JB004051.
- Reilinger, R., Ergintav, S., Bürgmann, R., McClusky, S., Lenk, O., Barka, A., Gurkan, O., Hearn, L., Feigl, K.L., Cakmak, R., Aktug, B., Ozener, H., & Töksoz, M.N., 2000. Coseismic and postseismic slip for the 17 August 1999, M=7.5, Izmit, Turkey earthquake. *Science*, 289, 1,519-1,524.
- Rice, J. R., 1993. Spatiotemporal Complexity of Slip on a Fault, *J. Geophys. Res.*, 98(B6), 9885-9907.
- Richard, P., 1991. Experiments on faulting in a two-layered cover sequence overlying a reactivated basement fault with oblique-slip. *Journal of Structural Geology* 13, 459–469.
- Richard, P. and Krantz, R.W., 1991. Experiments on fault reactivation in strike-slip mode. *Tectonophysics* 188, 117–131.
- Richard, P.D., Moquet, B. and Cobbold, P.R., 1991. Experiments on simultaneous faulting and folding above a basement wrench fault. *Tectonophysics* 188, 133–141.
- Richard, P.D., Naylor, M.A. and Koopman, A., 1995. Experimental models of strike-slip tectonics. *Petroleum Geoscience* 1, 71– 80.
- Richetti, G, Ciarafi, N., Luperto Sinni, E., Mongelli, F. and Pieri, P., 1992. Geodinamica ed evoluzione sedimentaria e tettonica dell'avampaese apulo. *Mem. Soc. Geol. It.*, 41, 57-82.
- Rosen, P., Werner, C., Fielding, E., Hensley, S., Buckley, S. and Vincent, P., 1998. Aseismic creep along the San Andreas Fault northwest of Parkfield, CA measured by radar interferometry, *J. Geophys. Res.*, 25, 825-828.
- Rosenau, M., Lohrmann, J. and Oncken, O., 2009. Shocks in a box: An analogue model of subduction earthquake cycles with application to seismotectonic forearc evolution, *J. Geophys. Res.*, 114, B01409, doi:10.1029/2008JB005665.
- Rossi, D. and F. Storti, 2003. New artificial granular materials for analogue laboratory experiments: Aluminium and siliceous microspheres, *J. Struct. Geol.*, 25, 1893–1899.
- Rowlands, D., 1978. The structure and seismicity of a portion of the southern Sulaiman Range, Pakistan, *Tectonophysics*, 51, 41–56.
- Salvi, S., Quattrocchi, F., Brunori, C.A., Doumaz, F., Angelone, M., Billi, A., Buongiorno, F., Funicello, R., Guerra, M., Mele, G., Pizzino, L. and Salvini, F., 2000. A multidisciplinary approach to earthquake research: implementation of a Geochemical Geographic Information System for the Gargano site, southern Italy. *Nat. Hazards* 20, 255–278.

- Savage, J.C. and Lisowski, M., 1998. Viscoelastic coupling model of the San Andreas fault along the big bend, southern California. *Journal of Geophysical Research*, v. 103, p. 7281–7292.
- Savage, J.C., 1990. Equivalent strike-slip earthquake cycles in half-space and lithosphere-asthenosphere earth models, *J. Geophys. Res.*, 95, 4873–4879.
- Savage, J. C., 1983. Strain accumulation in western United States, *Annu. Rev. Earth Planet. Sci.*, 11, 11-43.
- Savage, J., and Prescott W., 1978. Asthenosphere readjustment and the earthquake cycle, *J. Geophys. Res.*, 83, 3369–3376. doi: 10.1029/JB083iB07p03369.
- Savage, J. C. and Burford, R. O., 1973. Geodetic determination of relative plate motion in central California, *J. Geophys., Res.*, 78, 832-845. doi: 10.1029/JB078i005p00832.
- Schellart, W.P., 2000. Shear test results for cohesion and friction coefficients for different granular materials: scaling implications for their usage in analogue modeling. *Tectonophysics* 324, 1–16, 2000.
- Schellart, W.P., 2004. Kinematics of subduction and subduction-induced flow in the upper mantle. *Journal of Geophysical Research* 109, B07401, doi:10.1029/2004JB002970.
- Schelling, D. (1999), Geological map of the Bolan Block and Quetta Syntaxis regions, *EGI Technical Report 5-20885-99*, Energy and Geoscience Institute, University of Utah, Salt Lake City, Utah.
- Scholz C.H., 1998. Earthquakes and friction laws, *Nature*, 39 1, 37-42.
- Scholz, C.H., 1990. *The Mechanics of Earthquakes and Faulting*. Cambridge: Cambridge University Press.
- Scholz, C.H., & Kato, T. 1978. The behavior of a convergent plate boundary: crustal deformation in the south Kanto District, Japan. *J. Geophys. Res.*, 83, 783-791.
- Segall, P., 2002. Integrating geologic and geodetic estimates of slip rate on the San Andreas fault system, *Int. Geol. Rev.*, 44, 62–82.
- Selvaggi, G., 1998. Spatial distribution of horizontal seismic strain in the Apennines from historical earthquakes, *Annali di Geofisica*, 41, 241–251.
- Shabanian, E., Siame, L., Bellier, O., Benedetti, L., Abbassi, M. R. 2009a. Quaternary slip rates along the northeastern boundary of the Arabia–Eurasia collision zone (*Koppeh Dagh Mountains, Northeast Iran*). *Geophysical Journal International*, 1-23, doi: 0.1111/j.1365-246X.2009.04183.x.

- Shabanian, E., Bellier, O., Siame, L., Arnaud, N., Abbassi M. R., and Cocheme J.-J., 2009b. New tectonic configuration in NE Iran: Active strike-slip faulting between the Kopeh Dagh and Binalud mountains. *Tectonics*, 28, TC5002, doi: 10.1029/2008TC002444
- Shapiro, I.I., Zisk, S.H., Rogers, A.E.E., Slade, M.A., and Thompson, T.W. 1972. Lunar topography: global determination by radar. *Science*, 178, 939 - 948.
- Shimazaki, K. and Nakata, T., 1980. Time-predictable recurrence model for large earthquakes. *Geoph. Res. Lett.*, vol. 7, no. 4, 279-282.
- Sibson, R. H., 1982. Fault zone models, heat flow, and the depth distribution of earthquakes in the continental crust of the United States, *Bull. Seismol. Soc. Am.*, 72, 151-163.
- Simpson, R.W. and Reasenber, P.A., 1994. Earthquake-induced static stress changes on central California faults, Robert W. Simpson (Editor), *U.S. Geol. Surv. Profess. Pap.* 1550-F, F55-F89.
- Smith, B. and Sandwell, D., 2004. A three-dimensional semianalytic viscoelastic model for time-dependent analyses of the earthquake cycle, *J. Geophys. Res.*, 109, B12401, doi:10.1029/2004JB003185.
- Stein, R.S., King, G.C.P. and Lin, J., 1992. Change in failure stress on the southern San Andreas fault system caused by the 1992 magnitude = 7.4 Landers earthquake, *Science* 258, 1328-1332.
- Stein, R.S., King G.C.P. and Lin, J., 1994. Stress triggering of the 1994 M = 6.7 Northridge, California, earthquake by its predecessors, *Science* 265, 1432-1435.
- Steketee, J.A., 1958. On Volterra's Dislocations in a Semi-infinite Elastic Medium. *Can. J. Phys.*, 36, 192-205.
- Stocklin, J. & Nabavi, M.H. 1973. *Tectonic map of Iran, Scale, 1: 2 500 000*. Geol. Surv. of Iran, Tehran.
- Suhadolc, P., Zadro, M., and Panza, G. F., 1983. Seismic behaviour of the Gargano region in the frame of the Southern Apennines seismicity, *Boll. Geof. Teor. Appl.* 25, 97–104.
- Suhadolc, P. and Panza, G. F., 1989. Physical properties of the lithosphere-asthenosphere system in Europe from geophysical data, In: A. Boriani, M. Bonafede, G. B. Piccardo, and G. B. Vai. (eds), *The Lithosphere in Italy*, Vol. 80, Acc. Naz. Lincei, pp. 15–40.
- Sverrir Guemundsson, 2000. Crustal Deformation Mapped by Combined GPS and INSAR: [M. S.Thesis], Iceland: Technical University.
- Szeliga, W. M., 2010. Historical and Modern Seismotectonics of the Indian Plate with an Emphasis on its Western Boundary with the Eurasian Plate. *PhD thesis, University of Colorado*.

- Tavakoli, F., 2007. *Present-day kinematics of the Zagros and east Of Iran faults*. Ph.D. thesis, university of Joseph Fourier, Grenoble, France.
- Tchalenko, J. S. 1973a. The Kashmar (Turshiz) 1903 and Torbat-e-Heidariyeh (south) earthquakes in Central Khorassan (Iran). *Annali de geofisica*, 26(1), 29-40.
- Tchalenko, J. S., Berberian, M., Behzadi, H., 1973b. Geomorphic and seismic evidence for recent activity on the Doruneh Fault, Iran. *Tectonophysics*, 19, 333-341.
- Thatcher, W., 1975. Strain accumulation and release mechanism of the 1906 San Francisco earthquake, *J. Geophys. Res.*, 80, 4862-4872.
- Thatcher, W., 1978. Nonlinear strain buildup and the earthquake cycle on the San Andreas fault. *J. Geophys. Res.* 88, 5893–58902.
- Thatcher, W., 1983. Non linear strain build-up and the earthquake cycle on the San Andreas fault. *J. Geophys. Res.*, 88, 5893-5902.
- Thatcher, W., 1984. The earthquake deformation cycle, recurrence and the time-predictable model. *J. Geophys. Res.*, 89, 5,674-5,680.
- Thatcher, W., 2007. Microplate model for the present-day deformation of Tibet: *Journal of Geophysical Research*, v. 112, B01401, doi: 10.1029/2005JB004244.
- Thatcher, W., & Rundle, J.B., 1984. A viscoelastic coupling model for the cyclic deformation due roperiodically repeated earthquakes at subduction zones. *J. Geophys. Res.*, 89, 7,631-7,640.
- Tinti, S., Maramai, A. and Favali, P., 1995. The Gargano promontory: an important seismogenic tsunamigenic area, *Marine Geology* 122, 227–241.
- Tinti, S. and Piatanesi, A., 1997. Numerical simulations of the tsunami induced by the 1627 earthquake affecting Gargano, Southern Italy, *J. Geodynamics* 21, 141–160.
- Trasatti, E., Kyriakopoulos, C. and Chini, M., 2011. Finite element inversion of DInSAR data from the Mw6.3 L'Aquila earthquake, 2009 (Italy), *Geophys. Res. Lett.*, 38, L08306, doi:10.1029/2011GL046714.
- Tse, S. T. and Rice, J. R., 1986. Crustal earthquake instability in relation to the depth variation of frictional slip properties, *J. Geophys. Res.*, 91, 9452-9472.
- Turcotte, D. L., and Spence D. A., 1974. An analysis of strain accumulation on a strike-slip fault, *J. Geophys. Res.*, 79, 4407-4412.
- Usai, S., Hanssen, R., 1997. Long time scale INSAR by means of high coherence features, *Proc.3rd ERS Symposium*, Florence, Italy, March 1997, available at <http://florence97.erssymposium.org>:80.

- Usai, S. and Klees, R., 1998. On the Feasibility of Long Time Scale INSAR, *Proc. of 1998 Int. Geoscience and Remote Sensing Symp. (IGARSS'98)*, Seattle (WA) 6-10. vol. 5, pp. 2448-2450.
- Usai, S., Delgado, C., Borgstrom, S. and Achilli, V., 1999a. Monitoring terrain deformations at Phlegrean Fields with SAR interferometry, 2nd International *Workshop on SAR Interferometry (FRINGE99)*, European Space Agency, Liege, Belgium.
- Usai, S., Klees, R., 1999b. On the interferometric characteristics of anthropogenic features. *Proc. 1999 Int. Geoscience and Remote Sensing Symp. (IGARSS'99)*, vol. 3, Hamburg, June 28-July 2.
- Usai, S., 2001. *A new approach for long term monitoring of deformations by differential SAR interferometry*, Ph.D. thesis, Delft Univ. of Technol., Delft, The Netherlands. Williams.
- Usai, S., 2002. A least-squares approach for long-term monitoring of deformations with differential SAR interferometry, in *Proc. IGARSS 2002*, vol. 2, Toronto, ON, Canada, pp. 1247–1250.
- Valensise, G., Pantosti, D. and Basili, R., 2004. Seismology and tectonic setting of the 2002 Molise, Italy, earthquake: *Earthquake Spectra*, v. 20, p. S23–S37, doi: 10.1193/1.1756136.
- Vannucci G., Pondrelli S., Argnani A., Morelli A., Gasperini P. and Boschi E., 2004. An Atlas of Mediterranean Seismicity, *Ann. of Geophys.*, Volume spec., 47,1, 247-306.
- Vendeville, B., Cobbold, P.R., Davy, P., Brun, J.P. and Choukroune, P., 1987. Physical models of extensional tectonics at various scales, in Coward M.P., Dewey J.F. & Hancock P.L. (eds) *Continental Extensional, Tectonics*, 1987.
- Vernant, P., Nilforoushan, F., Hatzfeld, D., Abbassi, M.R., Vigny, C., Masson, F., Nankali, H., Martinod, J., Ashtiani, A., Bayer, R., Tavakoli, F., Chéry, J., 2004. Present-day crustal deformation and plate kinematics in the Middle East constrained by GPS measurements in Iran and northern Oman. *Geophys. J. Int.*, 157, 381–398.
- Volterra, Par M. Vito, 1907. L'Equilibre des Corps Elastiques. *Ann. Ec. Norm.*, 3(XXXIV), 401-517.
- Walker, R. & Jackson, J., 2004. Active tectonics and late Cenozoic strain distribution in central and eastern Iran. *Tectonics*, 23, TC5010, doi:10.1029/2003TC001529.
- Wallace, K., Yin, G.H. and Bilham, R., 2004. Inescapable slow slip on the Altyn Tagh fault: *Geophysical Research Letters*, v. 31, L06613, doi: 10.1029/2004GL021014.
- Ward, S.N., 1994. Constraints on the seismotectonics of the Central Mediterranean from Very Long Baselines Interferometry, *Geophys. J. Int.*, 117, 441-452.

- Weijermars, R. and Schmeling, H., 1986. Scaling of newtonian and non newtonian fluid dynamics without inertia for quantitative modelling of rock flow due to gravity (including the concept of rheological similarity), *Physics of the Earth and Planetary Interiors*, 43, 316-330.
- Wellman, H.W., 1966. Active wrench faults of Iran, Afghanistan and Pakistan. *Geologische Rundschau*, 55, 716–735.
- Wells, D.L., and Coppersmith, K.J., 1994. New empirical relationships among magnitude, rupture length, rupture width, and surface displacements: *Bulletin of the Seismological Society of America*, v. 84, p. 974-1002.
- Werner, C., Wegmüller, U., Strozzi, T. and Wiesmann, A., 2003. Interferometric Point Target Analysis for Deformation Mapping, *IGARSS'03*, Toulouse, France, 21-25 July 2003.
- Wiley, C.A. 1965. *Pulsed doppler radar methods and apparatus*. United States Patent No. 3,196,436.
- Wright, T, Parsons, B. and Fielding, E., 2001. Measurement of interseismic strain accumulation across the North Anatolian Fault by satellite radar interferometry, *Geoph. Res. Lett.*, 28 (10), 2117-2120.
- Wright, T., 2000. *Crustal Deformation in Turkey from Synthetic Aperture Radar Interferometry*. PhD thesis, Wolfson College, Oxford
- Yu, T., Rundle, J., & Fernandez, J., 1999. Correction to “Surface deformation due to a strike-slip fault in an elastic gravitational layer overlying a viscoelastic gravitational half-space” by Ting-To Yu, John B. Rundle and José Fernández., *J. Geophys. Res.*, 104(B7), 15,313-15,315.
- Zebker, H. A. and Villasenor, J., 1992. Decorrelation in interferometric radar echoes, *IEEE Trans. Geosci. Remote Sens.*, 30(5), 950– 959.
- Zhu, L., 2000. Crustal structure across the San Andreas fault, southern California from teleseismic converted waves, *Earth Planet. Sci. Lett.*, 179, 183– 190.